Arno Godeke

Performance Boundaries in Nb_3Sn Superconductors

PERFORMANCE BOUNDARIES IN Nb_3Sn SUPERCONDUCTORS

Ph.D. committee:

Prof. dr. ir. A. Bliek, University of Twente (Chairman and Secretary)
Prof. dr. R. Flükiger, University of Geneva
Dr. ir. B. ten Haken, University of Twente
Prof. dr. ir. J.W.M. Hilgenkamp, University of Twente
Prof. dr. ir. H.H.J. ten Kate, University of Twente
Prof. dr. P.H. Kes, Leiden University
Prof. dr. D.C. Larbalestier, University of Wisconsin
Prof. dr. H. Rogalla, University of Twente
Prof. dr. ir. H. Tijdeman, University of Twente

The work described in this thesis was performed in collaboration between the Low Temperature Division, the Special Chair for Industrial Application of Superconductivity at the Faculty of Science and Technology, University of Twente, The Netherlands and the Applied Superconductivity Center at the University of Wisconsin-Madison, USA.

This work was supported by the European Union through the European Fusion Development Agreement, the Netherlands Organization for Scientific Research (NWO) through the Technology Foundation STW, the U.S. Department of Energy, Division of High Energy Physics (Grant No. DEFG02-91ER40643), and also benefited from NSF-MRSEC (Grant No. DMR-9632427) supported facilities. All contributions are greatly acknowledged.

A. Godeke
Performance boundaries in Nb_3Sn superconductors
Ph.D. thesis, University of Twente, Enschede, The Netherlands

ISBN 90-365-2224-2

Cover: A SEM fracture image of A15 in a reacted Powder in Tube wire. Courtesy of P.J. Lee.

Printed by PrintPartners Ipskamp, Enschede

PERFORMANCE BOUNDARIES IN Nb_3Sn SUPERCONDUCTORS

PROEFSCHRIFT

ter verkrijging van
de graad van doctor aan de Universiteit Twente,
op gezag van de rector magnificus,
prof. dr. W.H.M. Zijm,
volgens besluit van het College voor Promoties
in het openbaar te verdedigen
op vrijdag 15 juli 2005 om 15.00 uur

door

Albertus Godeke

geboren op 12 september 1967

te Markelo

Dit proefschrift is goedgekeurd door de promotoren:

prof. dr. ir. H.H.J. ten Kate
prof. dr. D.C. Larbalestier

Assistent promotor:

dr. ir. B. ten Haken

“I remember my friend Johnny von Neuman used to say, with four parameters I can fit an elephant, and with five I can make him wiggle his trunk.”

Quoted after Enrico Fermi by F. Dyson, *Nature* **427**, 297 (2004).

“What I cannot create, I do not understand.”

Richard P. Feynman (1988).

Preface

In front of you is the condensed result of a number of years of investigations on Nb_3Sn superconductors. It is rather amazing that after Nb_3Sn celebrated its 50 year's anniversary in 2004, it is still possible to write a Ph.D. thesis on the subject. This, to my opinion, demonstrates the difficulties we face in understanding the world that surrounds us. Fortunately, we can use Nb_3Sn in technological applications without a complete understanding on a more fundamental level. The applications will benefit, however, from improved properties as a result of a better knowledge of the intrinsic capacities of Nb_3Sn.

This Ph.D. work emerged almost naturally from transport critical current measurements on wires as function of magnetic field, temperature and strain, which were performed at the end of the 1990's in the Low Temperature Division at the University of Twente. These characterizations were done in the frame of the world-wide conductor tests for the International Thermonuclear Experimental Reactor. Part of the task description was to summarize the results using then existing scaling relations for the critical current. It soon became clear that it was not possible to accurately scale the results using existing relations. Moreover, the existing relations were empirical and did not yield any insight on the underlying physics. We therefore modified them and found that improvements in fit accuracy were indeed possible. We thus arrived at the level of fitting von Neuman's elephant on the previous page. The improved set of relations yielded an accurate description of the critical surface of Nb_3Sn wires on a macroscopic level, but with a significant number of free parameters with an unclear meaning. It was evident that mainly the field-temperature phase boundary of wires was very vaguely defined. Also, we realized that superconductivity in Nb_3Sn could be reasonably well described by the microscopic theory, but we had no idea to what extend that knowledge could be applied to technological wires. At the same time the achieved non-copper critical current density was slowly but surely progressing, partly as a result of the US conductor development program. This rose the question to what level the current densities could be ultimately improved.

We wanted to arrive at the next level of knowing what exactly limits the achievable critical current density in Nb_3Sn wires, and thus allowing moving these limits according to Feyman on the previous page. To do this, we needed to look inside the wire and approach the problem on a microscopic level. At that time, the Applied Superconductivity Center at the University of Wisconsin-Madison was studying the effects of various reaction conditions on the critical properties of Nb_3Sn wires using magnetic techniques. Agreements were made so that I could stay a few years in Madison and learn about the material science of superconductors. In this way, we could combine some of the specific expertises of both institutes. The research in Madison focused towards a detailed investigation of the field-temperature phase boundary in wires and how it is influenced by the compositional inhomogeneities that are always present. The effects of inhomogeneities on the critical current carrying capabilities became one of the main thrusts of this thesis work.

In analyzing all the results I became aware of the magnitude of the task I confronted myself with. Attempting to improve empirical scaling relations with better founded alternatives requires thorough knowledge of material science, mechanics, pinning theories and solid state physics. I felt especially humbled by the mathematics involved in the microscopic theory of superconductivity. As an experimental physicist, I simply do not follow all the calculations involved and have to interpret the publications on the subject as described by Dirac who said: "I understand what an equation means if I have a way of figuring out the characteristics of its

solution without actually solving it." I further hope that choosing such a broad subject still results in sufficient depth in the research involved. Maybe through clarification of the upper critical field versus temperature that appears in wires and by improving on the temperature and strain dependent descriptions in scaling relations for the critical current density, I have contributed a few cents to 50 years of Nb_3Sn knowledge.

Arno Godeke Enschede, June 2005

Acknowledgments

First off, I want to emphasize that research like this is always a group effort. In contrast to a scientific publication, where through the author list the contributors are credited, only my name is on the front cover of this thesis. This thesis work would have been impossible, however, without the contributions and support of numerous others.

I would like to thank David Larbalestier for allowing me to work in his group, for broadening my view on science as well as on life, for his amazingly cheerful personality, and for being an excellent, always positive advisor. Bennie ten Haken has guided me from my first acquaintance with superconductivity. I want to thank him for this and for allowing me to grow within the High Current Superconductivity group, for stimulating me to do more than I trusted myself, for all the things he arranged for me of which I have no knowledge, and for VI. I would like to thank Herman ten Kate for allowing me to do a Ph.D., for driving up and down from Chicago to Madison to talk to me for half an hour, and for his constructive criticism.

My colleagues in Twente assured a pleasant working environment. I want to thank Sander Wessel and Eric Krooshoop for always being a solid support in the lab. Eric also developed and optimized the variable temperature barrel system and performed a significant amount of characterizations together with Hennie Knoopers. Arend Nijhuis introduced me in the ITER community and had to listen to my frustrations while writing my thesis since he occupies the desk in front of me. Harald van Weeren and Yuri Ilyin also share the same office and helped making the long hours behind my PC bearable. I am always impressed by Andries den Ouden's accurate memory and want to thank him, and also Marc Dhalle, for the stimulating discussions. Many thanks go to Sasha Golubov for his help with the theory. Alessio Morelli designed the Pacman device and Wouter Abbas helped with the practical implementation. Rob Bijman is presently developing a new method for strain dependence measurements on bulk Nb_3Sn samples. I thank also the other people from the Low Temperature Division. Although I did not mention you explicitly, I am grateful for the time spent together.

I would to thank all the people at the Applied Superconductivity Center in Madison. Matt Jewell has assisted significantly with the field-temperature characterizations and shot down politely but also ruthlessly my wildest ideas. His skills in material science have been very helpful to me. The magic microscopist Peter Lee is greatly acknowledged for numerous SEM cross-sections and for his wonderful sense of humor. I am highly impressed by the multidisciplinary skills of Alex Squitieri and also thank him for introducing us to sailing and for lending us so many things. Bill Starch is acknowledged for manufacturing the probes, for his help with the furnaces and the polishing lessons (something I'll probably never learn properly). Alex Gurevich has answered many questions I had regarding the theory. Lance Cooley always provided more suggestions than can be investigated. Valeria Braccini introduced Italian espresso in the lab. Chad Fischer, Mike Naus, Ben Senkowicz and Sang Il Kim were my office mates. All the others not explicitly mentioned: You really made us feel at home in Wisconsin.

I am also grateful to the people at the NHMFL which supported me during the long measurement sessions. I would like to thank specifically Luis Balicas, Bruce Brandt, Huub Weijers, Ulf Trociewitz and the magnet operators. Shape Metal Innovation, JAERI and the ITER European Home Team supplied the wires that were used in the investigations in this thesis. Their approval to publish many detailed results is highly appreciated.

Finally, I want to thank my wife, children, family and friends for their support and for enriching my life so much.

Contents

Chapter 1

Introduction

This study was initiated by the observation that the properties of Niobium–Tin superconductors are relatively well understood on the basis of microscopic theories which were developed in the late 1960's, whereas the behavior of the critical current in technical multifilamentary composite wires is described mainly in terms of empirical relations. Wires, in contrast to well defined laboratory samples, are always substantially inhomogeneous in composition, leading to significant internal variations of the superconducting properties. The sole use of empirical relations, however, frustrates our understanding of the origin of observed performance limitations in wires. Moreover, it leads to ongoing discussions in the literature which is the most useful relation to describe the behavior of the critical current in wires. These discussions obstruct well-considered definitions of wire development goals. The question therefore arose whether wire behavior could be explained more precise through the use of alternatives which remain as close as possible to well accepted microscopic theories. Generating a better insight in the performance boundaries of multifilamentary composite wires and thus defining a properly founded upper limit is the main goal of this thesis. This Chapter provides a basic introduction to the general aspects of superconductivity, introduces existing Nb_3Sn multifilament wires and their applications, and ends with a presentation of the objective and scope of this thesis.

1.1 Introduction

Superconductivity in Nb_3Sn was discovered by Matthias *et al.* in 1954 [1], one year after the discovery of V_3Si, the first superconductor with the A15 structure by Hardy and Hulm in 1953 [2]. Its highest reported critical temperature is 18.3 K by Hanak *et al*. in 1964 [3]. Ever since its discovery, the material has received substantial attention due to its possibility to carry very large current densities far beyond the limits of the commonly used NbTi. The discovery of the "bronze route" process [4] demonstrated the feasibility to fabricate multifilamentary composite wires, which is required for nearly all practical applications. It has regained interest over the past decade due to the general recognition that NbTi, the communities' present workhorse for large scale applications, is operating close to its intrinsic limits and thus exhausted for future application upgrades. The material Nb_3Sn approximately doubles the available field–temperature regime with respect to NbTi and is the only superconducting alternative that can be considered sufficiently developed for large scale applications.

For a general description of superconductivity the reader is referred to the many textbooks on this subject [5–14]. A concise introduction of general terminology of superconductivity of relevance for this thesis is given below in Section 1.2. Excellent overviews of specific aspects of A15 superconductors in general can be found in [15–24]. A complete review of the superconducting properties of Nb_3Sn alone appears lacking in the literature. An introduction of the Niobium–Tin intermetallic on the basis of the available literature on defined laboratory compounds is therefore given in Chapter 2. The main part of this knowledge was generated with homogeneous thin films fabricated using electron-beam coevaporation methods [25–29] and homogeneous bulk materials produced by levitation melting under high Argon pressure [30] and by hot isostatic pressure synthesis [31]. Additional single crystal analyses complement the thin film and bulk data [32–38]. Recently new homogeneous bulk material has become available which is produced by a hot isostatic pressure sintering technique [39]. The basic properties of these well defined laboratory samples are used as a basis to describe the properties of wires which have, due to intrinsic compositional inhomogeneities that result from their manufacture, a property distribution of their Nb_3Sn regions.

The general introduction of superconductivity is followed by a description of the primary existing wire fabrication processes in Section 1.4. Next, a concise overview is presented of the main applications using Nb_3Sn technology. The Chapter is concluded with a presentation of the objectives and scope of this thesis.

1.2 Concise introduction of superconductivity

1.2.1 Critical temperature, critical field and critical current

When a superconductor is cooled below a material specific critical temperature T_c its resistance suddenly drops to zero and it becomes a perfect electrical conductor. This behavior was first observed in Mercury by Kamerlingh Onnes in 1911 [40]. A rough separation into two groups can be made on the basis of the attainable T_c in superconducting compounds. The first group of Low Temperature Superconductors (LTS) has a record T_c of approximately 23 K for Nb_3Ge. This group of superconductors is relatively well understood in terms of lattice mediated electron pairing (described below). The recently discovered superconductor MgB_2 [41], with a critical temperature of about 40 K, can arguably be placed within the LTS group of materials. Microscopic models based on non-phonon-mediated electron-electron interaction, as first

initiated by Little in 1964 [42], suggested the possibility to achieve much higher critical temperatures and even superconductivity at room temperature is not excluded. In 1986 a breakthrough occurred with the discovery of the cuprates by Bednorz and Müller [43]. Superconductivity in these materials is based on the copper-oxide planes, in which pairing is initiated by embedding them in a specific lattice. These represented the first materials in the second group of High Temperature Superconductors (HTS) with T_c values ranging from about 40 K ($LaBa_2CuO_x$) up to a record of approximately 165 K ($HgBa_2Ca_2Cu_3O_{8+x}$ under high pressure).

In the presence of an applied magnetic field H two types of superconductors can be distinguished. These are generally referred to as Type I and Type II. In Type I superconductors (most often the single elements) the magnetic flux is perfectly shielded from the interior of the superconductor by shielding currents along its surface up to a thermodynamic critical field H_c. This Meissner [44] effect differentiates a superconductor and a perfect electrical conductor. The magnetic field exponentially decays from the surface of the superconductor over a magnetic penetration depth λ. Above H_c the magnetic flux completely penetrates the interior and superconductivity is lost. Type II superconductors (most often multiple elements) only exhibit perfect magnetic flux exclusion up to a lower critical field H_{c1} ($H_{c1} \ll H_c$). Above H_{c1} magnetic flux penetrates the interior in the form of quantized flux vortices of magnitude $\phi_0 = h / 2e$ which are referred to as Abrikosov vortices [45, 46] or flux-lines. These flux-lines form a lattice of normal conducting regions with an approximate diameter of 2 times the superconducting coherence length ξ (described below). The superconducting bulk is shielded from these normal regions by super-currents encompassing the flux-line approximately over a depth λ into the bulk. As the applied magnetic field is increased above H_{c1}, the flux-line density, starting from zero, increases until at an upper critical field H_{c2}, the flux-lines start to overlap ($B = \mu_0 H$) and the superconductor undergoes a second order phase transition to the normal state. The coherence length, the penetration depth and the upper critical field are temperature dependent.

If a Type II superconductor carries a transport current a Lorentz force will act on the flux-line lattice. Movement of the flux-line lattice will result in dissipation and thus destroys zero resistivity. The flux-lines can, however, be prevented from moving (be "pinned") by lattice imperfections such as impurities, defects or grain boundaries. A critical current density J_c can be defined when the Lorentz force, which acts on the flux-line lattice, becomes larger than the bulk pinning force F_P that prevents the flux-lines from moving. This pinning force, and thus J_c, depends on the applied field and temperature. The function $J_c(H, T)$ represents a critical surface below which the material can carry a superconducting current density (see Figure 1.3). This critical surface is also affected by the presence of strain, i.e. deformation of the structure so that $J_c \rightarrow J_c(H, T, \varepsilon)$.

1.2.2 Theory of superconductivity

The early theories of superconductivity were phenomenological. The London theory [47] is based on a two fluid model of superconducting and normal conducting electrons and can explain the Meissner effect. The Ginzburg-Landau (GL) theory [48, 49] generalizes the London theory through the introduction of a superconducting order parameter ψ in terms of the Landau theory of phase transitions [50]. The order parameter is a complex wave function that describes the superconducting electrons whose local density is given by $|\psi|^2$. Gor'kov [51] showed that the GL theory is a limiting case (valid near T_c at zero magnetic field) of the more general

microscopic theory introduced in 1957 by Bardeen, Cooper and Schrieffer [52]. The by Gor'kov generalized GL theory, combined with the Abrikosov flux-line lattice description is generally referred to as the GLAG theory.

Fröhlich [53] first suggested the role of electron-lattice interactions to explain superconductivity on a microscopic scale. At the same time Maxwell [54] discovered the isotope effect ($T_c \propto M^{-½}$, where M is the atomic mass) which represented a strong indication for a lattice contribution to superconductivity. Electrons are Fermions and behave according to Fermi-Dirac statistics for which the Pauli exclusion principle applies, i.e. only one electron per energy state is allowed. Cooper [55] showed that the Fermi sea of electrons is unstable and electrons form bound pairs (Cooper pairs) if there exists a net attractive interaction between them. This resulted in a microscopic understanding of superconductivity in the form of the BCS theory [52]. A simplified model to physically understand the attraction is that a first electron attracts positive ions. The resulting displacement of positive ions in turn attracts the second electron, resulting effectively in an attraction between the electron pair through the exchange of lattice vibration quanta (phonons with frequency ω). If this attraction is sufficiently strong to overcome the Coulomb repulsion, a net attraction (coupling) remains. This is referred to as electron-phonon coupling and is, in the BCS framework, described by a dimensionless electron-phonon interaction parameter $\lambda_{ep} = N(E_F)V_0$. In this, V_0 is a constant, weak attractive interaction potential which becomes zero outside a cutoff energy $\hbar\omega_c$ away from E_F, the Fermi energy level (in the BCS theory $\omega_c = \omega_D$, the Debye frequency). $N(E_F)$ is the electron density of states (DOS) at the Fermi level, used as an approximation for the DOS in the energy window $E_F \pm \hbar\omega_c$. The characteristic distance over which this phonon mediated electron-electron interaction occurs is called the coherence length ξ.

Cooper pairs are quasi-particles that follow Bose-Einstein statistics for which the exclusion principle does not apply. The Cooper pairs can therefore, in contrast to electrons, collectively condense into a lower energy state described by a single complex wave function. This BCS ground state or superconducting state has a lower total energy and thus destabilizes the normal state. The superconducting state results in the formation of an energy gap Δ on both sides of the Fermi energy in the single electron excitation spectrum. Scattering does not sufficiently excite the electrons to overcome this gap and dissipation-free electron transport is possible. The BCS theory describes this energy gap in terms of the phonon frequency ω and the electron phonon interaction constant λ_{ep}. Requiring that $\Delta(T) \rightarrow 0$ as $T \rightarrow T_c$ additionally results in a description of the critical temperature in terms of ω and λ_{ep}.

The BCS theory does not account for the details of the interaction as function of the phonon frequency (lattice vibration) spectrum. BCS is valid only in the so-called weak coupling approximation ($\lambda_{ep} \ll 1$). A generalization of the BCS theory that includes the actual phonon spectrum and strong electron-phonon coupling was performed by Eliashberg [56]. According to Eliashberg the electron-phonon interaction parameter is related to a quantity $\alpha^2(\omega)F(\omega)$, which is the product of the electron-phonon interaction and the phonon DOS, both as function of energy. The interaction constant is then described by a specific summation of an attractive interaction λ_{ep} and a repulsive Coulomb pseudo potential μ^*, which depend on a material specific phonon spectral function and phonon density of states. This summation of attraction and repulsion results in an effective interaction constant λ_{eff}. A first attempt to derive a relation for the critical temperature in the strong coupling case based on the Eliashberg equations was made by McMillan [57] and is valid for $\lambda_{ep} \leq 1.5$ [8]. The more general case of a coupling strength independent description for the critical temperature was later derived by Kresin [58].

Strong coupling will, apart from more generally applicable descriptions of T_c, also result in corrections on microscopic formulations for $H_{c2}(T)$ as will be treated in Chapter 3.

1.3 Superconducting Nb_3Sn

Intermetallic Niobium-Tin is superconducting at all its thermodynamically stable compositions ranging from about 18 to 25 at.% Sn. In this composition range it exists as a cubic A15 lattice, but undergoes a cubic to tetragonal phase transition at a temperature $T_m \cong 43$ K above about 24.5 at.% Sn. The crystal structure of Nb_3Sn is denoted as the A15 structure. An overview of the characteristic parameters for the stoichiometric composition is presented in Table 1.1. The main parameters important for wire performance (H_{c2}, T_c and λ_{ep}), however, depend strongly on atomic Sn content and on the absence of the tetragonal distortion, as will be explained in Chapter 2. This means that the parameters can differ significantly from the values in Table 1.1.

Table 1.1 *Characteristic parameters of Nb_3Sn [27, 28, 59]. *At zero temperature.*

Superconducting transition temperature	T_c	18	[K]
Lattice parameter at room temperature	a	0.5293	[nm]
Martensitic transformation temperature	T_m	43	[K]
Tetragonal distortion at 10 K	a / c	1.0026	
Mean atomic volume at 10 K	V_{Mol}	11.085	[cm^3/Mol]
Sommerfeld constant	γ	13.7	[mJ/K^2Mol]
Debye temperature*	Θ_D	234	[K]
Upper critical field*	$\mu_0 H_{c2}$	25	[T]
Thermodynamic critical field*	$\mu_0 H_c$	0.52	[T]
Lower critical field*	$\mu_0 H_{c1}$	0.038	[T]
Ginzburg-Landau coherence length*	ξ	3.6	[nm]
Ginzburg-Landau penetration depth*	λ	124	[nm]
Ginzburg-Landau parameter ξ / λ*	κ	34	
Superconducting energy gap	Δ	3.4	[meV]
Electron-phonon interaction constant	λ_{ep}	1.8	

The A15 sections in wires are formed through a solid state diffusion reaction, as will be discussed in the next Section. This inevitably results in the occurrence of significant variations in Sn content over the A15 volume. This means that all compositions from about 18 to 25 at.% Sn can be expected in wires. In wires the A15 is also often alloyed with ternary additions such as e.g. Ta or Ti, and Cu is present as a catalyst for lower temperature A15 formation. The A15 in wires is furthermore polycrystalline and its morphology strongly determines the transport properties. This stems from the fact that the grain boundaries in Nb_3Sn are the main pinning centers and ideally the grain size should be comparable to the flux-line spacing, so that each flux-line is pinned optimally. This will be explained in more detail in Chapter 2. The properties are in addition highly sensitive to strain, which is always present in a composite wire, especially when it is loaded by e.g. Lorentz forces in a magnet. Investigating

how variations in composition, A15 morphology and strain influence the experimentally observed limitations is one of the main thrusts in this thesis.

1.4 Multifilament wire fabrication techniques

Applications using Nb_3Sn wires generally require the A15 to be embedded in a normal conducting matrix for electrical and thermal stability reasons. These stability considerations further require the A15 to be distributed in fine filaments (preferably smaller than about 50 µm) which need to be twisted. Required wire unit lengths are generally > 1 km at about 1 mm diameter. In a fabrication process the separate components of a wire are stacked in about 5 to 30 cm diameter billets. These are mostly extruded and then drawn into wires. Since the A15 phase is brittle the wires are drawn while the components are not yet reacted to the A15 phase and remain ductile. The A15 formation reaction occurs after the wires are drawn to their final diameter and usually after coil winding. This formation occurs through a solid state diffusion reaction at high temperature (about 700 °C) in a protected atmosphere. Three present large scale fabrication processes can be distinguished, as depicted in Figure 1.1.

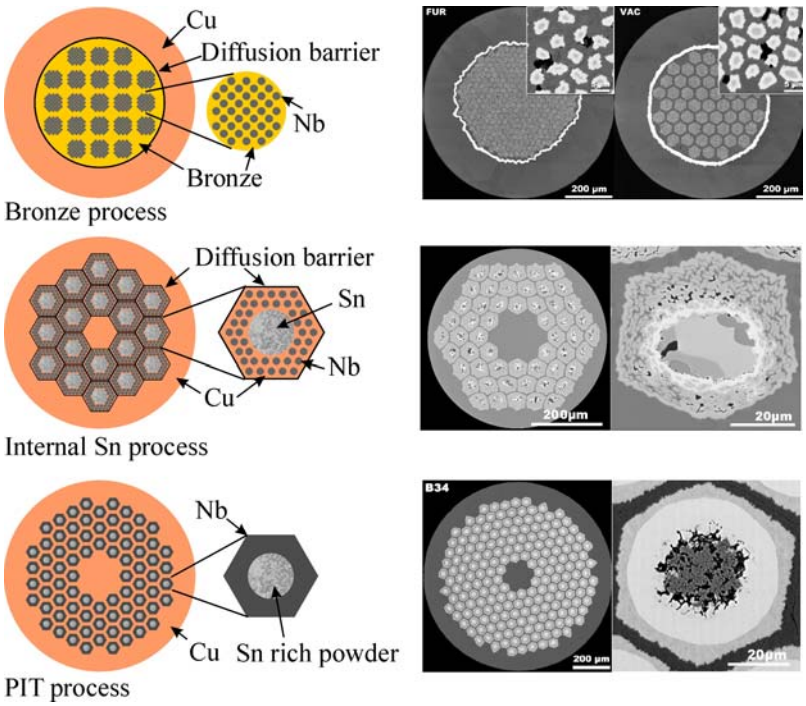

Figure 1.1 *Schematic presentation of the three main Nb_3Sn wire fabrication techniques. From top to bottom: The bronze process, the internal Sn (IT) process and the Powder-in-Tube (PIT) process. To the right SEM cross-sections are shown of actual wires manufactured according to the specific processes, courtesy of M.T. Naus and P.J. Lee.*

1.4.1 Bronze process

In the bronze process, which was the first viable wire fabrication process [4], Nb rods are inserted in a high Sn bronze matrix which is surrounded by stabilization Cu. Then the complete billet is drawn to final diameter. The bronze area represents the Sn source and is surrounded by a barrier (mostly Ta) that prohibits the Sn from diffusing into the high purity stabilization Cu. Ternary elements can be added by e.g. replacing the Nb with Nb(Ta) or adding Ti to the bronze. The main advantage of this method is the very fine filaments ($\leq 5\,\mu m$) and a relative straightforward wire fabrication. Also the entire non-Cu cross-section can be used for A15 formation. However, the main drawback of the bronze process is the work hardening of the bronze, which results in the need for annealing steps after about every 50% area reduction. Other drawbacks are the Sn solubility in the bronze which is limited to about 9 at.% Sn, and the relatively low Sn activity resulting in long reaction times and A15 layers exhibiting large Sn gradients. The maximum non-Cu current densities that are achieved in bronze process wires are about 1000 A/mm^2 at 12 T and 4.2 K.

1.4.2 Internal tin process

In the Internal Tin (IT) process [60] a Sn core is surrounded by Cu embedded Nb rods [Rod Restack Process (RRP)] or by expanded Nb mesh layered with Cu [Modified Jellyroll (MJR) process]. These filamentary regions are surrounded by a Sn diffusion barrier [typically Nb or Nb(Ta)]. Sometimes the soft, low melting point Sn is temporarily replaced by salt to allow for an initial hot billet extrusion step and often the Sn is hardened by alloying it with a additional elements (e.g. Mg, Cu or Ti) to improve wire drawing behavior. Advantages of the IT process are the higher overall Sn : Cu ratio, resulting in high-Sn A15 layers and the possibility to draw to final size without the need for intermediate annealing steps. Drawbacks are the loss of the Sn core region as A15 area and the interconnection of the filaments during A15 growth. These interconnections result in a large effective filament size of 70 to 200 µm. Maximum non-Cu current densities that are achieved in IT process wires are about 3000 A/mm^2 at 12 T and 4.2 K.

1.4.3 Powder-in-Tube process

In the Powder-in-Tube (PIT) process [61] a powder (e.g. $NbSn_2$ plus additional elements) is embedded in Nb rods that are stacked in a high purity Cu matrix. The main advantages of this method are the high Sn activity, resulting in very short (about 3 days) and relatively low temperature reactions that inhibit grain growth and small (30–50 µm), well separated filaments. Drawbacks are the non-ductility of the powder core which complicates wire drawing and, as for the IT process, the loss of the core region for A15 formation. Maximum non-Cu current densities that are achieved in PIT process wires are about 2300 A/mm^2 at 12 T and 4.2 K.

1.4.4 General remarks

All present fabrication processes have one major disadvantage: The Sn sources are spatially located far from the Nb and therefore a solid state diffusion is needed to transport the Sn into the Nb before A15 can be formed. This inevitably results in Sn gradients in the A15 regions, resulting from the A15 stability range from about 18 to 25 at.% Sn (Section 2.1). Energy Dispersive X-ray Spectroscopy (EDX) and Transmission Electron Microscopy (TEM) analysis on the Sn gradients in technical wires indicate Sn gradients of 1 to 5 at.% Sn/µm in bronze route wires [135, 62, 63] and about 0.35 at.% Sn/µm in PIT conductors [64, 65]. The field-

temperature phase boundary strongly depends on Sn concentration as described in Section 2.4, resulting in large property inhomogeneities over the A15 layers. The available A15 area is therefore far from being used optimally. Attempts to overcome these gradients by bringing Sn spatially closer to the Nb, thereby reducing the diffusion distances indicate strong improvements in property homogeneities [e.g. 66–68].

1.5 Applications using Niobium–Tin wires

Applications that use Nb_3Sn superconducting technology can be separated into three main fields: NMR for biological and material research applications, High Energy Physics (HEP) and energy research (Fusion).

1.5.1 NMR in Biological and material research

For the research and characterization of materials Nuclear Magnetic Resonance (NMR) systems with a higher NMR resonance frequency and thus a higher magnetic field are required to improve the resolution. The latest state of the art commercial systems are able to achieve 900 MHz (21.1 T), but resolution is substantially improved at even higher fields, e.g. 1 GHz (23.4 T) or 1.14 GHz (26.7 T) [69]. Some estimates can be made to see what these NMR requirements mean in relation to wire performance. The NMR requirements at a typical operating temperature for commercial NMR systems (2.2 K) in relation to present Nb_3Sn wire performance at this temperature are depicted in Figure 1.2.

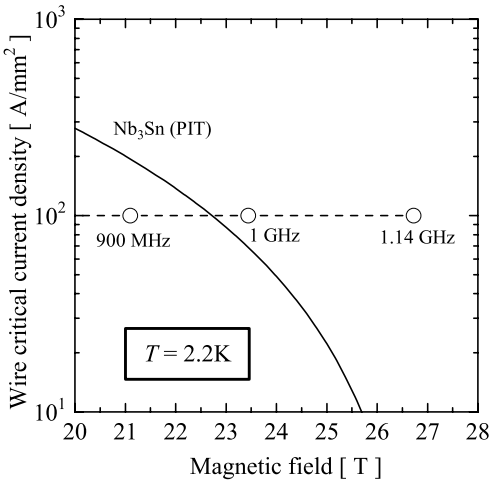

Figure 1.2 *Wire current density requirements for NMR as function of attainable field and NMR frequency. Included is a curve representing present wire performance.*

The exact operating current density in commercial 900 MHz systems is not directly available due to the commercial sensitivity in this highly competitive market. Non-commercial wide bore 900 MHz designs operate at wire current densities of 40 to 50 A/mm^2 with a relatively large safety margin of 60 to 70% [70–73]. A wire current density of 100 A/mm^2 in commercial 900 MHz systems, using a smaller bore and operating at slightly smaller safety margins, seems therefore a valid order of magnitude [69]. This value is depicted in Figure 1.2, including

extrapolations of this requirement for a 1 GHz and a 1.14 GHz system assuming constant magnet dimensions.

1.5.2 High Energy Physics

Particle accelerators which are used in High Energy Physics rely for a significant part on high magnetic fields generated by superconducting magnets. Dipole magnets are used in circular colliders (e.g. the Large Hadron Collider (LHC) which is presently constructed at CERN) to provide the perpendicular magnetic field required to balance the centripetal force which acts on the circulating particles. Quadrupole and higher order magnets are used to focus the particle beams. These magnets presently rely on NbTi. The LHC will operate close to the (intrinsic) performance limit of NbTi. Future luminosity upgrades requiring higher magnetic field strengths and are therefore based on Nb_3Sn. Such upgrades can be expected in the coming decades. Development of the enabling magnet technologies is therefore occurring to date. Development of Nb_3Sn based accelerator magnets occurs mainly, but not exclusively, at Fermi lab, Brookhaven National Laboratory (BNL) and Lawrence Berkeley National Laboratory (LBNL) in the USA and at the University of Twente in The Netherlands. Two specific examples can be highlighted. A magnetic field of 11 T in a 50 mm bore at 4.4 K was achieved in a two layer cosine theta dipole magnet developed at the University of Twente using PIT wire manufactured by Shape Metal Innovation (SMI) [74]. A magnetic field of 13.5 T in a 50 mm bore at 1.8 K was achieved in a four layer cosine theta dipole magnet developed at LBNL using Teledyne Wah Chang and Intermagnetics General IT wire [75]. Recent research magnets at LBNL have reached a record dipole magnetic field of 16 T using the latest generation IT wires developed by Oxford Instruments Superconducting Technology [76, 77].

1.5.3 Fusion

Fusion reactors rely on superconducting magnets to generate the plasma confining magnetic fields. Additionally, in Tokamak designs like the International Thermonuclear Experimental Reactor (ITER), a central solenoid is ramped rapidly to induce plasma currents. ITER is designed to use plasma confining toroidal field (TF) coils and a central solenoid (CS). These will both be constructed using Nb_3Sn wire technology [see e.g. 78−80]. The ITER design requires more than 500 tons of Nb_3Sn wire.

1.5.4 Applications view of present wire performance

The above applications each have their own specific requirements with respect to conductor performance. NMR focuses on the very high fields (> 20 T) that are available at 2 to 4 K. The combination of very high field and high transport current results in large mechanical loads on the conductors. These have to be accounted for. The magnet systems for HEP will have to operate in the field regime of about 10 to 15 T at about 2 to 4 K. Wires are generally used in so-called Rutherford cables, on which transverse loads of 100 to 200 MPa will act. Fusion combines average fields around 13 T with high ramp rates which translates to a requirement for smaller filament sizes and larger temperature margins.

In Figure 1.3 the requirements for the main applications are summarized in a $J_c(H,T)$ plot. Generally speaking, there exists a demand for large critical current density. Design limitations, however, such as mechanical loads on the conductors, can limit the current density to a maximum. The depicted boundaries will thus depend on specific demands in each application.

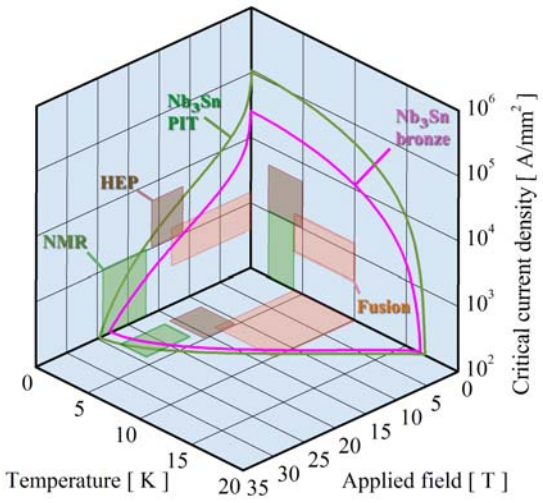

Figure 1.3 *Three dimensional plot of the requirements in applications using Nb_3Sn wire technology in comparison to presently available wire performance.*

Figure 1.3 should be regarded to sketch roughly the application demands. In addition also the wire performance is outlined for present bronze and PIT processed wires. The curves were partly generated using the results of this thesis. It can be concluded from Figure 1.3 that there is a need for wire improvement mainly in the NMR and HEP areas. Fusion applications do not place requirements on wire performance that is significantly beyond what is presently available but will benefit from cost reductions resulting from over-specification of wire performance. This cost aspect is a key factor for e.g. ITER, considering the very large quantity of wire that is needed.

1.6 Scope of this thesis

Efforts over the past decade have resulted in a substantial increase in the maximum achievable critical current density in wires. This increase occurred approximately linear with time, as was recently shown by Parrell *et al.* [76]. This gradual increase, reproduced in Figure 1.4, immediately raises the core question that forms the basis of this thesis:

- What is the upper limit for achievable critical current densities in Nb_3Sn multifilamentary composite wires?

In fact, this question can be separated in two:

a) What would represent a general intrinsic limit to the current carrying capabilities of Nb_3Sn in the idealized case?

b) What is the maximum current carrying capacity in a wire considering what practically is possible using existing fabrication technologies?

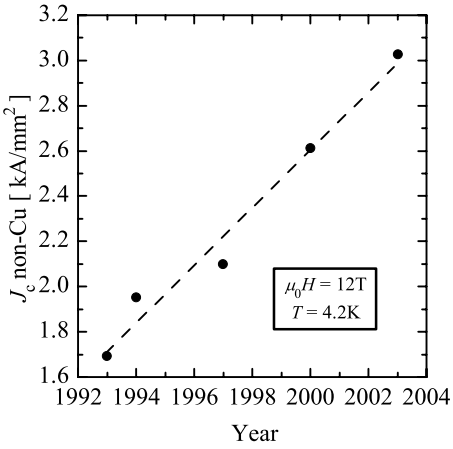

Figure 1.4 *Record critical current density in Nb_3Sn wires at 12 T and 4.2 K versus time. After Parrell et al. [76].*

Roughly speaking, question a) can be directly answered by assuming the ideal limit of exactly one pinning center per flux-line, in combination with the approximate upper limit of the field-temperature phase boundary at $\mu_0 H_{c2}(0) \cong 30$ T and $T_c(0) \cong 18$ K (Chapter 2). This will result in a J_c value on the order of 10% of the depairing current density J_d. At $T = 0$ K, this results in $0.1 J_d \cong H_c / \lambda = 3 \times 10^5$ A/mm^2 [22].

Question b), however, is much more difficult to answer, as it requires detailed answers to the following six questions:

1) What is the influence of compositional variations and strain on the critical parameters?

It is well known that the critical parameters vary significantly with composition and more specifically, with Sn content in the A15. For transport properties of wires, mainly the variations in T_c, H_{c2} and λ_{ep} are important. Reviewing and summarizing the available literature on homogeneous and well defined laboratory samples related to this is the subject of Chapter 2.

2) What represents an accurate description of the $J_c(H,T,\varepsilon)$ behavior?

The behavior of $J_c(H,T,\varepsilon)$ in the literature is generally described by empirical relations [81]. Although accurate in limited ranges, through the use of empirical the correlation with the underlying physics is lost. Better alternatives, based on the microscopic theory or at least with some degree of physics background, are readily available throughout the literature for example for the $H_{c2}(T)$ and $T_c(\varepsilon)$ dependencies in these empirical $J_c(H,T,\varepsilon)$ relations. Investigating to what extend empirical relationships can be replaced by better founded alternatives, thereby improving general validity as well as understanding, is the subject of Chapter 3.

3) What is the A15 composition and morphology in wires?

Since the critical parameters of Nb_3Sn strongly depend on composition as well as morphology, detailed knowledge is required of the inhomogeneities and grain size in the A15 sections in present wires. Investigating this is the subject of Chapter 4.

Detailed descriptions of $J_c(H,T,\varepsilon)$ can only be verified with extensive and accurate measurements. The experimental equipment that is used for the characterization of samples as function of magnetic field, temperature and strain is described in Chapter 5.

4) What is the upper critical field as function of temperature in wires?

Considering the large variations of $H_{c2}(0)$ and $T_c(0)$ with composition (Chapter 2) and the fact that all wires are inhomogeneous raises the question which field-temperature boundary appears in measurements. A detailed investigation of $H_{c2}(T)$ in wires over the full field-temperature range will answer this and is therefore the subject of Chapter 6.

5) What is the critical current density as function of magnetic field, temperature and strain in wires?

Accurate and extensive data for $J_c(H,T,\varepsilon)$ in wires is required to verify the improved relationships that will be derived in Chapter 3. Based on the results in Chapter 2 to Chapter 6 the existing descriptions for $J_c(H,T,\varepsilon)$ will be investigated through systematic comparison to measurements. The inconsistencies in the existing descriptions will be highlighted and a new description will be developed based on the $H_{c2}(T)$ dependence discussed in Chapter 3.

6) What are the estimates of the maximum achievable critical current density in wires on the basis of the knowledge collected in 1) through 5)?

In the second part of Chapter 7 the data collected in Chapter 4, Chapter 6 and Chapter 7 will be summarized and modeled using parameterizations based on the relations from Chapter 2 and Chapter 3 to predict the limits for the critical current density in wires fabricated using present processes.

Finally, the main results of this thesis will be summarized in Chapter 8.

Chapter 2

Properties of Intermetallic Niobium–Tin

The transport current capacity of wires depends on A15 composition, morphology and strain state. The A15 sections in wires contain, due to the compositional inhomogeneities, a distribution of superconducting properties. The A15 grain size can be different from wire to wire and is also not necessarily homogeneous across the A15 regions. Strain is always present in composite wires and the strain state can change under thermal contraction differences and Lorentz forces in magnet systems. It is thus required to identify how composition, grain size and strain state influence the superconducting properties. This is not accurately possible in inhomogeneous spatially complex systems such as wires. This Chapter gives an overview of the available literature on simplified, well defined homogeneous laboratory samples. It starts with a basic description of the Niobium-Tin intermetallic. After this it maps the influence of Sn content on the field-temperature phase boundary and on the electron-phonon interaction strength. The literature on the influence of Cu, Ti and Ta additions will be briefly summarized. This is followed by a review on the effects of grain size and strain. This Chapter reviews the available datasets of the upper critical field and critical temperature as function of composition.

2.1 Introduction

Intermetallic Niobium–Tin is based on the superconductor Nb, which exists in a *bcc* Nb structure ($T_c \cong 9.2$ K) or a metastable Nb_3Nb A15 structure ($T_c \cong 5.2$ K) [24, 82]. When alloyed with Sn and in thermodynamic equilibrium, it can form either $Nb_{1-\beta}Sn_\beta$ ($\sim 0.18 \leq \beta \leq \sim 0.25$) or the line compounds Nb_6Sn_5 and $NbSn_2$ according to the generally accepted binary phase diagram by Charlesworth *et al.* ([83], Figure 2.1). The solid solution of Sn in Nb at low concentrations ($\beta < 0.05$) gradually reduces the critical temperature of *bcc* Nb from about 9.2 K to about 4 K at $\beta = 0.05$ (Flükiger in [15]). Both the line compounds at $\beta \cong 0.45$ and 0.67 are superconducting with $T_c < 2.8$ K for Nb_6Sn_5 [84, 85] and $T_c \leq 2.68$ K for $NbSn_2$ [85, 86] and thus are of negligible interest for practical applications.

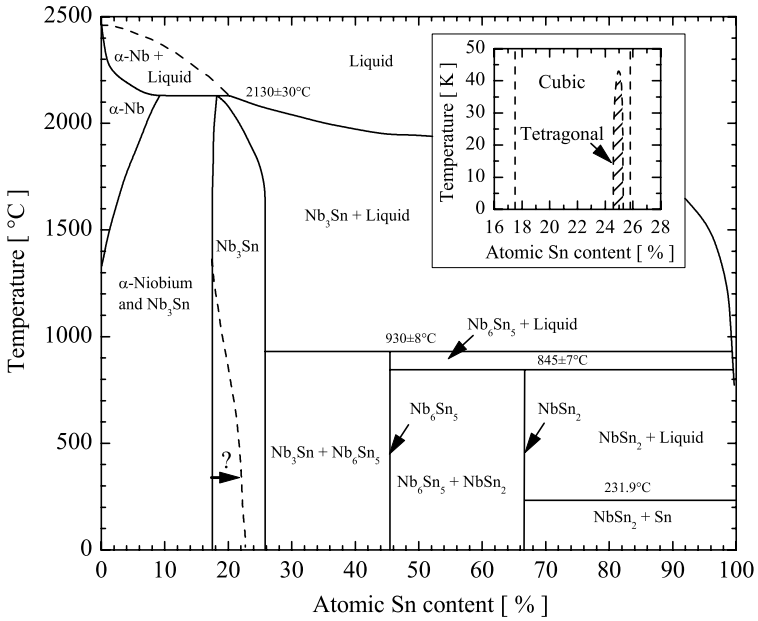

Figure 2.1 *Binary phase diagram of the Nb–Sn system after Charlesworth et al. [83], with an optional modification to suggested preference for Sn rich A15 formation [30, 39, 87–90]. The inset depicts the low temperature phase diagram after Flükiger [96], which includes the stability range of the tetragonal phase.*

The Nb–Sn phase of interest occurs from $\beta \cong 0.18$ to 0.25. It can be formed either above 930°C in the presence of a Sn–Nb melt, or below this temperature by solid state reactions between Nb and Nb_6Sn_5 or $NbSn_2$. Some investigations suggest that the nucleation of higher Sn intermetallics is energetically more favorable for lower formation temperatures [30, 39, 87–90]. This is indicated by the dashed line within the $Nb_{1-\beta}Sn_\beta$ stability range in Figure 2.1. The critical temperature for this phase depends on composition and ranges approximately from 6 to

18 K [30]. At low temperatures and at $0.245 < \beta < 0.252$ it can undergo a shear transformation at $T_m \cong 43$ K. This results in a tetragonal structure in which the reported ratio of the lattice parameters $c / a = 1.0026$ to 1.0042 [22, 34, 91–96]. This transformation is schematically depicted in the low temperature extension of the binary phase diagram as shown in the inset in Figure 2.1.

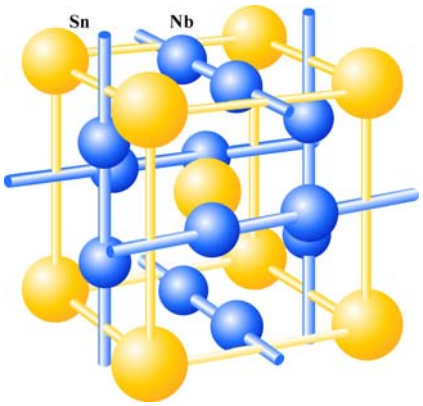

Figure 2.2 *Schematic presentation of the Nb_3Sn A15 unit cell. The light spheres represent Sn atoms in a bcc lattice. The dark spheres represent orthogonal chains of Nb atoms bisecting the bcc cube faces.*

$Nb_{1-\beta}Sn_{\beta}$ exists in the brittle A15 crystal structure with a cubic unit cell, as schematically depicted in Figure 2.2. The Sn atoms form a *bcc* lattice and each cube face is bisected by orthogonal Nb chains. The importance of these chains is often emphasized to qualitatively understand the generally high critical temperatures of A15 compounds. An excellent review on this subject is given by Dew-Hughes in [22] and can be summarized specifically for the Nb-Sn system. In *bcc* Nb the shortest spacing between the atoms is about 0.286 nm, starting from a lattice parameter $a = 0.330$ nm [97]. In the A15 lattice, with a lattice parameter of about 0.529 nm for the stoichiometric composition [30], the distance between the Nb atoms is about 0.265 nm. This reduced Nb distance in the chains is suggested to result in a narrow peak in the d-band density of states (DOS) resulting in a very high DOS near the Fermi level. This is in turn believed to be responsible for the high T_c in comparison to *bcc* Nb. Variations in T_c are often discussed in terms of long-range crystallographic ordering [22, 24, 98–100] since deviations in the Nb chains will affect the DOS peak. Tin deficiency in the A15 structure causes Sn vacancies, but these are believed to be thermodynamically unstable [24, 101]. The excess Nb atoms will therefore occupy Sn sites, as will be the case with anti-site disorder. This affects the continuity of the Nb chains which causes a rounding-off of the DOS peak. Additionally, the *bcc* sited Nb atoms cause there own broader d-band, at the cost of electrons from the Nb chain peak.

The above model is one of many factors that are suggested to explain effects of disorder on the superconducting transition temperature [100]. It is presented here since it intuitively explains the effects of Nb chain atomic spacing and deviations from long range crystallographic ordering and also is mostly cited. In the Nb_3Nb system with a lattice constant of 0.5246 nm [82] the distance between the chained Nb atoms of about 0.262 nm is, as in the A15 Nb–Sn phase, lower than in the *bcc* lattice. This would suggest an increased T_c compared to *bcc* Nb. Its lower T_c of 5.2 K [24] could possibly be explained in the above model by assuming that "Sn sited" Nb

atoms create their own d-band at the cost of electrons from the chained Nb atoms, thereby reducing their DOS peak and thus degrading the expected T_c gain.

2.2 Variations in lattice properties

Variations in superconducting properties of the A15 phase are throughout the literature related to variations in the lattice properties through the lattice parameter (a), atomic Sn content (β), the normal state resistivity just above T_c (ρ_n) or the long range order (LRO). The latter can be defined quantitatively in terms of the Bragg-Williams order parameters S_a and S_b for the chain sites and the cubic sites respectively. These can be expressed in terms of occupation factors [24, Flükiger in 15]:

$$S_a = \frac{r_a - \beta}{1-\beta} \text{ and } S_b = \frac{r_b - (1-\beta)}{1-(1-\beta)}, \tag{2.1}$$

where r_a and r_b are the occupation factors for A atoms at the chain sites and B atoms at the cubic sites respectively in an A15 $A_{1-\beta}B_\beta$ system. At the stoichiometric composition $S = S_a = S_b = 1$ and $S = 0$ represents complete disorder. Qualitatively, the more general term "disorder" is used for the LRO since any type of disorder (e.g. quenched in thermal disorder, off-stoichiometry, neutron irradiation) reduces T_c [100]. A review of the literature suggests that the aforementioned lattice variables (a, β and S) and ρ_n are, at least qualitatively, interlinked throughout the A15 phase composition range. This makes it possible to relate them back to the main available parameter in multifilamentary composite wires, i.e. the atomic Sn content.

The lattice parameter as function of composition was measured by Devantay *et al.* [30] and combined with earlier data from Vieland [87]. These data are reproduced in the left graph in

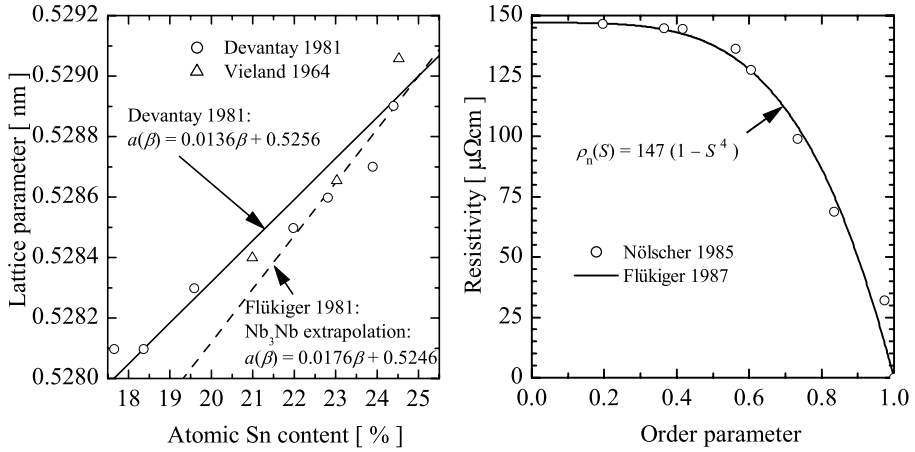

Figure 2.3 *Left plot: Lattice parameter as function of atomic Sn content after Devantay et al. [30] including proposed linear dependencies after Devantay et al. and Flükiger in [15]. Right plot: Resistivity as function of order parameter including a fourth power fit after Flükiger et al. [99].*

Figure 2.3. The solid line is a fit to the data similar as given by Devantay *et al.*:

$$a(\beta) = 0.0136\beta + 0.5256 \quad [\text{nm}]. \tag{2.2}$$

The dotted line is an alternative line fit proposed by Flükiger in [15]:

$$a(\beta) = 0.0176\beta + 0.5246 \quad [\text{nm}], \tag{2.3}$$

in which the lattice parameter is extrapolated from 0.529 nm at $\beta = 0.25$ to a Nb_3Nb value of 0.5246 nm [82] at $\beta = 0$. The argument for doing so is that from analysis of the lattice parameter of a wide range of $Nb_{1-\beta}B_\beta$ superconductors as function of the amount of B element, it appears that most lattice parameters extrapolate to the Nb_3Nb value for $\beta = 0$. It is interesting to note that the rise in lattice parameter with Sn content is apparently contrary to all other A15 compounds, for which a reduction in lattice parameter is observed with increasing B-element. For the analysis in this thesis, (2.2) is presumed an accurate description for the lattice parameter results as measured by Devantay *et al.* and Vieland for the Nb–Sn A15 stability range.

The amount of disorder, introduced by irradiation or quenching is often related to changes in resistivity. Furthermore, the amount of disorder is important in discussions on the strain sensitivity of the superconducting properties in the Nb–Sn system in comparison to other A15 compounds (Section 2.8). A relation between ρ_n and the order parameter S in Nb_3Sn was established by Flükiger *et al.* [99] after analysis of ion irradiation data obtained by Nölscher and Seamann-Ischenko [102] and data from Drost *et al.* [103]. This is reproduced in the right graph in Figure 2.3. Flükiger *et al.* proposed a fourth power fit to describe the $\rho_n(S)$ data:

$$\rho_n(S) = 147(1-S)^4 \quad [\mu\Omega\text{cm}], \tag{2.4}$$

represented by the solid curve through the data points.

The superconducting properties of the Nb–Sn system are mostly expressed in terms of either resistivity or atomic Sn content. Resistivity data as function of composition were collected by Flükiger in [17] and [24] from Devantay *et al.* [30], Orlando *et al.* [29], and Hanak *et al.* [3] and

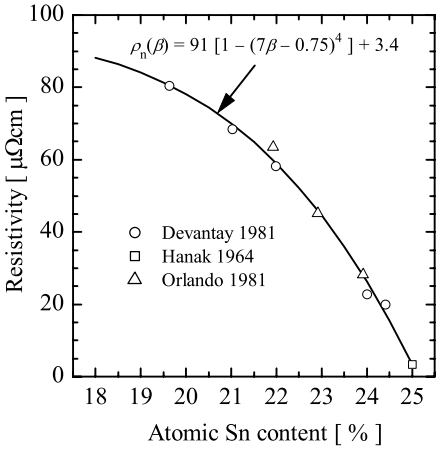

Figure 2.4 *Resistivity as function of atomic Sn content after Flükiger [17, 24]. The solid curve is a fit to the data according to (2.5).*

is reproduced in Figure 2.4. The relation between the two parameters from various sources is consistent. Since Sn deficiency will result in anti-site disorder (Section 2.1) it is assumed here that $\rho_n(\beta)$ will behave similarly to $\rho_n(S)$, i.e. a fourth power fit, identical to (2.4) will be appropriate. The solid curve in Figure 2.4 is a fit according to:

$$\rho_n(\beta) = 91\left[1-(7\beta-0.75)^4\right]+3.4 \quad [\mu\Omega\text{cm}], \tag{2.5}$$

which accurately summarizes the available data.

2.3 Electron–phonon interaction as function of atomic Sn content

The Nb_3Sn intermetallic is generally referred to as a strong coupling superconductor. Any connection to microscopic formalisms, however, requires some level of understanding of the details of the interaction since, as will be shown in Section 3.4.2, it changes the way in which physical quantities can be derived from measured data. More specifically, it requires a description for the interaction strength that varies with composition.

The BCS theory [52] provides a weak coupling approximation for the energy gap at zero temperature:

$$\Delta_0 \cong 2\hbar\omega_c \exp\left[-\frac{1}{\lambda_{ep}}\right], \tag{2.6}$$

which is valid for $\lambda_{ep} \ll 1$. Evaluation of the temperature dependency of the gap $\Delta(T)$ and requiring that the gap becomes zero as $T \to T_c$ yields the following description for the critical temperature in the weak coupling approximation:

$$T_c(0) \cong \frac{2e^{\gamma_E}}{\pi k_B}\hbar\omega_c \exp\left[-\frac{1}{\lambda_{ep}}\right], \tag{2.7}$$

in which $\gamma_E \cong 0.577$ (Euler's constant). The ratio between the zero temperature gap (2.6) and the zero field critical temperature (2.7) $2\Delta_0 / k_B T_c = 3.528$ is a constant and represents the BCS weak coupling limit. For strong coupling (2.6) and (2.7) are no longer valid since they become dependent on the details of the electron-phonon interaction. This will be treated in more detail in Chapter 3. For now, it is sufficient to state that this effectively results in a rise of the ratio $2\Delta_0 / k_B T_c$ above the weak coupling limit of 3.528.

Moore *et al.* [27] have analyzed the superconducting gap and critical temperature of Nb–Sn films as function of atomic Sn content by tunneling experiments. Their main result is reproduced in Figure 2.5. In the left plot the inductively measured midpoint (i.e. halfway the transition) critical temperatures, and from tunneling current-voltage characteristics derived gaps are reproduced as function of composition. The dotted curves are fits to the data using a Boltzmann sigmoidal function:

$$y(\beta) = \frac{y_{min} - y_{max}}{1-\exp\left(\dfrac{\beta-\beta_0}{d\beta}\right)} + y_{max}, \tag{2.8}$$

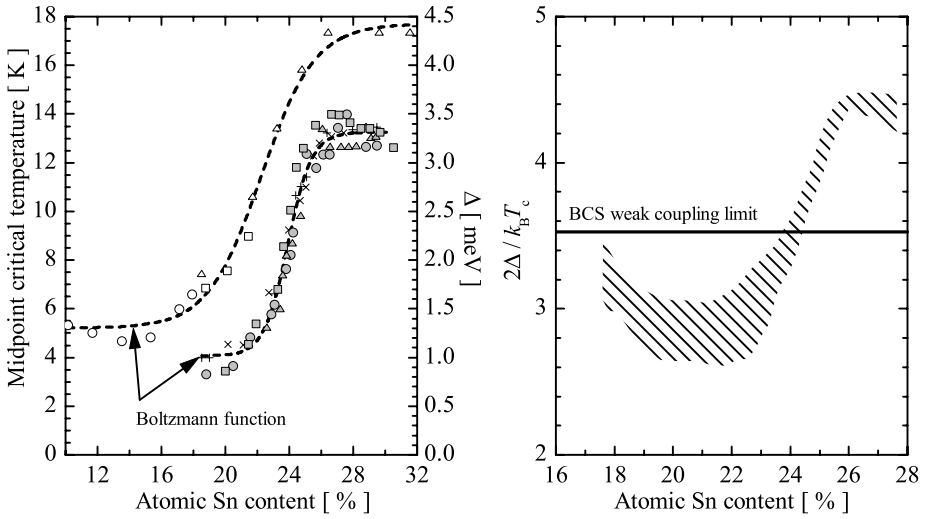

Figure 2.5 *Critical temperature and superconducting gap as function of composition (left plot) and the ratio* $2\Delta_0 / k_B T_c$ *as function of composition (right plot). The ratio indicates weak coupling for compositions below 23–24 at.% Sn and strong coupling for compositions close to stoichiometry. After Moore et al. [27].*

where y represents T_c or Δ, β is the atomic Sn content and y_{min}, y_{max}, β_0 and $d\beta$ are fit parameters. Both $T_c(\beta)$ and $\Delta(\beta)$ are accurately described by (2.8).

The A15 composition range as used by Moore *et al.* is slightly wider than generally accepted on the basis of the binary phase diagram of Charlesworth *et al.* (Figure 2.1, [83]). Nevertheless, following [27] the ratio $2\Delta_0 / k_B T_c$ can be derived from these data sets and is reproduced in the right graph in Figure 2.5. The BCS weak coupling limit of 3.528 is indicated by the solid line. The weak coupling value of about 3 for low Sn content A15 was attributed by Moore *et al.* to the finite inhomogeneity in their samples of 1 to 1.5 at.% Sn, in combination with an inductive measurement of T_c which preferably probes the highest Sn fractions. These T_c values could thus be higher than representative for the bulk. It is also known that in tunneling experiments the gap at the interface can be lower than in the bulk, lowering the effectively measured value. Also, the gap measurement was performed at finite temperature, which also reduces its value. A fourth possible origin is the existence of a second gap in Nb_3Sn, as was recently postulated by Guritanu *et al.* [59]. Nevertheless it is clear that the Nb–Sn system shows weak coupling for most of its A15 composition range and only becomes strong coupled for compositions above 23 to 24 at.% Sn. The general statement that Nb_3Sn is a strong coupling superconductor therefore only holds for compositions close to stoichiometry. Strong coupling corrections to microscopic descriptions (Section 3.4.2) thus become only relevant for compositions approaching stoichiometry.

2.4 T_c and H_{c2} as function of atomic Sn content

Compositional gradients will inevitably occur in wires since their A15 regions are formed by a solid state diffusion process as was discussed in Section 1.4. It is therefore important to know the variation of the critical temperature and upper critical field with composition. The most complete datasets of $T_c(\beta)$ that exist in the literature are those of Moore *et al.* ([27], Figure 2.5) and Devantay *et al.* [30]. The data of Moore *et al.* suggests, as mentioned in the previous Section, a slightly broader A15 composition range than is generally accepted to be stable according to the binary phase diagram by Charlesworth *et al.* ([83], Figure 2.1). The data from Devantay *et al.*, however, are in agreement with the accepted A15 stability range and are therefore assumed to be more accurate.

The results from Devantay *et al.* are reproduced in the left plot in Figure 2.6. Some points are reproduced from Flükiger in [17], who credited these (partly) additional data points also to Devantay *et al*. The linear $T_c(\beta)$ fit, indicated by the dashed line, was originally proposed by Devantay *et al.* to summarize the data:

$$T_c(\beta) = \frac{12}{0.07}(\beta - 0.18) + 6 \,. \tag{2.9}$$

The dotted curve summarizes the data of Moore *et al.* using (2.8). The general tendency of the data sets of Devantay *et al.* and Moore *et al.* is similar; although the latter covers a wider A15 stability range and its T_c values are slightly lower. The solid curve represents a fit to the data of Devantay *et al.* according to a Boltzmann function identical to (2.8):

$$T_c(\beta) = \frac{-12.3}{1 + \exp\left(\dfrac{\beta - 0.22}{0.009}\right)} + 18.3 \,. \tag{2.10}$$

Equation (2.10) assumes a maximum T_c of 18.3 K, the highest recorded value for Nb_3Sn [3].

The right plot in Figure 2.6 is a reproduction of a $H_{c2}(\beta)$ data collection that was made by Flükiger in [17] with some modifications. After Flükiger, it represents a collection of data from Devantay *et al.* [30], Orlando *et al.* [29] and the close to stoichiometric Arko *et al.* single crystal [37]. The dotted line in the plot separates the cubic and tetragonal phases at 24.5 at.% Sn. The Foner and McNiff data in Figure 2.6 are, in contrast to Flükiger's collection, here separated in the cubic and the tetragonal phase with assumed identical composition. The composition that was used here was taken from the Flükiger collection, which showed a single $\mu_0 H_{c2}$ point at a value of about 27 T (the average between the cubic and tetragonal phase). It is unclear where this compositional value is attributed to or whether the cubic single crystal in fact has a lower Sn content.

In addition to the results collected by Flükiger also recent $H_{c2}(\beta)$ results from Jewell *et al.* [39] are added. A slightly different route was followed than given in [39] for the analysis of the $H_{c2}(T)$ results. The compositions of the homogenized bulk samples in [39] were calculated from the T_c values assuming a linear $T_c(\beta)$ dependence as given by (2.9). The resulting $H_{c2}(\beta)$ using these compositions is linear and deviates from the collection by Flükiger, as shown in [39]. Here, the compositions were recalculated based on the T_c values using the Boltzmann fit on the Devantay *et al.* data as given by (2.10). The Jewell *et al.* bulk results then become consistent with the earlier $H_{c2}(\beta)$ data. The highest $\mu_0 H_{c2}$ value of 31.4 T represents, although

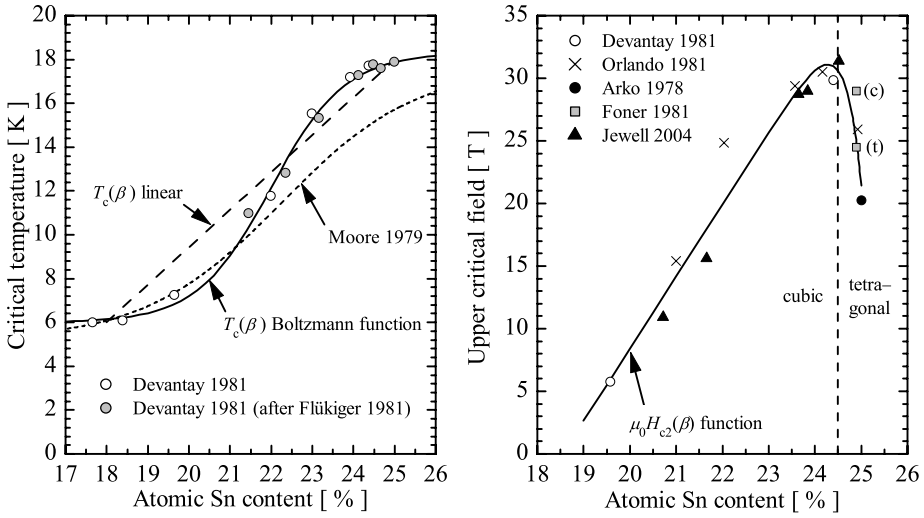

Figure 2.6 *Literature data for the critical temperature (left pot) and upper critical field at zero temperature (right plot) as function of Nb–Sn composition. The $T_c(\beta)$ Boltzmann function and the $\mu_0 H_{c2}(\beta)$ function are empirical relations that summarize the available literature results.*

extrapolated [39], a record for binary Nb–Sn. The existing $H_{c2}(\beta)$ data can be summarized by a summation of an exponential and a linear fit according to:

$$\mu_0 H_{c2}(\beta) = -10^{-30} \exp\left(\frac{\beta}{0.00348}\right) + 577\beta - 107 \,, \qquad (2.11)$$

The solid curve in the right graph in Figure 2.6 is calculated using (2.11).

Equations (2.10) and (2.11) summarize the consistent existing literature data on well defined, homogeneous laboratory samples for the main superconducting parameters T_c and H_{c2} as function of composition. They will be used throughout the remainder of the thesis to discuss variations in the superconducting properties in wires that can be attributed to compositional gradients.

2.5 Changes in $H_{c2}(T)$ with atomic Sn content

To describe the critical currents in wires, not only the upper critical field at zero temperature and zero field critical temperature are important. Also an accurate description of the entire field-temperature phase boundary is required. The temperature dependence of the upper critical field as function of temperature [$H_{c2}(T)$] is well investigated up to about $0.5 H_{c2}$, mainly since the field range up to about 15 T is readily available using standard laboratory magnets. Behavior at higher fields is often estimated by using an assumed $H_{c2}(T)$ dependence or by using so called "Kramer" [104] extrapolations of lower field data that rely on an assumed pinning mechanism (see Section 3.3). Estimates of $\mu_0 H_{c2}(0)$ or Kramer extrapolated critical fields [$\mu_0 H_K(0)$] in wires that are derived in this way range from 18 T to > 31 T [18, 105–112]. It is

obvious that this wide range of claimed $H_{c2}(0)$ values in wires complicates understanding of their behavior. It is therefore required to analyze data over the full field range in better defined samples. Three datasets which are measured over nearly the full field-temperature range on well defined laboratory specimen exist in the literature.

2.5.1 $H_{c2}(T)$ of cubic and tetragonal phases in single- and polycrystalline samples

The articles by Foner and McNiff [36, 38] contain data over the entire magnetic field range on single- and polycrystals in the cubic and tetragonal phase. In addition, single crystals are investigated in the [100] and [110] directions to analyze the anisotropy in $H_{c2}(T)$. These results are reproduced in the left plot in Figure 2.7, together with the results of Foner and McNiff on the approximately stoichiometric Arko *et al.* single crystal [37]. Their characterizations were performed using a RF technique and the resulting $H_{c2}(T)$ are claimed to correspond to a 50 to 90% resistive criterion. The curves are fits (after Foner and McNiff) to the data (in the [100] directions) according to microscopic theory assuming a dirty Type II superconductor and no Pauli paramagnetic limiting (see Section 3.4.2). The anisotropy in $H_{c2}(T)$ is 3 to 4%, both in the cubic and in the tetragonal phase. The shape of the $H_{c2}(T)$ phase boundary and $T_c(0)$ appear similar despite the 9 T difference in $\mu_0 H_{c2}(0)$ between the three crystals. The $\mu_0 H_{c2}(0)$ value for the tetragonal phase is about 4.5 T lower than for the cubic phase. A slightly smaller difference in $\mu_0 H_{c2}(0)$ of about 3.5 T was observed by Foner and McNiff for polycrystalline sample material in the cubic and tetragonal phase. The reduced $H_{c2}(0)$ of the (partly?) tetragonal polycrystalline sample was combined with a 0.1 to 0.2 K rise in $T_c(0)$. Their cubic polycrystalline sample averaged the [100] and [110] directions of the cubic single crystal. The

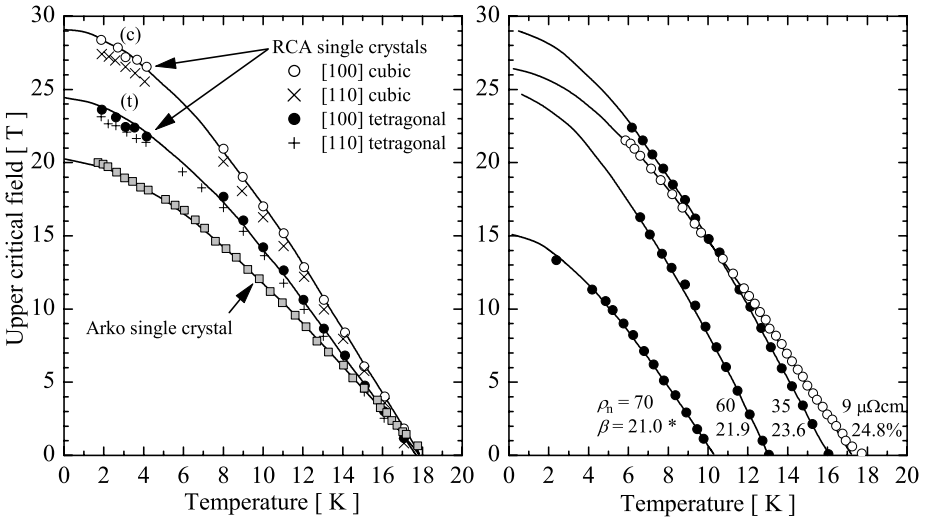

Figure 2.7 *The upper critical field versus temperature for single crystals after Foner and McNiff [38] at approximately a 50 – 90% resistive criterion (left plot) and for thin films with varying resistivity after Orlando et al. [29] at a 50% resistive criterion (right plot). *Compositions were calculated from the resistivity values using (2.5).*

single- and poly-crystal results of Foner and McNiff can explain differences in $H_{c2}(0)$ values for Sn rich A15 compounds in terms of differences between the cubic and tetragonal phases.

2.5.2 $H_{c2}(T)$ of thin films with varying resistivity

Thin film $H_{c2}(T)$ results on films with varying resistivity are available from Orlando *et al.* [28, 29] for fields up to 23 T. They used a resistive technique with a 50% normal state criterion. Their results are reproduced in the right plot in Figure 2.7. The curves are fits (after Orlando *et al.*) to the data according to microscopic theory in the absence of Pauli paramagnetic limitations (see Section 3.4.2). Orlando *et al.* quote the resistivities of the films. In Figure 2.7 also the compositions are given, which were calculated from the resistivity values using (2.5). Lowering the resistivity, or increasing the Sn content, increases the field-temperature phase boundary. Low resistivity (9 μΩcm), close to stoichiometric (24.8 at.% Sn) A15 has a $T_c(0)$ of close to 18 K, but a reduced $\mu_0 H_{c2}(0)$ of about 26.5 T. An apparently optimal dirty thin film (35 μΩcm, 23.6 at.% Sn) reaches $\mu_0 H_{c2}(0) \cong 29$ T at the cost of a reduced $T_c(0) \cong 16$ K. The lowest phase transition that was measured occurred for $\rho_n = 70$ μΩcm ($\beta = 21$ at.% Sn) at $\mu_0 H_{c2}(0) \cong 15$ T and $T_c(0) \cong 10.5$ K. The shape of the phase boundaries are again very similar and apparently independent of composition. The Orlando *et al.* results yield explanations for the placement of the phase boundary in terms of resistivity and composition.

2.5.3 $H_{c2}(T)$ of bulk materials

New $H_{c2}(T)$ for the full field range has recently become available on bulk samples from Jewell *et al.* [39]. Their results are reproduced in Figure 2.8. The curves are fits to the data according to microscopic theory using the Maki-de Gennes approximation as described in Section 3.4.2. The depicted compositions and resistivities were calculated from the $T_c(0)$ values using (2.10) and (2.5). All samples were measured in a Vibrating Sample Magnetometer (VSM) using the first observable diamagnetic deviation from reversible normal state paramagnetic behavior as

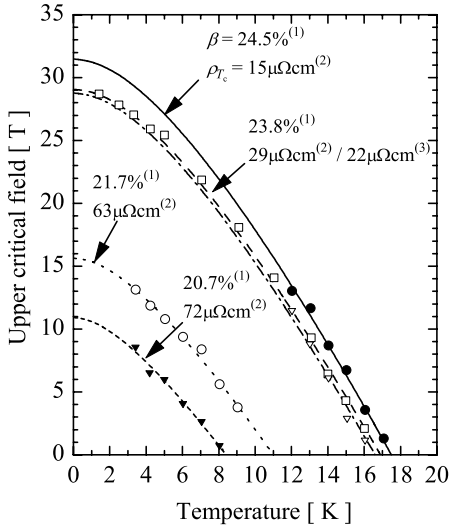

Figure 2.8 *Upper critical field as function of temperature on homogenized bulk samples with varying composition after Jewell et al. [39] at approximately a 90% resistive criterion. (1): Compositions calculated from $T_c(0)$ using (2.10). (2) Resistivities calculated from compositions (1) using (2.5). (3) Resistivity extrapolated from $\rho_n(H)$ data.*

criterion for H_{c2} (which approximately corresponds to a 90% resistive criterion as is explained in Section 6.4), except the $\beta = 23.8$ at.% Sn sample which was measured resistively, using a 90% normal state criterion. All magnetically measured bulk samples were homogenized but not the resistively measured sample. Its measured resistivity value (extrapolated to zero applied magnetic field from $\rho_n(H)$ data) amounted 22 μΩcm. That this value is lower than the calculated value of 29 μΩcm (from T_c) can be attributed to inaccuracies in voltage tap separation length which were about 30% and/or percolation of the measuring current. These results are in qualitative agreement with the thin film data of Orlando *et al.* in the previous Section, i.e. the field-temperature phase boundary increases dramatically if the A15 Sn content is increased. The shift of the boundary with composition appears proportional, i.e. without the tilt that occurred in the Orlando *et al.* results between the low resistivity and optimal dirty thin film. The value of $\mu_0 H_{c2}(0) = 31.4$ T is, although extrapolated from low field data, the highest ever observed in binary A15. Again, the shape of the phase boundary is apparently independent of composition.

2.5.4 Concluding remarks

The three $H_{c2}(T)$ data sets on defined laboratory samples are highly consistent. Bulk sample materials are arguably the closest representation of A15 layers in wires. More experiments on bulk materials will therefore be welcome to clarify the inconsistency between the $T_c(\beta)$ data sets of Moore *et al.* and Devantay *et al.* and to generate a larger quantity and more accurate $H_{c2}(\beta)$ database using the these days readily available high field magnet systems. The existing data can be summarized by plotting their extremes [$H_{c2}(0)$ and $T_c(0)$] as function of composition as was done in Figure 2.6. This is valid provided the shape of the phase boundary indeed is constant and independent of composition (and thus independent of the electron phonon interaction strength), or whether the material is in the cubic or the tetragonal phase. The full field-temperature dependence of the Nb–Sn could then be summarized to depend solely on composition using (2.10) and (2.11) if a single function to describe the $H_{c2}(T)$ behavior of all sample material can be found. Finding such a function and testing its validity on the above data sets as well as on wire data is one of the main focus points of Section 3.4.2 in this thesis.

2.6 Copper, Tantalum and Titanium additions to the A15

2.6.1 Copper additions

Wires are different from pure binary Nb–Sn systems since they are always at least ternary due to the presence of Cu. The addition of Cu lowers the A15 formation temperature, thereby limiting grain growth and thus retaining a higher grain boundary density required for pinning (see Section 2.7). Understanding of how Cu catalyzes the reaction requires detailed knowledge of ternary phase diagrams. Although ternary phase diagrams of the Nb–Sn–Cu system are sparsely available in the literature (mostly at fixed temperatures) [113–118], they do not complement and in regions contradict each other. It can therefore be argued that the exact influence of Cu additions is not thoroughly known. It is clear that the presence of Cu destabilizes the line compounds $NbSn_2$ and Nb_6Sn_5 [15, 23]. It was further suggested that the presence of the Nb–Sn melt is extended to far below 930 °C, enabling rapid A15 formation [116]. Very low temperature A15 formation has been recorded at temperatures down to about 450 °C in a ternary system containing 5.4 at.% Cu [116]. Although Cu can be detected in the

A15 layers [119, 120], it is generally assumed to exist only at the grain boundaries and not to appear in the A15 grains [121, 122]. In the remainder of this thesis binary will therefore be referred to as "pure binary", binary plus Cu as "binary" and if non-Cu elements are present the terms "ternary" or "quaternary" will be used. The absence of Cu in the A15 grains might explain why the binary A15 phase diagram can often be used to, at least qualitatively, interpret compositional analysis in wires. Also, to first order, the addition of Cu does not dramatically change the superconducting behavior of wires as compared to binary systems, as will be emphasized in Section 6.5. Finally, the presence of Cu was recently stated to be a possible origin for $H_{c2}(0)$ suppression in wires [39].

2.6.2 Titanium and Tantalum additions

Possibilities to improve the superconducting properties of the Nb–Sn system by the use of third and fourth element additions have been extensively investigated (see [103, 108, 109, 123–135]) and reviewed [24, 107]. Of a wide range of possible ternary additions Ta and Ti are most widely applied in wires, and more specifically in the wires dealt with in this thesis. Both Ta and Ti occupy Nb sites in the A15 lattice [136]. The effect of these third elements is to suppress the low temperature cubic to tetragonal transition for ≥ 2.8 at.% Ta or for ≥ 1.3 at.% Ti (see e.g. [24] and the references therein). Increasing Ta or Ti content has shown to increase deviations from stoichiometry which in itself is sufficient for stabilization of the cubic phase (Figure 2.6). Retaining the cubic phase results in an increased $H_{c2}(0)$, while retaining $T_c(0)$ ([38], Figure 2.7). Also the resistivity increases with increasing Ta or Ti additions [24] which is often referred to as the main cause for an increase in $H_{c2}(0)$. The latter is, according to the GLAG theory in the dirty limit, proportional to ρ_n through (Tinkham [6, p. 162], modified using $1/\nu_F \ell = {}^1/_3\, e^2 N(E_F)\rho_n$):

$$\mu_0 H_{c2}(0) \cong k_B e N(E_F)\rho_n T_c(0) = \frac{3e}{\pi^2 k_B}\gamma\rho_n T_c(0), \qquad (2.12)$$

where ν_F, ℓ and e represent the velocity of the electrons at the Fermi level, the electron mean free path and the elementary charge quantum respectively and γ is the electron specific heat constant or Sommerfeld constant. Orlando *et al.* [29] showed for pure binary films, that $H_{c2}(0)$ [and $H_{c2}(4.2\ \mathrm{K})$] both increase with resistivity, peak at $\rho_n \cong 25\ \mu\Omega$cm and then start to decrease. Similarly, $H_{c2}(4.2\ \mathrm{K})$, as measured in alloyed wires [107] initially increases with Ti or Ta additions, peaks at about 1.5 at.% Ti or 4 at.% Ta, and then reduces with increasing alloy content. The $T_c(0)$ in the pure binary films is about 18 K in the clean limit and initially not influenced by increasing resistivity. However, $T_c(0)$ starts to decrease above $\rho_n \cong 30\ \mu\Omega$cm. At $\rho_n = 35\ \mu\Omega$cm, $\mu_0 H_{c2}(0)$ is still high at 29 T, but $T_c(0)$ has lowered to 16 K (Figure 2.7). The critical temperature in alloyed wires peaks only slightly at about 1 at.% Ti and 2 at.% Ta. A clear reduction in $T_c(0)$ occurs above about 1.5 at.% Ti and 3.5 at.% Ta.

The above summary shows that the effects of Ta and Ti additions are similar but Ti is approximately a factor two more effective in increasing the resistivity. Indeed 1.3 at.% Ti addition results in $\rho_n \cong 40\ \mu\Omega$cm whereas 2.8 at.% Ta addition results in $\rho_n \cong 30\ \mu\Omega$cm [24]. Consistent overall behavior emerges when the initial increase in $H_{c2}(0)$ [while retaining a constant $T_c(0)$] with alloying can be attributed to a suppression of the tetragonal phase and above $\rho_n \cong 30\ \mu\Omega$cm (or about 1.5 at.% Ti and 3.5 at.% Ta) the increased resistivity suppresses both $H_{c2}(0)$ and $T_c(0)$. Note that this suggestion is contrary to the general assumptions in the

literature that $H_{c2}(0)$ rises as a result of increased resistivity due to its proportionality with ρ_n. It can be argued that such an assumption represents an oversimplification, since it neglects the occurrence of the ternary phase and contradicts combination of the well established datasets of $\rho_n(\beta)$, $H_{c2}(\beta)$ and $H_{c2}(T)$: Increasing the resistivity at compositions below 24.5 at.% Sn strongly *reduces* $H_{c2}(0)$ as follows from right plot in Figure 2.6, since increasing ρ_n is equivalent to reducing the Sn content (Figure 2.4). The latter can be physically understood in terms of a reduction of the d-band peaks and thus in $N(E_F)$ in (2.12), which influences $H_{c2}(0)$ directly, as well as through λ_{ep} in $T_c(0)$ [see (2.7)]. This can counteract the increase of $H_{c2}(0)$ through ρ_n. The binary summary (Figure 2.6) remains consistent, at least qualitatively, with Ta or Ti ternary additions if it is assumed that their main effect is to push the composition increasingly off-stoichiometric and simultaneously increasing the resistivity and preventing the tetragonal transformation. It should be emphasized that this argument is not well supported, since all knowledge on ternary systems with Ta and Ti stems from inhomogeneous wires as opposed to homogenized laboratory samples.

2.7 Grain size and the maximum bulk pinning force

A15 Nb–Sn behaves as a Type II superconductor. Its current carrying capabilities for any practical field (above $\mu_0 H_{c1} \cong 38$ mT [59]) thus rely on its capability to pin the flux-lines. The bulk pinning force at J_c can be calculated from its critical balance with the Lorentz force, as will be discussed in Section 3.2:

$$\mathbf{F_P} \equiv -\mathbf{J_c} \times \mathbf{B} \,. \tag{2.13}$$

The bulk pinning force depends on the magnetic field and mostly has a maximum which is positioned roughly between 0.1 to 0.4 H_{c2} ([137], Section 3.3). The magnetic field value at which the maximum occurs depends on the details of the flux-line to lattice interactions [104, 137, 138]. From (2.13) it is clear that the bulk pinning force determines the conductors' current carrying capabilities. The general assumption is that the grain boundaries in the A15 phase represent the primary pinning centers. This is supported by strong experimental evidence in which the maximum pinning force is related to the reciprocal grain size and thus the grain boundary density [139–143]. These results were summarized by Fischer [144] who also obtained additional results for the maximum bulk pinning force versus grain size from VSM characterizations. A reproduction after Fischer, including his own additions is shown in Figure 2.9.

The calculated value for F_P from transport current depends on the area for J_c, which can be normalized to e.g. the non-Cu area or the A15 area (see Section 1.4). Most pinning force data from the literature are calculated from the non-Cu J_c and Figure 2.9 shows that all pre-2002 results are consistent. They follow a single line on a semi-logarithmic plot summarized with:

$$F_{P,\,max} = 22.7 \ln\left(\frac{1}{d_{av}}\right) - 10 \quad \left[\mathrm{GN/m^3}\right], \tag{2.14}$$

in which d_{av} represents the average grain size in μm. Additionally the maximum bulk pinning force data from Fischer, calculated from VSM derived non-Cu J_c values are included in the graph (black squares). These results approximately correspond to the earlier literature data. If, however, the values obtained by Fischer are calculated from J_c values which are normalized to

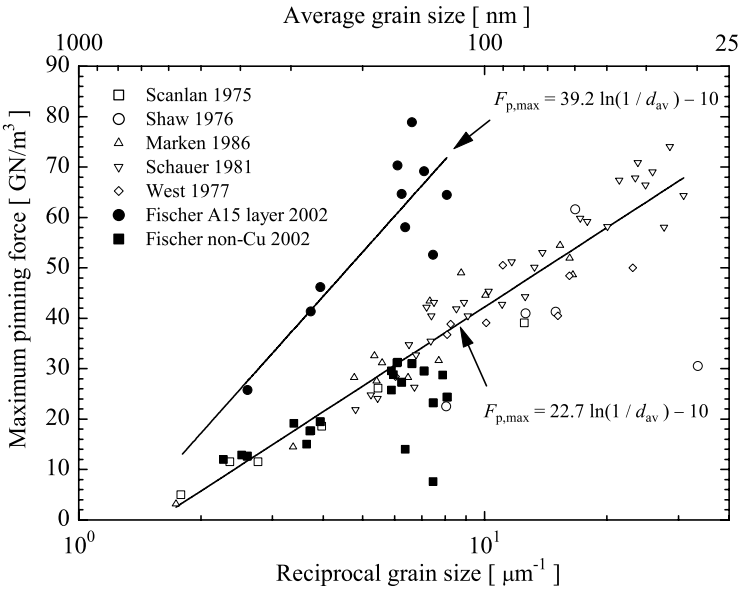

Figure 2.9 *Maximum pinning force as function of reciprocal grain size after Fischer [144].*

the A15 area, the calculated maximum pinning force becomes higher due to the increased J_c values. The slope in the semi-logarithmic plot effectively increases and Fischer's A15 area results can thus be summarized by:

$$F_{\mathrm{P,\,max}} = 39.2 \ln\left(\frac{1}{d_{\mathrm{av}}}\right) - 10 \quad \left[\mathrm{GN/m^3}\right], \tag{2.15}$$

in which again d_{av} is in μm.

The most objective inter-wire comparisons can be made when the pinning force is normalized to the available grain boundary length resulting in an effective pinning force Q_{GB} [144]:

$$Q_{\mathrm{GB}} = \left(\frac{1}{\eta}\right)\left(\frac{F_{\mathrm{P}}}{GB_{l/A}}\right), \tag{2.16}$$

in which η represents an efficiency normalization (assumed 1/3 for equiaxed grains) and $GB_{l/A}$ represents the grain boundary length per area. The effective pinning force can be interpreted as a measure of the effective pinning strength of a grain boundary. Calculation of (2.16), however, requires an accurate determination of $GB_{l/A}$ which, although thoroughly analyzed by Fischer [144], is often not available.

The optimum grain size to achieve the ideal limit of one pinning site per flux-line can be estimated, since the grain boundaries are the primary pinning centers in Nb_3Sn. This limit will be approached if the grain size is comparable to the flux-line spacing at a given field. The flux-line spacing can be calculated by assuming a triangular flux-line lattice [6]:

$$a_{\triangle}(H) = \left(\frac{4}{3}\right)^{1/4} \left(\frac{\phi_0}{\mu_0 H}\right)^{1/2}, \qquad (2.17)$$

which results in 14 nm at 12 T. The smallest grain sizes in Figure 2.9 are about 35 nm but technical wires have, as will be shown in Section 4.4, grain sizes of 100 to 200 nm and are thus far from optimized. In NbTi in contrast, the ideal limit of one flux-line per pinning site has been closely approached through specific heat treatments that introduce a fine distribution of normal conducting alpha–Ti precipitates that act as pinning sites [145]. NbTi is (under present understanding) close to fully optimized.

2.8 Variations of the superconducting properties with strain

2.8.1 Microscopic origins of strain dependence

The superconducting properties of all materials are to a certain extent sensitive to strain, although the effect can be marginal as for example for NbTi. The strain influences on the critical current in the Nb–Sn system originate from shifts in the field-temperature phase boundary, i.e. J_c varies through a change in $H_{c2}(T)$ and possibly a direct influence on the maximum bulk pinning force, as will be detailed in Section 3.7. Strain influences can be separated into two regimes. Obviously, large strain can evoke serious and irreversible damage to the superconductor in the form of cracks in the brittle A15 material. Lower strain can vary the superconducting properties through strain induced lattice instabilities that result in a tetragonal distortion [146, 147] and by influencing the electron-electron interactions which can both be reversible. The latter can, in the case of A15 Nb–Sn, be discussed in terms of lattice distortions that influence the Nb chain integrity and thus $N(E_F)$, or in terms of changes in lattice vibration modes which influence the electron-phonon interaction spectrum [which includes changes in $N(E_F)$].

Since distorting the lattice will modify $N(E_F)$, it can be argued that the net effect is similar to an increase in the amount of disorder. This would render strain effects to be qualitatively similar to irradiation damage, or also similar to Sn deficiency if $\rho_n(S)$ (Figure 2.3) and $\rho_n(\beta)$ (Figure 2.4) can be considered of identical origin (Section 2.2). Snead and Suenaga [148] have performed irradiation experiments on A15 filaments with and without pre-strain and concluded that irradiation increases the effect of pre-strain on T_c. This supports the above hypothesis since the fact that pre-strain and irradiation amplify each other could imply that these effects are based on a similar microscopic principle [i.e. a modification of $N(E_F)$]. Reversing this line of thought it can be argued that increasing the amount of disorder in a highly ordered system will have a relatively larger effect on its superconducting properties compared to a system which is already substantially disordered. Flükiger *et al.* collected strain sensitivity data of the critical current for various A15 wires with a varying degree of ordering and suggested to attribute changes in strain sensitivity to the degree of ordering [98]. The collection is reproduced in Figure 2.10. Specifically, when comparing Nb_3Sn (S = 1) and Nb_3Al ($S_a = 0.95$), the latter being always decidedly off-stoichiometric due to the instability of the stoichiometric phase at lower temperatures, the differences are large, despite roughly comparable H_{c2} and T_c values. If the above argument is correct, it can be expected that strain sensitivity of the A15 Nb–Sn system depends on composition.

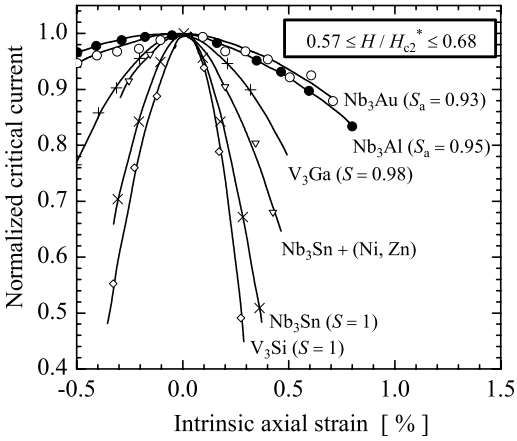

Figure 2.10 *Strain sensitivity of the critical current for different A15 superconductors with varying amounts of disorder after Flükiger et al. [98].*

Strain sensitivity in terms of variations in electron-phonon interaction strength can be explained within the weak coupling BCS theory and also in the more general Eliashberg formalism by a pressure dependence of $T_c(0)$ [149]. However, strong indications exist throughout the literature that hydrostatic strain has only a negligible influence in comparison to non-hydrostatic or distortional strain components [149, 150, 151]. Following these initial publications, which were based on strong coupling renormalized BCS theory, a recent attempt has been made to couple a microscopic full strain invariant analysis to Eliashberg-based relations for the critical temperature through strain-induced modifications in the electron-phonon spectrum [152–154]. This analysis will be discussed in more detail in Section 3.6.2. These recent descriptions are based on T_c variation through a change in the electron-phonon interaction constant by a change in the lattice vibration modes. The latter is modeled by strain induced modifications to the frequency dependent electron-phonon interaction (in which $N(E_F)$ is implicit) and phonon DOS. These models were verified using literature results for T_c versus hydrostatic strain on a single crystal and T_c versus axial strain on wires and tapes. It should be emphasized, however, that for a precise description of the strain influences also the strain dependence of $H_{c2}(T)$ should be correlated to the microscopic theory.

Strain induced changes in $N(E_F)$ in the full invariant analysis for T_c are only accounted for through a strain-modified frequency dependence of the electron-phonon interaction, i.e. the change in $N(E_F)$ is not directly calculated, but this apparently yields sufficient accuracy. For a microscopic description of the strain dependence of $H_{c2}(T)$, however, the exact change in $N(E_F)$ with strain should be known, as is evident from (2.12). This direct influence of a change in $N(E_F)$ on $H_{c2}(0)$ would hypothetically result in a higher strain sensitivity for $H_{c2}(0)$ compared to $T_c(0)$. This is verified by experimental results where the relative strain dependence of $H_{c2}(0)$ is roughly a factor 3 times higher than for $T_c(0)$ as will be further discussed in Section 3.6.1.

2.8.2 Available strain experiments on well defined samples

The previous Sections showed that the main superconducting properties (T_c and H_{c2}) are well investigated on laboratory samples with defined composition. The available literature presents a clear and consistent composition dependence which differs only in details between the various results. Strain sensitivity experiments on defined laboratory samples are, in contrast to this, seriously lacking. Abundant results are available on technical wires which focus on the influences of axial strain on the critical current density. Wires are, however, due to their fabrication processes (see Section 1.4) always decidedly inhomogeneous in composition as well as strain. The foregoing discussions on the possible microscopic origins of strain dependence emphasized the need for results, obtained from samples with a fixed and known composition. Results on laboratory specimen with defined composition are limited to hydrostatic experiments on single crystals or polycrystalline layers [e.g. 92, 155] and one uniaxial experiment, also on a single crystal [156]. These result in $dT_c/dP = -0.14$ and -0.22 K/GPa for a single crystal [92] and a polycrystalline layer [155] respectively. One result exists for the pressure dependence of H_{c2} on an inhomogeneous tape conductor [149], which resulted in $d\mu_0 H_{c2}/dP = -1.2 \pm 0.2$ T/GPa.

Next to inhomogeneities, also the three dimensionality of strain complicates the analysis in wires. Ten Haken [149] made attempts to overcome this problem by switching to deformation experiments on two dimensional tape conductors. Although this has resulted in many new experimental insights that emphasize the importance of non-hydrostatic strain components (see Chapter 3), the tape conductors used in his research still suffered from compositional imperfections.

The lack of extensive strain experiments on well defined laboratory samples thus limits the ability to develop a description for T_c and H_{c2} [or more specifically $H_{c2}(T)$] versus strain, due to the possible different strain sensitivity with composition. These data are required to accurately analyze wire behavior. The data sets needed for this would preferably be analyzed in simplified model samples for which the three dimensional strain can be calculated and which separate the strain dependencies for well defined compositions.

2.9 Conclusions

Superconductivity in the A15 Nb–Sn intermetallic is microscopically well described in general terms of electron-phonon coupling of Cooper pairs. Strong coupling corrections to the microscopic theory become necessary above 23 at.% Sn. Below this concentration the material is weak coupling. The A15 lattice contains Nb chains in which the atoms are closely spaced resulting in an increased density of states around the Fermi level, which is believed to be the main origin for the high critical temperature. The binary phase diagram is well established although a preference for the formation of close to stoichiometric A15 can be argued. Effects of off-stoichiometry can be discussed in terms of lattice parameter, long range ordering, resistivity or atomic Sn content. These terms are equivalent and consistent behavior is observed throughout the literature. The field temperature phase boundary varies substantially with Sn content, but the observations can be explained in terms of off-stoichiometry and the occurrence of the tetragonal phase close to stoichiometry. The dependence of the critical temperature and upper critical field on compositional variations varies only in detail throughout the literature and is well established for the binary system. This consistent behavior arguably also remains valid when ternary additions such as Cu, Ti or Ta are present.

Consistent ternary or quaternary phase diagrams are not available but the pure binary phase diagram can be used, at least qualitatively for the A15 phase, to describe compositional variations in higher order systems. The addition of Cu allows for lower temperature A15 formation. It is present at A15 grain boundaries but does not appear to exist in the A15 grains. Additions of Ti and Ta occupy Nb sites and apparently result in distortions of the Nb chain integrity, cause off-stoichiometry, increase the resistivity and prevent the low temperature tetragonal transformation.

Abundant and consistent data on the bulk pinning force as function of reciprocal average grain size represent solid experimental evidence that the grain boundaries are the main pinning centers. A consistent relation emerges between the maximum bulk pinning force, calculated from the critical current density normalized to the non-Cu area, and the average grain size. This maximum bulk pinning force, combined with the field-temperature phase boundary and strain effects, determines the attainable critical current density.

The influence of hydrostatic deformations can be qualitatively predicted from microscopic theory and limited data from hydrostatic deformation experiments are available. Distortional (non-hydrostatic) deformations, however, dominate the strain sensitivity. Although deformation experiments on wires are abundant, no general statements can be made. This is due to the lack of non-hydrostatic deformation experiments on homogeneous, and spatially simplified samples since it is plausible that strain sensitivity varies with composition.

Chapter 3

Descriptions of the Critical Surface

Prediction of conductor performance requires accurate measurements suitable for interpolation or extrapolation. Knowledge of the dependence of the critical current density on magnetic field, temperature, strain and composition is essential. This Chapter deals with the existing empirical scaling relations for the critical current density and confronts these with alternatives that are more fundamental. It will be shown that the present usual scaling relations for the critical current density can be substantially improved by replacing empirical parts with readily available microscopic or semi-empirical alternatives. A description of the critical surface of Nb_3Sn wires is proposed which features essential improvements with respect to the temperature and strain dependence.

3.1 Introduction

Critical current measurements of Nb_3Sn wires are commonly interpolated and extrapolated using a set of empirical relations for $J_c(H,T,\varepsilon)$, generally referred to as "Summers scaling" [81]. Although this relation shows acceptable accuracy for the description of limited data ranges [157], large discrepancies appear between the fitted values for $T_c(0)$ and $H_{c2}(0)$ and actual measurements [158]. Also at temperatures above about 13 K and for large compressive and tensile axial strains the Summers scaling is inaccurate. It is thus not suitable for precise extrapolations of measured results across a wide range. Finally, it does not account for the microscopic structure and inhomogeneities which are always present. These deficiencies are generally recognized and lead to continuing discussions in the literature on improvements [111, 112, 157–163].

A series of relations resulting from microscopic theory exist for Type II superconductivity. Although the critical current cannot be related quantitatively to the microstructure, various bulk pinning force models have been developed [19, 104, 138, 164–166]. These can be combined with theory on strain dependence [152–154] and the field-temperature phase boundary [5, 7, 167–185]. The latter have been shown to accurately describe measurements on well defined, quasi-homogeneous laboratory samples [28, 29, 36, 38, 173, 181–184].

It is questionable, however, whether such relations can directly describe the behavior of Nb_3Sn in technical wires due to the inhomogeneities present. Moreover, microscopic based relations can be relatively complex and use a significant number of parameters to describe the material involved. The main goal of this Chapter is to find an improved scaling relation which balances the need for better founded formalisms and practical applicability to wire measurements.

3.2 Pinning, flux-line motion, and electric field versus current

A15 Nb–Sn behaves as a Type II superconductor. Hence, the current carrying capability is determined by pinning of the flux-line lattice. Although various pinning models have been developed, they are not yet capable of satisfactorily predicting the critical current density in a real material. This lack of predictability renders a thorough discussion of the various pinning theories outside the scope of this thesis. For an overview of pinning theory the reader is referred to an introduction by Dhallé [186] and the more extensive reviews of Blatter [12] and Brandt [187]. Here, the discussion on pinning mechanisms will be limited to an introduction of the main concepts. Flux motion and the concept of a bulk pinning force are introduced and $E(J)$ relations describing the transition to the normal state are presented.

Consider a Type II superconducting slab in an external magnetic field in the $+z$ direction as depicted in Figure 3.1. Above H_{c1}, flux-lines, each of magnitude $\phi_0 = h / 2e$, penetrate the superconductor. The interaction between the magnetic field in one flux-line and the shielding current density corresponding to this field arising from another flux-line, results in a repulsive force between two neighboring flux-lines [6, 14]. The repulsive interaction between flux-lines leads to a uniform distribution of flux-lines in a triangular lattice, since this implies the largest flux-line spacing and thus the lowest energy state. If the slab carries a transport current in the $+y$ direction, the magnetic field generated by the current will add to the applied magnetic field at the $-x$ side of the slab and subtract from it on the $+x$ side. This results in a gradient in the flux-line density, as depicted in Figure 3.1, which can be quantified using Maxwell's equation $\nabla \times \mathbf{B} = \mu_0 \mathbf{J}$.

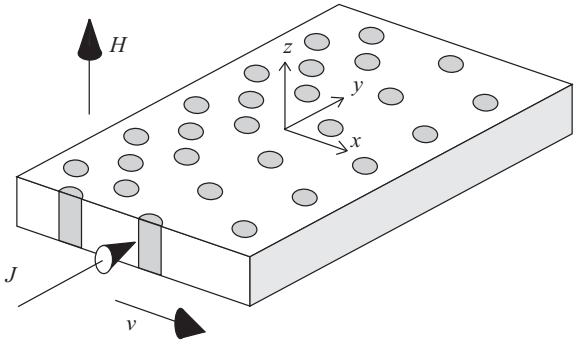

Figure 3.1 *Schematic of a Type II superconducting slab in magnetic field and carrying transport current.*

The repulsive interaction between flux-lines causes them to move from the high density to the low density region, i.e. in the $+x$ direction. The resulting force on the flux-line lattice is equivalent to the Lorentz force acting on a macroscopic current density [188]. To prevent movement of the flux-line lattice, it has to be pinned for example to the grain boundaries in Nb_3Sn superconductors. In this way, the Lorentz force is balanced by a bulk pinning force per unit volume (F_P) as given by (2.13).

If the Lorentz exceeds the bulk pinning force, the flux-lines will start to move and according to Faraday's law an electric field E_y is generated along the slab. This electric field is in parallel to the transport current density and results in an ohmic loss J_yE_y, originating from so-called flux flow resistivity. The electric field can be modeled using the Anderson-Kim flux creep model [189, 190] by using a pinning potential energy U_P which has minima at pinning sites. For a flux-line (or flux-line bundle) to move from one energy minimum to another it has to overcome (hop) the energy barrier U_P, which can occur through thermal activation with an energy W. The presence of a macroscopic transport current density effectively lowers U_P, thereby facilitating thermal activation until at the critical current density, this initiates the superconducting to normal transition. Assuming thermal activation of the flux-lines and using Maxwell-Boltzmann statistics, leads to the following expression for the electric field [186]:

$$E = \mu_0 H \upsilon d \exp\left(-\frac{W(J)}{k_B T}\right), \tag{3.1}$$

in which υ is a so-called hopping attempt frequency and d is the average distance between the minima in U_P. Several forms for the activation energy $W(J)$ are used, e.g. $W(J) = W_0(1 - J / J_c)$, leading to an exponential $E(J)$ relation:

$$E = E_c \exp\left[-n(H,T)\left(1-\frac{J}{J_c(H,T)}\right)\right], \tag{3.2}$$

where E_c is an electric field criterion to define the critical current density J_c. Alternatively, $W(J) = W_0 \ln(J_c / J)$ can be used, leading to a power-law type $E(J)$ relation:

$$E = E_c \left[\frac{J}{J_c(H,T)} \right]^{n(H,T)} . \qquad (3.3)$$

The latter is most often used to describe $E(J)$ measurements in technical superconductors as Nb_3Sn wires. Both (3.2) and (3.3) use:

$$n(H,T) = \frac{W_0(H,T)}{k_B T}, \qquad (3.4)$$

which is often referred to as the n-value of the material. For $n \gg 1$, (3.2) and (3.3) give the same slope of the $E(J)$ relation and both will be practically linear on a double logarithmic scale for $n \gg 1$, as is demonstrated in Figure 3.2. Typical values for n in Nb_3Sn wires are 20 to 60. The n-value is often stated to be a measure of the "quality" of the conductor, but from (3.4) it is clear that the term "quality" reflects improved pinning through deeper minima in U_P. In practical conductors, the n-value will depend on the distribution of pinning energies. The presence of inhomogeneities, and thus H_{c2} and T_c distributions, will result in a smearing of the transition and a lowering of the n-value as compared to homogenous materials. The n-value therefore also reflects the inhomogeneity of a conductor.

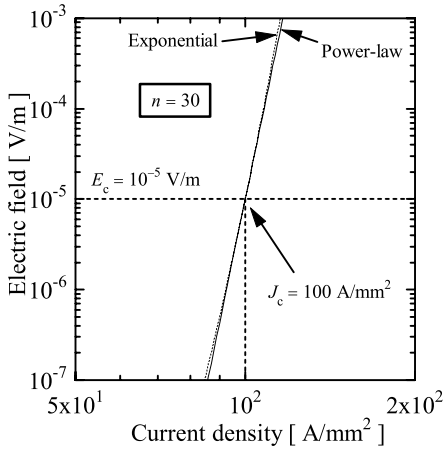

Figure 3.2 *Electric field as function of current density according to an exponential (3.2) and a power-law (3.3) E(J) relation with $n = 30$, $E_c = 10^{-5}$ V/m and $J_c = 100$ A/mm^2.*

Thermally activated flux-line movement results in a de-pinning field which can be substantially lower than the upper critical field for superconductors with a high critical temperature. For high temperature superconductors (HTS), which have T_c values around 100 K, this leads to the occurrence of a thermally activated, so-called irreversibility field (H_{irr}), which defines the transition to zero pinning energy well below H_{c2} [191]. Above H_{irr} the critical current density is zero due to the loss of pinning potential, but the material is still superconducting. This is sketched in the left graph in Figure 3.3. The irreversibility field can be defined as the field at which the activation barrier disappears, i.e. $W_0(H_{irr},T) \cong k_B T$. The scaling field for the critical current density in HTS is thus, due to the high temperatures, mainly determined by thermally activated flux-line flow.

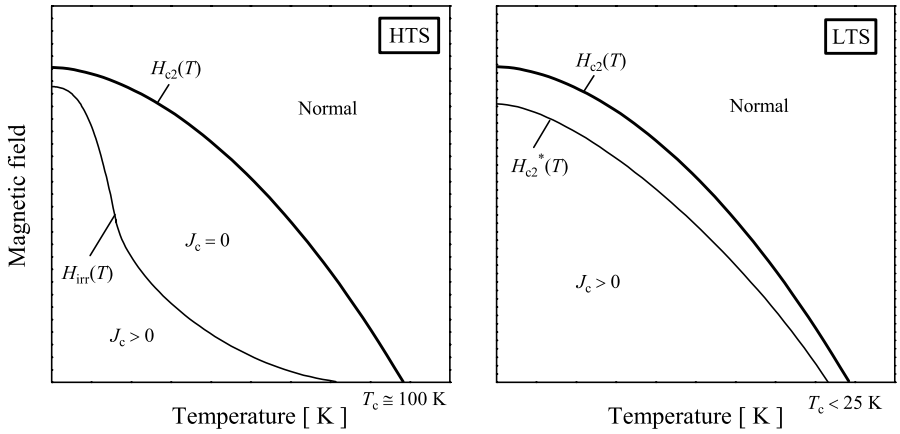

Figure 3.3 *Sketch of the field-temperature limitation in high temperature superconductors (left) and low temperature superconductors (right).*

The inevitable presence of inhomogeneities in any superconducting bulk material will additionally lead to some average upper critical field by which the critical current density is scaled. This average depends on the characterization method and can be referred to as H_{c2}^*. Its value will obviously also be lower than the maximum H_{c2} value present in the sample. In LTS materials thermally activated de-pinning (flux-line melting) will still be present, but due to the much lower temperature (< 25 K), it will be less pronounced. This means, as will be shown in Chapter 6 and Chapter 7, that the scaling field for the critical current density in LTS, in contrast to HTS, is mainly determined by an inhomogeneity averaged critical field. A typical field-temperature boundary as observable in LTS is sketched in the right graph in Figure 3.3. In HTS thermal de-pinning thus will dominate above inhomogeneity averaging due to the high temperatures whereas in LTS the latter dominates. The lower sections of superconducting to normal transitions in Nb_3Sn wires are, in analogy to thermally activated de-pinning in HTS, often referred to as flux-line melting [192], whereas this is in error if inhomogeneity effects dominate. The presence of thermal de-pinning in a perfectly homogeneous Nb_3Sn conductor will obviously result in a finite transition width, but for practical, inhomogeneous wires, the onset to the normal state is determined by the lesser quality sections, as will be emphasized in Section 6.3. Since in practice, however, no distinction can be made between thermally activated flux flow and inhomogeneity averaging, the "irreversibility field" in Nb_3Sn will, within this thesis, be referred to as H_{c2}^*, or H_K if Kramer extrapolations are used to determine the critical field (as described in the next Section).

3.3 Magnetic field dependence of the bulk pinning force

The magnetic field dependence of the critical current density in Nb_3Sn is determined by de-pinning of the flux-line lattice and thus by the magnetic field dependence of the bulk pinning force. The latter depends on the microscopic de-pinning mechanism. A general description for

the magnetic field dependence of the bulk pinning force results from the observation that, for a multitude of low temperature superconductors, the bulk pinning force scales according to:

$$\begin{aligned} F_P &\propto F_{Pmax} f(h) \\ &\propto \frac{H_{c2}^{\nu}}{\kappa_1^{\gamma}} f(h) \end{aligned}, \tag{3.5}$$

as was first pointed out by Fietz and Webb [193]. In (3.5), h represents the reduced magnetic field H / H_{c2}, κ_1 is the Ginzburg-Landau (GL) parameter and $f(h)$ is a function which, at low magnetic fields rises with h, peaks at a certain value for h (yielding a maximum bulk pinning force) and then decreases with h at higher magnetic fields as sketched in Figure 3.4. The values of ν and γ are independent of temperature and microstructure. The value for ν is generally obtained by neglecting the GL constant and plotting the maximum bulk pinning force against H_{c2} on a double logarithmic scale. Values for ν are usually between 2 and 3 and for Nb_3Sn values of 2 and 2.5 are mostly cited. Because κ_1 may change up to 50% with temperature (see Section 3.5), its temperature dependence cannot be neglected for an accurate description of the critical surface of Nb_3Sn.

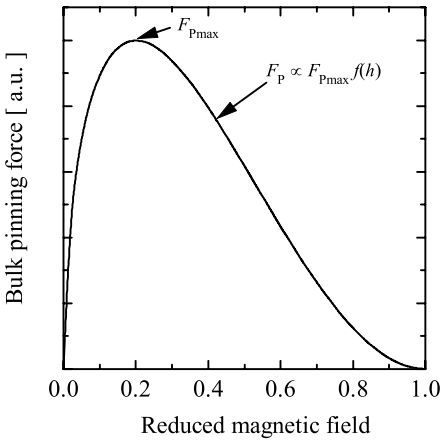

Figure 3.4 *Sketch of the magnetic field dependence of the bulk pinning force.*

The subscript 1 in κ_1 arises from the fact that the GL parameter can be determined in several ways. At temperatures close to T_c, various characterization methods yield the same value for κ equal to the GL value $\lambda(T) / \xi(T)$, but at lower temperatures deviations can occur between the various ways to determine κ. Maki [167] treated these deviations microscopically and defined three different GL constants (κ_{1-3}) depending on the determination method. Following his definitions:

$$\kappa_1 = \frac{H_{c2}}{\sqrt{2} H_c} . \tag{3.6}$$

Several models for $f(h)$ exist [104, 138, 194], but most often the Kramer version is used. Kramer derived two models for $f(h)$, using two regimes. For the regime below the peak in $f(h)$ he assumed that flux motion primarily occurs by de-pinning of individual flux-lines, whereas in the regime above the peak in $f(h)$ de-pinning occurs by synchronous shear of the flux-line lattice around line pins which are too strong to be broken. The latter is referred to as the flux shear model and for this regime Kramer proposed [104]:

$$F_P = \frac{C_{66}}{12\pi^2 \left(1 - a_0\sqrt{\rho}\right)^2 a_0}, \tag{3.7}$$

where C_{66} represents the elastic shear stiffness of the flux-line lattice, a_0 is the flux-line spacing for a set of planar pins and $\sqrt{\rho}$ represents the density of the pinning planes. In bulk Nb_3Sn, the grain boundaries are the main pinning centers and can thus be interpreted as the pinning planes yielding $1 / \sqrt{\rho} = d_{av}$, the average grain size.

The shear modulus of the flux-line lattice of a high field superconductor without paramagnetic limiting (Section 3.4.2), was derived by Labusch [195]:

$$C_{66}(H) = 7.4\times10^4 \frac{\left(\mu_0 H_{c2}\right)^2}{\kappa_1^2}(1-h)^2 \quad \left[\mathrm{N/m^2}\right]. \tag{3.8}$$

Combining (3.7) with (3.8), assuming $1 / \sqrt{\rho} = d_{av}$ and a triangular flux-line lattice with a spacing as given by (2.17) results in:

$$F_P(H) = 12.8 \frac{\left(\mu_0 H_{c2}\right)^{2.5}}{\kappa_1^2} \frac{h^{0.5}(1-h)^2}{\left(1 - a_\triangle(H)/d_{av}\right)^2} \quad \left[\mathrm{GN/m^3}\right]. \tag{3.9}$$

Using the Kramer form therefore results in $\nu = 2.5$ and $\gamma = 2$ in (3.5), if $f(h)$ is defined as $f(h) \propto h^{0.5}(1-h)^2$ and $(1 - a_\triangle(H) / d_{av}) \cong 1$, which will be validated below. Many authors indeed state $\nu = 2.5$ [104, 138, 81, 196–198].

Higher values for ν can be found if experimental data are described with non-Kramer like pinning. Deviating values for ν in (3.5) are reported by Kroeger *et al.* [105] who claim $\nu \cong 3.0$ and by Cheggour and Hampshire [112] who state $\nu \cong 3.2$. It should be noted that both studies neglect κ_1 and fit the experimental results to a non-Kramer like $F_P \propto (1-h)^3$ and $F_P \propto (1-h)^{3.5}$ respectively. This choice suggests different pinning behavior. It was already pointed out by Kramer [104] that ignoring the GL parameter can change the experimentally determined ν. It will be explained below that such high values for the power above $(1-h)$ can arise when sample inhomogeneities are ignored. Here, they will be accounted for, which results in the experimentally supported assumption that $F_P \propto (1-h)^2$, as will be discussed in more detail in Section 7.3.

Combining (3.9) with the reverse definition of the Lorentz force (2.13) gives (Suenaga and Welch in [18]):

$$J_c^{0.5}\left(\mu_0 H\right)^{0.25} = \frac{1.1\times10^5}{\kappa_1} \frac{\mu_0\left(H_{c2} - H\right)}{\left(1 - a_\triangle(H)/d_{av}\right)}. \tag{3.10}$$

In most technical wires d_{av} is 100 to 200 nm as will be shown in Section 4.4, whereas the flux-line spacing decreases rapidly below 50 nm for magnetic fields above 1 T. Therefore $a_{\triangle}(H) / d_{av} \ll 1$ and $J_c^{0.5}(\mu_0 H)^{0.25}$ will approximately be linear in H and can be referred to as a Kramer function f_K:

$$f_K(H) \equiv J_c^{0.5}(\mu_0 H)^{0.25} \cong \frac{1.1\times 10^5}{\kappa_1}\mu_0(H_{c2} - H) \quad [\,A^{0.5}T^{0.25}/m\,]. \tag{3.11}$$

A linear extrapolation of (3.11) to $J_c = 0$ then yields H_{c2} and the slope can be used to calculate κ_1. The Kramer extrapolated critical field will be referred to as H_K to distinguish between such an extrapolated and the actual value.

The pinning force, as given by (3.9), peaks at $h = 0.2$ if $a_{\triangle}(H) \ll d_{av}$ to yield the maximum pinning force:

$$F_{Pmax} = \frac{3.7(\mu_0 H_{c2})^{2.5}}{\kappa_1^2} \quad \left[\mathrm{GN/m^3}\right]. \tag{3.12}$$

The dependence $F_P \propto (1-h)^2$ occurs when shear deformation of the flux-line lattice is the primary de-pinning mechanism as was mentioned above. This was shown experimentally by Cooley *et al.* [137] to be the case when the grain size is substantially larger than the flux-line spacing [$d_{av} > 2a_{\triangle}(H)$]. If the grain size is comparable to the flux-line spacing, a direct summation of individual pinning interactions between grain boundaries and flux-lines occurs which corresponds to $F_P \propto (1-h)$ [137, 165, 195]. Plots of the Kramer function f_K from (3.11) versus magnetic field (a "Kramer plot"), calculated from J_c data measured on Nb_3Sn conductors, are generally linear in the "standard" J_c measurement regime of about $0.2 < h < 0.6$. This supports shearing of the flux-line lattice as the primary de-pinning mechanism, provided that the grain size is larger than about 100 nm [137]. Moreover, Kramer plots resulting from magnetization data on Powder-in-Tube processed wires, reacted at various temperature and time combinations, were shown to be perfectly straight down to $h = 0.07$ at various temperatures by Fischer [144]. Also transport J_c measurements on different bronze processed wires indicated straight Kramer plots at various temperatures down to $h = 0.04$ [163, 196]. These observations validate the application of (3.9) to very low fields and support the assumption that the $(1 - a_{\triangle} / d_{av})$ term has negligible influence and can be approximated by $(1 - a_{\triangle} / d_{av}) \cong 1$. Moreover, they indicate that for technical wires, which have an average grain size above 100 nm, shear deformation of the flux-line lattice apparently remains the primary de-pinning mechanism also below the maximum in F_P. The assumptions used to arrive at the Kramer model have received some criticism [199]. In practice, however, using the high magnetic field description of Kramer appears to hold for polycrystalline composite conductors.

Outside the regularly investigated regime of about $0.2 < h < 0.6$, non-linearities are sometimes observed in Kramer plots of wire measurements, mainly at magnetic fields approaching the maximum H_{c2} that is present in the wire. The pinning force function (3.9), combined with the approximation $(1 - a_{\triangle}(H) / d_{av}) \cong 1$ is therefore often written in a more general form:

$$F_P(h) = F_{Pmax} h^p (1-h)^q, \tag{3.13}$$

where p and q are constants determining $f(h)$. This allows for insertion of different values of p and q that implicate a different pinning behavior, but most probably originate from

inhomogeneity averaging. It will be shown below how deviating values of p and q from the Kramer form are correlated to experimentally observed behavior. The maximum pinning force in the general form (3.13) is given by:

$$F_{\mathrm{Pmax}} = C\frac{\left(\mu_0 H_{\mathrm{c2}}\right)^{\nu}}{\kappa_1^{\gamma}}, \tag{3.14}$$

where C, ν and γ are constants. The temperature dependence of κ_1 is sometimes neglected by inserting it in the normalization constant C. The general form (3.13) and (3.14) with the various constants enables to use the function for data fitting by which families of conductors can be compared and properties can be tabulated in terms of these constants.

Least squares fits on the data using (3.13) result, in the case of an inhomogeneous sample, in values for p and q which deviate from 0.5 and 2 respectively, but yield a better fit to the measurements (see e.g. [112]). These different values for p and q lead to still ongoing discussion in the literature whether or not a general pinning mechanism, or $f(h)$, can be assumed for Nb_3Sn wires, since a change in p and q can be interpreted as a change in pinning behavior.

The field dependence of the bulk pinning force as given by (3.13) is shown in Figure 3.5 and combined with Kramer plots for various values of p and q around 0.5 and 2 respectively. A $\pm$ 40% variation of p mainly influences the low field region. The aforementioned observations of perfectly straight Kramer plots at lower magnetic fields for bronze and Powder-in-Tube processed wires, however, render strong deviations of p from 0.5 unlikely.

A $\pm$ 25% variation in q results in a change in the maximum pinning force and its position and an up- or downward curvature in the Kramer plot for $h \to 1$. The effect of a lowering of q, i.e. an increase of the maximum pinning force combined with a shift of its position towards higher

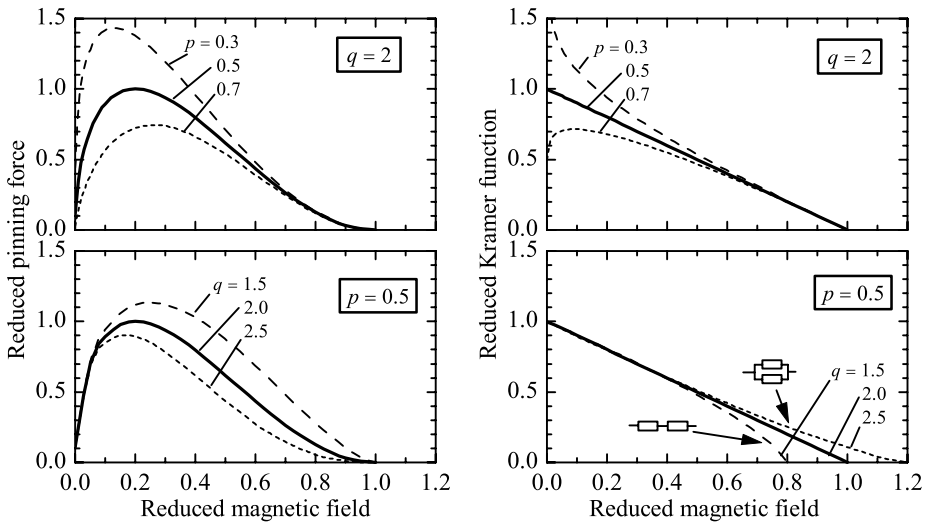

Figure 3.5 *Simulated changes with p and q in the field dependence of the bulk pinning force (left plots) and Kramer function (right plots).*

magnetic field is identical to what has been observed experimentally through grain refinement in Powder-in-Tube wires by Cooley *et al.* [137]. Upward and downward tails in Kramer plots have both been observed experimentally (e.g. Suenaga in [15], Ekin in [19], [200]) and have been attributed to microstructural [24] and compositional (Suenaga and Welch in [18], Ekin in [19], Cooley *et al.* [197]) origins.

The most convincing support for attributing curvature in Kramer plots when $h \to 1$ to inhomogeneities is given by Cooley *et al.* [197], who numerically modeled the filaments in a Powder-in-Tube processed wire as concentric shells with varying Sn content and thus varying H_{c2} and T_c. It was further assumed that each composition behaves according to $q = 2$. An area weighted summation of the transport current density of such a system of parallel paths of variable property showed that a concave tail appears in the overall Kramer plots when the maximum available H_{c2} is approached. Increasing the severity of the Sn gradient in the A15 sections increases the occurrence of such tails in otherwise linear overall Kramer plots. When approaching higher magnetic field, initially the lowest H_{c2} A15 sections lose their superconductivity until finally, at $f_K = 0$, superconductivity is lost in the sections with the highest H_{c2}. Such an area weighted summation over parallel paths of lesser and better A15 quality results in a similar overall Kramer plot as for $p = 0.5$ and $q = 2.5$ in Figure 3.5. This argument is a strong indication that the curvature is not due to different de-pinning mechanisms but to inhomogeneity effects and thus that q should be 2.

It can thus be assumed that the Kramer flux-line shear model, at constant composition, is valid over nearly the full magnetic field range, i.e. up to H_{c2} and down to a magnetic field where the flux-line lattice spacing becomes approximately more than half of the A15 grain size [137], which is below 1 T from (2.17). Non-linearities in Kramer plots when approaching the maximum H_{c2} are thus attributed to inhomogeneity averaging. The local $H_{c2}(x,y,z)$ and $T_c(x,y,z)$ in the A15 regions depend on the local Sn concentration $\beta(x,y,z)$ through (2.10) and (2.11). The effective bulk values $H_{c2}^*(0)$ and T_c^*, as detected by critical current measurements, are weighted averages over the A15 volume of the form:

$$H_{c2}^*(0) = \frac{1}{V}\int_V H_{c2}\left(\beta(x,y,z)\right)dV \quad \text{and} \quad T_c^* = \frac{1}{V}\int_V T_c\left(\beta(x,y,z)\right)dV \,. \tag{3.15}$$

For the regular filament cross-sections in PIT wires, Cooley *et al.* [197] have shown that it is sufficient when $\beta(x,y,z)$ is only a function of filament radius, i.e. $\beta(x,y,z) = \beta(r)$, leading to an averaging of the form:

$$H_{c2}^*(0) = \frac{1}{A}\int_A H_{c2}\left(\beta(r)\right)dA \quad \text{and} \quad T_c^* = \frac{1}{A}\int_A T_c\left(\beta(r)\right)dA \,, \tag{3.16}$$

where A represents the cross-sectional A15 area. This parallel path model can be supported by measurements on similar PIT processed wires (Section 7.8, [202]). Relations (3.16) will be used in Section 7.8 to estimate $H_{c2}^*(0)$ and T_c^* from measured Sn gradients in PIT processed wire.

A downward tail in Kramer plots, as is often observed in bronze processed wires, can be described with $q < 2$ as shown in Figure 3.5, thereby implicitly assuming a different de-pinning mechanism. However, assuming a serial connection of lesser and better A15 quality regions for the more irregular filaments in bronze processed wires, also results in a downward tail in

Kramer plots when $h \to 1$, since the lower quality A15 sections will determine the overall transport properties.

The discussion above leads to the conclusion that there is no reason to deviate from $F_P \propto h^{0.5}(1-h)^2$, provided that the inevitable presence of A15 inhomogeneities in wires is recognized. This will be supported by measurements in Chapter 6 and Chapter 7.

3.4 Temperature dependence of the upper critical field

To come to an overall description for $J_c(H,T,\varepsilon)$, the temperature dependence of the pinning force is considered. In observing (3.13) and (3.14) it is clear that temperature dependence occurs through temperature dependence of the upper critical field and the GL parameter:

$$F_p(H,T) \cong C \frac{\left[\mu_0 H_{c2}(T)\right]^{\nu}}{\kappa_1(T)^{\gamma}} f(h), \tag{3.17}$$

with $h = H / H_{c2}(T)$. The exponents ν and γ are constant values predicted as 2.5 and 2 respectively. It is thus required to discuss the available descriptions for the temperature dependence of the upper critical field and the GL parameter. For both parameters, empirical as well as microscopic alternatives are available. In the Summers relation [81] empirical forms are used. It will be shown here, and in Section 3.5, how these can be replaced by alternatives with a better connection to the microscopic theory.

3.4.1 Empirical temperature dependence

First, the empirical temperature dependence of the upper critical field, as used in the Summers relation, is introduced. Based on earlier work by Suenaga in [15] and Hampshire *et al.* [196], Summers *et al.* [81] proposed an empirical relation for the temperature dependence of the upper critical field, thereby improving the correspondence between the available scaling relations and measured results:

$$\frac{H_{c2}(T)}{H_{c2}(0)} = \left(1-t^2\right)\frac{\kappa_1(T)}{\kappa_1(0)} = \left(1-t^2\right)\left[1-0.31t^2\left(1-1.77\ln t\right)\right], \tag{3.18}$$

where $t = T / T_c$. In this relation an empirical temperature dependence for the GL parameter is inserted in (3.6) and for the temperature dependence of the thermodynamic critical field $H_c(t) / H_c(0) = 1 - t^2$ is used. This temperature dependence has been applied extensively to describe temperature dependent critical current data of Nb_3Sn wires. Relation (3.18) apparently is sufficiently accurate to describe temperature dependent critical current measurements [81, 157].

3.4.2 Microscopic based temperature dependence

Before introducing a microscopic based temperature dependence of the upper critical field, some general terminology used in microscopic theory needs to be discussed. The microscopic theory can roughly be separated into three approaches. The first, and simplest, approach is an application of the BCS and GLAG theories, which is valid for weak electron-phonon interactions. In the second approach, strong coupling effects are accounted for by a renormalization of the quasiparticle parameters used in the BCS and GLAG theories. The

renormalization is done by a multiplication or division of the parameters by a factor $(1 + \lambda_{ep})$, where λ_{ep} is the electron-phonon coupling constant defined by Eliashberg as [56]:

$$\lambda_{ep} = 2\int \frac{\alpha^2(\omega)F(\omega)}{\omega} d\omega, \tag{3.19}$$

in which $\alpha^2(\omega)F(\omega)$ is, as mentioned in Section 1.2.2, the product of the electron-phonon interaction and the phonon density of states. These renormalized BCS approaches are generally validated for $\lambda_{ep} < 1.5$ [8, 58]. The third approach is valid for any given electron-phonon interaction strength, but involves accounting for the details of the interaction spectrum and solving the nonlinear Eliashberg equations. Depending on Sn content in the A15, a wide range of electron-phonon interaction strengths, also $\lambda_{ep} > 1.5$, can be expected in Nb_3Sn superconductors, as was shown in Section 2.4. This means that generally valid microscopic descriptions for Nb_3Sn should be based on the third approach and thus the full Eliashberg theory.

Relations for the upper critical field

An early microscopic description for the temperature dependence of the upper critical field was simultaneously derived in 1964 by Maki ([167], Maki in [7]) and De Gennes [5, 168] which, written in the De Gennes form yields the implicit relation (MDG function):

$$\ln\left(\frac{T}{T_c(0)}\right) = \psi\left(\frac{1}{2}\right) - \psi\left(\frac{1}{2} + \frac{\hbar D \mu_0 H_{c2}(T)}{2\phi_0 k_B T}\right). \tag{3.20}$$

The function uses only two parameters, namely $T_c(0)$ (which can be measured) and the diffusion constant of the normal conducting electrons D. The other parameters are the reduced Planck constant ($\hbar$), the magnetic flux quantum (ϕ_0) and the Boltzmann constant (k_B). The terms $\psi(x)$ represent the digamma function [201]. The description was derived assuming a dirty superconductor (i.e. $\ell \ll \xi$), it uses a spherical Fermi surface approximation and assumes a constant $N(E_F)$ and a weak electron-phonon interaction (the BCS approximation). Furthermore it assumes no paramagnetic limitation of $H_{c2}(T)$ and an absence of spin-orbit scattering.

For convenience, a normalized form of (3.20) with respect to temperature will be defined:

$$\mathrm{MDG}(t) = \frac{H_{c2}(t)_{\mathrm{MDG}}}{H_{c2}(0)_{\mathrm{MDG}}}, \tag{3.21}$$

in which $H_{c2}(t)_{MDG}$ represents the temperature dependence of the upper critical field calculated using (3.20) and $t = T / T_c(0)$.

The diffusion constant in (3.20) is inversely proportional to the slope of the $H_{c2}(T)$ dependence at $T_c(0)$ which follows from an expansion of (3.20) combined with taking the derivative for $T \to T_c(0)$ [5]:

$$\left(\frac{\partial \mu_0 H_{c2}(T)}{\partial T}\right)_{T=T_c(0)} = -\frac{4\phi_0 k_B}{\pi^2 \hbar D}. \tag{3.22}$$

In addition, expanding for $T \to 0$ and combining with (3.20) results in [5]:

$$\mu_0 H_{c2}(0) = 1.764 \frac{\phi_0 k_B}{Dh} T_c(0) = -0.693 T_c(0) \left(\frac{\partial \mu_0 H_{c2}(T)}{\partial T} \right)_{T=T_c(0)} . \quad (3.23)$$

in which h is Planck's constant.

It can be convenient for practical applications to avoid the need to solve the implicit MDG relation by replacing it with an explicit expression. From (3.23) it can directly be seen that (3.20) can be approximated for temperatures close to $T_c(0)$ with:

$$\mathrm{MDG}(t)_{T \to T_c} \cong \left(1 - t^{1.44}\right), \quad (3.24)$$

since taking the derivative of (3.24) with respect to temperature at $T_c(0)$ will result in (3.23). An approximation of (3.20) for the entire temperature range yields a similar form with a slightly different power:

$$\mathrm{MDG}(t) \cong \left(1 - t^{1.52}\right). \quad (3.25)$$

This power of 1.52 is practically identical to the value of 1.5 which was found from a similar fit as (3.25) to (partly) extrapolated $H_{c2}^*(T)$ results by Cheggour and Hampshire [112]. Combining (3.20) – (3.23) with (2.10) and (2.11) gives the opportunity to determine the field-temperature phase boundary of Nb_3Sn as function of Sn content if strain influences are neglected.

More advanced descriptions for $H_{c2}(T)$ were developed after the Maki-De Gennes version (3.20) by Werthamer and collaborators to include varying degrees of impurity [169, 170], electron spin and spin-orbit effects [171], Fermi surface anisotropy [172] and strong coupling effects [173]. This set is generally referred to as WHH after the authors Werthamer, Helfand and Hohenberg. Further work towards an arbitrary interaction strength, including retardation effects, was carried out by Eilenberger and Ambegaokar [174]; Usadel [175, 176]; Rainer, Bergman and Eckhardt [177, 178, 179]; and Schopohl and Scharnberg [180, 181]. These descriptions are all based on the weak coupling BCS formalism in which strong coupling effects are included through a renormalization of the quasiparticle parameters as described above.

The BCS based descriptions yield acceptable agreement to experimental data close to $T_c(0)$, but at low temperatures, where the effects of stronger interaction are enhanced, they result in too low values for the upper critical field. This is mostly corrected for by the introduction of significant amounts of spin-orbit scattering (described below), as was done by Orlando *et al.* [28]. A more exact description, independent of the interaction strength, however, should include the details of the phonon spectrum and be based on the Eliashberg equations. Such a full Eliashberg theory of $H_{c2}(T)$ was formulated by Schossmann and Schachinger in 1986 [182]. They concluded that the need for significant amounts of spin-orbit scattering in the BCS based formalisms resulted from not sufficiently accounting for strong coupling effects. They found excellent agreement of theory and experiment using the full Eliashberg equations without the need to include spin-orbit scattering. A summary of the formalisms involved in the descriptions above is given by Rieck *et al.* [183]. Very recently, *ab inito* calculations of the temperature dependence of the upper critical field were published by Arai and Kita [184, 185], but these are mainly applicable to idealized systems with perfect lattices.

Although application of the full Eliashberg based formalisms is the most correct approach, there are two reasons for applying only the simplest form of the microscopic descriptions [i.e. (3.20)]

to wire results. First, since wires are inherently inhomogeneous there is no single $H_{c2}(T)$ but a distribution of properties, as was discussed in Section 3.3. Also, the inaccessibility of the normal state resistivity (which is a prime parameter in the microscopic theory) of the A15 in wires renders a proper connection to the theory practically impossible. Second, the use of the formal descriptions results in an increased number of parameters compared to (3.20). This can be avoided by implementing the additional parameters that are required for a proper connection to the microscopic theory in D [and thus in the slope at $T_c(0)$, (3.23)], $T_c(0)$ and $H_{c2}(T)$ in (3.20). To allow this it has to be assumed that the shape of $H_{c2}(T)$, at least to first order, remains unchanged, which can be supported experimentally ([202], Chapter 6) and, at least partly, also from microscopic theory [178]. This approximation will be described in more detail below after a discussion of the parameters that are required to connect the microscopic theory with the experimental results.

Parameters for connection to the microscopic theory

Most advanced descriptions are applied in terms of a reduced magnetic field introduced by WHH as:

$$h_{c2}(0) \equiv \frac{H_{c2}(0)}{T_c(0)\left[-\frac{\partial H_{c2}(T)}{\partial T}\right]_{T=T_c(0)}}, \tag{3.26}$$

for which was shown by WHH that $h_{c2}(0) = 0.693$ in the dirty limit and $h_{c2}(0) = 0.727$ in the clean limit. The dirty limit value is identical to what was derived on the basis of the MDG function [(3.20) and (3.23)]. The connection to material parameters occurs by calculating the slope at $T_c(0)$ on the basis of microscopic theory, e.g. using renormalized BCS descriptions as was demonstrated by Orlando *et al.* [28].

For a complete description also paramagnetic lowering of H_{c2}, which occurs when the applied magnetic field flips the electron spin of one of the electrons forming a Cooper pair, should be considered. Additionally spin-flip scattering occurring through the interaction of the orbital magnetic moment and the electron spin, generally referred to as spin-orbit scattering, can be considered. As mentioned above, however, the latter effect was claimed to be irrelevant provided that strong coupling effects are properly accounted for through the use of the full Eliashberg equations [182]. Paramagnetic limitations, often referred to as Pauli Paramagnetic Limitation (PPL), however, could occur considering the high critical magnetic fields observed in Nb_3Sn conductors.

The theory of H_{c2} describes pair-breaking by a magnetic field through its interaction with the orbital motion (resulting e.g. in flux-line penetration in Type II superconductors) and through the alignment of the electron spin of Cooper pairs (i.e. PPL). The observed critical magnetic field can be expressed as [100, 203]:

$$H_{c2}(0) = \frac{H_{c2}^{+}(0) H_P(0)}{\left[2H_{c2}^{+}(0)^2 + H_P(0)^2\right]^{\frac{1}{2}}}, \tag{3.27}$$

where $H_{c2}^{+}(0)$ represents the critical magnetic field due to orbital pair breaking alone, given by (3.26) and $H_P(0)$ represents the critical magnetic field due to PPL alone which has the BCS value:

$$\mu_0 H_P^{BCS}(0) \equiv \frac{\Delta_0^{BCS}}{\mu_B \sqrt{2}} = 1.86 T_c(0), \tag{3.28}$$

usually accredited to Clogston [204] and Chandrasekhar [205] and referred to as the Clogston limit. It was realized by Rainer *et al.* [178] and Orlando and Beasley [203] that this BCS Pauli limiting field was too low and should be renormalized:

$$H_P(0) = H_P^{BCS}(0)\left(1 + \lambda_{ep}\right), \tag{3.29}$$

In Chapter 6 it will be shown that for the highest H_{c2} sections in most wires $T_c(0) \cong 18$ K and $[\partial \mu_0 H_{c2}(T) / \partial T]_{T=T_c} \cong -2.4$ T/K resulting in $\mu_0 H_{c2}^{+}(0) \cong 30$ T and $\mu_0 H_P^{BCS}(0) \cong 33.5$ T. Assuming the usual $\lambda_{ep} \cong 1.8$ in (3.29) results in $\mu_0 H_P(0) \cong 94$ T. Using (3.27), this results in observable critical magnetic fields of about 27 T. Since the measured values correspond to $H_{c2}^{+}(0)$, i.e. $\mu_0 H_{c2}(0) \cong \mu_0 H_{c2}^{+}(0) \cong 30$ T, no PPL is observed, in agreement with what was concluded by Orlando *et al.* [28] and Beasley [100].

If spin-orbit scattering is present, it will counteract PPL limitation [171] and raise $H_P(0)$, bringing $H_{c2}(0)$ closer to $H_{c2}^{+}(0)$. Exact account of spin-orbit scattering over the full temperature range requires re-calculation of $\ln(t)$ in (3.20) in terms of a summation of multiple digamma functions [171]. In the limit of strong spin-orbit scattering, however, the Pauli magnetic field becomes $H_P^{SO} \cong 1.2 \lambda_{SO} H_P(0)$ [22], in which λ_{SO} represents the spin-orbit scattering frequency [171]. From this the increase $H_P(0)$ through spin-orbit scattering is immediately visible. Since the rate of spin-orbit scattering is strongly dependent on atomic number ($\propto Z^4$, Larbalestier in [15]), the addition of high-Z, strong spin-orbit scattering elements, can be used to eliminate the possible presence of PPL [100].

From these arguments it can be concluded that the possible presence of PPL or spin-orbit scattering will lower the measured zero temperature upper critical field, below the value in for example the GLAG expressions. This change in $H_{c2}(0)$ can be expressed as a change in the slope at $T_c(0)$ through (3.26). The relevant information on PPL and spin-orbit scattering is therefore contained in this slope.

Generalization of the Maki-De Gennes relation

The simplest form of the microscopic descriptions, the MDG relation (3.20), was tested and found to fit $H_{c2}(T)$ for all available literature Nb_3Sn data with very high accuracy (Section 6.7.2). This accuracy holds for the Orlando *et al.* thin film results [28] at all Sn concentrations, the Foner and McNiff single- and polycrystalline results [36, 38], and the Jewell *et al.* bulk results [39]. The single crystals are close to stoichiometry and thus strong coupling (Figure 2.5) and most probably clean (ℓ is of order ξ or larger). The thin films and bulk samples are of varying degree of resistivity and Sn content and cover therefore a large range from approximately clean to dirty and weak to strong coupling. This leads to the conclusion that the shape of the field-temperature phase boundary is, within the experimental error bars, independent of the electron-phonon coupling strength (which can also be confirmed from the theory [178]), independent on whether the material is clean or dirty, and not influenced by the (unlikely) presence of PPL and spin-orbit scattering. It can thus be expected that it can be

validated for the entire range of compositions that are present in wires. Whether the MDG relation indeed can be validated for wires and whether it can be used to describe the scaling critical field for the critical current density, will be investigated in Chapter 6 and Chapter 7.

Considering the discussion in the previous Sections and the observable general validity of (3.20), it appears that all the relevant microscopic mechanisms are included in the value of D [i.e. the slope at $T_c(0)$] and $T_c(0)$, with the assumption that the shape of $H_{c2}(T)$ is constant. The Maki-De Gennes relation can thus be generalized for all literature Nb_3Sn results. The quasiparticle and normal state parameters can be calculated from the resulting slope at $T_c(0)$ and the value of $T_c(0)$ through expressions resulting from the renormalized BCS or Eliashberg theory. This means that D does not have the originally intended connection to the resistivity through $1/\rho_n = e^2N(E_F)D = e^2N(E_F)v_F\ell/3$, but is merely a fit parameter representing the slope at $T_c(0)$ and should therefore be called for example D^* for the general application of the MDG relation. Connections to e.g. the normal state resistivity should occur through the slope at $T_c(0)$, calculated from D^* by (3.22) and a microscopic based description for the slope, as for example done by Orlando et al. [28].

3.5 Temperature dependence of the Ginzburg-Landau parameter

3.5.1 Empirical temperature dependence

An empirical fit of $\kappa_1(T)/\kappa_1(0)$, applicable to Nb_3Sn wire data and normalized to $T = 0$ K, was proposed by Summers *et al.* [81]. This expressions was already implicit in the empirical expression for the upper critical field (3.18):

$$\kappa_1(t) = \kappa_1(0)\left[1 - 0.31t^2\left(1 - 1.77\ln t\right)\right], \tag{3.30}$$

in which $t = T/T_c$. It has to be emphasized that Hampshire *et al.* claim a validity range only below 13.5 K for their calculated $\kappa_1(T)$ values. Sometimes a simpler, but very comparable version of this empirical fit is used:

$$\kappa_1(t) = \kappa_1(0)\left(1 - 0.33t\right). \tag{3.31}$$

The accuracy of these empirical fits will be investigated in Chapter 7 by comparison with the microscopic alternative that is derived below and with measurements.

3.5.2 Microscopic based temperature dependence

From the microscopic theory [179] it follows that for weak coupling superconductors in the dirty limit (the latter is true for compositions below about 23 at.% Sn [24]) according to the BCS theory:

$$\frac{\kappa_1(0)}{\kappa_1(T_c)} = 1.2, \tag{3.32}$$

i.e. a constant ratio between the 0 K value of κ_1 and its value at $T = T_c$. In the strong coupling limit this ratio saturates at [179]:

$$\frac{\kappa_1(0)}{\kappa_1(T_c)} \cong 1.5\,, \tag{3.33}$$

which means that the maximum change in $\kappa_1(T)$ is 50% from 0 K to T_c. It was shown in Figure 2.5 that the interaction strength for Nb_3Sn depends strongly on Sn content. For calculation of $\kappa_1(T) / \kappa_1(0)$ for a given interaction strength the nonlinear Eliashberg equations [56] will have to be solved as was done numerically by Rainer and Bergmann [179]. No general simple function for $\kappa_1(T) / \kappa_1(0)$, derived directly from the electron-phonon spectrum, can therefore be given for wires since a range of Sn concentrations, and thus a range of interaction strengths can be expected in the A15 cross-sections. Fortunately, the shape of the field-temperature phase transition is virtually independent of the interaction strength (Chapter 6, [178]). A generalized function can be given for $\kappa_1(T) / \kappa_1(0)$ through (3.6), using the microscopic form for $H_{c2}(T) / H_{c2}(0)$ (3.20) combined with the temperature dependence of the thermodynamic critical field.

It is well accepted that $H_c(t) / H_c(0)$ is for all superconductors very close to $(1 - t^2)$ [6]. The deviation from $(1 - t^2)$ is known for Nb_3Sn [59] and is within about 2%. A fit to the actual $H_c(t) / H_c(0)$ yields $(1 - t^{2.07})$. For practical applications a power of 2 will thus be sufficiently accurate:

$$\frac{H_c(t)}{H_c(0)} = \left(1 - t^2\right). \tag{3.34}$$

Combining (3.6) and (3.20)/(3.21) or (3.25) with (3.34) thus yields:

$$k(t) = \frac{\kappa_1(t)}{\kappa_1(0)} = \frac{\mathrm{MDG}(t)}{1 - t^2} \cong \frac{1 - t^{1.52}}{1 - t^2}\,. \tag{3.35}$$

This shows that by implementing an accurate microscopic form for $H_{c2}(T)$ in the scaling relations also the temperature dependence of the GL parameter is accurately known in a simple form, rendering an empirical version redundant.

3.6 Strain dependence

3.6.1 Strain sensitivity in composite wires

Strain sensitivity of Nb_3Sn was first reported in thin films by Müller and Saur [206] and in monofilament wires by Beuhler and Levinstein [207]. This initiated numerous investigations on the strain sensitivity of Nb_3Sn wires, from which the pioneering work of Ekin should be emphasized (e.g. [Ekin in 19, 208–211]), and limited work on single crystals [92, 156, 212].

When a Nb_3Sn composite wire is subjected to longitudinal compressive strain, the critical current density, upper critical field and critical temperature reduce approximately linearly and reversibly with strain. An illustration of this behavior was shown in Figure 2.10. When a wire is subjected to a longitudinal tensile strain, the critical parameters increase approximately proportionally and reversibly with strain until a parabolic like peak is reached, after which the properties reduce approximately linearly with strain. At a certain tensile strain, the behavior becomes irreversible, which can be attributed to crack formation in the A15 layers. The tensile

strain at which irreversible behavior starts to occur is referred to as the irreversible strain limit (ε_{irr}) and appears to be correlated to filament size [211]. The larger thermal contraction of the matrix materials (typically about −0.3% from $T = 300\ \mathrm{K} \rightarrow 4\ \mathrm{K}$) compared to the thermal contraction of the Nb_3Sn (about −0.18%) results in an axial pre-compression of the A15. When the wire is axially loaded after cool-down, this pre-compression is minimized and J_c, H_{c2} and T_c increase. The position of the maximum in the strain dependency curve appears at the point where the three-dimensional deviatoric strain components in the A15 are minimal. In practice this correlates closely to the point where the axial pre-compression of the A15 is minimal. The axial pre-compression is mostly identified by ε_m, whereas the position of the minimum in the deviatoric strain components is identified as δ. Several models have been introduced in the literature to describe this behavior, ranging from polynomial fits to relations based on the Eliashberg theory. These will be discussed below.

Although strain is clearly a three-dimensional parameter, few models account for this due to the complexity of multifilamentary composite wires. This three-dimensional nature has resulted in research on simplified model systems [149, 213, 214] and attempts to calculate the strain state in wires in three dimensions [149, 215–218]. The origins of strain sensitivity in Nb_3Sn cannot be explained in a simple way by area reduction, heat generation by slow plastic deformation or matrix degradation [208]. The reversible behavior of the strain dependence indicates that strain sensitivity of Nb_3Sn has a microscopic origin. When an A15 lattice is deformed, its vibration modes will change. In addition, the electronic structure will be modified and therefore $N(E_F)$. A modification of the lattice and grain structure can also result in a change in the flux-line to pinning center interactions. It is thus reasonable to expect a strain induced variation of the electron-phonon interaction spectrum and the phonon density of states and hence, through (3.19), a change in the interaction constant λ_{ep}. Some early publications suggested that changes in J_c could sufficiently be accounted for by strain induced changes in T_c and $H_{c2}(T)$ (e.g. [151]). Ekin, however, stated that a direct influence on the maximum pinning force is required to explain the experimental observations. This will be discussed in detail below.

The difference between the strain sensitivity of H_{c2} and T_c represents an important link to microscopic understanding since both depend differently on $N(E_F)$ and λ_{ep}. It is found experimentally that [151, 209]:

$$\frac{H_{c2}(4.2\mathrm{K},\varepsilon)}{H_{c2m}(4.2\mathrm{K})} \cong \left(\frac{T_c(\varepsilon)}{T_{cm}} \right)^{\varpi}, \tag{3.36}$$

where the index 'm' indicates the values of H_{c2} and T_c at the maximum of the axial strain dependency curve, i.e. at $\varepsilon = -\delta$. The power $\varpi \cong 3$, indicates that H_{c2} is roughly 3 times more sensitive to strain than T_c. This was found to be valid at all temperatures (e.g. [111, 158]). An attempt was made by Welch [151], following earlier work by Testardi [150, 219, 220], to explain the observed difference in strain sensitivity on the basis of the strong coupling renormalized BCS theory, using a McMillan [57] based, Allan and Dynes [221] strong coupling formulation for T_c. It was concluded that $\varpi \cong 3$ cannot be explained by either a change in $N(E_F)$ or λ_{ep} alone and the strain dependence should therefore be described by a combination of both. It should be pointed out, however, that McMillan based descriptions for T_c are valid for $\lambda_{ep} \leq 1.5$ [8], whereas reported values for Nb_3Sn are mostly higher (e.g. 1.8 [28]). A similar approach was performed very recently by Taylor and Hampshire who state values for ϖ ranging from 1.9 to 3.8 [222]. It is clear, however, that improved understanding of the value for ϖ

should result from exact calculations of strain induced modifications on the full electron-phonon interaction spectrum and the density of states. Finally, an important conclusion drawn by Welch should be mentioned. He concluded, that in a three-dimensional strain description the deviatoric strain components dominate the strain sensitivity of Nb_3Sn and that hydrostatic components have, in comparison, a negligible effect.

3.6.2 Models describing strain sensitivity in composite wires

Five models describing the strain sensitivity of Nb_3Sn can be distinguished throughout the literature. The simplest form is an introduction of hydrostatic strain though a pressure term. Although this yields a relatively simple connection to thermodynamic calculations to describe single crystal hydrostatic experiments, it is not suited for more practical systems such as wires due to the dominating deviatoric components. An empirical fit for axial deformations in wires was recently adapted by Hampshire and co-authors [159, 222, 223] in the form of a fourth-order polynomial. Although this will obviously result in accurate fits to experimental data, it lacks any connection to the underlying physics, and is thus not suited for the goals set out for the present work. The three remaining models that have been proposed to describe experiments on wires will be discussed next in chronological order.

Most dependencies are defined through the strain dependence of the upper critical field or the critical temperature. A general strain dependent term will therefore be defined:

$$s(\varepsilon)=\frac{H_{c2}(\varepsilon)}{H_{c2m}},\quad s(\varepsilon)=\frac{H_{K}(\varepsilon)}{H_{Km}}\quad \text{or}\quad s(\varepsilon)=\frac{H^{*}_{c2}(\varepsilon)}{H^{*}_{c2m}}, \tag{3.37}$$

where $s(\varepsilon)$ denotes a strain dependence which can be based either on upper critical field values which are directly measured (H_{c2}), extrapolated using a Kramer extrapolation [(3.9) and (3.11), H_K], or a more general magnetic field dependency extrapolation [(3.13)/(3.14), H^{*}_{c2}]. It has to be emphasized that these three different definitions of $s(\varepsilon)$ do not necessarily yield the same functionality. Application in an overall scaling relation further requires the definition of a strain dependent critical temperature through (3.36) and (3.37) under the assumption that $s(\varepsilon)$ is independent of temperature:

$$T_c(\varepsilon)=T_{cm}s(\varepsilon)^{\frac{1}{\varpi}}, \tag{3.38}$$

with $\varpi \cong 3$.

Power-law model

The first model that was proposed to describe the strain dependence of the critical properties of Nb_3Sn composite wires was the empirical so-called power-law model, introduced by Ekin in 1980 [209]. The model was based on critical current and extrapolated upper critical field data at 4.2 K versus axial applied strain, and $T_c(\varepsilon)$ data of Luhman *et al.* [224] on wires having various bronze to Nb ratios. The critical current measurements were performed on Nb_3Sn, V_3Ga, Nb_3Ge and NbTi wires, using an axial pull strain device. The investigated compressive strain range was therefore limited to the thermal pre-compression of the A15, introduced by the matrix components of the wires. A power-law dependence was proposed using the strain dependence of the extrapolated upper critical field:

$$s(\varepsilon) = 1 - a\left|\varepsilon_{\text{axial}}\right|^{u} = 1 - a\left|\varepsilon_{\text{applied}} - \varepsilon_{\text{m}}\right|^{u}, \tag{3.39}$$

where $\varepsilon_{\text{axial}}$ is the total axial strain on the A15, $\varepsilon_{\text{applied}}$ is the applied axial strain, ε_{m} is the thermal pre-compression of the A15 and a and u are constants. The constant u was determined to be approximately 1.7 for all Nb_3Sn wires. The constant a represents the strain sensitivity and is for binary wires equal to about 900 for $\varepsilon_{\text{axial}} < 0$ and about 1250 for $\varepsilon_{\text{axial}} > 0$. This asymmetry in the axial strain sensitivity can be attributed to the third strain invariant, as can be shown from the more sophisticated three dimensional strain models described below. For ternary wires with significant third element additions (roughly > 1 at.%) higher values for a were found, indicating a larger strain sensitivity (Ekin in [19]). For a 1.85 at.% Ti ternary wire $a = 1100$ for $\varepsilon_{\text{axial}} < 0$ and $a = 1450$ for $\varepsilon_{\text{axial}} > 0$. For a 2.2 at.% Ta ternary wire $a = 1400$ for $\varepsilon_{\text{axial}} < 0$ and $a = 1800$ for $\varepsilon_{\text{axial}} > 0$. Note that this is contrary to the hypothesis stated in Section 2.8, where it was postulated that Nb_3Sn with increased disorder (or ρ_{n}) could have lower strain sensitivity than perfectly ordered (i.e. close to stoichiometry) Nb_3Sn. Significant Ta or Ti additions will increase off-stoichiometry, increase resistivity and increase the amount of disorder. Unpublished results on binary and ternary PIT processed wires, behave in contrast to Ekin's observation on bronze processed wires and do behave according to the aforementioned hypothesis, i.e. ternary wires are less stain sensitive than binary versions. Further research on better defined systems (e.g. bulk or thin films) is required to clarify the contradicting results.

Deviatoric strain model

The compressive strain regime ($\varepsilon_{\text{axial}} < 0$) is of prime interest to the magnet community. This is due to the high axial pre-compressions (on the order of –0.5%) on the A15 resulting from the conduit in cable-in-conduit conductors or the construction materials in magnets. Such high pre-compressions are difficult to realize in an axial pull experiment unless e.g. the bronze to Nb ratio in a bronze processed wire is strongly increased [e.g. 224]. This might, however, also influence the A15 formation since more Sn becomes available and thus influence the superconducting properties during reaction. To enable investigations on the full axial strain regime, including high compressions, Ten Haken developed the first so-called U-shaped sample holders (Chapter 5) [149, 225], initially for two-dimensional tape conductors and later for wires. Samples are soldered rigidly onto these holders and compressing the holder thus allows for investigations in the compressive axial regime.

For high compressive strains Ten Haken found an approximate linear dependence of H_{K} on axial strain, deviating from the power-law behavior (3.39) [226, 227] which was later demonstrated also explicitly with critical current measurements for a large number of wire samples [162]. These deviations, combined with the results of experiments on quasi two dimensional Nb_3Sn tape conductors [149, 213, 214] which allow direct calculation of the three-dimensional strain components, led to an alternative description based on the non-hydrostatic, i.e. distortional or deviatoric strain. This represents a continuation of the previous work by Testardi [150, 219, 220] and Welch [151].

Three coordinate system independent parameters, the so-called strain invariants, exist. The first invariant represents the hydrostatic strain (isotropic change in volume). The second and third invariants are the symmetric and asymmetric components of the deviatoric strain tensor respectively (change in shape). Comparison of hydrostatic pressure and axial strain experiments on the critical properties of A15 materials has shown that the influence of the deviatoric strain, specifically the second invariant, is much stronger than the influence of the

hydrostatic strain [151]. A deviatoric strain model, based on the second strain invariant, was chosen by Ten Haken to describe the influence of deformations on the critical parameters. The second invariant will, within this Section, be referred to as the deviatoric strain, thereby neglecting the third invariant.

In an orthogonal coordinate system in which the principal strain axles coincide with the coordinate axles (x, y, z), only three components of the three-dimensional strain tensor remain: ε_x, ε_y and ε_z, which are referred to as the principal strain components. The (second) deviatoric strain invariant is then defined as:

$$\varepsilon_{dev} = \frac{2}{3}\sqrt{\left(\varepsilon_x - \varepsilon_y\right)^2 + \left(\varepsilon_y - \varepsilon_z\right)^2 + \left(\varepsilon_z - \varepsilon_x\right)^2} \ . \tag{3.40}$$

The quasi two-dimensional shape of the A15 layers in a tape conductor enables a relatively accurate calculation of the deviatoric strain component. Experiments on the strain sensitivity of such conductors resulted in an empirical linear $H_K(\varepsilon_{dev})$ dependence at 4.2 K [149, 161, 226]:

$$\mu_0 H_K\left(\varepsilon_{dev}\right) \cong \mu_0 H_K\left(0\right) - C_{dev}\varepsilon_{dev} \ , \tag{3.41}$$

where C_{dev} is a constant. This linearity was observed over the entire investigated deviatoric strain range from $\varepsilon_{dev} \cong 0.4\%$ to about 1%. Based on the relatively high value for $H_K(0)$ arising from the data-fit, it was concluded that a deviation from the observed linear behavior for small ε_{dev} is likely to occur. It can also be expected that $\partial H_{c2}(\varepsilon_{dev}) / \partial\varepsilon_{dev} = 0$ for $\varepsilon_{dev} \to 0$ [150]. This can be included in (3.41) through the introduction of a "remaining strain" term $\varepsilon_{0,d}$ in (3.41):

$$\mu_0 H_K\left(\varepsilon_{dev}\right) \cong \mu_0 H_K\left(0\right) - C_{dev}\sqrt{\left(\varepsilon_{dev}\right)^2 + \left(\varepsilon_{0,d}\right)^2} \ . \tag{3.42}$$

In a composite wire there is also a remaining strain component when the axial applied strain minimizes the deviatoric strain, since minimization of the three dimensional strain components cannot be complete though axial strain alone. This can be confirmed by a full invariant formulation of the strain dependence [152], in which it is shown that through the application of longitudinal strain on a specific wire layout, the second and third strain invariant both can disappear at the maximum of the strain dependency curve, but the first invariant (i.e. a hydrostatic strain) remains. In general, i.e. independent of a specific wire layout, the first and third strain invariants do not necessarily disappear when the second invariant is minimized. Based on available experimental results it can only be concluded that $|\varepsilon_{0,d}| < 0.4\%$.

An approximation for axially deformed composite conductors can be constructed from the general form (3.42). A linear relation is assumed between the change in the strain components in the principal strain directions and parallel to the z-axis, i.e. $\partial\varepsilon_z = \partial\varepsilon_{applied}$, $\partial\varepsilon_x / \partial\varepsilon_z = -\nu_x$ and $\partial\varepsilon_y / \partial\varepsilon_z = -\nu_y$, where $\varepsilon_{applied}$ represents the axial applied strain on a wire. In a uniform bar with isotropic elastic properties the constants ν_x and ν_y are equal to the Poisson ratio of the material. In the case of a composite conductor where also plastic deformations can occur, constant values for ν_x and ν_y will only be valid in a limited, elastic deformation range. Moreover, a certain average value over the entire cross section has to be considered for the non-axial strain components (ε_x and ε_y) in the A15. With these assumptions, and including $\varepsilon_z = \varepsilon_{applied} + \delta$, where δ represents the position of the minimum in the deviatoric strain, (3.42) in this approximation becomes:

$$\mu_0 H_K\left(\varepsilon_{applied}\right) \cong \mu_0 H_K\left(0\right) - C_a^{'}\sqrt{\left(\varepsilon_{applied}+\delta\right)^2+\left(\varepsilon_{0,a}\right)^2}\ , \tag{3.43}$$

in which $C_a^{'}$ is a constant and $\varepsilon_{0,a}$ represents the remaining strain components, as with the factor $\varepsilon_{0,d}$ in (3.42). The value of $\varepsilon_{0,a}$ is determined by ν_x, ν_y and the thermal pre-strain inside the conductor. The above form (3.43) was proposed by Ten Haken to describe axial strain dependence of Nb_3Sn composite conductors [149, 226]. The upper critical field increases linearly with applied axial strain below $\varepsilon_{applied} = -\delta$ and reduces linearly with applied strain above this point. Without $\varepsilon_{0,a}$ the maximum represents a physically unrealistic discontinuity, but $\varepsilon_{0,a}$ causes a rounding off of the peak which is proportional to the magnitude of $\varepsilon_{0,a}$.

The linearity for high compressive longitudinal strains, as observed in numerous experiments, can thus be accounted for using the Ten Haken model. The symmetry in (3.43) is in disagreement with experimental observations, in which beyond the maximum in the strain dependency curve the reductions are more severe than expected on the basis of a symmetric description. This was sometimes attributed to the fact that (3.43) assumes elastic behavior. It was reasoned that above the maximum plastic deformations and/or cracking occurred, rendering the model invalid. It was recently shown by Markiewicz [154], that the dominant symmetric parabolic-like behavior stems indeed from the second strain invariant. The generally observed asymmetry between compressive and tensile intrinsic strain, arises through the inclusion of the third invariant, which is not accounted for in the Ten Haken model.

Normalization to the maximum upper critical field value (H_{Km}) at the minimum in ε_{dev} by applying a division by H_{Km}, thereby creating $C_a = C_a^{'} / \mu_0 H_{Km}$, results in a form comparable to (3.37):

$$s\left(\varepsilon_{applied}\right) = \frac{H_K\left(\varepsilon_{applied}\right)}{H_K\left(\varepsilon_{dev}=\min\right)} = \frac{1 - C_a\sqrt{\left(\varepsilon_{applied}+\delta\right)^2+\left(\varepsilon_{0,a}\right)^2}}{1 - C_a\varepsilon_{0,a}}. \tag{3.44}$$

The maximum in $s(\varepsilon_{applied})$ occurs when the deviatoric strain is minimized, which is at $\varepsilon_{applied} = -\delta$. In practice δ will be close to the axial thermal pre-compression ε_m.

In an axially deformed sample with elastic properties, the strain constant C_a is proportional to C_{dev}, but is also determined by the sample specific parameters ν_x, ν_y and $H_K(0)$. It was mentioned earlier that the slope of the $\mu_0 H_{c2}(\varepsilon_{dev})$ dependency (C_{dev}) is possibly a material constant for Nb_3Sn [111, 161, 162]. This was based on the observation that the axial factor C_a showed only very little variation across a large range of investigated wires, i.e. $C_a = 39.5 \pm 2$. With hindsight, this is especially striking considering differences in composition and Sn gradients which can be observed between various wires. The investigated wires on which this conclusion was based were two ternary bronze processed, two ternary IT processed and two binary IT processed wires. Differences in C_a have been, however, unambiguously established between ternary and binary wires (e.g. Ekin in [19]), as was discussed in the previous Section and will also be emphasized in Chapter 7.

General strain invariant formulation

The deficiencies in understanding of the influences of strain on the superconducting properties and the recognition that in magnet systems the non-axial strain components are of significant importance, have led recently to a full three dimensional $T_c(\varepsilon)$ analysis for Nb_3Sn by Markiewicz [152–154]. This model is based on the assumption that the strain dependence of T_c results from the strain dependence of the phonon frequencies in the Nb_3Sn crystal lattice. The model uses a full invariant strain analysis which correlates the strain dependence of T_c to strain induced changes in the phonon frequency spectrum.

An extensive model of the A15 lattice under load is used to calculate the change in the elastic constants with strain through a scalar strain energy potential (U), representing a mechanical part of the thermodynamic free energy. In an isotropic material, U is a function of the first (I_1, hydrostatic), the second (J_2, non-hydrostatic) and third (J_3, non-hydrostatic) invariants of the strain tensor. In a cubic lattice (e.g. Nb_3Sn) the second and third invariants split: $J_2 \rightarrow J_{21}, J_{22}$ and $J_3 \rightarrow J_{31}, J_{32}, J_{33}$. The strain energy function can then be written as a function of harmonic and higher order anharmonic terms, where the latter determine the strain dependence of the lattice vibrations and the harmonic terms determine the strain free value for T_c. Only the anharmonic terms that are found to explain the observed strain dependence of T_c are included in the strain energy potential. Markiewicz postulates a form:

$$U = A_1 I_1^2 + A_2 J_{21} + A_3 J_{22} + B_1 I_1^3 + B_2 J_{21}^2 + B_3 J_{21} J_{31}\,, \tag{3.45}$$

where A_{1-3} are amplitudes of the harmonic terms and B_{1-3} are amplitudes of higher order anharmonic terms. It is demonstrated that B_1 determines the hydrostatic strain dependence of T_c, B_2 determines the dominant parabolic like behavior and B_3 determines the asymmetry of the strain dependence. The stresses and elastic constants of the lattice result from the first and second derivatives of U with respect to the components of strain.

The strain dependence of the elastic constants stiffens or relaxes the lattice and thus results in a strain dependence of the phonon frequencies (ω) and, more specifically, in a strain dependence of the phonon density of states $F(\omega)$. The electron-phonon interaction $\alpha^2(\omega)$ is determined from the ratio between measured electron-phonon spectral functions $\alpha^2(\omega)F(\omega)$ and a measured phonon density of states $F(\omega)$. The strain dependence of the electron-phonon coupling constant $\lambda_{ep}(\varepsilon)$ is then calculated using the Eliashberg definition as given by (3.19). From $\lambda_{ep}(\varepsilon)$ the critical temperature is then calculated using a relation between T_c and λ_{ep} which was postulated by Kresin *et al.* [8, 58], which is based on Eliashberg theory and valid for any interaction strength. This thus yields $T_c(\varepsilon)$ through the strain modified electron-phonon interaction spectrum.

The main result of the model that can be applied to wire data is that it is able to demonstrate the effect of the harmonic and anharmonic terms in (3.45) separately as is sketched in Figure 3.6 [228]. The harmonic terms do not result in strain dependence, but determine the maximum value for $T_c(\varepsilon)$. The anharmonic B_1 term represents the T_c reduction due to hydrostatic strain which decreases linearly with axial strain. The B_2 anharmonic term represents the symmetric components of the deviatoric strain and results in the parabolic like dependence. The B_3 anharmonic term finally yields the asymmetry which is also observed experimentally.

Markiewicz concluded that the main part of the strain dependence of T_c occurs through the strain dependence of the interaction constant λ_{ep}. This also suggests that the strain sensitivity

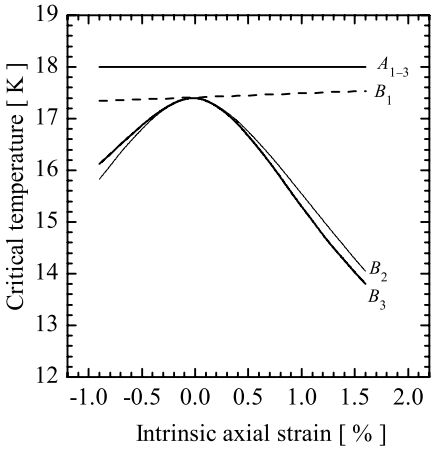

Figure 3.6 *Calculated dependencies of $T_c(\varepsilon_{axial})$ separated by harmonic and anharmonic terms in the strain energy potential function (3.45). Courtesy of W.D. Markiewicz.*

could differ with Sn concentration (Figure 2.5). It should be noted that in this invariant description only the strain sensitivity of the critical temperature is calculated. The strain sensitivity of the upper critical field can for now only be assumed to behave similarly, based on the postulated connection between $H_{c2}(\varepsilon)$ and $T_c(\varepsilon)$ defined by (3.37) and (3.38). An extension of the full invariant analysis should preferably include a direct calculation of $H_{c2}(\varepsilon)$ in a similar way as $T_c(\varepsilon)$. This is required to verify the empirical observation given by (3.38), i.e. $\varpi = 3$. The latter is, unfortunately, not trivial since this requires an analysis in terms of the Eliashberg formalisms due to the range of interaction strengths that can be expected in Nb_3Sn wires.

3.6.3 Empirical correction to the deviatoric strain model

The full invariant analysis is the most proper method available for the introduction of strain dependency of the critical properties. The resulting relations, however, remain somewhat complex compared to the empirical fits. It is clear that the empirical models all lack specific details in comparison to the full invariant analysis. Neither the power-law nor polynomial fits account for the three-dimensionality of strain, but they are able to include asymmetry. The power-law model, however, does not include a linear dependence for high compressive and tensile strain values. The deviatoric strain model, although empirical, does account for the three-dimensional nature of strain and linearity at high strain, but is a symmetrical description, comparable to using only the B_1 and B_2 terms of the full invariant analysis. The latter shows that asymmetry, through the third invariant, should be accounted for in an accurate model.

An empirical model that accounts for three-dimensionality, linearity at large axial strain, and asymmetry, in agreement with the invariant analysis, can be obtained by assuming a simple mathematical correction to the Ten Haken deviatoric strain model. The full invariant analysis indicates that a linear term (similar to the hydrostatic component) is missing, as can be seen from Figure 3.6. To account, in the axial form of the Ten Haken model, for a stronger reduction at tensile strains, a linear term causing a reduction of H_K with axial strain is required. That the hydrostatic term causes an increase of T_c with axial strain (and thus is working the opposite

way) is a strong indication that the required correction should account for the third invariant in the Ten Haken model. This can be achieved by including an additional linear term in (3.42):

$$\mu_0 H_K\left(\varepsilon_{dev}\right) \cong \mu_0 H_K\left(0\right) - C_{inv2}\sqrt{\left(\varepsilon_{dev}\right)^2 + \left(\varepsilon_{0,d}\right)^2} - C_{inv3}\varepsilon_{dev}\,, \tag{3.46}$$

where C_{inv2} and C_{inv3} are constants representing the second and third strain invariants. The term $\varepsilon_{0,d}$ now represents the initial suppression of H_K due to hydrostatic strain. A similar route can be followed for the axial version (3.43), resulting in:

$$\mu_0 H_K\left(\varepsilon_{axial}\right) = \mu_0 H_K\left(0\right) - C_{a1}^{'}\sqrt{\left(\varepsilon_{axial}\right)^2 + \left(\varepsilon_{0,a}\right)^2} - C_{a2}^{'}\varepsilon_{axial}\,, \tag{3.47}$$

in which $\varepsilon_{axial} = \varepsilon_{applied} + \delta$. The correction $C_{a2}^{'}\varepsilon_{axial}$ effectively rotates the strain dependency curve around its maximum. This causes the axial position of the maximum to shift by a factor $\varepsilon_{shift} = C_{a2}^{'}\varepsilon_{0,a} / [(C_{a1}^{'})^2 - (C_{a2}^{'})^2]^{0.5}$. For large asymmetry, δ (the axial strain at which the minimum in the deviatoric strain occurs) will then deviate significantly from the observable axial position of the maximum ε_m. In axial strain experiments it is more convenient to normalize the strain dependence function to the observable maximum, also to prevent the introduction of an additional parameter through the use of δ in combination with ε_m. A renormalization of (3.47) to the observable position of the maximum in axial strain dependency measurements leads to:

$$\mu_0 H_K\left(\varepsilon_{axial}\right) = \mu_0 H_K\left(0\right) - C_{a1}^{'}\sqrt{\left(\varepsilon_{axial} - \varepsilon_{shift}\right)^2 + \left(\varepsilon_{0,a}\right)^2} - C_{a2}^{'}\left(\varepsilon_{axial} - \varepsilon_{shift}\right), \tag{3.48}$$

where $\varepsilon_{axial} = \varepsilon_{applied} + \varepsilon_m$. The rotation around the maximum also causes the normalized form (3.44) to increase above 1 at the position of the maximum. This is undesirable since in scaling relations the reduction in e.g. H_K is usually normalized to the maximum observable value at the peak of the measured strain dependency curve, and not to the 'strain free' value since this is not accessible in an axial strain experiment. This can be prevented by renormalizing $s(\varepsilon)$ to the maximum observable critical field value. A renormalization of $s(\varepsilon)$ to the observable peak position and peak value in an axial strain experiment leads to the overall form:

$$\begin{aligned} s\left(\varepsilon_{axial}\right) &= \frac{C_{a1}\left[\sqrt{\left(\varepsilon_{shift}\right)^2 + \left(\varepsilon_{0,a}\right)^2} - \sqrt{\left(\varepsilon_{axial} - \varepsilon_{shift}\right)^2 + \left(\varepsilon_{0,a}\right)^2}\right] - C_{a2}\varepsilon_{axial}}{1 - C_{a1}\varepsilon_{0,a}} + 1, \\ \varepsilon_{shift} &= \frac{C_{a2}\varepsilon_{0,a}}{\sqrt{\left(C_{a1}\right)^2 - \left(C_{a2}\right)^2}}, \\ \varepsilon_{axial} &= \varepsilon_{applied} + \varepsilon_m. \end{aligned} \tag{3.49}$$

It has to be emphasized that this is an empirical correction to include the effects of the third strain invariant which, as suggested by the full invariant analysis, should be accounted for to describe asymmetry. It results in a simple description with four parameters that accounts for the overall behavior as expected on the basis of a full invariant analysis (and the observed behavior in experiments). The hydrostatic strain components are included in the remaining strain term $\varepsilon_{0,a}$ and the strain induced behavior resulting from the second and third invariants is accounted for through C_{a1} and C_{a2} respectively. It will be used through the remainder of this work since it

is the simplest form that still accounts for the three-dimensional nature of strain and is based on an underlying physics model.

3.7 Field, temperature and strain dependence of the bulk pinning force

The strain dependence described in the previous Section has to be included in the relation for the magnetic field and temperature dependent bulk pinning force (3.17) to arrive at a complete relation that can be used to inter- and extrapolate critical current measurements on wires. This requires the use of a strain dependent critical temperature as defined earlier by (3.38) and a temperature and strain dependent upper critical field:

$$H_{c2}(T,\varepsilon) = H_{c2m}(T)\,s(\varepsilon)\,. \tag{3.50}$$

Implementing this in the Kramer form of the field dependence of the bulk pinning force, i.e. (3.9), and assuming $(1 - a_{\triangle}(H) / d_{av}) \cong 1$ yields:

$$F_P(H,T,\varepsilon) \cong C\frac{\left[\mu_0 H_{c2}(T,\varepsilon)\right]^{2.5}}{\kappa_1(T,\varepsilon)^2} h^{0.5}(1-h)^2\,, \tag{3.51}$$

The upper critical field thus delivers a term $s(\varepsilon)^{2.5}$ acting directly on the bulk pinning force in addition to strain dependence arising through $f(h)$ and $T_c(\varepsilon)$. The strain dependence of κ_1 is, however, undefined since through its definition (3.6), this requires knowledge of the strain dependence of the thermodynamic critical field $H_c(\varepsilon)$ which can differ from $H_{c2}(\varepsilon)$. In addition, it is reasonable to assume some strain dependence through strain induced changes of the flux-line to lattice interactions. To arrive at an overall description, it is thus required to have knowledge of the strain dependence of $\kappa_1(T,\varepsilon)$, or to introduce a strain dependent constant $C(\varepsilon)$.

3.7.1 Ekin's unification of strain and temperature dependence

In analyzing critical current versus strain data at 4.2 K Ekin [209] found that the bulk pinning force scales, in analogy to the Fietz and Webb scaling law (3.5), as:

$$F_P(H,\varepsilon)_{4.2\,K} \propto \left[H^*_{c2}(\varepsilon)\right]^n f(h)\,, \tag{3.52}$$

where $n = 1.0 \pm 0.3$ and the star again indicates a bulk average. The power of 1 differs from the power of 2.5 that is required for magnetic field and temperature scaling, as discussed in Section 3.3 and Section 3.4. Ekin solved this inconsistency by postulating a combination in terms of explicit dependencies on temperature and strain. Neglecting the temperature and strain dependence of the GL parameter he proposed:

$$\begin{aligned} F_P(H,T,\varepsilon) &= Cs(\varepsilon)^n \left[\frac{H^*_{c2}(T,\varepsilon)}{H^*_{c2}(0,\varepsilon)}\right]^\nu f(h) \\ &\cong Cs(\varepsilon)^n \left(1-t^2\right)^\nu f(h) \end{aligned}\,, \tag{3.53}$$

where $h = H / H^*_{c2}(T,\varepsilon)$, $t = T / T^*_c(\varepsilon)$ (stars indicating bulk average values), $n \cong 1$, $\nu \cong 2.5$ and $s(\varepsilon)$ is given by (3.39). Note that the second term only describes the normalized temperature dependence of the upper critical field approximated as $(1 - t^2)$, in which strain sensitivity occurs

only through $T_c^*(\varepsilon)$. The combination of strain and temperature sensitivity was introduced on a fully empirical basis, based on 4.2 K critical current data. This implicates, as was pointed out by Ekin, that the term $C / \kappa_1(T,\varepsilon)^2$ in (3.51) has to produce a strain dependency $s(\varepsilon)^{-1.5}$ to counteract the $s(\varepsilon)^{2.5}$ term arising through the strain dependent upper critical field in (3.51). A similar magnetic field, temperature and strain dependence is used in various forms of generalized scaling relations which, by combining (3.53) with (2.13), result in an overall description for the critical current density in Nb_3Sn wires.

3.7.2 Unification of the Kramer form

The ratio $[\mu_0 H_{c2}(T,\varepsilon)]^{2.5} / \kappa_1(T,\varepsilon)^2$ in (3.51) can be normalized to zero temperature to express the direct strain influence on F_P (i.e. not through $T_c(\varepsilon)$] separately, so that the result only contains temperature dependence and strain dependence through $T_c(\varepsilon)$. With the definitions:

$$b\left(T,T_c(\varepsilon)\right) \equiv \frac{H_{c2}(T,\varepsilon)}{H_{c2}(0,\varepsilon)} \quad \text{and} \quad k\left(T,T_c(\varepsilon)\right) \equiv \frac{\kappa_1(T,\varepsilon)}{\kappa_1(0,\varepsilon)}, \tag{3.54}$$

this leads to:

$$F_P(H,T,\varepsilon) = \frac{C\left[\mu_0 H_{c2m}(0)\right]^{2.5}}{\kappa_1(0,\varepsilon)^2} s(\varepsilon)^{2.5} \frac{b\left(T,T_c(\varepsilon)\right)^{2.5}}{k\left(T,T_c(\varepsilon)\right)^2} h^{0.5}(1-h)^2 . \tag{3.55}$$

To retain consistency with Ekin's observation that $F_P(\varepsilon)_{4.2K} \propto s(\varepsilon)$ (under the assumption that this is valid for all temperatures) it can for example be postulated that:

$$\kappa_1(0,\varepsilon) = \kappa_{1m}(0)\, s(\varepsilon)^{\sqrt{1.5}}, \tag{3.56}$$

leading to:

$$F_P(H,T,\varepsilon) = \frac{C\left[\mu_0 H_{c2m}(0)\right]^{2.5}}{\kappa_1(0)^2} s(\varepsilon) \frac{b\left(T,T_c(\varepsilon)\right)^{2.5}}{k\left(T,T_c(\varepsilon)\right)^2} h^{0.5}(1-h)^2 . \tag{3.57}$$

The temperature dependencies in (3.54) can be empirical [e.g. (3.18), (3.30) and (3.31)] or microscopic based alternatives [e.g. (3.20), (3.25) and (3.35)].

The discussion above is used in the scaling relations that are available throughout the literature. The A15 layers in wires will always be inhomogeneous in composition and in strain. An extension that can be made is the inclusion of Sn content as an additional parameter, leading to $J_c(H,T,\varepsilon,\beta)$, where β represents the atomic Sn content. From the literature overview that was given in Chapter 2 it is clear that both H_{c2} and T_c depend strongly on composition. Fortunately, the literature data is consistent and can be summarized by relations (2.10) and (2.11). If the available data is assumed to be representative for the strain free values of H_{c2} and T_c, $s(\varepsilon)$ is independent of composition and if the flux-line lattice interactions do not change with composition, then (3.38) and (3.50) can be extended to include composition dependence through a shift in the field-temperature phase boundary by stating:

$$H_{c2m}(0) = H_{c2}(\beta) \quad \text{and} \quad T_{cm} = T_c(\beta), \tag{3.58}$$

where β represents the atomic Sn content. The composition averaging of the local $H_{c2m}(0)$ and T_{cm} over the A15 sections depends on the chosen summation but results in effective values for the upper critical field (H_{c2}^{*}) and the critical temperature (T_c^{*}) that should be used to scale the overall critical current density as was discussed in Section 3.3. Often critical current data are obtained only at low magnetic fields. This results in extrapolated effective values for the upper critical field, e.g. $H_{c2m} \rightarrow H_{Km}$ when a Kramer extrapolation is used.

3.7.3 The Summers relation

The general scaling relation that is most widely applied so far is the version proposed by Summers *et al.* [81]. They, following previous work by Hampshire *et al.* [196] and Ekin [209], and using $\varepsilon = \varepsilon_{axial}$, defined a strain dependent pre-constant:

$$C(\varepsilon) = C_0 s(\varepsilon)^{0.5}, \tag{3.59}$$

where $s(\varepsilon)$ is given by (3.39). The power of 0.5 is introduced in (3.59) to retain consistency with the strain dependence of the bulk pinning force as postulated by Ekin [(3.53)]. It can be shown that the Summers relation can be rewritten, using (2.13), in a form consistent with the previous Section as:

$$F_P(H,T,\varepsilon) = C_0 \left[\mu_0 H_{c2m}(0)\right]^{0.5} s(\varepsilon) \frac{b\left(T,T_c(\varepsilon)\right)^{2.5}}{k\left(T,T_c(\varepsilon)\right)^2} h^{0.5}(1-h)^2, \tag{3.60}$$

in which the empirical versions (3.18) and (3.30) are used for $b(T,T_c(\varepsilon))$ and $k(T,T_c(\varepsilon))$. The Summers relation is thus, apart from the pre-constant, consistent with (3.57). The difference in the pre-constant arises from the publication of Hampshire *et al.* [196], on which the Summers relation is based with respect to the magnetic field and temperature dependence. Hampshire *et al.* derived the starting point for the Summers relation in a slightly different way than used here in the unification of the Kramer form. They included an empirical relation credited to Suenaga in [15]:

$$\frac{\mu_0 H_{c2}(T)}{T_c} = C\left(1-t^2\right)\kappa_1(T), \tag{3.61}$$

in which C is a constant. Since no strain dependence was involved in the analysis of Hampshire *et al.*, T_c and $\kappa_1(0)$ were regarded constant and were included in the overall pre-constant. It has finally to be quoted that Hampshire *et al.* stated, in relation to substantial inhomogeneity of their samples, that the validity of their calculated $\kappa_1(T)$ results is expected to break down for $T > 13.5$ K. It will be shown in Chapter 7 that this, through comparison of the Summers form (3.30) to the microscopic based form (3.35) and measured results, indeed appears to be the case.

3.7.4 Alternative approaches

The empirical bases in the relations proposed by Ekin and Summers *et al.* and the extensive new $J_c(H,T,\varepsilon)$ data sets for wires that have become available over the past decade have evoked a re-analysis of overall scaling behavior in Nb_3Sn wires. Two alternative approaches can be

distinguished, focusing either on improving the strain and temperature dependent terms [111, 162], or focusing on improving the understanding of the strain dependence of $C / \kappa_1(T,\varepsilon)^2$ in (3.51) [112, 159, 160, 222].

In the first approach it is stated that, since the strain dependence through the power-law function (3.39) does not account for linearity at high compressive strains, it should be replaced by a function that does. This was done through a change in $s(\varepsilon)$ from the power-law form (3.39) to the Ten Haken form (3.44). Secondly, it was assumed that (3.57), and thereby the Summers version, is valid but that the empirical temperature dependencies as proposed by Summers *et al.* [i.e. (3.18) and (3.30)] are in error and can be improved upon. The general form (3.17) was chosen in [111, 162] under the condition that $s(\varepsilon)$ from (3.37) is independent of temperature, (3.36) has general validity and $(1 - a_{\Delta}(H) / d_{av}) \cong 1$.

The temperature dependence in (3.17) is determined by the ratio $[\mu_0 H_{c2}(T)]^{\nu} / \kappa_1(T)^{\gamma}$. Four-dimensional parameter least squares fits using extensive data sets on a six different wires and highly linear Kramer plots indicated $n \cong 1$ (as stated by Ekin), $p \cong 0.5$ and $q \cong 2$ (as stated by Kramer for $h > 0.2$). Since the temperature dependencies of H_{c2} and κ_1 were fully empirical in the Summers form, both powers ν and γ were regarded as free parameters to allow for errors in the temperature dependencies. Overall least squares fits on the data sets indicated that $\nu \cong 2$ and $\gamma \cong 1$ yielded the highest accuracy. The overall description (3.17) with $p = 0.5$, $q = 2$, $\nu = 2$ and $\gamma = 1$ yielded fits to experimental data with a standard deviation of about 2% over a limited magnetic field range from 5 to 13 T, but for all temperatures (4.2 K to T_c) and all investigated compressive strains ($-0.7 < \varepsilon_{axial} < 0$) [157]. It was expected that if correct dependencies for $H_{c2}(T)$ and $\kappa_1(T)$ were used, that similar accurate fits would be obtained with values for ν and γ, which are consistent with Kramer's pinning theory, i.e. $\nu = 2.5$ and $\gamma = 2$.

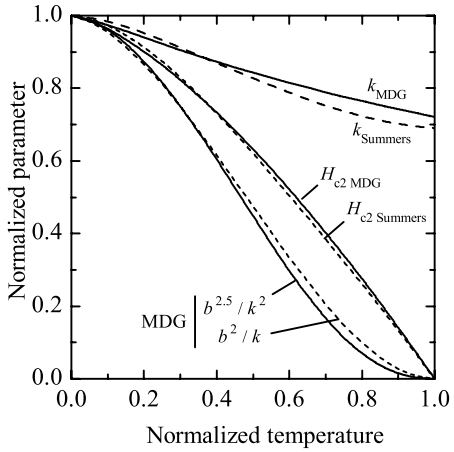

Figure 3.7 *Calculated $H_{c2}(t) / H_{c2}(0)$ and $\kappa_1(t) / \kappa_1(0)$ dependencies using the empirical forms proposed by Summers et al. [(3.30) and (3.18)] compared to microscopic based alternative forms resulting from the Maki-De Gennes relation [(3.24) and (3.35)]. Included also is the calculated overall temperature dependency term $[b(T,T_c(\varepsilon))^{\nu} / k(T,T_c(\varepsilon))^{\gamma}]$ using the Maki-De Gennes derived dependencies with $\nu = 2.5$ and $\gamma = 2$ compared to $\nu = 2$ and $\gamma = 1$.*

In Figure 3.7 a calculated comparison is shown between the empirical temperature dependence of H_{c2} and κ_1, as used in the Summers relation and the microscopic based alternative forms, resulting from the Maki–De Gennes relation. The empirical Summers form for $H_{c2}(T)$ [identified by ($H_{c2\ Summers}$)] is a good approximation to MDG(t) [identified by $H_{c2\ MDG}$]. The

empirical form for $k(T) = \kappa_1(T) / \kappa_1(0)$ [identified by (k_{Summers})], however, deviates significantly from MDG(t) / ($1 - t^2$) [identified by k_{MDG}], especially for temperatures above about $t = 0.5$, which is somewhat below the validity range that was suggested by Hampshire *et al.* [196] (< 13.5 K). This suggests, assuming (3.35) is the correct dependence, that in the Summers relation $H_{c2}(T)$ can only slightly be improved but $\kappa_1(T)$ can significantly be improved.

In Figure 3.7 also the difference of using $\nu = 2$ and $\gamma = 1$ compared to $\nu = 2.5$ and $\gamma = 2$ is shown. Both lines are calculated from the microscopic based alternatives to only yield the influence of different values for ν and γ. The difference that follows solely through the use of different powers is comparable in shape, but in opposite direction if the Kramer form ($\nu = 2.5$ and $\gamma = 2$) is assumed correct, to the deviations between k_{Summers} and k_{MDG}. This suggests that the higher accuracy in the data fits found through $\nu = 2$ and $\gamma = 1$ compared to $\nu = 2.5$ and $\gamma = 2$, may be caused by a wrong functionality for $k(T)$ for $T > 9$ K in the Summers description.

The second approach emphasizes on the different dependencies of the bulk pinning force on temperature and strain in an attempt to define a better founded combination of both dependencies. Following initial work by Kroeger *et al.* [105] this results in a general relation of the form [112, 159, 160, 222]:

$$F_{\text{p}}\left(H,T,\varepsilon\right) = A\left(\varepsilon\right)\left[\mu_0 H_{\text{c2}}^{*}\left(T,\varepsilon\right)\right]^{n} h^{p}\left(1-h\right)^{q}, \tag{3.62}$$

in which n, p and q are free parameters and $A(\varepsilon)$ is a function of strain alone. Several versions for $A(\varepsilon)$ have been applied [also including $\kappa_1(T,\varepsilon)$] in attempts to describe the strain induced modifications of the flux-line to pinning center interactions and the strain dependence of κ_1.

3.7.5 Selected general scaling law

In general it can be stated that much of the developments on overall scaling behavior remains empirical and it is unlikely that this empirical basis can be fully removed. As a final remark it should be mentioned that in a four-dimensional description with a large number of free parameters it often remains a somewhat subjective choice which parameters are fixed or allowed to vary, in addition to the choice of relationships that can be implemented.

The overall scaling law that is proposed in this thesis will now be summarized. It is assumed that the critical current density scales according to (3.51) in the most general form:

$$J_{\text{c}}\left(H,T,\varepsilon\right) \cong \frac{C}{\mu_0 H}\frac{\left[\mu_0 H_{\text{c2}}^{*}\left(T,\varepsilon\right)\right]^{\nu}}{\kappa_1\left(T,\varepsilon\right)^{\gamma}} h^{p}\left(1-h\right)^{q}, \tag{3.63}$$

where $h = H / H_{\text{c2}}^{*}(T,\varepsilon)$, in which H_{c2}^{*} represents the inhomogeneity (bulk) averaged critical field at which the critical current density extrapolates to zero. The microscopic based temperature dependencies are selected for the critical field (3.21) and the GL parameter (3.35). This leads to the general normalized form:

$$J_{\text{c}}\left(H,T,\varepsilon\right) \cong \frac{C}{\mu_0 H}\frac{\left[\mu_0 H_{\text{c2m}}^{*}\left(0\right)\right]^{\nu}}{\kappa_{\text{1m}}\left(0\right)^{\gamma}} s\left(\varepsilon\right)^{\nu-\alpha\gamma}\frac{\text{MDG}\left(t\right)^{\nu}}{k\left(t\right)^{\gamma}} h^{p}\left(1-h\right)^{q}, \tag{3.64}$$

where $t = T / T_c^*(\varepsilon)$. The term $s(\varepsilon)^{\nu-\alpha\gamma}$ arises from the strain dependence of the critical field through (3.37) and an unknown strain dependence of the zero temperature GL parameter, defined as:

$$\kappa_1(0,\varepsilon) = \kappa_{1m}(0)\, s(\varepsilon)^{\alpha}, \tag{3.65}$$

and $s(\varepsilon)$ is given by the improved deviatoric strain model (3.49).

The temperature and strain dependent bulk average critical field in (3.64) is given by a combination of the microscopic temperature dependence (3.21) and the strain dependence (3.50):

$$H_{c2}^*(T,\varepsilon) = H_{c2m}^*(0)\,\mathrm{MDG}(t)\, s(\varepsilon), \tag{3.66}$$

and the strain dependence of the critical temperature is defined by (3.38).

The constants p, q, ν, γ and α will have to be determined through systematic comparison to experiments, and $\varpi = 3$ is used in accordance with the experimental results of Ekin. Note that this approach significantly differs from the usual separation between the dependence of the bulk pinning force on $H_{c2}^*(T)$ and $H_{c2}^*(\varepsilon)$. Here this is not assumed *a priori* and strain dependency is simply introduced through a strain dependent upper critical field and GL parameter. This relation will be compared to measurements in Chapter 7 to determine the constants and to test its validity.

3.8 Conclusions

A new scaling relation was proposed which is based on a Kramer type pinning description. A number of improvements are made in comparison to the Summers form. A first improvement is a replacement of the empirical temperature dependency for the upper critical field with a microscopic based alternative. A second improvement is to replace the empirical temperature dependence of the Ginzburg–Landau parameter by a microscopic based alternative. A third improvement is made by replacing the power-law strain dependency with a new empirical deviatoric strain description that accounts for the effects of the third strain invariant and thus for asymmetry in the axial stain dependency curve. A fourth improvement involves accounting for the inhomogeneities that are present in the A15 regions in wires by recognizing that the critical current scales with a bulk, inhomogeneity averaged critical field, representing an unknown average of the H_{c2} distribution that is always present in the A15 in wires.

In Section 3.2 it was demonstrated that either an exponential or a power-law dependence of the electric field versus current transition can be expected in Type II superconductors. For high n-values these yield the same slope, and both yield a linear $E(J)$ dependence on a double logarithmic scale. Wire $E(J)$ transitions are commonly and very successfully described using a power-law dependence. The resulting n-value is determined by the pinning strength through the activation energy and the inhomogeneity in the conductor.

In Section 3.3 the magnetic field dependence of the bulk pinning force was discussed in terms of the Kramer flux shear model. It was emphasized that the arguments used by Kramer to arrive at this model have been criticized, but that in practice the high field version appears to describe experimental data rather well. From the field dependence of the bulk pinning force it can be derived that a Kramer plot can be expected to be linear, which is often observed in experiments over a large magnetic field range. When approaching the maximum present H_{c2},

however, non-linearities are often observed. It was shown that these can be attributed to inhomogeneities, thereby explaining differences between inhomogeneity averaged, and maximum detectable upper critical fields. It was concluded that there is no reason to deviate from a Kramer type flux shear model, as long as inhomogeneities are accounted for. The latter means that overall scaling can only be validated up to the magnetic field where inhomogeneity effects start to appear, i.e. until about 80% of the maximum upper critical field that is present in a wire.

The temperature dependence of the upper critical field was discussed in Section 3.4. It was shown that in the relation for the bulk pinning force an empirical fit is used, but that a microscopic based alternative is readily available in the form of the Maki–De Gennes relation. It was also shown in Section 3.5 that this leads to a microscopic based alternative for the temperature dependence of the Ginzburg–Landau parameter. Finally it was stated that the Maki–De Gennes relation, and the resulting microscopic based form for the temperature dependent Ginzburg–Landau parameter, can be used as better founded alternatives for the empirical forms.

In Section 3.6 the strain dependency of Nb_3Sn was discussed. A recent analysis demonstrates that strain sensitivity mainly occurs through a strain induced change of the electron–phonon coupling constant. This could suggest that the strain sensitivity depends on Sn concentration, as was also suggested in Chapter 2. It also shows that any simplified empirical alternative should account also for the third strain invariant, since this creates asymmetry in axial strain dependency curves. The choice was made to empirically expand the second invariant deviatoric strain model with an additional term related to the third invariant, thereby creating asymmetry in the model. At present, this asymmetry has to be determined empirically.

The strain dependence was included in the overall description of the bulk pinning force and a comparison was made to the Summers form. It was concluded that the general form of the Summers relation is in agreement with a Kramer based derivation, apart from a different pre-constant. A comparison of the empirical temperature dependence with the microscopic based alternatives suggests, in combination with earlier analysis, that the empirical fit for the Ginzburg–Landau parameter, as used in the Summers relation, is in error for temperatures above approximately 9 K.

Chapter 4

A15 Formation in Wires

Thorough knowledge of the microscopic layout of the superconducting layers in commercial Nb_3Sn wires is required for a proper understanding of the experimentally observed limitations. This Chapter deals with Electron Microscope analysis of the wires investigated. Backscatter Electron and fracture surface micrographs will be presented to visualize the wire layout and A15 morphology. Additionally, Energy Dispersive X-ray Spectroscopy data will be presented for selected wires to quantify microscopic compositional variations, mainly focusing on the tin gradients that are present within the A15 layers. In addition, the A15 growth process in wires and extracted filaments will be analyzed. The results will be used in Chapter 6 and Chapter 7 to explain macroscopically observed differences between various wires and to calculate a hypothetical upper performance boundary for the present generation of Nb_3Sn wires.

4.1 Introduction

Macroscopically observed wire parameters such as the critical current, field and temperature will have to be correlated to the microscopic compositional inhomogeneities and grain morphology to explain differences between wires. An accurate determination of the origin of real wire performance compared to idealized properties also requires thorough knowledge of the microstructure. This Chapter therefore focuses on a detailed investigation of the microscopic A15 formation and resulting morphologies and compositions of the A15 layers in the wires that are used throughout this thesis.

Table 4.1 *Overview of the main wire parameters.*

Name	Manufacturer	Type	∅ [mm]	Additions present	Cu/ non-Cu ratio	Twist pitch [mm]	$J_{c\ non\text{-}Cu}$ [a] 4.2K 12T [A/mm^2]
B27	SMI	PIT	1.0	Cu	0.852	…	1955[b]
B34	SMI	PIT	1.0	Cu, Ta	0.846	23	2250
B134	SMI	PIT	0.6	Cu, Ta	0.781	20	1961
FUR	Furukawa	Bronze	0.8	Cu, Ti	1.49	18	582
VAC	Vacuumschmelze	Bronze	0.8	Cu, Ta	1.49	9	556
Bulk	UW-ASC	Sintered	0.8×1.4	…	…	…	…

[a] At a voltage criterion of 10^{-5} V/m.

[b] Estimated from VSM results of Fischer [144].

Two wire types and one bulk sample were investigated within this thesis. An overview of the relevant conductor parameters is presented in Table 4.1. The table depicts manufacturer, manufacturing method, a short identification number, wire diameter, elements present in addition to Nb and Sn during A15 formation, the copper to non-copper cross-sectional area ratio, the twist pitch of the filaments and the non-copper critical current density at an electric field criterion of 10^{-5} V/m at $T = 4.2$ K and $\mu_0 H = 12$ T.

The ITER type Furukawa (FUR) and Vacuumschmelze (VAC) wires were selected because they have been characterized extremely well with respect to transport critical current density in various laboratories during the ITER benchmark tests [111, 162, 163, 229, 230]. They are representative of ternary conventional bronze-route manufacturing methods, have a relative low J_c, small filament size and probably large Sn gradients across the A15 areas [62, 135, 231].

The Powder-in-Tube (PIT) wires were all manufactured by Shape Metal Innovation, The Netherlands. These wires were selected since, due to the central location of the Sn source, they are transparent for magnetic characterization techniques [64, 65], have a relatively large A15 cross-section enabling microscopic composition analysis and are therefore favorable research wires that were already extensively characterized [144, 232]. They exhibit close to present record current densities and have, compared to bronze route wires, less steep Sn gradients.

A binary (B27) and two ternary versions (B34 and B134) of this wire type were selected. The main difference between the ternary versions is the presence of a Cu-Nb reinforcement tube around the outside of wire B134, as opposed to the pure Cu matrix for wires B34 and B27. This

results in slightly more deformation of the outer filaments and presumably a larger compressive strain state in the A15. The latter is caused by the increased strength of the Cu-Nb compared to a pure Cu matrix. The ternary conductor with pure Cu matrix (B34) was selected in addition for a homogenization experiment. By using increased reaction times, a thick A15 layer with a less steep gradient [144] was grown.

A bulk sample, manufactured by M.C. Jewell at the University of Wisconsin's Applied Superconductivity Center (UW-ASC) [39], was used to investigate the behavior of pure binary, Cu-free Nb_3Sn.

4.2 Powder-in-Tube wires

The first set of samples that will be discussed were manufactured by Shape Metal Innovation according to the Powder-in-Tube process. They were used to perform compositional analysis as function of reaction temperature and time as presented in this Chapter and additionally for investigating the field-temperature phase boundary, as will be presented in Chapter 6. A Backscatter Electron micrograph of a typical PIT filament is depicted in Figure 4.1. Typical filament sizes for PIT wires are 25 to 50 µm. The filaments consist of a hexagonal Nb 7.5 w.% Ta or pure Nb tubes which are embedded in a high purity Cu matrix. The tubes are filled with powder, containing a Sn rich Nb-Sn intermetallic, in combination with Sn and Cu. The powder cores act as a Sn source for the solid-state diffusion reaction which is performed at 650 °C or a higher temperature. A great advantage of the PIT method is the high Sn activity which results in a relatively short reaction time, without the need for initial Sn diffusion steps. During the reaction, Sn diffuses from the core into the Nb or Nb 7.5 w.% Ta tube to form the A15 phase. Large A15 grains, which occupy approximately 10% of the filament cross-section are visible in the proximity of the core and are believed not to contribute significantly to the critical current. The core residue and the unreacted tube after reaction occupy typically about 25% of the total filament cross-section each, leaving about 40% of the filament area effectively used for superconducting current transport. In the following Sections specific PIT wires are discussed that were used in this thesis.

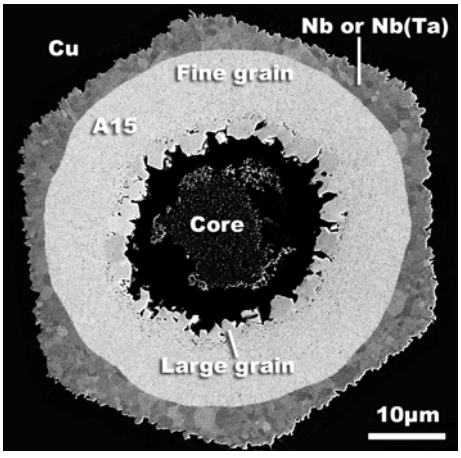

Figure 4.1 *High contrast FESEM back-scatter micrograph of the cross-section of a typical SMI-PIT filament after the A15 formation reaction, courtesy of P.J. Lee. The filament consists of a Nb or Nb 7.5 w.% Ta tube that is embedded in a high purity Cu matrix. The initial powder core containing Nb, Sn and Cu acts as a Sn source during the diffusion reaction during which a nearly perfectly cylindrical fine grain (100 - 200 nm) A15 layer is formed (40% of the filament area) while large grain A15 remains at the core interface (10% of the filament area). The residual 25% is unreacted Nb or Nb 7.5 w.% Ta that acts also as Sn diffusion barrier for the high purity Cu matrix.*

4.2.1 Binary Powder-in-Tube wire

The first sample in Table 4.1 (B27) is a binary PIT wire. This wire comprises pure Nb tubes surrounding the powder core. The manufacturer's recommended heat treatment time was 47 hours at 675 °C but the main investigations were performed on wires that were reacted beyond this time, since earlier magnetic characterizations on this wire indicated that a longer reaction of 128 hours yields slightly improved properties [144]. Cross-sectional micrographs are presented in Figure 4.2.

The lower left micrograph in Figure 4.2 is a backscatter electron image of the whole wire. The inset depicts an enlargement of part of the filament region. The elongated reaction causes the A15 diffusion front (light gray) to propagate very close to the Nb tube outside, risking Sn poisoning of the pure Cu matrix. This is undesirable for practical applications which require a high residual resistivity ratio (RRR) of the Cu matrix for stability and to provide protection during a quench. This is not relevant, however, for the field-temperature phase boundary (Chapter 6). The latter requires an A15 layer that is as Sn rich and homogeneous as possible and the extended reaction time is therefore acceptable.

The upper section of Figure 4.2 is a FESEM fracture micrograph of the A15 layer. The core is located at the right side in this image. Large grain A15 is visible at the interface with the core. The remainder of the A15 layer consists of equiaxed fine grain (about 150 nm) A15.

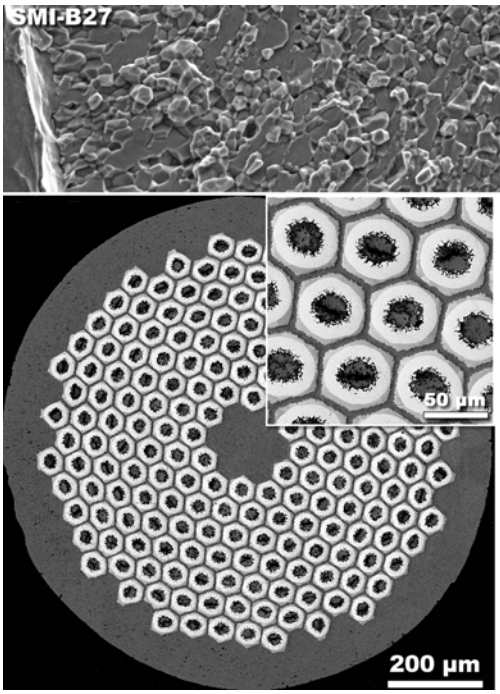

Figure 4.2 *FESEM micrographs of binary PIT wire manufactured by SMI and reacted for 128 hours at 675 °C, courtesy of P.J. Lee. The lower left section is an overall backscatter image with a close-up on the filamentary area depicted in the inset. The dark circular regions are the filament cores and the A15 is represented by the light cylindrical regions. Unreacted Nb surrounds the A15 and the matrix is Cu. The micrograph above depicts an A15 layer fracture surface with the core region located at the right and the unreacted Nb tube to the left. The morphology changes from equiaxed fine grains to large grains close to the core.*

4.2.2 Ternary Powder-in-Tube wire

The second wire in Table 4.1 (B34) is a ternary Powder-in-Tube conductor. An overall backscatter electron micrograph cross-section of this wire is shown in the top left part of Figure 4.3. The layout is identical to the binary wire (Figure 4.2) but it uses Nb 7.5 w.% Ta as tube material. The Ta represents the ternary element in the A15 formation. Since Ta atoms are comparable in size to Nb atoms [22], they occupy Nb sites in the A15 intermetallic [136].

Enlarged views of the filament regions are shown to the right of the overall cross-section for 4, 16, 64 and 768 hour reaction times at 675 °C. Below, further enlargements of single filaments are depicted. The diffusion controlled A15 formation (light gray) progress with increased reaction time. The contrast and brightness of the 4 hour reaction cross-section are artificially manipulated to emphasize the two phases that are present at the core-A15 interface in the initial stage of the reaction. The light gray region around the core is Nb_6Sn_5 and the darker gray shell

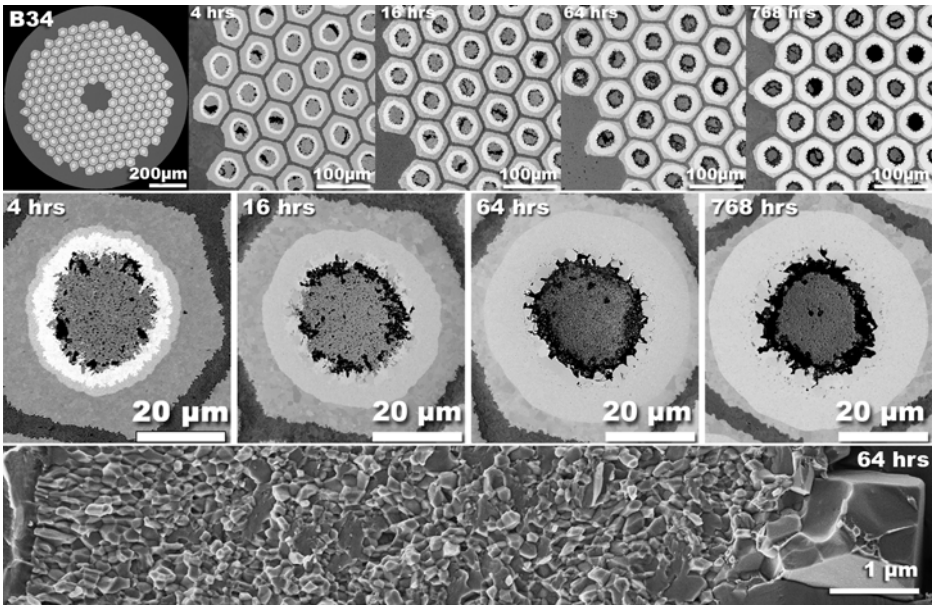

Figure 4.3 *FESEM micrographs of ternary PIT wire manufactured by SMI and reacted for 4, 16, 64 and 768 hours at 675 °C, courtesy of C.M. Fischer and P.J. Lee. The upper left image depicts a backscatter micrograph of the overall cross-section. The four micrographs to the right and the central row depict the reaction progress versus time. The A15 layers, represented by the light gray cylindrical sections grow outwards as time progresses. Not all available Nb 7.5 w.% Ta is transformed into A15, even after 768 hours at 675 °C. After 4 hours an initial Nb_6Sn_5 phase can be distinguished by the lightest gray cylindrical area that surrounds the core. On its outer perimeter fine grain A15 is formed, identified by the slightly darker cylindrical region. The lower micrograph depicts an A15 fracture surface with the core located to the right and the Nb 7.5 w.% Ta tube located to the left. Columnar grains can be distinguished at the Nb 7.5 w.% Ta interface, in contrast to the binary wire. A central region of equiaxed fine grain A15 is observed and large grains are visible in the proximity of the core.*

around this is A15. At 16 hours reaction the initial Nb_6Sn_5 phase is no longer unambiguously distinguishable. Even after a relatively long reaction time of 768 hours the diffusion front did not propagate completely through the Nb 7.5 w.% Ta tube. It will be shown in Section 4.8, that Sn depletion of the core-A15 interface region is the main cause that stops the Sn propagation.

The bottom image in Figure 4.3 shows a surface fracture micrograph of an A15 layer in the ternary PIT wire after 64 hours at 675 °C. The core is located to the right and the Nb 7.5 w.% Ta to the left. As with the binary wire (Figure 4.2) large grains are visible in the vicinity of the core. The majority of the A15 layer consists of equiaxed fine grain (about 150 nm) A15. Columnar grains are visible in the last 1 µm before the Nb 7.5 w.% Ta tube, in contrast to the binary wire. A possible cause for the formation of columnar grains is Sn shortage caused by Sn depletion of the source. A major difference compared to the binary version is that the fine grain area is about 25% wider in the ternary wire.

4.2.3 Reinforced ternary Powder-in-Tube wire

The third sample in Table 4.1 (B134) is again a ternary PIT wire manufactured by SMI. A cross-section of this wire is shown in Figure 4.4 and is similar to B34 but has a Cu-Nb reinforcement tube surrounding the Cu matrix. It can be expected that the reinforcement results in a larger thermal pre-compression in the A15 caused by the higher strength of the Cu-Nb as compared to solely a Cu matrix. The inset in Figure 4.4 indicates that the Cu-Nb reinforcement results in additional deformation of the outer filaments as compared to the not-reinforced version. This deformation, combined with a slightly smaller filament size and rapid Sn propagation causes the diffusion front to locally touch the pure Cu matrix already after an 80 hours reaction heat treatment at 675 °C.

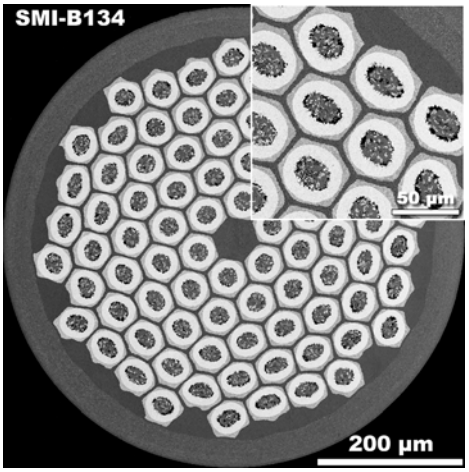

Figure 4.4 *FESEM micrographs of a reinforced ternary PIT wire manufactured by SMI and reacted for 80 hours at 675 °C, courtesy of P.J. Lee. The micrograph shows an overall backscatter cross-section and the inset shows an enlargement of the filament region. Wire construction is identical to the regular ternary PIT wire (Figure 4.3) apart from the presence of an outer sheath of Cu-Nb reinforcement that surrounds the Cu matrix, distinguishable by the lighter gray cylindrical region that surrounds the matrix. Compared to Figure 4.3, a more pronounced deformation of the outer filaments is visible.*

4.3 Bronze process wires

The second set of samples in Table 4.1 are wires manufactured according to ITER specifications following the traditional bronze route process. The wires were investigated extensively with respect to critical current density as function of applied field, temperature and axial strain in the ITER benchmark tests. The results of critical current analyses are presented in Chapter 7.

4.3.1 Ternary bronze process wire manufactured by Furukawa

The first bronze process wire in Table 4.1 (FUR) was manufactured by Furukawa. The wire was heat treated according to the manufacturer's recommended schedule of 240 hours at 650 °C. An overall backscatter electron micrograph cross-section of the wire is presented in the left image in Figure 4.5. The inset depicts a magnification of part of the filamentary area and a fracture micrograph of a single filament is presented in the right image of Figure 4.5.

The wire is built up with Nb rods which are embedded in a 1 at.% Ti containing Sn-rich bronze [202]. The Ti represents the ternary element in the A15 formation. The bronze is surrounded by a Ta diffusion barrier (white) and the outer layer consists of pure Cu. The filaments are 3 to 5 µm in diameter and the 19 filament sub-bundles can be identified. Voids are visible in the filament area magnification, a result of Kirkendall porosity during the A15 formation reaction.

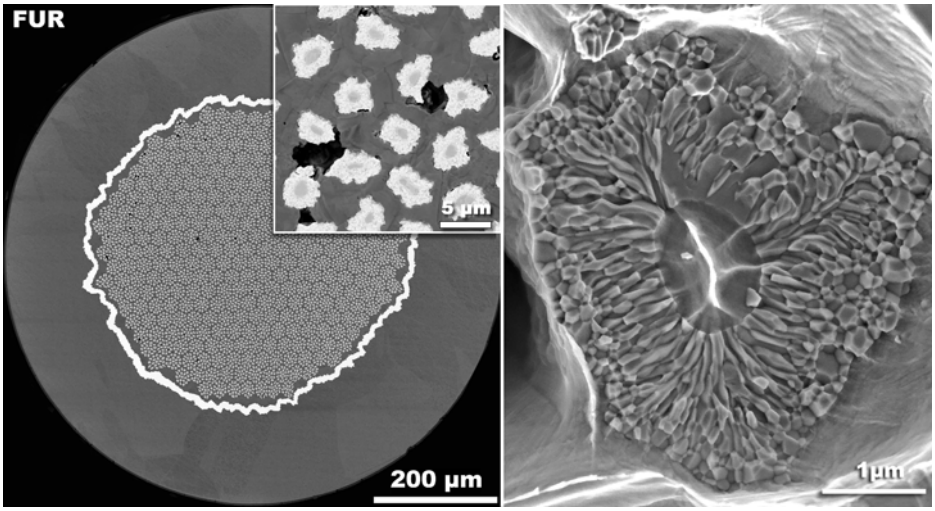

Figure 4.5 *FESEM cross-section micrographs of a ternary bronze process ITER wire manufactured by Furukawa, reacted for 240 hours at 650 °C, courtesy of P.J. Lee. The left image depicts an overall cross-section with bundles of filaments embedded in a bronze with Ti addition matrix surrounded by a Ta diffusion barrier (white) and a high purity Cu stabilizer. The inset shows a magnification of the filament region in which the A15 is visible as light gray shells that surround the unreacted Nb. Some voids are visible in the inter-filament bronze. The right micrograph depicts a fracture surface of a filament. Mainly columnar A15 grains are formed but a small region of equiaxed grains is visible at the A15-bronze interface.*

The outer 100 to 200 nm, located next to the bronze in the filament surface fracture micrograph consists mainly of equiaxed grains of approximately 100 nm diameter, whereas the inner area contains columnar grains of about 100 nm × 400 nm. The formation of columnar grains is an indication of low-Sn A15. The inner region is unreacted Nb. A substantially lower Sn diffusion speed as compared to the Powder-in-tube wires is visualized by the thin, 1 µm size A15 layer that was formed at substantially longer reaction time in comparison to the 8 to 10 µm thick A15 layers in the PIT wires.

4.3.2 Ternary bronze process wire manufactured by Vacuumschmelze

The second bronze process wire in Table 4.1 (VAC) was manufactured by Vacuumschmelze. This wire was also heat treated according to the manufacturer recommended schedule. The reaction follows an initial step of 220 hours at 570 °C probably for initial Sn diffusion, followed by 175 hours at an A15 formation temperature of 650 °C. An overall backscatter electron micrograph of this wire is depicted in the left image in Figure 4.6. A magnification of a filament region and a single filament are presented in the inset and to the right of this overall cross-section.

This bronze process wire is manufactured with Nb 7.5w.% Ta rods that are embedded in a Sn rich bronze matrix that is surrounded by a Ta diffusion barrier and embedded in a pure Cu

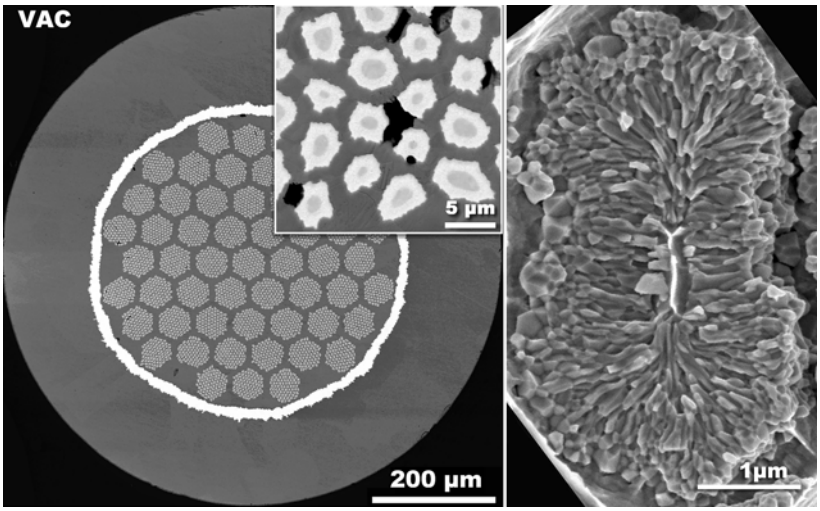

Figure 4.6 *FESEM micrographs of a ternary bronze process wire manufactured by Vacuumschmelze, reacted by a diffusion step of 220 hours at 570 ℃ followed by an A15 formation step for 175 hours at 650 ℃, courtesy of P.J. Lee. The left image shows an overall cross-section with bundles of filaments embedded in a bronze matrix surrounded by a Ta diffusion barrier (white) and a high purity Cu stabilizer. The inset shows a magnification of the filament region in which the A15 is visible as light gray shells that surround the unreacted Nb 7.5 w.% Ta. As with the Furukawa wire in Figure 4.5, some voids are distinguished in the remaining bronze. The right micrograph depicts a fracture surface of a filament. Mainly columnar grains are formed but some equiaxed grains are visible at the A15-bronze interface.*

matrix. The Ta in the Nb 7.5 w.% Ta tubes is the ternary element in the A15 formation. It is visible in the overall cross-section that the Nb rods are bundled into sub-elements which are more coarsely distributed than in the Furukawa wire (Figure 4.5). In the inset 3 to 5 µm diameter filaments are shown with the light gray areas representing the A15. In the inset voids are visible in the post-reaction bronze, similar to the Furukawa wire. The single filament cross-section shows that again a thin layer of about 100 nm diameter equiaxed grains is formed in the proximity of the bronze, whereas further inside about 100 nm × 400 nm columnar grains are formed at the Nb 7.5 w.% Ta interface. The latter are comparable in morphology to the columnar grains at the Nb interface in the Furukawa wire and the Nb 7.5 w.% Ta interface in the ternary PIT wire. This supports low Sn activity as possible cause for the formation of columnar grains. Again, a much lower Sn diffusion speed occurs in this bronze process wire as compared to the PIT process wires.

4.4 Average grain size

The importance of A15 grain size for the current carrying capability was demonstrated in Section 2.7. Fracture surface micrographs as depicted in Figure 4.2 and Figure 4.3 have been analyzed in detail by Fischer [144], arriving at a relation between average grain sizes and reaction time and reaction temperature. In Figure 4.7 some of his results on the binary and ternary SMI-PIT wires are summarized, in combination with results from the literature.

The left plot in Figure 4.7 shows that the average grain size (excluding the large grains in the proximity of the core) increases only slightly with reaction duration. The average grain size

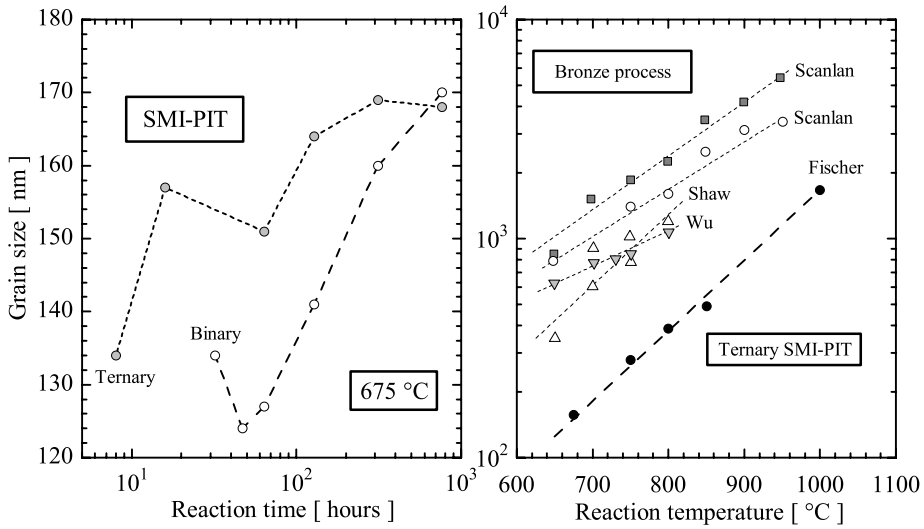

Figure 4.7 *Average grain size (excluding the large grains in the proximity of the core) versus reaction time (left) and temperature (right). The grain size is only slightly dependent on reaction time at 675 °C (a stronger dependence is observed for the binary version) but increases strongly with reaction temperature.*

after the diffusion has approximately halted is around 130 nm for the binary PIT wire and around 150 nm for the ternary PIT wire. This is comparable to modern bronze process wires as well as high current density Internal Sn process wires. The average grain size in the Vacuumschmelze bronze process wire (Figure 4.6), using an A15 formation temperature of 650 °C is about 150 nm for the interior and about 90 nm for the outer 100 nm thick layer of the filament [231]. The Furukawa bronze process wire, reacted at 650 °C has an average grain size of about 150 nm [229]. Modern high critical current density Internal Sn process wires also exhibit grain sizes of 90 to 140 nm [231]. As with the Vacuumschmelze wire, some position dependence exists in the Furukawa wire and modern Internal Sn wires and also columnar grains can be present. In conclusion, the grain sizes in modern Nb_3Sn wires with relatively complete reactions at 650 to 675 °C are very comparable and between 90 and 150 nm.

The right plot in Figure 4.7 shows that, in contrast to the reaction time dependence at 675 °C, grain size is strongly dependent on reaction temperature. The results on the ternary PIT wire were collected by Fischer [144]. For comparison, older literature results on bronze process wires are included from Scanlan *et al.* [139], Shaw [140] and Wu *et al.* [62]. It should be noted that the lower Scanlan line is for incomplete reactions. The 675 °C, 750 °C and 800 °C Fischer data is averaged over 8 to 768 hours, 16 to 64 hours and 16 to 32 hours respectively whereas the 850 °C point is for a 16 h / 750 °C + 24 h / 850 °C reaction and the 1000 °C point for a 16 h / 750 °C + 24 h / 1000 °C reaction. The overall dependence of grain size on reaction temperature is consistent, apart from the apparent progress in grain size reduction since around 1980.

4.5 Bulk Nb_3Sn

In addition to the wires also a bulk, quasi-homogeneous sample manufactured by M.C. Jewell was analyzed. This was done to distinguish the behavior of pure binary, Cu free Nb_3Sn, from Nb_3Sn in Cu matrix wires. The bulk sample was cut into the shape of a needle to allow a resistive measurement. It was not fully equilibrated to homogeneous distributed Sn content and exhibits therefore three dimensional local agglomerations of various Sn content. This type of inhomogeneity is in contrast to the wire samples, which show mainly a radially distributed Sn gradient. Cross-sections of not equilibrated bulk materials show local A15 areas that are stoichiometric in Sn and areas that are low in Sn as more extensively described elsewhere [39]. This results in a strongly percolative current flow in the sample. The sample is a cutout from a larger bulk section, produced by a Hot Isostatic Pressing (HIP) sintering technique. Field Emission Scanning Electron Microscopy (FESEM) in combination with Energy- and Wavelength Dispersive X-ray Spectroscopy analysis, more details on the production, as well as more extensive characterization on a larger bulk sample set, were published earlier [39].

4.6 Wire cross-section

Inter-comparison of critical currents of wires was performed using non-Cu critical current densities. This yields an objective comparison of the quality and efficiency of the non-Cu area (which is used for A15 formation). Alternatively, the critical current density in the A15 layer itself is used to compare the quality of the A15 layer. A third alternative is to normalize the A15 layer critical current density to the grain boundary density, effectively yielding the quality of pinning in the A15 layer. Usually the non-Cu critical current density at $\mu_0 H = 12$ T and $T = 4.2$ K is compared to examine suitability for applications. In the case of high critical

current wires, 15 T can be used as reference field to limit the current in the characterization equipment.

Accurate determination of the non-Cu area is required to calculate the non-Cu critical current density. Two methods are used here. The first method involves accurate weighing of a wire section before and after chemical etching of the Cu (and bronze). This method was applied on both bronze process wires and yielded values comparable to those supplied by the manufacturers [263]. The second method involves digital image analysis of backscatter electron micrographs. This method was applied to the PIT process wires. The principle of this method is depicted in Figure 4.8 for a ternary PIT conductor.

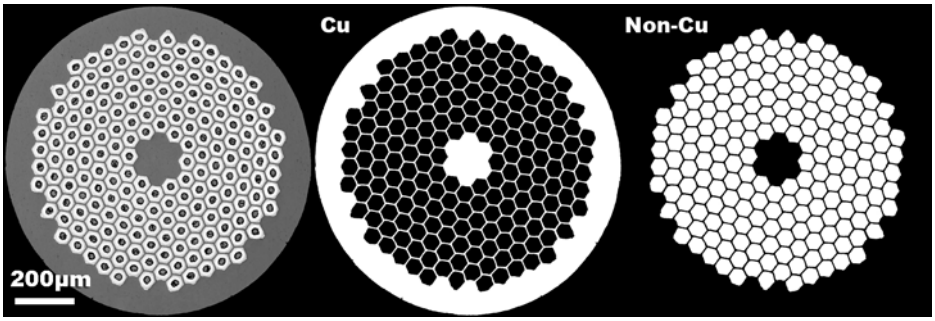

Figure 4.8 *Determination of Cu versus non-Cu ratios demonstrated on a SMI-PIT wire cross-section, courtesy of P.J. Lee. Brightness and contrast are manipulated starting from a high contrast Backscatter Electron micrograph and the resulting white pixel counts are used for determination of the Cu/Non-Cu ratio.*

The relative brightness in backscatter electron images is proportional to atomic mass. Contrast and brightness of a high resolution backscatter electron image were manipulated using digital image analysis software. Composition dependent black and white bitmaps were generated by applying a threshold brightness value, as shown in Figure 4.8. The pixel counts in the bitmaps, combined with the magnification, were used to arrive at accurate area determinations.

4.7 Composition analysis on Powder-in-Tube wires

The critical properties of Nb_3Sn conductors depend strongly on the Sn content of the A15 phase, as was explained in Chapter 2. All Nb_3Sn wires exhibit inherent Sn inhomogeneities, arising from their design and reaction procedure which is always based on a solid-state diffusion reaction. The influence of the Sn content in the A15 on the upper critical field and critical temperature is relatively well established. In the literature, details are discussed, as the exact influence of the occurrence of low temperature cubic to tetragonal transitions and ternary elements on the field-temperature phase boundary, as was summarized in Chapter 2.

The microscopic Sn inhomogeneities will have to be characterized to analyze to what extent experimentally observed differences between various conductors can be attributed to variations in wire architecture. Compositional analysis on bronze process wires is complicated by the limited spatial resolution of available probing techniques. Few publications describe therefore

the Sn variation across the A15 layers in bronze process conductors by Transmission and Scanning Electron Microscopy [62, 135] or by advanced analysis of backscatter electron micrographs [231]. The general impression is that bronze process wires are strongly inhomogeneous with Sn gradients across the A15 layers between 2 and 5 at.% Sn/µm. Recent investigations on the Sn gradients in PIT wires [64, 65] pointed out that this wire manufacturing process delivers much lower Sn gradients of about 0.35 at.% Sn/µm. The main advantage of PIT process wires, however, is the large volume fraction of Sn rich A15 in comparison to bronze process wires.

In the following sections of this Chapter Sn gradients in the PIT wires are analyzed in detail using Electron Dispersive X-ray Spectroscopy (EDX). This technique has a limited spatial resolution, caused by the penetration depth of the electron beam which results in a spherical region of typically 1 to 2 µm in diameter from which photons are emitted at relaxation. Simulations by P.J. Lee [233] on relevant Nb–Sn lattices indicated an overall positional resolution of ± 750 nm for a 20 kV accelerating voltage which can be reduced to about ± 100 nm for a 7 kV accelerating voltage. The technique is therefore not suited for compositional analysis in bronze process conductors. EDX is not sufficiently accurate for absolute concentrations but relative changes, which depend mainly on relative variations in X-ray signal peak heights, are assumed to be sufficiently reliable for gradient determination. A major advantage of the technique is that it can be directly combined with Scanning Electron Microscopy (SEM) and is relatively easily automated, enabling a high sample throughput and thus improved statistics.

The majority of the data was collected by automated EDX on a thermal emission SEM (JEOL 6100) using commercial WINEDS spectrum analysis software. The electron beam was targeted at typically 8 to 10 equidistant spots radially across an A15 layer in an arbitrary filament. Selected samples were analyzed by manual spot positioning on a high resolution Field Emission SEM (LEO 1530).

4.7.1 Automated TSEM composition analysis

Typical automated EDX energy spectra, using a beam accelerator voltage of 20 kV are depicted in Figure 4.9. The spectra result from overall emissions on an area as shown in the inset for the reacted binary plot. The number of counts that were used was sufficient for automatic peak identification by the software, forcing the detection of only Nb, Sn, Cu and Ta. A clear difference exists between the ternary and binary spectra, mainly in the presence of Ta peaks in the spectrum.

The reliability of the compositional information was verified by the accuracy of the Ta ratio in the ternary Nb 7.5 w.% Ta tube. The Nb–Ta tubes in the ternary PIT wires contain 7.5 w.% or 4 at.% Ta according to the manufacturer's specification. The Ta peaks are relatively small and the main Ta peaks ($Ta_{M\alpha}$ and $Ta_{M\beta}$) are positioned close to the Nb_{LI} peak and overlap the main Si peak, which will be present if sample contamination has occurred during polishing. The accuracy of the Ta ratio determination is therefore very sensitive to correct peak identification and peak fitting statistics. The detected amount of Ta in Nb 7.5 w.% Ta in unreacted sections of the ternary tube across 10 investigated ternary samples ranged from 3.9 at.% to 4.7 at.% and averaged out to 4.2 at.%, which is very close to the 4 at.% specified by the manufacturer.

Typical standard deviations in overall element ratio determinations as given by the software, resulting from peak fitting statistics are 0.9 at.% for Cu, 0.6 at.% for Nb, 0.3 at.% for Sn and 0.5 at.% for Ta. The latter covers the range that was observed for the 10 separate samples above.

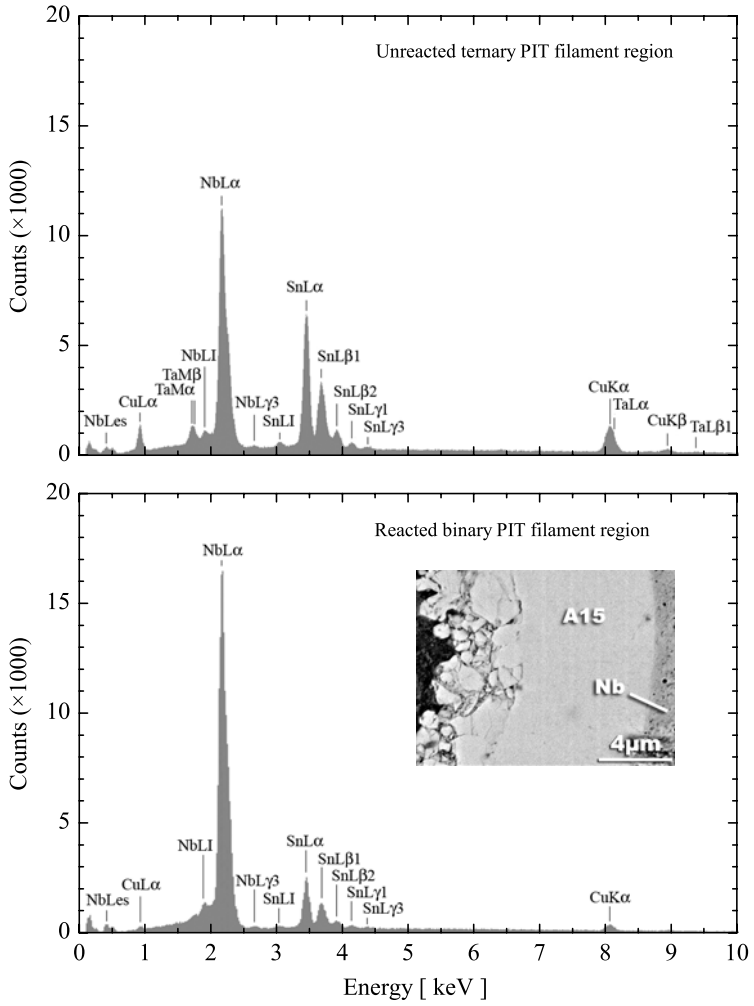

Figure 4.9 *Overall EDX spectra for filament sections of an unreacted ternary PIT wire (top) and a reacted binary PIT wire (below). The main differences are the absence of Ta peaks in the binary plot and different relative amounts of the Nb, Sn and Cu peaks which are attributed to differences in electron beam area position and reaction originated composition changes.*

Reproducibility of automated composition analysis

The reproducibility of compositional analysis was investigated by analysis of three filaments within the same ternary PIT wire that was reacted for 64 hours at 675 °C. The selected filaments and selected A15 regions are depicted in Figure 4.10. For each filament the electron beam spot positions are depicted. At each spot a spectrum, identical to Figure 4.9, was collected and spectrum analysis was performed to identify the element ratios.

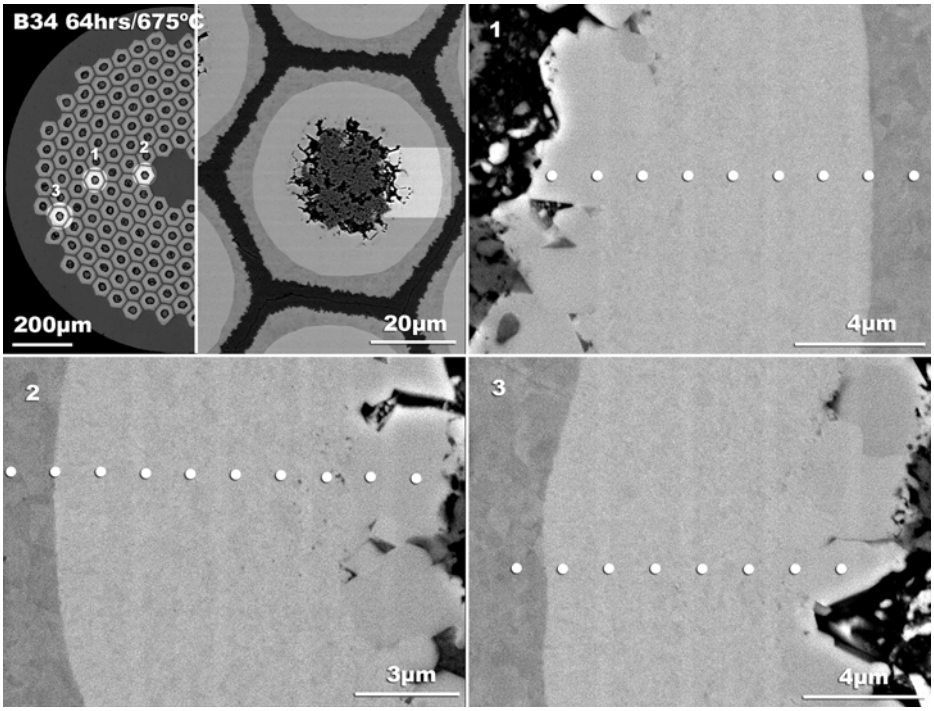

Figure 4.10 *Electron beam spot positions on a central (#1), inner (#2) and outer (#3) filament A15 area in a ternary PIT wire, reacted for 64 hours at 675 °C. Scans were made starting in the large grain region, through the fine grain A15 and into the unreacted Nb 7.5 w.% Ta.*

A typical overall element ratio plot as function of position relative to the A15-Nb 7.5 w.% Ta interface is depicted in Figure 4.11 for a filament located centrally in the filament package (#1). The Sn concentration in the Nb-Ta-Sn-Cu combination starts at about 23.5 at.% in the large grains next to the core and is relatively flat at about 21.5 at.% across the A15 layer. At the Nb 7.5 w.% Ta interface the Sn concentration shows a steep reduction and ends at zero in the unreacted Nb 7.5 w.% Ta tube. The amount of Ta in Nb 7.5 w.% Ta in the unreacted tube amounts to 4.7 at.% which, as mentioned in the previous section, is the highest value detected. It is interesting to note a Cu signal throughout the whole investigated area. The error bars that are depicted at the −2.8 µm position represent the standard deviations resulting from the

spectrum analysis software and are representative for all points. This error bar represents the statistical error from the integrated count totals assuming a Gaussian peak shape. It does not include systematic errors, or errors associated with peak overlap.

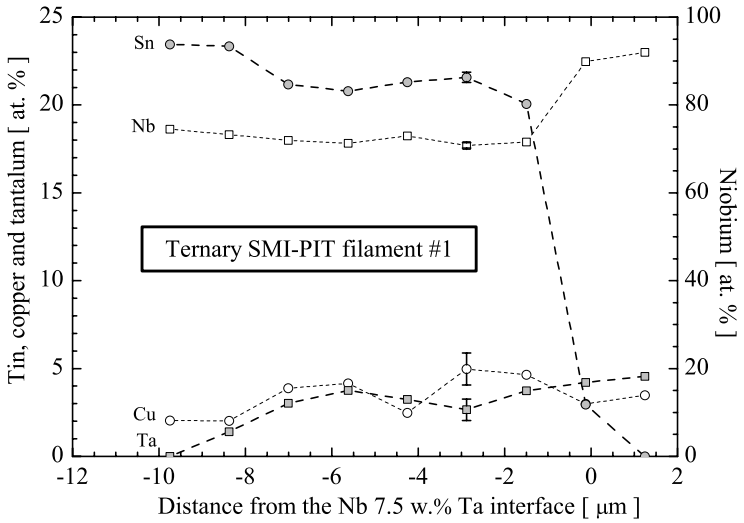

Figure 4.11 *Overall element ratios as determined by EDX on a central filament in a ternary Powder-in-Tube wire that was reacted for 64 hours at 675 °C. The spot position is relative to the Nb 7.5 w.% Ta-A15 interface. The atomic percentages represent the relative fraction in Nb + Ta + Sn + Cu.*

The overall composition graphs for filaments #2 and #3 are comparable to Figure 4.11. The Sn content of the A15 phase, or more specifically the amount of Sn in Nb 7.5 w.% Ta-Sn can be derived from these overall ratios. The resulting Sn contents are plotted in Figure 4.12 for the three filaments from Figure 4.10. A fracture surface micrograph (from Figure 4.3) of an arbitrary filament in the same wire is included in the plot to illustrate the A15 morphology at the spot positions.

The tendencies are very similar although local compositional variations result in some scatter of the data. The error bars on the points around −7 μm represent the standard deviations from the spectrum analysis software. The standard deviations show an uncertainty of ± 0.3 at.% Sn and are representative for all points. Note that T_c measurements in Chapter 6 indicate that the TSEM EDX system results in Sn content values that are approximately 1.5 at.% too low as a result of standardless EDX software. This will be further detailed in Section 7.8.1. The analysis in Figure 4.12 results, within the scatter of the data, in a two region behavior: A high Sn content of about 23.5 at.% occurs in the large grains. A slightly lower 22 at.% composition with small gradient occurs over the fine grains. The literature data on a different PIT wire concluded a Sn gradient of 0.35 at.%/μm over the A15 layer [64]. The local variation of the compositional analysis does not include sufficient statistics for an accurate determination of the

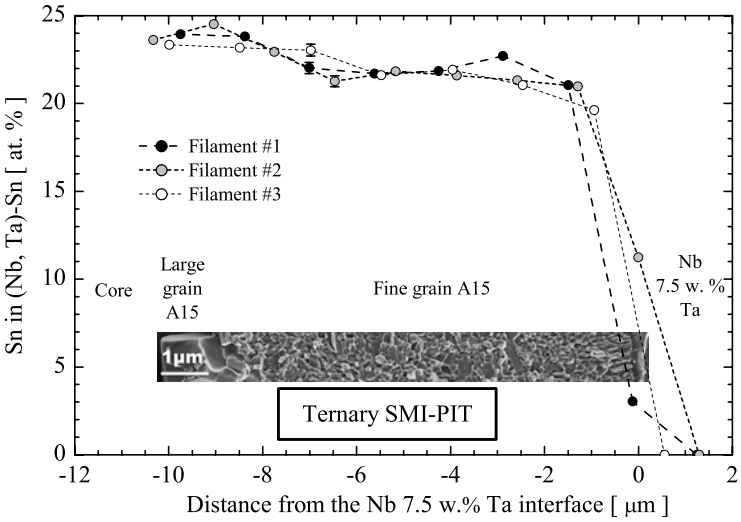

Figure 4.12 *Atomic Sn content in (Nb, Ta)-Sn for three filaments in a SMI Powder-in-Tube wire that was reacted for 64 hours at 675 °C. Spot positions are relative to the Nb 7.5 w.% Ta-A15 interface. The inset shows a high resolution fracture micrograph of an arbitrary filament to indicate the approximate position of the EDX spots.*

gradient, but about 0.2 at.%/μm appears a reasonable average across the fine grains. In summary it is concluded that the Sn gradient is small over most of the A15 layer and that three filaments from different locations agree.

Composition differences between three PIT wires

The Sn content versus position was analyzed for the three PIT wires (Table 4.1) to investigate the differences that might appear between binary and ternary versions of this wire. The Sn content in Nb-Sn or in Nb 7.5 w.% Ta-Sn is plotted versus relative position for all three PIT wires in Figure 4.13. The spot positions are relative to the average large grain to fine grain interface to enable direct comparisons of the fine grain areas. The insets show the positional information for the binary and reinforced ternary wires. The positional information for the ternary wire is depicted in the filament #1 plot in Figure 4.10. The ternary wire was reacted for 64 hours at 675 °C, the binary for 128 hours at 675 °C and the reinforced ternary wire for 80 hours at 675 °C. The error bars on the points around 4 μm again represent the standard deviations from the spectrum analysis software.

The behavior of the three PIT wires is strikingly similar. The existence of a two region behavior is similar to the results on the ternary wire, but the stepwise transition between the large- and fine grain region that is visible in the ternary and reinforced ternary wires is more gradual in the binary wire. About 2 at.% lower Sn content is observed in the fine grain regions with respect to the large grain regions in all the wires. The binary wire appears to have less local variation in composition. This might originate from the long reaction time which could homogenize the fine grain region. An interesting observation is the increased layer thickness of

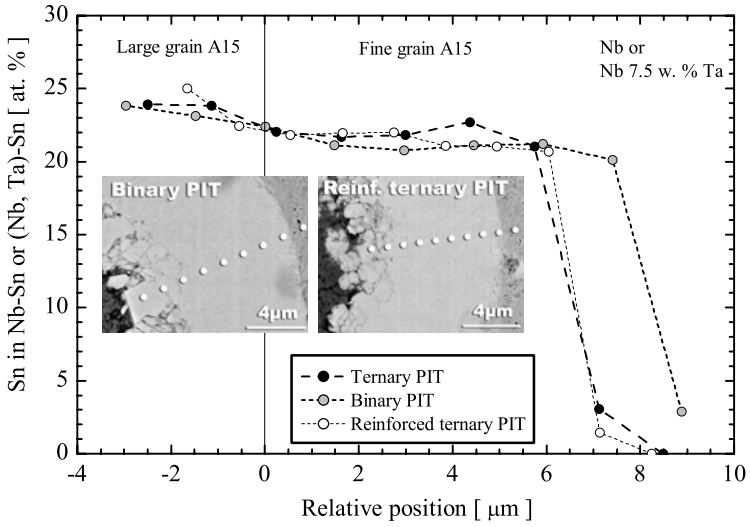

Figure 4.13 *EDX determined A15 Sn content for central filaments in a ternary SMI-PIT wire (from Figure 4.12, 64 h at 675 °C), a binary SMI-PIT wire (128 h at 675 °C) and a reinforced ternary SMI-PIT wire (80 h at 675 °C). Spot positions are relative to the approximate large- to fine grain interface. All Sn profiles are remarkably similar. The large grain region is about 2 at.% richer in Sn compared to the fine grain regions. The ternary wire fine grain regions appear to be similar within the scatter of the data but the binary wire fine grains are on average about 1 at.% lower in Sn and its fine grain area is wider.*

fine grain A15 in the binary wire in comparison to the ternary versions. This is in contrast to the fracture micrographs in Figure 4.2 and Figure 4.3, which led to the conclusion that the fine grain area in the ternary wire is 25% wider than for the binary wire.

Influence of reaction time on composition

The ternary PIT wire at various stages in the reaction at 675 °C was analyzed to investigate the influence of reaction time on A15 layer Sn content. The investigated samples were reacted for 4, 16, 64 and 768 hours at 675 °C. Backscatter electron cross-section micrographs of the investigated A15 areas are depicted in Figure 4.14, including the electron beam spot positions.

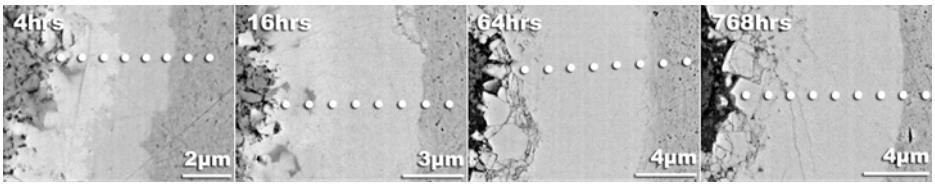

Figure 4.14 *EDX spot positions for composition analysis on filaments in a ternary SMI-PIT wire, heat treated for 4, 16, 64 and 768 hours at 675 °C.*

The resulting Sn contents as function of relative position are depicted in Figure 4.15. The relative positions are approximately normalized to the large- to fine grain interface.

The progression of the diffusion and A15 formation with reaction time is clearly visible from Figure 4.15. The powder core of this wire contains the Sn rich intermetallic $NbSn_2$, Cu and additional Sn. Assuming the binary phase diagram (Figure 2.1) remains valid for the ternary Nb 7.5 w.% Ta-Sn system in the presence of Cu, this Sn richness at the Nb 7.5 w.% Ta-core interface dictates an initial formation of $(Nb, Ta)_6Sn_5$ of composition 52.4 at.% Nb, 2.2 at.% Ta and 45.4 at.% Sn, as was also indicated in Section 4.2.2.

The presence of this phase has unambiguously been identified by Fischer [144] and Cooley *et al.* [137]. The 4 and 16 hour reaction composition analyses in Figure 4.15 indicate that in addition to $(Nb, Ta)_6Sn_5$ some inter-granular Sn is present at the regions in proximity of the core. After 64 hours reaction Sn has diffused further into the Nb 7.5 w.% Ta tube and the $(Nb, Ta)_6Sn_5$ is completely transformed to A15.

It is interesting to observe that the diffusion front stops progressing beyond 64 hours. It will be shown in Section 4.8 that this is caused by Sn depletion at the core-A15 interface.

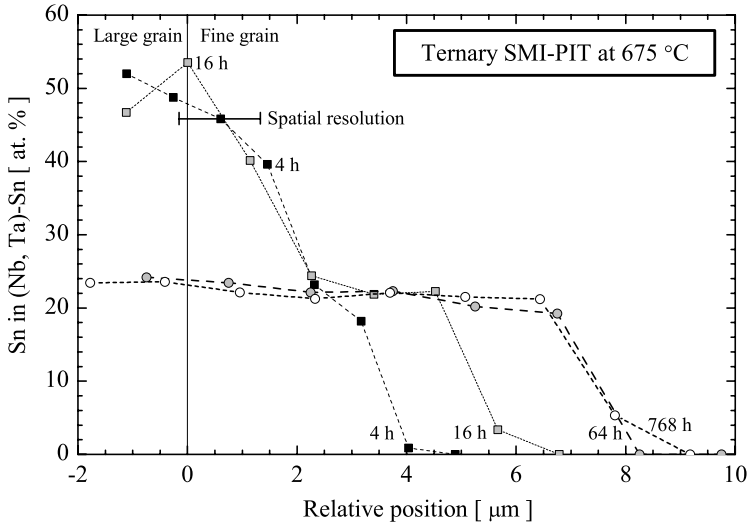

Figure 4.15 *Relative atomic Sn content in the filaments from Figure 4.14. EDX spot positions are relative to the large- to fine grain interface. The initial high Sn content close to the core, caused by the initial Nb_6Sn_5 phase combined with free Sn, has diffused into the A15 after 64 hours reaction. The propagation of the diffusion front is visible but reacting beyond 64 hours (the optimal current density reaction) does not widen the A15 layer further nor appears to enrich the A15, but a slight homogenization of the fine grain Sn content can be distinguished.*

4.7.2 Manual FESEM composition analysis on a ternary PIT wire

In this Section FESEM EDX scans, performed by P.J. Lee, are summarized. In these characterizations the beam spot positions were manually selected. The manual scans were performed on a higher resolution Field Emission SEM, also using a standardless EDX program, to yield an impression of the errors that might occur from the use of a different analysis system.

Manual FE-SEM EDX was performed on a central and an outer filament of the same wire as used for the automated analysis. The resulting atomic Sn concentrations in Nb 7.5 w.% Ta-Sn at indicated electron beam spot positions are depicted in the high resolution backscatter secondary electron micrographs in Figure 4.16. The micrographs to the left indicate the positions of the selected filaments and the selected A15 areas for the compositional analysis in the right micrographs.

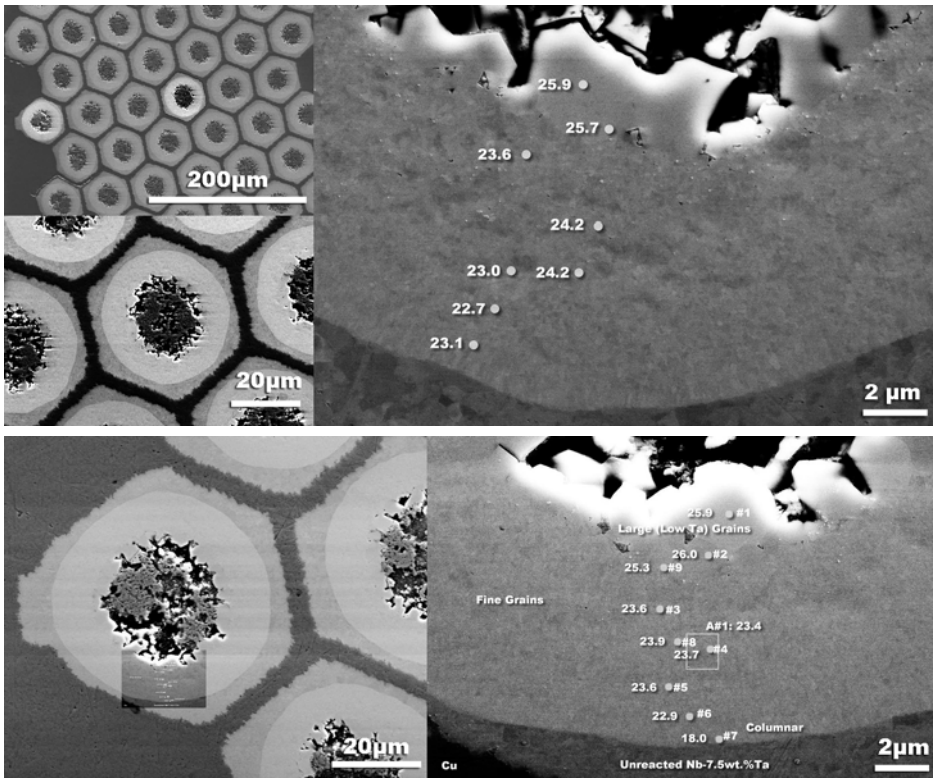

Figure 4.16 *Manual EDX spot positioning performed in a different (Field Emission) Scanning Electron Microscope system than used for the automated EDX analysis (a thermal emission SEM), but on the same ternary SMI-PIT wire, courtesy of P.J. Lee. The spot positions are combined with high resolution backscatter micrographs to identify their position. The upper half depicts a central filament and the lower half an outer filament. In the outer filament also an area of about 3 μm^2 is analyzed, to quantify possible differences between local (1 μm^2) and more global (3 μm^2) composition analysis.*

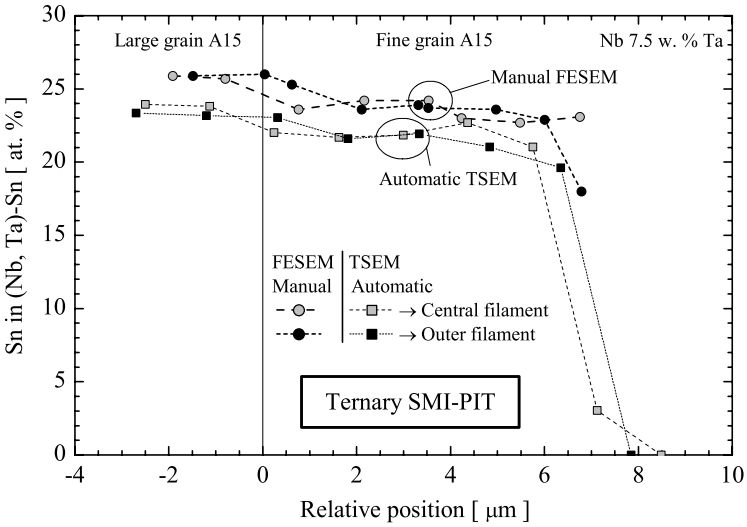

Figure 4.17 *Comparison of two EDX composition analysis methods. Manual was performed on a Field Emission SEM and automated was performed on a thermal emission SEM. Both analyses were performed on filaments in the same ternary SMI-PIT wire that was reacted for 64 hours at 675 °C. The EDX spot positions are relative to the large- fine grain interfaces. The detected gradients and the relatively higher Sn content for the large grain regions are identical within the scatter of the data. The absolute Sn concentrations, however, differ by about 2 at.%.*

The manually determined atomic Sn contents in the central and outer filaments are plotted in Figure 4.17 as function of approximate average radial distance with respect to the large to small grain interface. For comparison, also the automatically positioned, TSEM determined gradients from Figure 4.12 are included. The gradient found with both techniques is identical. However, the absolute Sn contents differ by approximately 2 at.% Sn, due to the use of two different standardless EDX programs. As was mentioned before, T_c measurements in Chapter 6 indicate that the TSEM EDX system results in Sn content values that are approximately 1.5 at.% too low, resulting in the conclusion that the FESEM systems yields values which are about 0.5 at.% too high. It should be emphasized that these numbers not exact but only an indication.

4.8 Composition analysis of pre-reaction extracted PIT filaments

From Figure 4.3 and Figure 4.15 it is evident that in the ternary PIT wire the diffusion stops beyond 64 hours reaction at 675 °C. Earlier variable heat treatment analysis by Fischer [144] on this wire, using microscopy as well as resistivity ratio (ρ_{300K} / ρ_{77K}), indicated that Sn breakthrough of the Nb(Ta) barrier into the Cu occurred for reactions of 128 hours and more at 675 °C. In addition, EDX data on the core residue and core-A15 interface regions indicated local concentrations of about 6 and 2 at.% Sn respectively. It was therefore concluded that the diffusion front stops due to Sn depletion of the core-A15 interface.

Some Sn thus remains present in the core after the diffusion has halted and some unquantified Sn loss to the Cu matrix occurs. The question can therefore be raised whether it is possible to retrieve a higher A15 yield from this wire without the presence of the Cu matrix. In addition, the influence of the matrix on the solid state diffusion reaction is unknown. It cannot be excluded that the presence of the Cu matrix influences the reaction characteristics. From Figure 4.11 it is appears that 3 to 5 atomic percent Cu is present throughout the A15 layer, but it is also visible in the unreacted Nb 7.5 w.% Ta. The latter could arise from the limited spatial resolution rendering the Cu signal spurious by the detection of matrix Cu. The general understanding is that Cu is not soluble in the A15 and therefore only exists at the grain boundaries [121, 122]. The presence of Cu is further required to enable low temperature A15 formation as was discussed in Chapter 2. The influence of the matrix Cu on the A15 formation reaction is thus uncertain and it cannot be excluded that Sn loss to the matrix occurs. To investigate these possible influences of the Cu matrix, and to find out whether a Sn enrichment of the A15 is possible by removing the matrix, filaments were extracted from unreacted wires and reacted without the presence of Cu. Consequently, they were analyzed with respect to cross section, composition and superconducting properties.

The filaments were prepared by chemical etching of the Cu matrix from approximately 70 mm long sections of unreacted wires with a 50 vol.% nitric acid solution in H_2O. Initial attempts included sealing of the filament ends by Cu plating to prevent Sn leakage during reaction, as was performed successfully by M.T. Naus on wire ends [234]. Sections of bare filaments and filaments with Cu plated ends were sealed in evacuated quartz tubes after flushing with Ar and reacted following a heat treatment matrix. The use of pressurized Ar was considered to prevent evaporation of Sn but appeared not to be required. The filaments with Cu plated seals at each end exhibited Sn deposition on the quartz at the Cu plated end sections whereas the bare filaments exhibited no Sn deposition on the quartz. It was concluded that Sn has a strong Nb affinity and sealing the filament ends by Cu plating only provoked Sn leakage into the vacuum and deposition onto the quartz. Only the central sections of the unsealed filaments were used as sample material since approximately 10 mm of the ends Sn diffused not only from the core but additionally around the filament ends and A15 was formed on the outer perimeter of the filament ends. It is assumed that a central section is representative for a sealed filament, since no Sn was detected on the outer perimeter of these sections.

4.8.1 Diffusion progress during bare filament reactions

As a first step in the analysis of the diffusion progress with heat treatment in bare filaments Backscatter Secondary Electron micrographs were taken at various stages in the reaction. The bare filaments were reacted at 675 °C to enable direct comparisons to the in-wire reactions and additionally at 800 °C in an attempt to increase the solid state diffusion and reaction processes to develop a thicker, more Sn-rich, A15 layer. The resulting backscatter micrographs at 675 °C are presented in Figure 4.18 for 4 through 526 hours reaction time. The diffusion process observed in the bare filaments is qualitatively comparable to the wire reactions analyzed by Fischer [144] as summarized in Figure 4.3.

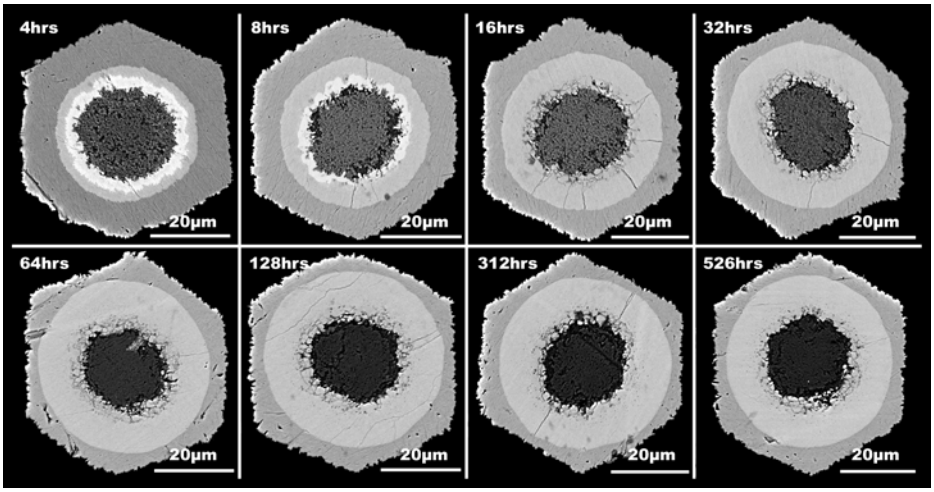

Figure 4.18 *Backscatter micrographs of filaments that were extracted from ternary SMI-PIT wire and then reacted for various times at 675 °C.*

After 4 hours at 675 °C the initial combination of Nb_6Sn_5 (white) and A15 (light grey) is visible. The brightness difference between the region close to the core containing Nb_6Sn_5 and the A15 was artificially enhanced in Figure 4.18 for better visibility. The Nb_6Sn_5 is also clearly distinguishable in the original backscatter micrograph. After 8 hours reaction, the difference in brightness resulting from the heavier Nb_6Sn_5 was less emphasized in the original backscatter image, indicating that some of the Nb_6Sn_5 has already transformed to A15. The region around the core for which still a difference in brightness was observable was artificially emphasized in Figure 4.18. The 8 hour backscatter micrograph indicates that some of the outer part of the 4 hour Nb_6Sn_5 region has already been transformed into large grain A15. From the lower intensity of the remaining Nb_6Sn_5 area in the original 8 hour backscatter micrograph in comparison to the original 4 hour micrograph, it can be concluded that this region contains a mixture of Nb_6Sn_5 and A15.

For the 4 through 64 hours reactions at 675 °C in Figure 4.18 a steady progress of the reaction is observed. Beyond 64 hours at 675 °C no additional A15 layer growth is distinguishable. This rules out Sn loss into the Cu matrix as possible origin for discontinuation of the diffusion process, assuming that the central region of a long bare filament is representative for a bare filament without Sn loss at the ends. A separation is visible at the core-A15 interface. The radial cracks in the brittle A15 regions are believed to originate from post-reaction handling of the 50 µm filaments. The separations between the large grains may result from polishing or also from post-reaction mishandling.

Reaction of bare filaments was also performed at 800 °C to develop a higher Sn content and increased layer thickness (although at the cost of grain growth) by a more aggressive heat treatment. The resulting backscatter micrographs versus reaction time at 800 °C are presented in Figure 4.19. At 800 °C, up to about 8 to 16 hours, the diffusion front progresses much faster than at 675 °C. Beyond 16 hours no additional A15 layer growth is visible. No initial Nb_6Sn_5

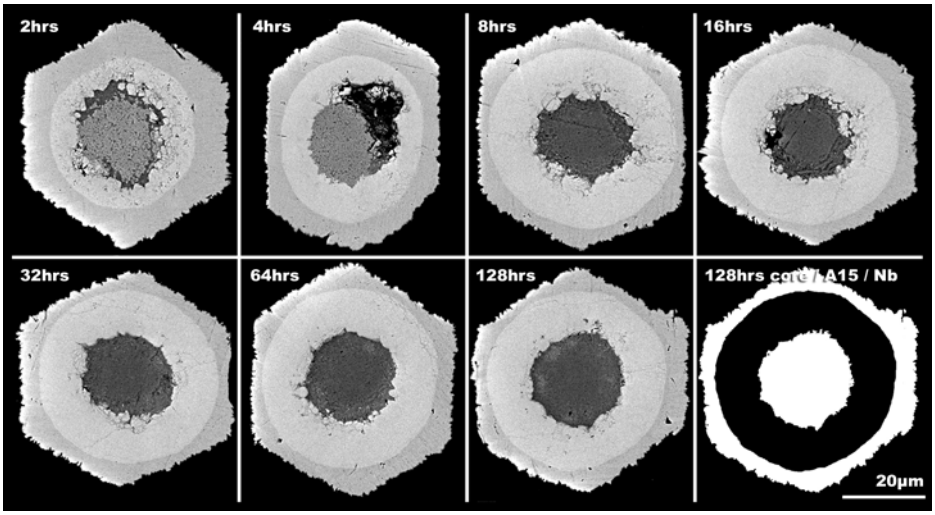

Figure 4.19 *Backscatter micrographs of filaments that were extracted from ternary SMI-PIT wire and then reacted for various times at 800 °C. The 4 hour filament is strongly deformed before or after reaction and the A15 layer is damaged. The bottom-right graph indicates the selection of the core-, A15- and remaining Nb 7.5 w.% Ta regions via digital image analysis software. The pixel counts of these regions were translated to areas to calculate the A15 area for the diffusion progress.*

phase can be distinguished at 800 °C. A clear difference with the 675 °C reaction is the absence of visible gap between the core region and the A15 beyond 2 hours reaction time. In addition, the large grains appear less separated.

Growth of A15 area with time

The A15 (small A15 grains, large A15 grains and transient Nb_6Sn_5) areas were determined using image analysis software to enable a more objective comparison of the Sn diffusion from Figure 4.18 and Figure 4.19. Additionally, the total filament areas and core regions were determined. The last cross-section in Figure 4.19 depicts the graphical area determination by the image analysis software for the 128 hours at 800 °C bare filament reaction. This area determination is representative for all analyses. The resulting areas versus reaction time are plotted in Figure 4.20. For comparison, similar analyses were performed on backscatter micrographs of filaments in wires and these data are included in the plots.

The area growth versus reaction time for the regions containing diffused Sn (large and small grain A15 plus Nb_6Sn_5) is depicted in the upper plot of Figure 4.20 for the bare filaments (SF 800 °C, SF 675 °C) and for filaments in a wire (Wi 675 °C). For the wire data also the fine grain A15 area growth is included (Wi 675 °C fine grains). The area growths can be fit accurately using

$$Area = C_1 - C_2 \exp\left(-\frac{time}{C_3}\right), \tag{4.1}$$

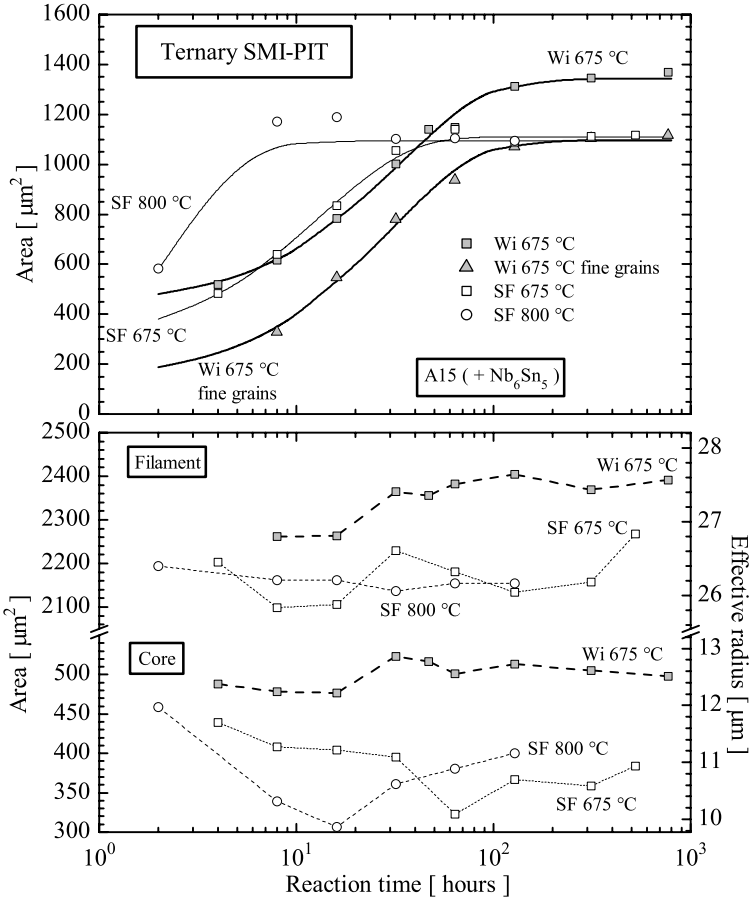

Figure 4.20 *Areas versus reaction time determined using digital image processing software. The upper plot depicts the diffusion progress using the A15 (plus Nb_6Sn_5) areas for the wire (Wi) and single filament (SF) reactions at various temperatures. The curves are calculated using (4.1) with constants as given in Table 4.2. The bottom plot depicts the total filament and core residue areas. Its right axis represents effective filament and core outer radii assuming the areas are circles.*

indicating exponential growth of the diffused Sn areas. The constant C_1 represents the maximum area, C_2 the slope on a semi logarithmic scale and C_3 the transition sharpness between the slope and the final area. The fit values for C_{1-3} are given in Table 4.2.

The large grain A15 + Nb_6Sn_5 area remains approximately constant during the reaction at 675 °C, as is seen when comparing the fine grain and total areas in the wire heat treatment. The layer growth in the bare filament reaction at 675 °C is comparable to the wire, although the bare filament heat treatment saturates at a smaller final area. That its final area is comparable to the

Table 4.2 *Parameters for area growth with reaction time*

	Wi 675 °C fine grains	Wi 675 °C	SF 675 °C	SF 800 °C
C_1 [μm^2]	1097	1344	1110	1094
C_2 [μm^2/h]	972	916	847	1400
C_3 [–]	30.4	34.0	13.5	2.00

final wire fine grain area is incidental. The area growth for the bare filament reaction at 800 °C is much more rapid than at 675 °C and saturates at the same final area after only 8 hours reaction time. It is interesting to observe the "overshoot" which occurs for both bare filament reactions just before reaching the final area. The wire reaction in comparison reaches its plateau much more gradually.

The total A15 + Nb_6Sn_5 area in the wire saturates at a 20% higher value than in the bare filament reactions at 675 °C and 800 °C. In addition, the bare filaments reach their final area after about 64 hours at 675 °C, whereas the wire reaches its final area beyond 100 hours reaction. In the bottom graph of Figure 4.20 the total filament and core areas are shown versus reaction time. The right axis represents the effective radius assuming cylindrical areas. The total filament area for the wire is consistently about 10% larger for reactions beyond 10 hours. The core area in the wire is consistently about 30% larger than in the bare filaments for reactions beyond 10 hours. This indicates that the apparent quicker saturation in the bare filaments in the upper plot might be attributed to a volumetric effect. The main conclusion, however, is that no increase in A15 area is obtained by heat treatment of bare filaments at 675 °C or 800 °C compared to the in-wire reaction.

The wire filament area shows approximately a 5% increase at about 20 hour reaction. This increase was observed in this wire and also in its binary version by Fischer [144]. It was concluded that this increase can be attributed to the volume expansion during A15 formation. It is interesting to observe that a similar area increase is also present in the core area. The area increase in the filament area as well as in the core area occurs between 16 and 32 hour reaction at 675 °C. The areas remain constant beyond this time while A15 is still formed. This might indicate that the filament increase is not correlated to A15 formation but to the disappearance of the Nb_6Sn_5 phase. No clear stepwise increase in the filament or core area is observed in the bare filament reaction. Additionally, no clear trends can be observed for the total filament and core areas in the bare filament reactions, although the initial areas for the bare filaments tend towards comparable values as in the wire.

Error sources for area determination

The filament areas in the wire were averaged over about 5 filaments. The core areas for the wire and for the bare filaments and the filament areas for the bare filaments were determined in a single filament. It is possible that some of the apparent scatter in the bare filament area determinations is caused by the limited number of measurements, although the wire core diameter, which is also determined on one filament, is consistent with the averaged total filament area increase and thus indicates that multiple filament averaging does not substantially change the analysis.

Two error sources arise from the twist pitch of 23 mm in the ternary PIT wire. The first source is the projected area increase when a filament is at an angle with the SEM observed cross-

section. The maximum error occurs if the A15 area in the wire is determined from an outermost filament in the cross-section (i.e. at a radial position of about 420 μm). The area error for these filaments amounts to +0.27%. The second error source comes from the fact that filaments that are twisted become longer by a factor $(L^2 + (2\pi R)^2) / L$, where L and R represent the twist pitch and the radial filament position respectively. If volume is conserved this will reduce the effective diameter of the outermost filaments by –0.3%. Both error sources that originate from wire twisting are therefore insufficiently large to explain the observed differences between the wire and bare filament areas and this issue remains unresolved.

4.8.2 Composition analysis in bare filaments

Although in the previous Section it was shown that no A15 area gain is obtained, it is possible that the absence of the Cu matrix does influence the A15 composition. Compositional analysis using TSEM EDX was performed on the bare filaments that were reacted at 675 °C and 800 °C and these data were compared to the wire data to analyze whether compositional differences are present.

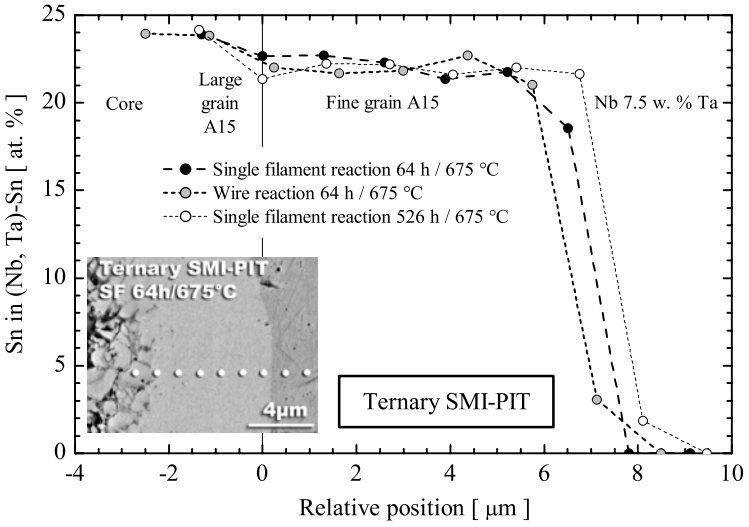

Figure 4.21 *Sn content versus radial position, measured using automatic TSEM EDX, for heat treated bare filaments and a filament heat treated in a wire.*

In Figure 4.21 a comparison is shown between the A15 composition of a filament reacted in a wire for 64 hours at 675 °C (filament 1 from Figure 4.12) and the A15 composition for bare filament reactions for 64 and 526 hours at 675 °C. The wire EDX spot positions are depicted in Figure 4.10, the 526 hours bare filament EDX spot positions are depicted in Figure 4.22 and the inset shows the EDX spot positions for the 64 hour bare filament reaction.

The variations in atomic Sn content in the A15 between the bare filament and wire reactions for 64 hours are comparable to the variations between various filaments inside the wire

(Figure 4.12). It has to be concluded therefore that both the wire and the individual filament A15 systems are comparable and that little change in A15 Sn content occurs by removal of the Cu matrix, although the integral amount of Sn that has diffused from the core is less in the individual filament as was shown in Figure 4.20. The data for the 526 hour bare filament reaction might be interpreted as showing slightly less gradient, but no clear argument can be made that this reaction indeed yields a more homogeneous A15 layer.

It can be concluded that the removal of the Cu matrix, within the accuracy of the EDX composition determination, does not change the A15 quality, even though it was concluded by Fischer [144] that for wires reactions beyond 128 hours at 675 °C some Sn is lost into the Cu matrix. In addition, it appears not possible to force the 6 at.% Sn that remains in the central residue of the core in the wire [144] into the A15 by using bare filament reactions. The volumetric differences between the wire and the individual filament analysis in Figure 4.20 rule out unambiguous statements on differences in A15 quantity. It is clear that in the wire 20% more A15 is formed. The origin of the observed lower filament and core diameters in the individual filaments as compared to filaments in wires, however, is not clarified.

The compositions of the core-A15 interface regions in the bare filaments were analyzed to investigate whether Fischer's conclusion that the diffusion in wires halts following Sn depletion of this area also remains valid in bare filaments. The overall TSEM EDX determined composition for a bare filament, reacted for 526 hours at 675 °C is shown in Figure 4.22.

The Sn content in Figure 4.22 indicates that up to about 6 μm into the core Sn is exhausted, indicating that the diffusion progress indeed stops due to Sn depletion of the core region close to the A15. In addition to this, it is interesting to observe that the A15 apparently prefers to be Sn rich, i.e. the A15 area does not increase at the cost of its Sn content.

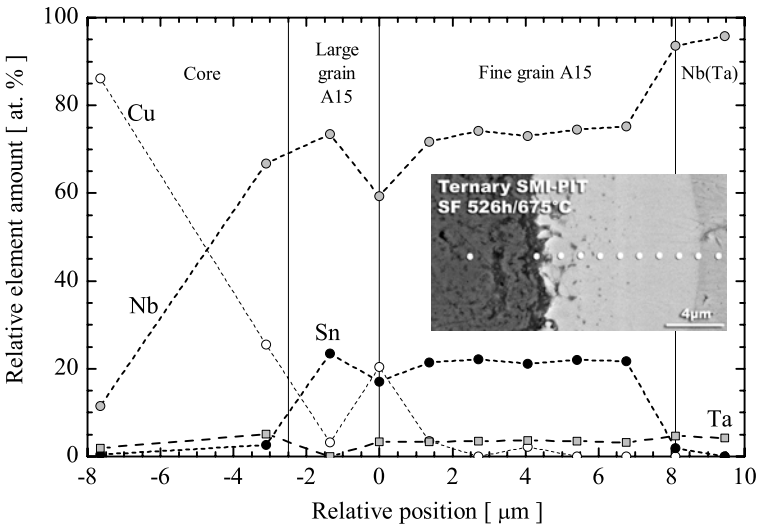

Figure 4.22 *Overall element ratios as function of radial position relative to the large- to fine grain interface for a single ternary SMI-PIT filament reacted for 526 hours at 675 °C.*

An important observation from Figure 4.22 is that there is no Cu present in the A15 layer further away from the core region, in contrast to the in-wire reaction, where about 3 to 5 at.% Cu is present in the whole Nb 7.5 w.% Ta tube (Figure 4.11). The detection of Cu in the wire is therefore likely to result from parasitic signals from the matrix Cu or overpolishing of the sample. Nevertheless, in the bare filaments no Cu is detected beyond the large grain region, whereas A15 is still formed at a low reaction temperature.

A TSEM EDX scan on a bare filament, reacted for 64 hours at 800 °C is depicted in Figure 4.23. No clear separation can be distinguished between large and fine grain A15, presumably since all is larger (about 400 nm, Figure 4.7) comparable grain A15 resulting from the higher reaction temperature. The position is therefore normalized to the A15-Nb 7.5 w.% Ta interface.

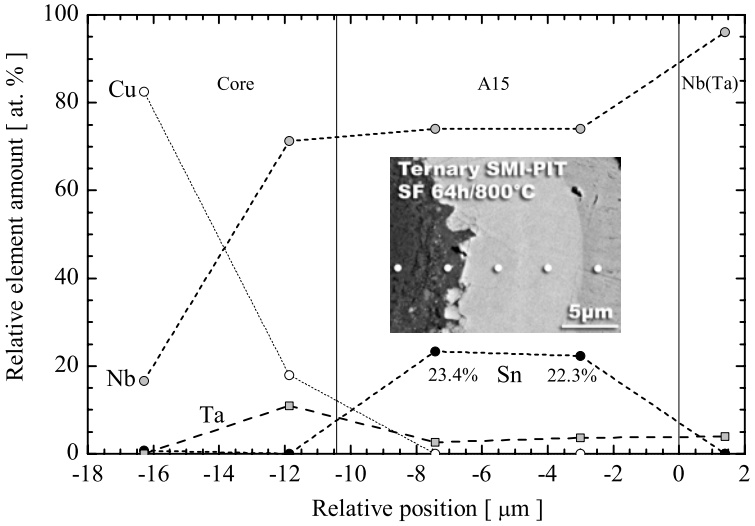

Figure 4.23 *Overall element ratios as function of radial position relative to the A15-Nb 7.5 w.% Ta interface for a bare filament reacted for 64 hours at 800 °C.*

Again, Sn depletion of the core-A15 interface region is visible. Also, no Cu was detected in the A15 region, whereas low temperature A15 formation still occurs. The Sn content in the A15 region of 23.4 and 22.3 at.% are comparable to the 675 °C reaction (Figure 4.21). As before, these values are most probably about 1.5 at.% lower than would be expected based on observable T_c values as a result from standardless EDX. This will be discussed further in Section 7.8.1. The observed Sn content indicates that also at elevated temperatures, thereby evoking a more rapid diffusion, it appears not possible to enrich the A15 in individual filament reactions. For wire heat treatments, a 5% increase in 12 K Kramer extrapolated upper critical field (Section 3.3) is observed for samples reacted at 800 °C compared to 675 °C, as was demonstrated by Fischer [144]. This indicates a slight enrichment of the A15 in wires when reacted at higher temperature. This is, within the accuracy of the EDX composition

determination, not observable in the individual reacted filaments. A visibly better connection between the core and the A15 in the 800 °C bare filament reaction, i.e. the absence of the gap that is observable in the 675 °C reactions does still result in a Sn depleted interface region.

4.9 Conclusions

The sample material was introduced and their microscopy morphology and chemical composition were discussed. This information will be referred to in the remainder of this thesis to explain the measured superconducting behavior of the wires.

In Section 4.4 the A15 grain sizes were analyzed in earlier and modern multifilamentary Nb_3Sn wires. It is concluded that the average grain sizes in modern wires are very comparable, independent of the manufacturing process and mainly depends on heat treatment temperature.

The automated TSEM EDX compositional characterizations in Section 4.7 were shown to be highly reproducible and they indicate low Sn gradients in PIT wires compared to bronze processed wires [135], in agreement with initial compositional analysis by Hawes *et al.* [64]. They are however, still significant, indicating possibilities for improvement regarding the A15 quality that is formed. Additionally it is concluded that this gradient is strikingly similar for all PIT wire types investigated. The use of uncalibrated EDX on two systems indicates identical Sn gradients in the same wire but an absolute difference of about 2 at.% Sn. The latter demonstrates the need for accurate calibration. This was not done within this work, but observed T_c values suggest that Sn contents from the TSEM and FESEM EDX systems have to be corrected by about +1.5 at.% and −0.5 at.% respectively as will be discussed in Section 7.8.1.

The solid-state diffusion reaction was analyzed using backscatter micrographs and EDX composition analysis. The progress of the reaction is clearly visualized by backscatter images and confirmed by the composition changes with reaction progress.

The bare filament reactions presented in Section 4.8 show that Sn loss into the Cu matrix is a negligible factor in halting the diffusion for longer reaction times. It is also concluded that the Cu matrix does not significantly influence the A15 quality with respect to Sn content, within the accuracy of the EDX composition analysis. The apparent earlier saturation in the bare filament reactions can be attributed to volumetric differences, resulting from the smaller effective filament and core diameters in the individual filaments in comparison to the in-wire filaments. It remains unclear why the observed differences in diameter occur. The latter renders solid conclusions with respect to differences in A15 quantity between wires and bare filaments unjustified.

The overall composition analysis for wires and bare filaments has learnt that the Cu that is detected throughout the A15 and Nb 7.5 w.% Ta tube for the in-wire reactions, is likely the result from spurious Cu signals. No Cu is detected throughout the bare filament A15 or Nb 7.5 w.% Ta. The latter raises the question why A15 can still be formed at a low reaction temperature, apparently without the presence of Cu.

The attempts to generate Sn richer and/or larger A15 regions by removal of the Cu matrix were not successful since the main origin for halting of the diffusion is Sn depletion at the core-A15 interface, in agreement with Fischer's conclusions based on wire analysis [144]. It is possible that the reaction occurs too fast with insufficient time for the Sn in the central regions of the core to diffuse to the A15 interface region, since the core is porous and connectivity is much worse than in the A15. A slower bare filament reaction at lower temperature would indicate

whether this indeed is true. As a side effect of this lower temperature heat treatment less grain growth would occur. This will also be beneficial for the current carrying possibilities.

A final remark is that the ternary PIT wire, as used for the bare filament reactions, was designed to hold high RRR, even at very long reaction times [235] even though, as Fischer has shown, Sn does poison the Cu matrix for very long reaction times. The suitability of bare filament reactions as a model system is, however, clearly established and future experiments on Sn richer wire layouts might be successful in achieving the generation of thicker, Sn richer A15 regions.

Chapter 5

Cryogenic Instruments for Conductor Characterization

The goals of this thesis require extensive experimental work to analyze the performance level of the present generation Nb_3Sn wires under various conditions. The superconducting to normal transitions were investigated using temperatures ranging from 1.4 to 20 K in background fields of 0 to 30 T, combined with axial strains ranging from –1 to +1% and transport currents from 0 to 1000 A. These conditions require highly specialized cryogenic equipment. A number of novel instruments have been developed specifically within the frame of this work to enable accurate investigations of Nb_3Sn over the entire spectrum. This Chapter describes their development and resulting instruments, which have also successfully been adapted for characterizations of High Temperature Superconductors and MgB_2.

5.1 Introduction

Three types of instruments can be distinguished. The first three instruments (Sections 5.2-5.4) were used to analyze the behavior of the critical current density versus field, temperature and applied axial strain by transport current-voltage characterizations. The second type (Section 5.5) was used to determine the field-temperature phase boundaries using low current resistive techniques. The last Section (5.6) gives a concise summary of the main parameters obtained with magnetic measurements on various samples.

The performance of the developed instruments was tested on a ∅ 0.8 mm Furukawa ternary bronze conductor (see Chapter 4). This wire was selected since it has highly reproducible properties and was extensively characterized at the University of Twente, as well as other laboratories around the world. It has become a reference sample for verification of device performance due to the available large critical current database and accurate parameterizations (Chapter 7).

5.2 Variable temperature critical current measurements

Determination of present conductor performances requires accurate measurement of the critical current with respect to field and temperature. For this purpose a new insert was developed that fits in a superconducting solenoid with a cold bore of ∅ 60 mm.

5.2.1 Helical sample holders

The insert is based on the standardized wire holders used for the world wide conductor benchmark for the International Thermonuclear Energy Reactor (ITER). A schematic of this so- called ITER barrel is depicted in Figure 5.1.

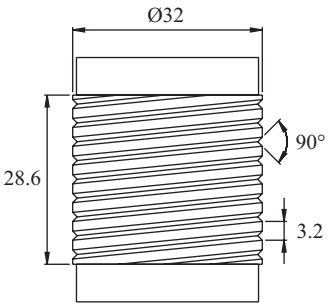

Figure 5.1 *The standard Ti-6Al-4V helical sample holder.*

The barrel is a grooved Ti-6Al-4V cylinder, on which a wire can be spiraled with a pitch of 3.2 mm. At both ends a copper ring is mounted, for soldering a connection to the wire. In this way approximately 1 m of wire is mounted of which about 0.5 m is available for voltage measurement due to current entrance effects at both wire ends. Voltages have to be measured where the current is uniform at some distance from the current terminals. A required voltage resolution of about 10^{-6} V/m, combined with 1000 A transport current results in a current transfer length of about 50 mm to be respected [236]. The applied magnetic field is parallel to the axis of the barrel. The current is not perfectly perpendicular to the magnetic field, but angular effects are negligible for small angles between the field and the wire axis [237]. The

material choice for the ITER barrel is Ti-6Al-4V since it is non-magnetic and matches the thermal contraction of Nb_3Sn.

5.2.2 Self-field correction

The self field, generated by the wire in its helical shape has to be taken into account for measurements at lower fields and higher currents. The complex layout of modern twisted multi-filamentary wires complicates exact calculations of the self-field. The effect can be approximated to be only a function of filamentary area diameter (Chapter 4) by calculating the field that is generated on the outermost filament region in a barrel configuration. One side of the filament area will thus see a maximum field which is equal to the applied field plus the generated self field. The outer filaments in a wire will be exposed to this maximum field periodically since the filaments in wires are twisted. These filaments will experience the first onset of normal conducting behavior. Such an approximation has been described in the literature to be valid for coiled wires with a large spacing between the turns [238]. Using an approximation for an infinitely long, straight conductor:

$$H_{\text{Peak}} = H_{\text{Applied}} + \frac{I}{\pi d_{\text{fil. A}}}, \tag{5.1}$$

in which I is the transport current and $d_{\text{fil. A}}$ is the filament area diameter, yields a self-field correction of about 0.8 T/kA for a ∅ 0.5 mm filamentary region. A more accurate calculation which takes into account the helical wire geometry on ITER barrels was performed numerically by den Ouden [239]. This results in self-field corrections that are lowered with respect to the infinite straight wire approximation.

Table 5.1 *Self-field corrections for wire samples mounted on the ITER helical sample holder as depicted in Figure 5.1. Courtesy of A. den Ouden.*

Filament area diameter [mm]	1	0.9	0.8	0.6
Self field correction [T/kA]	0.305	0.353	0.399	0.563

5.2.3 Sample preparation

The large amount of critical current characterizations performed at the University of Twente has developed an optimized barrel preparation method, which is schematically depicted in Figure 5.2. A sample holder is prepared by oxidizing the outer Ti-6Al-4V surface to prevent sintering of the wire to the holder. The test wire is wound on the barrel with a tension of 10 N and fixed by bolts in the copper end-rings at each end. Excess wire is folded back along the first turn to shunt the current entrance region. The holder plus wire is heat treated in a vacuum furnace. Sample manipulations after reaction are kept to a minimum. The wire ends are soldered to the copper end-rings with Sn-5 w.% Ag after which the holder is cleaned. The sample is fixed to the holder with Stycast®2850FT epoxy. Excess epoxy is wiped off to maximize heat transfer from the wire to the Helium. The finished sample is shown in Figure 5.2(d).

The typical reproducibility in measured critical currents that can be achieved with this preparation method, using various samples that are reacted together is depicted in Table 5.2.

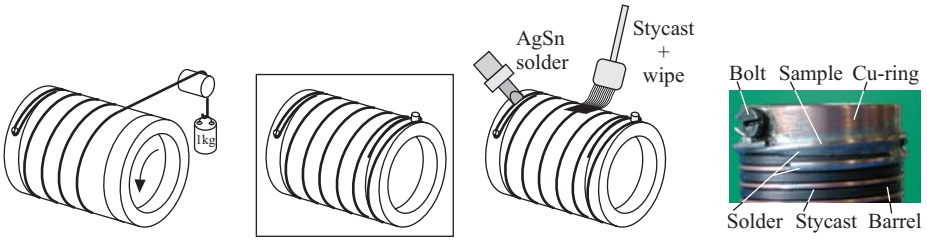

a) Controlled sample coiling b) Heat treatment c) Post reaction fix d) Finished sample

Figure 5.2 *Preparation method for helical wire samples.*

Sample number	I_c, 12 T, 4.2 K, 10^{-5} V/m [A]	n-value [-]
1	117.6	35
2	118.3	34
3	118.6	34
4	117.5	35
Average	118.0	
Max. rel. error [%]	0.5	

Table 5.2 *Reproducibility of critical current measurements on a helical sample holder.*

These data were measured on a ∅ 0.8 mm Furukawa ternary bronze wire which was reacted for 240 hours at 650 °C. The reproducibility at 12 T and 4.2 K is very good and the critical current data fall within 1% over 4 specimens.

5.2.4 Variable temperature

Elevated temperatures above liquid Helium temperatures can be achieved either by pressurizing the Helium bath, or by creating a Helium gas or vacuum volume as thermal insulator to the liquid. The latter becomes preferable above about 5 K since the former requires substantial pressures for higher temperatures, thereby placing very high demands on the cryostat construction. The main problem with variable temperature critical current measurements in Helium gas or vacuum at currents beyond e.g. 100 A, is heating due to the large current in the resistive sections of the probe and heating of the sample during measurement of a voltage-current transition. This will result in an undesired drift in the temperature.

A Helium gas flow cryostat is not suitable for high critical current measurements at accurately stabilized elevated temperatures. This is due to its slow thermal response time, which does not allow rapid corrections for resistive heating. A second alternative route using a vacuum as thermal insulator has proven to work, but is limited in current to about 200 A at temperatures above 4.2 K [240]. A third method that uses a cold Helium gas volume is claimed to retain stable elevated temperatures up to 500 A but results in a complicated probe design [230].

A new method was developed at the University of Twente by which the sample holder is covered by a polyimide insulator cup to create a Helium gas environment around the sample [241]. A schematic view is given in Figure 5.3. The helical holder is clamped between two copper terminals, using a bolted copper tension rod, which simultaneously acts as current path

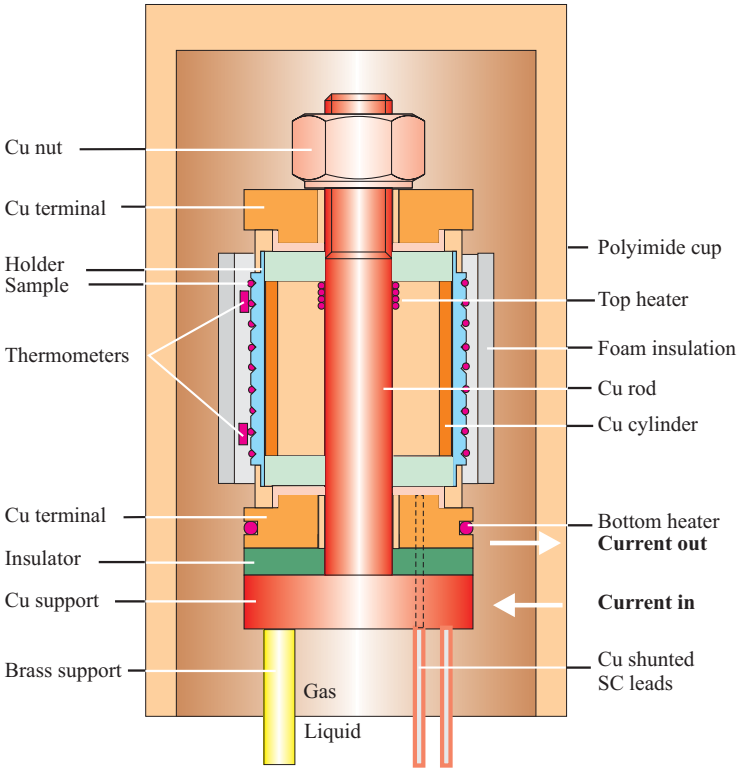

Figure 5.3 *Schematic representation of the variable temperature $J_c(H)$ probe.*

and cooling path through the shunted superconducting leads and brass support. The bottom copper terminal and the copper rod are equipped with heaters. In this way, two-sided cooling and heating is achieved that can be balanced by variation of the power distribution between both heaters. The sample is surrounded by Neoprene foam to prevent local convection cooling and thermometers are mounted directly on the sample. A copper cylinder is inserted in the sample holder to further homogenize the temperature along the sample. The entire system is accessed from the bottom, which enables covering the device with a polyimide thermal insulating cup to create a volume filled with Helium gas for temperatures above 4.2 K. The sample temperature is regulated by one of the thermometers using a PID temperature control system.

The thermal response time of the system is small enough to enable rapid regulation in heating power during measurement of a voltage-current transition. Critical currents exceeding 600 A have been measured at elevated temperatures in a Helium gas environment using this method. The temperature variation during a measurement can be kept below 50 mK.

5.2.5 Compensation for parasitic current

The accurate determination of properties of the superconducting regions inside multi-filamentary wires should preferably not be influenced by the specific measurement technique, or by the matrix surrounding the filaments. Critical current data, resulting from the ITER barrel characterization method, therefore have to be corrected for parasitic currents in the normal conducting regions parallel to the superconductor.

A typical set of voltage-current transitions as measured with the variable temperature critical current probe is depicted in Figure 5.4 on a $^{10}\log(E)$-$^{10}\log(I)$ scale. At low currents the uncorrected transitions display curvature for high electric field levels. This curvature originates from currents that run parallel to the superconducting current at any given electric field level and is therefore a parasitic addition to the superconducting to normal transition of the A15 in the wire caused by the finite resistivity of the A15 during a transition. The measurement errors caused by the parasitic current become relatively larger for smaller currents and higher voltage criteria. At $E_c = 10^{-5}$ V/m the corrections are negligible, but at higher criteria they become substantial, e.g. 20% for the 12 T, 11 K data at $E_c = 10^{-4}$ V/m.

The normal state resistivity of the wire and holder as function of magnetic field was determined by raising the temperature above the critical temperature. The resulting resistivities were translated to parallel resistive currents that were subtracted from the total current to yield the actual current in the superconductor. From the corrected data points in Figure 5.4 it is seen that

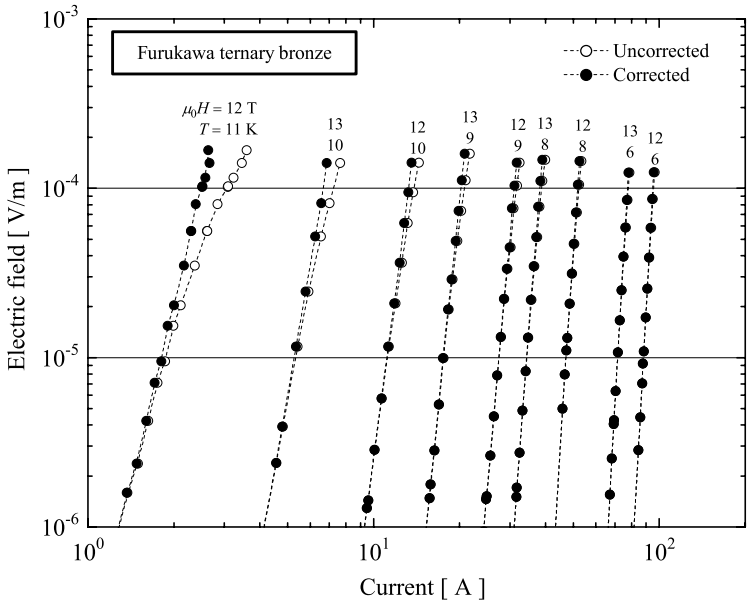

Figure 5.4 *Electric field versus transport current at various magnetic field and temperature combinations. Corrections are applied to voltage-current transitions for ohmic currents that run parallel to the superconducting current in the matrix and helical sample holder, resulting in a linearization of the log(E) - log(I) transitions.*

the transitions become linear on a $\log(E) - \log(I)$ scale. This shows that a power-law dependence as given by (3.3) is a good description for voltage-current transitions of multifilamentary Nb_3Sn wires.

5.2.6 Critical current and n-value

The main parameter of interest in superconducting wires is the critical current density, generally specified as the maximum amount of current that flows in the non-copper cross-section of the wires, since this allows for direct quality comparisons. The critical current has to be derived from the measured voltage-current transition to arrive at a critical current density for the wire under investigation. A critical current is mostly defined either using a resistive criterion, in which a certain resistivity level is defined as the critical state, or an electric field criterion. The latter is used throughout this thesis to derive the critical current of a sample from measured voltage-current transitions.

A typical set of transitions, corrected for self-field and the parallel resistive currents as described in the previous Sections, is shown in Figure 5.5 for a ∅ 0.8 mm Furukawa ternary bronze wire which was reacted for 240 hours at 650 °C. The transitions were measured on the variable temperature $J_c(H)$ probe as described in Section 5.2.4 and given at various combinations of temperature and magnetic field. The critical electric field level was defined as

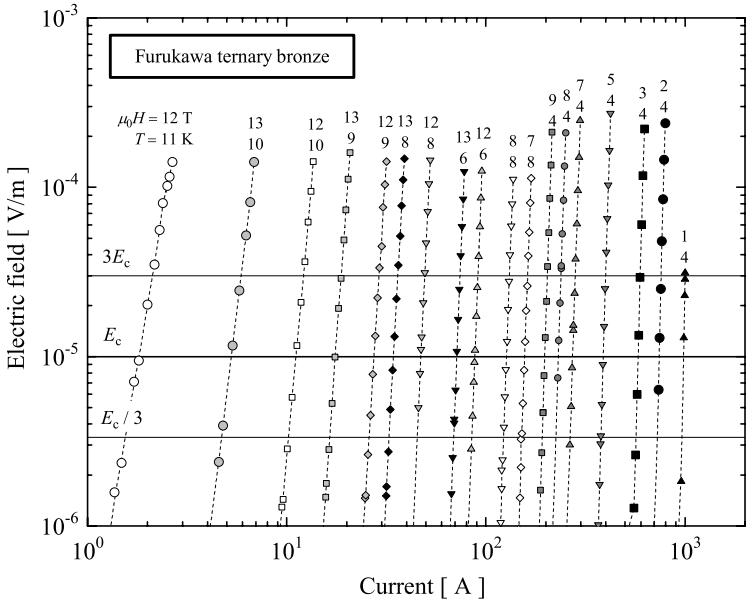

Figure 5.5 *Electric field versus current at various temperatures and applied magnetic fields. The data have been corrected for self-field and for parallel resistive current, resulting in perfectly straight log(E) versus log(I) behavior. Indicated are the electric field criterion and a window ($3E_c$-E_c / 3) where the log(E) - log(I) data are fitted to a line in order to calculate the average intersection with E_c and the n-value at this criterion.*

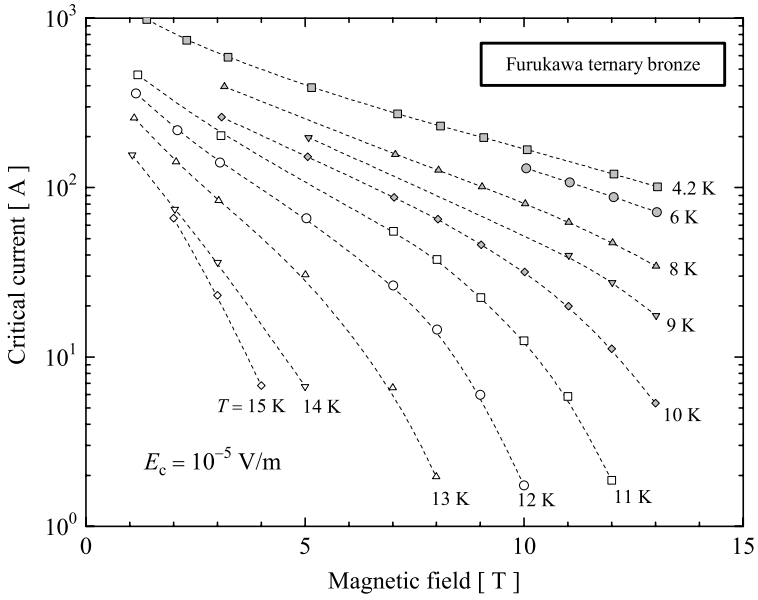

Figure 5.6 *Typical critical current versus magnetic field behavior at various temperatures as measured on the $J_c(H,T)$ probe.*

$E_c = 10^{-5}$ V/m. All points within a window ranging from $E_c / 3$ to $3E_c$ were approximated by the linear fit $\log(E / E_c) = n \times \log(I / I_c)$. This allows calculation of the average intersection with E_c, resulting in I_c at 10^{-5} V/m and the corresponding n-value.

The resulting critical current values, at various fields and temperatures are plotted in Figure 5.6. The linearity of the transitions in Figure 5.5 combined with the smooth data sets in Figure 5.6 indicate reliable behavior of the variable temperature $J_c(H)$ insert.

5.3 Critical current versus strain on U-shaped bending springs

Lorentz loads in practical applications cause strain and consequently the critical parameters are affected. Knowledge of the influence of strain on the critical field, temperature and current in technological superconductors is therefore of major importance. Three principal approaches to characterize the critical parameters versus axial strain can be distinguished.

In the first method a force is applied to a free hanging sample, with strain as a resulting parameter [198, 242–245]. The sample length is limited by the homogeneous field region (usually a few cm) and the sample shape is simple. Care has to be taken to support the sample against Lorentz forces and to avoid local strain concentrations. The main advantages of this method are that stress can be easily obtained in combination with strain and that the initial thermal pre-compression originating from the matrix in composite conductors can be measured. However, the technologically very important compressive strain regime cannot be attained.

In the second method, a sample is mounted on a spiraled substrate material by soldering it either along its entire length [246, 247] or only at the ends [247, 248]. The main advantage of this so-called Walters spring is that the sample length can be long (about 1 m), but the device is relatively complicated. The sample is well supported and can also be brought into the compressive regime when soldered to the substrate along its entire length. Stress-strain characterizations are possible with the Walter spring design [249]. The thermal pre-compression in composite conductors can be obtained through an initial measurement with only the ends connected to the substrate [247]. Temperature variations can be applied using a Helium gas flow cryostat or by placing the sample in a vacuum can. Care has to be taken to avoid thermal runaway during the voltage-current transitions caused by a slow response time in the temperature regulating system. This drawback can limit the attainable critical current values at elevated temperatures. The literature mentions an initial limit of about 85 A [246], which has recently been improved to about 200 A by careful optimization of resistive probe sections [240].

The third method is based on a straight beam section that is part of a U-shaped bending spring [111, 149, 250]. This method has been applied at the University of Twente for more than a decade to analyze axial strain dependencies in various superconductors. Several versions have been developed, ranging from small cross-section beams for the characterization of tape conductors to larger cross-section beams for the measurement of wires [149]. The sample layout is simple; it is well supported and homogeneously loaded. The sample length is limited to the magnet bore. The compressive strain regime is easily accessible due to the rigid connection to the substrate. The latter additionally results in a very high reproducibility in the measurements. In principle it could be possible, using the same method as for the spiraled substrates [247], to determine the intrinsic pre-strain in composite conductors through a preceding cool down cycle with only the sample ends soldered to the substrate. This has, however, never been tested. Sample stress is not attainable with the U-spring method.

The large quantity of samples that has been characterized successfully with U-springs and the consistency of the data with published results obtained with other methods, indicate that it is a proper and convenient method for the determination of the $J_c(H,T,\varepsilon_{axial})$ behavior of superconductors. The U-spring method is adapted throughout this thesis for the strain analysis of the critical parameters. A new version was designed which specifically allows for temperature variation and has improved mechanical properties compared to earlier versions through the application of Ti-6Al-4V as substrate material.

5.3.1 Design of a Ti-6Al-4V U-spring

The substrate material of earlier U-spring designs was brass. A major drawback of the use of brass is that the sample is initially in a large axial compressive strain state, enforced by the high thermal contraction of the brass. If the central region is strained, its overall axial strain state will become smaller, resulting in a rise in critical current density. The unstrained outer regions remain, however, in a compressed state with the result that the current has to pass this degraded region before it enters the section that is under investigation. This means that current redistributions will occur, resulting in undesired voltages which are detected by the voltage taps while the investigated region is still completely superconducting. This effect can be a substantial source of errors and will result in an early voltage rise and nonlinearities in the $\log(E)$ - $\log(I)$ plots showing the transitions. This makes the curves not representative for the actual critical state of the area under investigation. A substrate constructed from Ti-6Al-4V will minimize this problem, since its thermal contraction matches the contraction of Nb_3Sn, resulting

in a starting situation which has the wire close to its maximum properties. A second disadvantage of brass is its low elastic strain limit of about 0.35%. It was tried to overcome this relatively low limit and the resulting neutral line shift. When actually measuring the strain with two strain gauges the strain can be controlled even in the plastic regime [251]. Operation beyond its elastic limit followed by a return to zero applied axial strain, however, results in an elongated substrate and thus an unknown shift in the zero-strain state of the sample.

The above drawbacks of brass as a substrate material triggered the development of a new Ti-6Al-4V version, which has a larger elastic strain limit of about 1.2%. This is higher than any realistic axial strain state in composite Nb_3Sn wires and thus sufficient. A problem with this alloy is that Titanium oxides prevent low temperature soldering. This can be overcome by vacuum brazing a thin (0.2 mm) copper buffer layer to the substrate with 72 w.% Ag-28 w.% Cu solder at 1140 K, which is well below the $(\alpha+\beta) \rightarrow \beta / (\alpha+\beta)$ phase transition temperature of Ti-6Al-4V at 1260 K. Samples can then be soldered onto this copper buffer layer with regular Sn-5 w.% Ag solder at about 500 K [163].

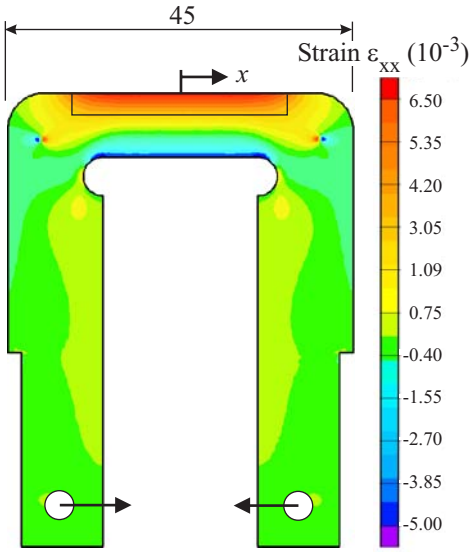

Figure 5.7 *Finite element calculated strain profiles of the U-shaped bending spring. The strain is homogeneous within 0.01% over a central region of about 18 mm length.*

Finite element calculations of the mechanical behavior of the Ti-6Al-4V U-spring designed for this thesis work is depicted in Figure 5.7. The requirement to comply with the bore of a ∅ 60 mm superconducting solenoid and the space needed for the optional polyimide insulator cup yields about 45 mm available beam length. A central section of about 18 mm is strained homogeneously. Outside this region the current path changes from perpendicular to the applied field to parallel to the applied field. This causes a redistribution of the current over the cross-section of the conductor. The length needed for full current redistribution depends on specific details of individual conductors and the transport current density. Redistribution does further limit the effective gauge length below the 18 mm homogeneously strained section to an effective 2 to 5 mm length for voltage-current measurement.

5.3.2 Variable temperature

Force is applied to the legs of the Ti-6Al-4V U-spring by an H-shaped device, as depicted in Figure 5.8. The legs of the strain device are operated by an opposite-threaded rod and a worm-gear combination. This allows operating the device with the sample in the upper position.

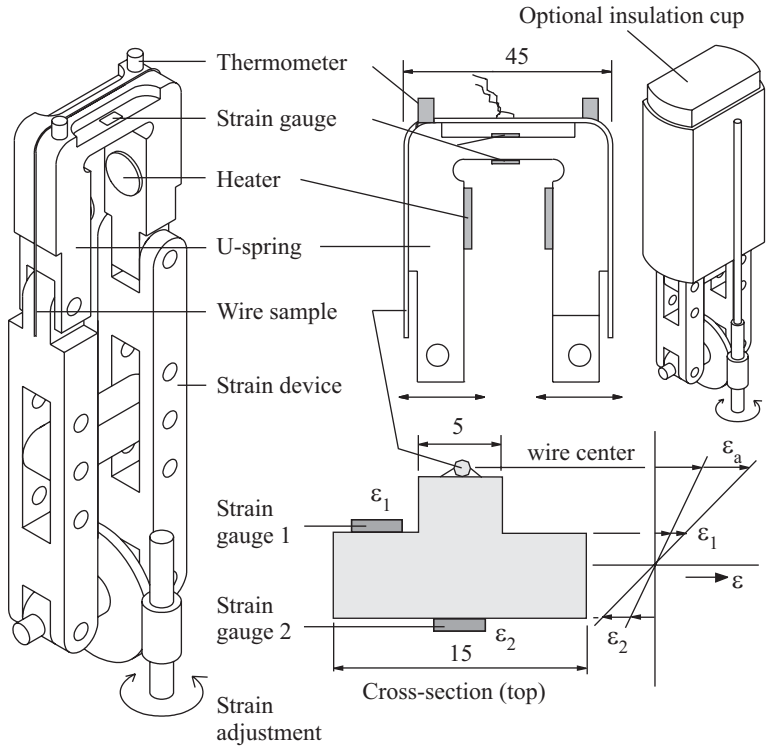

Figure 5.8 *The U-shaped bending spring instrument which was developed to characterize $J_c(H,T,\varepsilon)$ behavior of multi-filamentary Nb_3Sn wires. Strain is adjusted by rotation of a worm-gear set, which turns a left- and right-threaded rod that pushes the legs of the strain device apart. The strain device legs rotate around two fixed points and move the legs of the U-shaped bending spring. The entire device can be covered with a polyimide insulator cup to create a Helium gas volume in which the temperature can be regulated via a set of heaters and thermometers. Two strain gauges are used that enable extrapolation of the measured strains at the gauge positions to the central wire axis.*

Data at temperatures above 4.2 K can also be obtained by placing the instrument under a polyimide insulator cup, thus creating a helium gas volume, in the same way as described in Section 5.2.4 for the variable temperature barrel measurements. Cooling and heating paths on the U-spring are symmetrical. Two thermometers are used so that temperature gradients over the sample can be measured and minimized. The heating power is regulated and, due to the

short thermal response time (on the order of 1 second), it is possible to compensate for dissipation in the sample itself during the measurement of a voltage-current transition. Using this method, critical currents exceeding 600 A have been measured at temperatures above 4.2 K in a helium gas environment.

5.3.3 Voltage-current transitions measured on a Ti-6Al-4V U-spring

A typical set of transitions, measured on the variable temperature strain insert, is plotted in Figure 5.9 for an applied strain of 0% (top) and +0.4% (bottom). The results were measured on a ∅ 0.8 mm Furukawa ternary bronze wire that was reacted for 240 hours at 650 °C. The

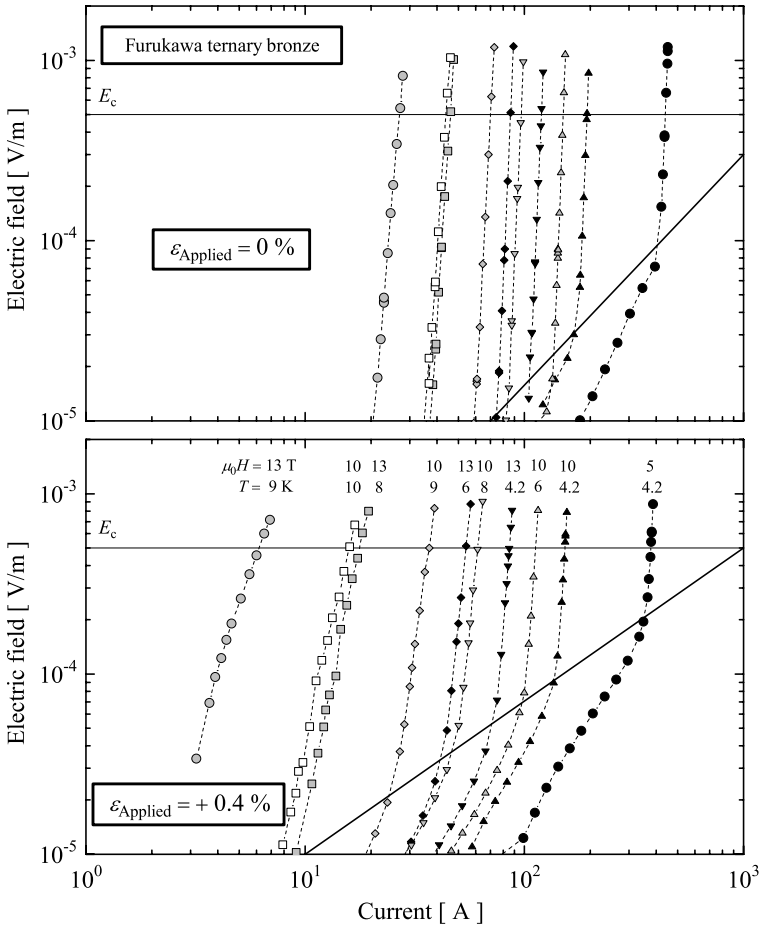

Figure 5.9 *Voltage–current transitions at various temperatures and fields on a ∅0.8 mm Furukawa ternary bronze wire soldered to a Ti-6Al-4V U-spring. Increasing the applied strain from 0% (top) to +0.4% (bottom) reduces the critical current, as is indicated by a shift of the E(I) transitions to lower currents.*

sample was soldered to the substrate at about 500 K using Sn-5 w.% Ag and cooled down without initial strain application. Voltage-current transitions are presented for a selected range of field and temperature combinations. The application of +0.4% strain results in a shift of the transitions towards lower current values, combined with a reduced steepness of the transitions (presumably due to a broadening of the property distribution).

For higher currents non-linear tails can be observed at low electric field levels in the otherwise

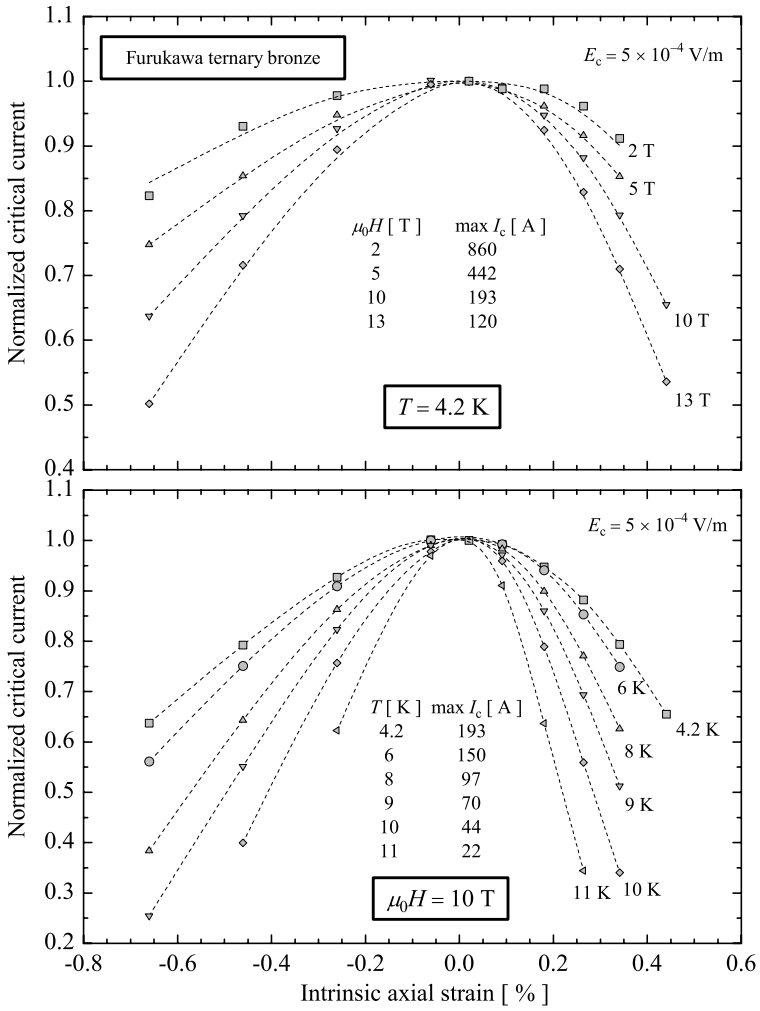

Figure 5.10 *Typical normalized critical current versus axial strain data, measured on a Furukawa ∅0.8 mm ternary bronze wire soldered to the Ti-6Al-4V U-spring. The critical current criterion is $E_c = 5 \times 10^{-4}$ V/m. Strain dependencies have been analyzed in fields ranging from 2 to 13 T and temperatures ranging from 4.2 K up to the critical temperature.*

linear log(E) - log(I) transitions. Earlier measurements with multiple voltage tap pairs showed that such tails increase to higher electric field levels if the voltage tap separation is increased, indicating that they originate from current redistribution effects. After application of +0.4% strain the tails become much more pronounced. They can therefore possibly be attributed to an increase in current redistribution originating from crack formation in the A15 at high tensile strains, which were recently revealed by metallographic analysis on deformed wires [252]. A similar conclusion has been stated recently from high resolution $E(J)$ characterizations on a Walters spring [249].

Without sufficient low-voltage resolution (due to the short length between the voltage taps) no unambiguous conclusions can be drawn, however, and the tail effects (the regions under the bold lines in Figure 5.9) have to be considered unreliable since they possibly originate from measurement errors. Therefore the critical current and n-value analysis have to be confined to a higher electric field criterion. At the level of 5×10^{-4} V/m no tail effects are present and critical current and n-values can reliably be extracted. This criterion is therefore adapted in the strain sensitivity measurements on U-spring devices.

5.3.4 Critical current versus strain

A typical set of results of critical current versus field, temperature and strain is presented in Figure 5.10. Part of the results is derived from the transitions in Figure 5.9. The indicated axial strain is relative to the applied strain that results in a maximum critical current. The applied strain which results in maximum critical current is the axial thermal pre-compression that is present in the wire after cool down (soldered to Ti-6Al-4V) which is –0.06%. The sum of the external applied strain and thermal pre-compression is referred to as the intrinsic axial strain, or the actual strain that is present in the superconducting filaments. The critical currents have been normalized to the value at 0% intrinsic axial strain.

The sensitivity for axial strain is increasing with magnetic field (above) and this elevated strain sensitivity also appears at elevated temperatures (below). The increased noise in the 2 T, 4.2 K results is due to the heating effects at high currents complicating accurate voltage-current measurements.

5.4 Long samples on a circular bending spring

All the strain dependency data presented in this thesis were characterized on U-shaped bending springs at an electric field criterion of $E_c = 5 \times 10^{-4}$ V/m, measured across 2 to 5 mm of sample located centrally in the strained section of 18 mm. The large number of experiments performed has highlighted the device specific complications as described in the previous Section. The distance between the voltage taps (2 to 5 mm) on the U-shape holder is also smaller than the filamentary twist pitches, which are typically about 5 to 10 mm for Nb_3Sn wire conductors. This is undesirable since macroscopic conductor properties over multiple twist pitches (which are characteristic for applications) might be different from the behavior within one twist pitch.

The above arguments have led to the design of a new instrument that combines the advantages of the U-spring device (simple sample layout, a substrate solder mounting method and the possibility to create a fast response variable temperature system) with a longer sample length. The design of this new instrument and its initial results are the subject of the next Section.

5.4.1 Design of a circular bending beam

The required increase in available sample length is achieved by changing the shape from a straight beam section whose length is limited to the magnet bore diameter, to a curved beam, limited by the magnet bore circumference. The design is based on the mechanical principle that when a pure torque is applied to the ends of a circular beam section (Figure 5.11a-*a*), the beam diameter changes but its shape remains a perfect circle (Figure 5.11a-*b*). If a conductor is connected to the outer perimeter it will be strained due to the change of the outer circumference.

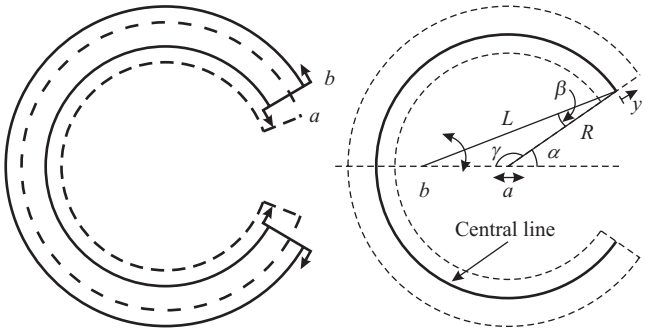

Figure 5.11 *(a) Design of a circular beam, longer-length strain device and (b) determination of the offset of a fixed rotation point with respect to the center line of the beam. Offsetting the rotational point with respect to the beam center is required for homogeneous deformation of the beam.*

The torque is transferred from room temperature into the low temperature region by two concentric tubes. When transferring the applied torque from this concentric tubing to the beam by torque transfer arms that rotate around a fixed point, it is necessary to offset this point with respect to the centre of the central line circumference. Without this offset, the beam shape would not remain perfectly circular, since this would require the length of the transfer arm to change. This is schematically depicted in Figure 5.11b, where *a* is the centre of the circular beam, *b* is the fixed centre of rotation and *L* is a torque transfer arm which rotates around the fixed point *b*, causing the beam centre *a* to shift in the depicted direction. *R* is the radius of the central line that changes with application of torque, α is half the opening angle of the beam, β is a fixed angle between the torque transfer arm *L* and the beam and γ is the polar angle. Using the boundary condition that *L* and β are constant, β can be derived by requiring $dL / d\gamma = 0 \; \forall \gamma$ at a given angle β:

$$\tan\beta = \frac{\sin^2\gamma}{\gamma + \sin\gamma\cos\gamma}, \tag{5.2}$$

and for distance $a - b$:

$$a - b = \frac{R}{\sin(\gamma + \beta)} \sin \beta \,, \tag{5.3}$$

yielding the distance $(a - b)$ between the fixed rotation point and the beam centre at a given opening angle α and radius R.

5.4.2 Model calculations on a circular bending beam

The practical shape of the circular bending beam is presented in Figure 5.12. The new device is named 'Pacman', for obvious reasons. The property that torque can be shifted in the plane of application was used to arrive at this shape. In this way the torque application points were transferred to four pins that rotate with respect to each other and are connected to holes in the torque transfer arms of the Pacman. The initial shift between the centre of rotation b and the beam centre a was determined to be 1.61 mm for the specific beam cross-section and planar shape with an initial opening angle of 30°. The final shape was optimized with Finite Element Modeling (FEM), resulting in simulations shown in Figure 5.12 for an angular strain $\varepsilon_{\Theta\Theta} = -0.7\%$ at the outer circumference (which has a neutral diameter of 36 mm). The maximum shift of the beam in the radial direction is located at the surface at $x = 0$ and amounts to 1 mm at −0.7% applied strain, which is small enough for a sample to remain in constant applied magnetic field. It can be seen that the simulated strain pattern is perfectly homogeneous around the circumference and only starts to deviate very close to the connection to the torque transfer arms.

In addition to the FEM simulations, the strain of Figure 5.11a can be solved analytically using

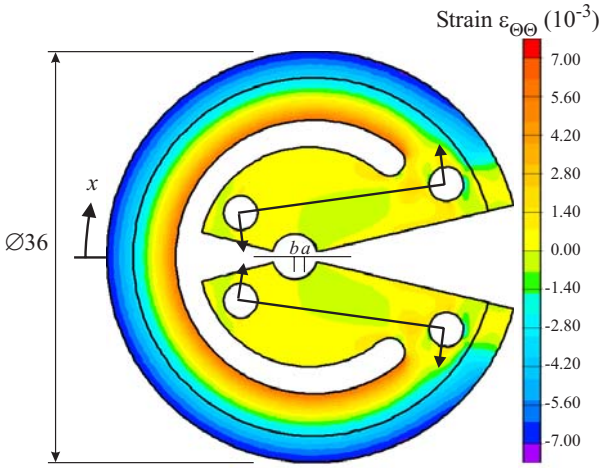

Figure 5.12 *Finite element simulations on the practical planar shape of the Pacman. Application of pure torque on the Pacman as indicated by the arrows makes the initial curved beam change its diameter but it remains a perfect circle, resulting in a homogeneous strain around its outer circumference.*

Winkler's theory of initially curved beams [253], which is valid if the beam thickness is small compared to the initial radius of the central line. The theory states that:

$$E\varepsilon_{xx} = \frac{M}{AR_0}\left[1 + \frac{R_0^2 y}{h^2\left(R_0 + y\right)}\right], \tag{5.4}$$

where ε_{xx} is the strain at a radial distance y from the central line, R_0 is the initial radius of the central line, A is the beam cross-sectional area, M is the applied torque, E is the Young's modulus of the spring and h^2 is a beam-shape factor defined by:

$$h^2 = \frac{1}{A}\int \frac{R_0 y^2}{R_0 + y} dA\,, \tag{5.5}$$

which results in 2.15 mm^2 for the chosen beam cross-section. The position of the central line is defined by the usual $\int y dA = 0$. This analytical approach results in the same strain profiles as the FEM simulations, validating the geometry of the Pacman.

In Figure 5.13 the FEM simulated surface strains are plotted as function of position in the x-direction for both the Pacman and the U-spring. The length gain in the Pacman is obvious. The region over which the surface strain homogeneity $\Delta\varepsilon = \pm 0.01\%$ is about 78 mm for the Pacman, compared to about 18 mm on the U-spring. The total sample length on the Pacman is about 104 mm, so an additional 13 mm is available for current redistribution at either end of the homogeneously strained zone. Experience with the U-spring has indicated that current redistribution occurs over distances of 20 to 30 mm per side for technical Nb_3Sn wires (details depend on the used sample material), meaning that effectively about 50 mm sample length is

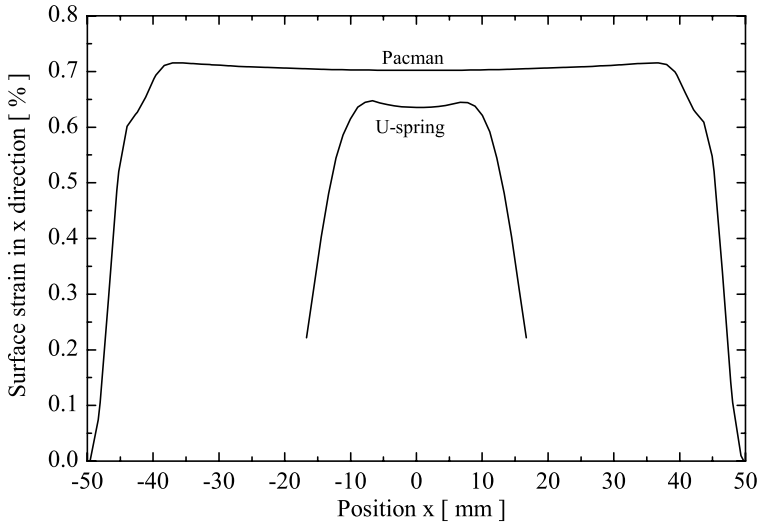

Figure 5.13 *Strain along the sample mounting surfaces of the Pacman in comparison with the U-spring as simulated by finite element calculations. The region with a homogeneous strain within ±0.01% is about 78 mm on the Pacman, compared to about 18 mm on the U-spring.*

available on a Pacman with a initial outer diameter of 36 mm. This is at least a factor 10 larger than the central 2 to 5 mm that can typically be used on the U-spring.

Extensive mechanical calibrations at low temperature [254] have confirmed the strain homogeneities on the Pacman outer perimeter as predicted by the FEM and analytical calculations, as well as the position of the central line and predicted strain profiles over the beam cross-section indicating consistent, predictable behavior.

5.4.3 Practical design of a circular bending beam

For the practical shape of the beam cross-section, a T-shape as shown in Figure 5.14, similar to that of the original Walters spring [248] and the wire U-springs was chosen, since it has advantages over a rectangular cross-section. To reduce the strain gradient that inevitably occurs across the sample section, the beam height has to be large in comparison to the sample thickness. The T-shape reduces the torque needed to achieve a given deformation, while retaining as much height as possible. Furthermore, it shifts the central line causing the largest strains to appear only at the sample position. Since the strain gradient over an initially curved beam cross-section is non-linear, the exact T-dimensions can be refined to further reduce the gradient across the wire section. Besides, this cross-section allows mounting of strain gauges on the plateau of the T, to verify the modeled strain gradients over the beam. The dimensions depicted in Figure 5.14 result from an optimization between the required torque and acceptable strain gradients over a typical wire sample. The torque that is needed to achieve 1% axial strain in the centre of a ∅ 1 mm wire using a Ti-6Al-4V alloy Pacman amounts to $M = 28.6$ Nm, using a Young's modules $E = 119$ GN/m^2 for the Pacman.

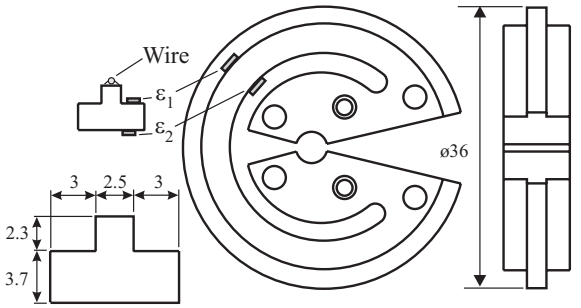

Figure 5.14 *Final shape of the Pacman device, equipped with 2 strain gauges to verify its elastic behavior and to calculate the axial strain in the sample center. The indicated dimensions are in mm.*

In Figure 5.15 the practical implementation of the complete instrument is shown. Two concentric tubes are used. One is fixed and the second transfers a rotation, induced by a worm-gear combination at room temperature, down to the low-temperature region. The rotation is transferred to two blocks which are connected to a concentric stainless steel tube and rod which move up again and in turn drive two half cylindrical shapes. The torque is transferred to the Pacman by four pins. Stable elevated temperatures can be obtained by placing a polyimide insulator cup over the device, which creates a helium gas volume around the Pacman.

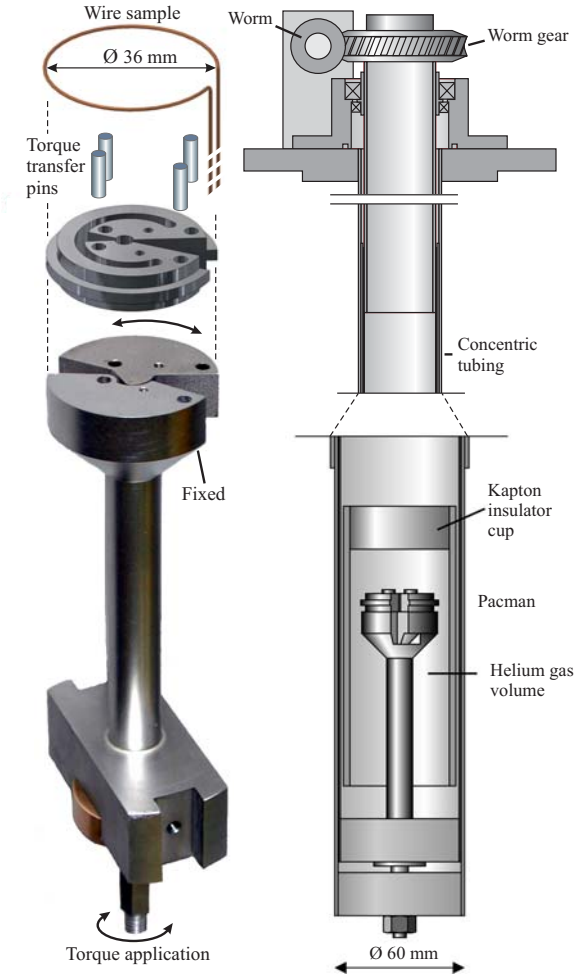

Figure 5.15 *Practical implementation of the Pacman strain device.*

5.4.4 First test on a circular bending beam

Test measurements were performed on the ∅ 0.8 mm Furukawa ternary bronze conductor, heat treated for 240 hours at 650 °C to verify the applicability of the new device. The sample was not reacted together with the other Furukawa wires throughout this thesis, but in a separate heat treatment run at the University of Geneva. As will be discussed below and in Chapter 7, this can result in slightly different properties for description of the observed behavior with scaling relations for the critical current density. The wire was tested on the new Pacman device at $\mu_0 H = 12$ T and $T = 4.2$ K. Selected voltage-current transitions are plotted for various applied strain values in Figure 5.16. A damaged spot in the wire, originating from post reaction

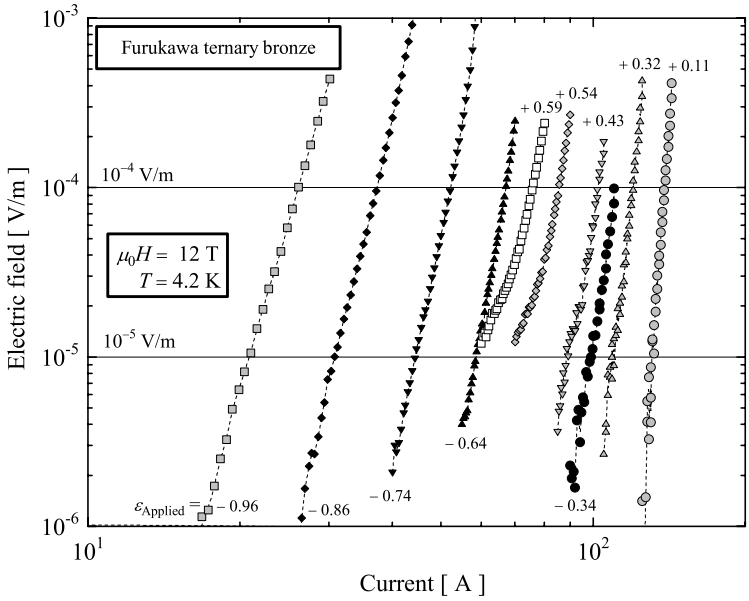

Figure 5.16 *First measurements of electric field versus current at various strain values across 27 mm length on a ∅0.8 mm Furukawa ternary bronze wire at $\mu_0 H = 12$ T and $T = 4.2$ K.*

mishandling, only allowed for 27 mm sample length between the voltage taps to be investigated.

In comparison to the U-spring data (Figure 5.9) the enhanced sample length results in a) at least one decade more electric field resolution which allows the use of criteria that are comparable to the barrel data; b) perfectly straight log(E) - log(I) behavior for higher current transitions that showed non-linear tail effects on the U-spring; c) a clear deviation from perfect linearity for applied axial strains above about +0.4%, confirming the earlier suggestion that tails can be attributed to crack formation in the A15 at high tensile strain. The latter should be investigated more thoroughly using a more focused measurements combined with metallographic analysis. It can be concluded that the enhanced resolution allows for a separation between device originated non-linearities, which are basically a measurement error and non-linearities that originate from changes in the sample.

In Figure 5.17 a comparison is made between $J_c(\varepsilon_{applied})$ results that have been measured on the Ti-alloy U-spring and on the new Ti-alloy Pacman device. Since the results were not recorded at identical applied field values, a comparison is included using the scaling relations as described in Chapter 3 and Chapter 7 (with (3.44) to describe the strain sensitivity), that are known to describe the $J_c(H,T,\varepsilon_{applied})$ data for the Furukawa wire within a typical standard deviation of 2% [157]. The parameters yielding the calculated lines are given in Table 5.3. Of these parameters, only C_a (which describes the strain sensitivity), δ (the matrix induced thermal pre-compression of the A15) and C (the overall pre-constant to scale the critical current density) were variable in the least squares fitting procedure. The remaining parameters are identical to

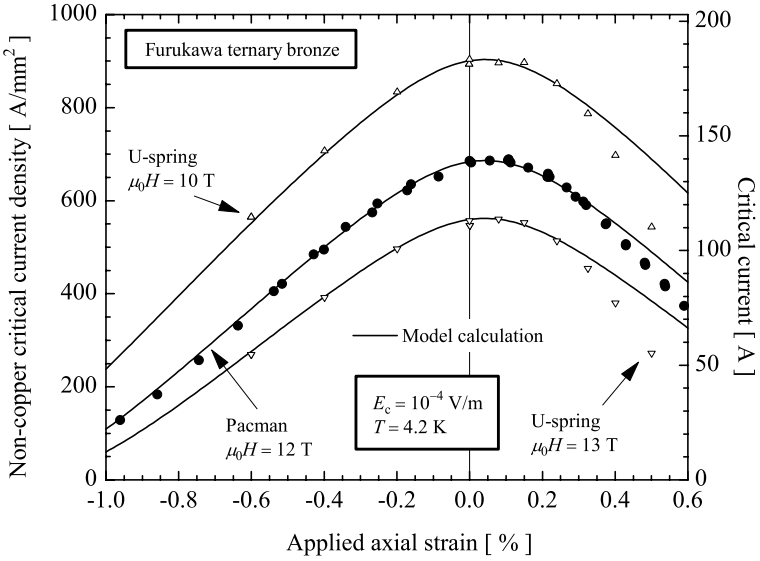

Figure 5.17 *A comparison between critical current versus strain data as measured on the U-spring and Pacman devices, both at a criterion of $E_c = 10^{-4}$ V/m.*

earlier U-spring analysis on this wire [163]. The motivation to allow C_a in the model fit to change is the more extensive strain range that was characterized with the Pacman. The additional experimental data between −1% and −0.6% strain show slightly increased strain sensitivity, compared to the value found on the basis of measurements with the U-spring, in which the data were limited to −0.6% axial strain. The thermal pre-compression was allowed to change because of the higher quality of the new data around the maximum in the strain dependency curve, which justifies a more accurate determination of the thermal pre-compression. The resulting value for the thermal pre-compression at $T = 4.2$ K in the A15 for a Furukawa wire that is soldered at about 500 K on the Ti-alloy ($\delta = -0.042\%$) is relatively close to the value $\delta = -0.06\%$ which was found based on the U-spring data alone.

An accurate fit to the Pacman data could, however, not be found without allowing the overall pre-constant to be slightly different between the samples measured on the U-spring and the Pacman. The wire section measured on the Pacman was heat treated about 7 years after the section of the same production batch that was characterized on the U-spring, using a different furnace in a different institute. Small differences in heat treatment temperatures or ramp rates

Table 5.3 *Model parameters for inter-comparison of U-spring and Pacman data on Furukawa ternary bronze wires.*

Holder	$\mu_0 H_{Km}$(0 K) [T]	T_{cm}(0 T) [K]	ε_{0a} [%]	C_a	δ [%]	C [kAT/mm^2]
U-spring	32.87	17.25	0.247	*43.5*	*-0.042*	*43.9*
Pacman						45.4

could easily account for the observed 3.4% increase in J_c, by the formation of a 3.4% larger A15 cross-section area (corresponding to a 1.8% thicker A15 layer) in the filaments. Although unfortunate, the pre-constant influences only quantitatively the comparison. It is therefore concluded that the $J_c(\varepsilon)$ characterizations on the Pacman yield improved results compared to characterizations on the U-spring device with an enhanced electric field resolution.

It is interesting to note that deviations from symmetrical, elastic behavior as indicated by the model calculations start to occur at +0.35% applied axial strain. This corresponds to the strain value for which deviations from linear behavior start to appear in the log(E) - log(I) transitions as measured on the Pacman device (Figure 5.16). It may be that these deviations from elastic model calculations originate from crack formation in the A15 layer. This was also emphasized in a recent presentation by Uglietti *et al.* [249], who concluded that irreversibility at large tensile strain depends on the applied electric field criterion, since non-linearities due to crack formation are enhanced at low electric field criteria.

5.5 Variable temperature, high magnetic field resistivity probes

Earlier investigations on the field-temperature phase boundary of selected filamentary Nb_3Sn conductors by magnetic techniques up to $\mu_0 H = 14$ T have indicated substantial differences between the phase boundary that is representative for the transport current properties and the upper critical field [144, 232]. These differences were attributed to compositional inhomogeneities that are present in the A15 layers in technical Nb_3Sn wires. To extend this research to the complete field-temperature range that is relevant for Nb_3Sn superconductors and to accurately identify the field-temperature phase boundary, a new characterization system was developed that is usable in very high field resistive magnet systems.

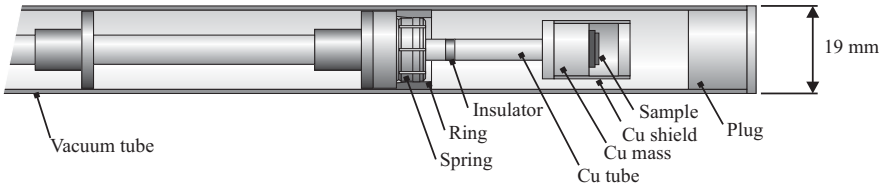

Figure 5.18 *Variable temperature probe for resistive characterizations of the field-temperature phase transitions.*

A resistive technique was chosen since this method is consistent with transport critical current characterizations. A new probe has been built specifically for the purpose of measuring sensitive $\rho(H,T)$ transitions in superconducting magnets up to 15 T at the Applied Superconductivity Center of the University of Wisconsin-Madison (UW-ASC) and very high field resistive magnets at the National High Magnetic Field Laboratory (NHMFL) in Tallahassee, FL. The design, shown in Figure 5.18, is optimized to have a homogeneous temperature across a substrate and its samples. It consists of a stainless steel vacuum tube of 19 mm diameter with a soldered plug at the cold end and a vacuum seal at room temperature to avoid vacuum leaks at low temperature. A copper mass on a copper tube containing a thermal resistance can be inserted and the cold end is clamped with a spring inside a ring that is soldered to the wall of the tube, thus forming a 4.2 K point. The copper mass forms a thermal dead end

such that temperature gradients are avoided by cooling and heating from the same side. A copper shield having the same temperature as the copper substrate holder surrounds the samples to prevent radiation heat loss. A wire heater is wound around the copper tube, and a thermometer is placed on the substrate, directly next to the sample set. Signal wires arriving from room temperature are thermally anchored at the 4.2 K point and again at the elevated temperature Cu tube. A small amount of exchange gas was needed to reach temperatures just above $T = 4.2$ K. This was caused by insufficient thermal conduction at the circular spring to ring connection which should create the 4.2 K buffer point. Later incarnations were designed with a threaded connection to increase thermal conduction in this area.

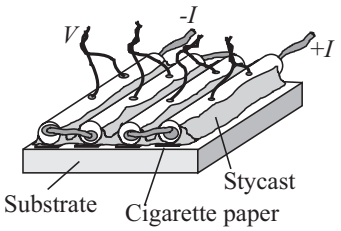

Figure 5.19 *Sample mounting technique for resistive field-temperature characterizations. The samples are glued with cryogenic epoxy onto a substrate material to attempt to mount them in a undefined but reproducible strain state. The samples are insulated from the substrate with cigarette paper. Voltage and current contacts are soldered as indicated.*

The samples used for the resistivity characterizations were wire sections of about 8 mm length, which were glued onto a substrate with cryogenic epoxy in an attempt to force the samples in a fixed, reproducible pre-strain. The wires were insulated from the substrate by cigarette paper (Figure 5.19). Current contacts were soldered to the wire ends and voltage taps were soldered about 1 to 3 mm apart in the wire center. A Cernox® thermometer was glued with G.E. Varnish® directly next to the wires on the substrate. All signal wires were thermally decoupled from room temperature and from the cold end. Care was taken to avoid signal wire movements, especially during measurements at very high field in resistive magnets. Temperatures registered above 4.2 K were corrected for the known small magneto-resistance of Cernox® thermometers [255]. Temperatures at helium bath and below were calibrated at zero fields and then regulated by bath pressure.

As a first step, $\rho(T)|_H$ characterizations were performed with a slow ramping temperature ($dT / dt = 3$ mK/s) at the UW-ASC to test the new probe. Heating followed by cooling cycles showed, within the noise, no hysteretic behavior; an indication for the absence of any gradients in temperature. The majority of the field-temperature investigations in this thesis were performed by small current density (generally 0.2 to 0.6 A/mm^2) resistive characterizations at constant temperature ($\rho(H)|_T$) and a slow ramping field ($d\mu_0 H / dt = 10$ mT/s). Typical variations in temperature during a constant temperature sweep ranged from ± 5 mK in the best case to ± 50 mK in the worst case. The $\rho(H)|_T$ characterizations were confirmed to deliver the same $H_{c2}(T)$ data as the swept temperature characterizations. Data for fields ranging from 12 to 30 T were taken at the NHMFL using a resistive high field magnet and data up to 15 T were obtained using a superconducting solenoid at the UW-ASC.

A typical set of transitions as measured with the resistivity probe on a ∅ 0.8 mm Furukawa ternary bronze wire, glued with cryogenic epoxy onto a Ti-6Al-4V substrate and on a brass substrate, is shown in Figure 5.20. The data at $T = 11.2$ K in the left plot were measured in a superconducting solenoid at the UW-ASC. The noise in the $\rho(H)|_T$ transitions as measured at

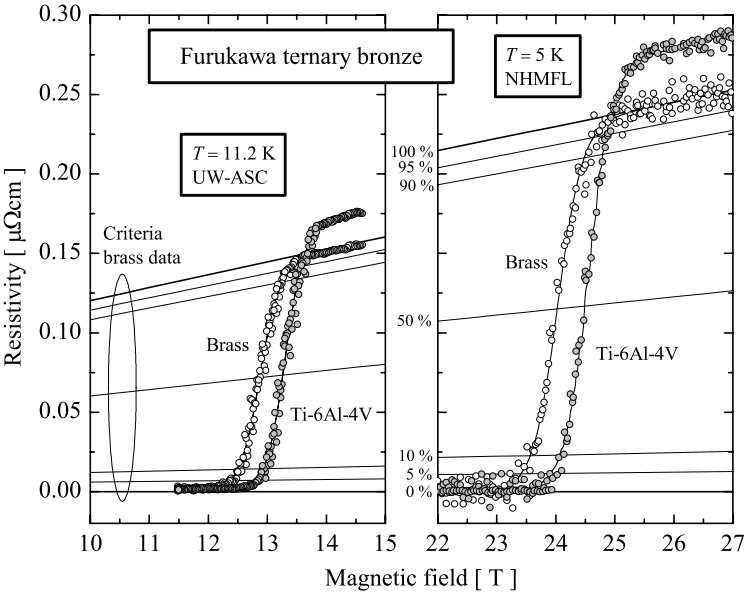

Figure 5.20 *Resistivity as function of magnetic field for a ∅0.8 mm Furukawa ternary bronze wire at T = 11.2 K, measured at UW-ASC (left) and T = 5 K, measured at the NHMFL (right) using the resistivity probe from Figure 5.18.*

the UW-ASC was increased in comparison to a $\rho(T)|_H$ transition, since it is much easier to keep the applied magnetic field constant than to fix an arbitrary temperature. In the data in the right plot, measured at the NHMFL for $T = 5$ K, the noise is additionally increased by the background noise of the very high current, low inductance resistive magnet.

The lines through the data points are least squares fits using a shifted and normalized tangent hyperbolic function, multiplied by a polynomial term that describes the magneto-resistance:

$$\rho(H) = \frac{\exp\left[4e\times\left(\frac{\mu_0 H - \mu_0 H_{½}}{\mu_0 H_{\mathrm{W}}}\right)\right]}{\exp\left[4e\times\left(\frac{\mu_0 H - \mu_0 H_{½}}{\mu_0 H_{\mathrm{W}}}\right)\right]+1}\times\left(\frac{\rho(0)+C_1\mu_0 H + C_2\mu_0 H^2}{1+C_3\mu_0 H}\right), \qquad (5.6)$$

in which H represents the applied magnetic field, $H_{½}$ is the applied field at half the transition height, H_{W} is the transition width, $\rho(0)$ is the zero field normal state resistivity and C_{1-3} are constants. The lines indicated by 'criteria brass data' represent depicted percentages of the normal state magneto-resistivity of the Furukawa sample that was mounted on a brass substrate and were used to calculate $H_{c2}(T)$ using e.g. a 90% normal state criterion. A clear difference is observed between samples that are mounted with cryogenic epoxy on a brass substrate or on a Ti-6Al-4V substrate. The differences in magnetic field values are due to differences in strain states caused by the different thermal contractions of Brass (–0.35%) compared to Ti-6Al-4V

(–0.18%), emphasizing the need to fix the samples rigidly. The difference in absolute resistivity value for the brass mounted wire in comparison to the Ti-6Al-4V mounted wire is due to inaccuracies in voltage tap length determination. This inaccuracy results from the use of solder connections of about 0.5 mm in diameter in relation to a tap separation of 1 to 3 mm and can be as large as 30%.

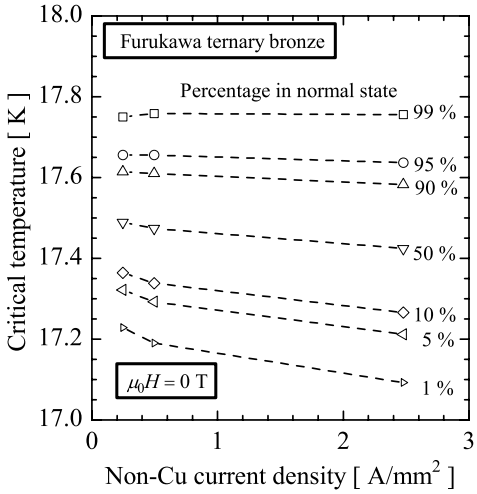

Figure 5.21 *Dependence of the detected zero field critical temperature on the excitation current density and applied resistivity criterion.*

The influence of the excitation current on the transition widths has been investigated using the $\rho(T)|_{H=0}$ characterizations. It was found that the width of the transition broadens with increased excitation current, but that the upper shelf (i.e. above 90% normal state) is independent of excitation current density as is shown in Figure 5.21. This results in only the upper shelf criteria (90 to 99%) being independent of the excitation current density. It is assumed that this observation holds for the $\rho(H)|_T$ characterizations since a higher excitation current density will result in the detection of a larger distribution in $H_{c2}(T)$ as more of the lesser quality A15 will be probed. In resistive analysis this dependence has to be taken into account, rather than using an arbitrary criterion (e.g. at 50% of the transition) at an arbitrary current. The majority of the detected distributions range from 10% and 90% normal state, as indicated in Figure 5.20. The upper shelves of the transitions (i.e. 90 to 99%) are interesting since they represent the best A15 sections that are detected in the samples. Magnetic characterizations on similar samples have indicated that magnetically determined $H_{c2}(T)$ using the onset of superconducting behavior as criterion (Section 5.6.1), approximately correspond to the onset of superconductivity (i.e. a 99% normal state criterion) in the resistive transitions, as will be shown in Section 6.4. Additional measurements of the transition were performed using a cantilever magnetometer and excellent agreement was found between the magnetization discontinuity at H_{c2} and the 99% resistive transition [262].

The low-noise threshold in the low-field measurements (up to 15 T) allows using any transition criterion and the resistivity description follows the data points across the full transition. Higher noise levels at high field call into question the validity of transition criteria above 90%. A

criterion of 99% at high field can, however, be found by interpolation of the resistivity fit over data from 10% to 90% and the normal state, assuming similar transitional behavior as in the lower field range where the fit is valid. Derivation of the 99% points in this way enables objective identification of the upper limit of the property distributions also at fields approaching 30 T, if the uncertainty that will occur through interpolations using the resistivity function, which is on the order of a few tenths of a Tesla, is accepted.

A systematic inconsistency of about 4% exists between the NHMFL and UW-ASC datasets for some of the investigated conductors. Temperature measurements in both institutes were confirmed to be correct and the same probe was used in both systems. The magnets in both institutes were recalibrated but no errors were detected. The ∅ 0.8 mm Furukawa sample has been re-measured in a different resistive magnet over the full temperature range at the NHMFL. These results average out the jump that was initially visible between the separate low- and high field datasets. An additional error source might be that the strain changes with thermal cycling, despite the attempts to force the samples into a reproducible strain state. An axial strain difference of 0.06% could result in the observed 4% inconsistency [111]. No corrections are made on the data sets since no unambiguous error source could be found and the resistively derived field-temperature data should therefore be regarded to be reliable within ± 2%.

A disadvantage of resistive characterizations is that only part of the full property distributions is detected, due to relatively low excitation current densities. In some conductor layouts such as the Powder-in-Tube design where the highest T_c component of the A15 layer is on the inside, magnetic shielding does not occur and the T_c gradient across the A15 layer can be directly observed with magnetic characterizations [64, 65] (Section 5.6.2). It will be shown in Section 6.4 that indeed magnetic analysis of Powder-in-Tube wires results in the detection of a much broader property distribution than the small current resistive technique. A second disadvantage is that the normal state signal of the wires typically was only on the order of 200 nV at zero magnetic field, whereas the background noise in the high field resistive magnet area is typically 50 to 150 nV. The strong magneto-resistance of the wires fortunately delivered an enhanced factor 4 to 10 in signal at high field due to increased resistivity, enabling the measurements. A great advantage of the resistive technique is, however, that it is possible to characterize multiple samples at once, saving valuable high field magnet time and enabling therefore the analysis of a significantly larger sample set than would have been possible using magnetic techniques.

5.6 Magnetic characterizations

The majority of the field-temperature analysis in this thesis was performed using transport measurement techniques since they correlate directly to the main parameter of interest, i.e. the transport critical current density. However, since the conclusions should not rely on a single characterization technique and since some aspects, as for example compositional inhomogeneities, are better visualized by alternative methods, also a number of magnetic investigations were made on selected samples. These were performed in commercial instruments, namely an Oxford Instruments 14 T Vibrating Sample Magnetometer and a 5.5 T Quantum Design Superconducting Quantum Interface Device (SQUID) magnetometer. In Sections 5.6.1 and 5.6.2 typical results, measured using these apparatus will be shown as well as the way in which the relevant parameters were derived from these results.

5.6.1 Vibrating Sample Magnetometer

A typical characterization, as performed with an Oxford Instruments 14 T Vibrating Sample Magnetometer (VSM) on a ∅ 0.8 mm Furukawa ternary bronze wire with the applied field parallel to the wire axis is depicted in Figure 5.22. Such a plot is obtained by registering the magnetic moment during a stable temperature applied field ramp at $d\mu_0 H / dt|_{T=12\text{K}} = 10$ mT/s using $\mu_0 H_{\text{Applied}} = 0 \rightarrow 14 \rightarrow 0$ T, combined with accurate offset subtraction. The first visible deviation of the acquired data from reversible linear magnetization is defined as $H_{c2}(12\text{ K})$, as depicted in Figure 5.22. In the magnetic moment versus field signal the irreversibility field (i.e. the field value at which bulk pinning disappears resulting in reversible magnetic behavior) can be distinguished as the loop closure point $H_{\text{LC}}(12\text{ K})$. A possibly more accurate determination of this point can be achieved when $(\Delta m)^{1/2}(\mu_0 H)^{1/4}$ is plotted against $\mu_0 H$, resulting in a Kramer plot (see Section 3.3) which can be linearly extrapolated to $\Delta m = 0$ to derive the loop closure magnetic field, or more strictly $H_{\text{K}}(12\text{ K})$. This extrapolation does, however, assume the bulk pinning force to be proportional to $(1 - h)^2$, in which $h = H / H_{c2}$. The fact that Kramer plots of magnetic data on Nb_3Sn conductors at various reaction stages are perfectly linear for practically observed grain sizes [144, 137] supports this assumption. The non-zero $(\Delta m)^{1/2}(\mu_0 H)^{1/4}$ data points in Figure 5.22 above $H_{\text{K}}(12\text{ K})$ result from residual uncertainty in offset signal subtraction and magnetic moment registration.

The main advantages of VSM characterizations are the large number of data points and their accuracy, combined with a high sample throughput in comparison to transport current

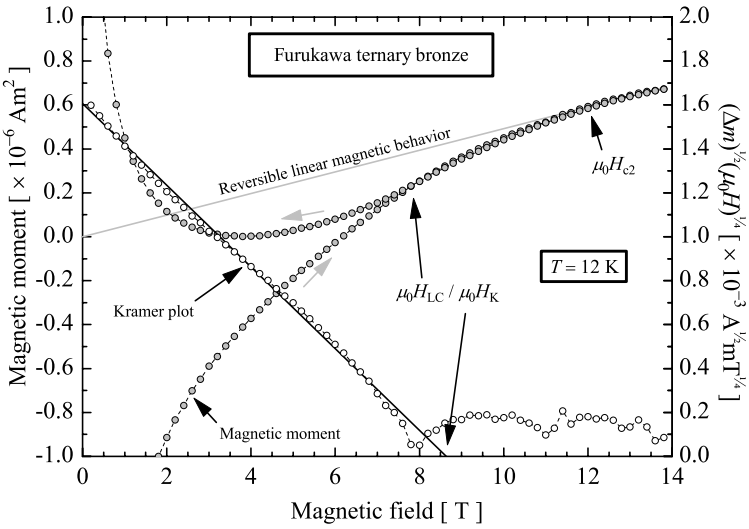

Figure 5.22 *Magnetic moment as function of magnetic field, measured using a Vibrating Sample Magnetometer (VSM) on a Furukawa bronze wire with an Oxford Instruments 14 T VSM at T = 12 K. The applied field direction is parallel to the wire axis. The loop closure field and the upper critical field can be derived from the magnetic moment data. Additionally, $(\Delta m)^{1/2}(\mu_0 H)^{1/4}$ is shown against $\mu_0 H$, resulting in a Kramer plot which can be linearly extrapolated to $\Delta m = 0$ to derive a Kramer extrapolated critical field.*

measurements. This enables rapid analysis of heat treatment variations on technological superconducting wires, as was strikingly demonstrated by Fischer *et al.* [144, 232]. In analyzing the results, however, the possibility of shielding of lesser A15 regions by higher quality A15 has to be considered. This is especially true for the Furukawa wire, which has tin rich A15 regions surrounding the tin poorer A15 areas (Section 4.3.1). In the Powder-in-Tube wires this effect is virtually absent since the higher tin regions are located at the inner perimeter. Such an absence of shielding effects enables correlations between the magnetic signals and radial A15 property distributions as was demonstrated recently [197]. A second disadvantage is the circular current path which is perpendicular to the normally measured longitudinal transport current direction. This can result in different critical current values derived from the magnetic moment signal as was recognized by Fischer [144], who found magnetically determined critical current densities to be about 20% below values determined in transport measurements.

5.6.2 Superconducting Quantum Interference Device Magnetometer

The normalized magnetic moment versus temperature plot in Figure 5.23, measured in a 5.5 T Quantum Design SQUID magnetometer, demonstrates the specific ability of this instrument to scan the critical temperature distribution of a wire which has the higher tin regions located at the inner perimeter. For the demonstration of a typical critical temperature distribution measurement a switch is made from the 'standard' Furukawa sample to a ternary Powder-in-Tube filament. The magnetic shielding that occurs in bronze route produced wires through the presence of tin richer A15 at the outer filament perimeter (Section 4.3.1) prohibits proper magnetic property distribution analysis[1]. A SEM cross-section of the measured Powder-in-Tube filament is depicted in the inset in Figure 5.23. The filament was heat treated for 527 hours at 675 °C. The generated A15 region is almost perfectly cylindrical and the analyses in Section 4.8.2 have indicated that the tin rich regions are located at the inner perimeter that surrounds the core. It was shown there that the tin content becomes gradually lower, starting from the core-A15 interface, until a steep fall-off occurs at the A15-Nb 7.5w.% Ta interface.

The normalized magnetic moment versus temperature was obtained by zero magnetic field cooling of the filament to T = 5 K, followed by application of a 5 mT field parallel to the filament axis to introduce shielding currents and raising the temperature while registering the magnetic moment. At 5 K full flux exclusion from the whole Nb filament cross-section can be observed. Just before 8 K the Nb 7.5 w.% Ta tube goes normal at temperatures somewhat below the pure Nb transition of 9.2 K. From around 16 K to 17.5 K the A15 transition of interest occurs, indicating that the tin poor outer perimeter region has a critical temperature of about 16 K and the tin rich inner perimeters have critical temperatures around 17 to 17.5 K.

Since identical transitions will be used in Chapter 6 to analyze reaction progression in Powder-in-Tube systems, a method was developed to retrieve a more objective determination of critical temperature values from the measured transitions. The A15 transition in Figure 5.23 is least squares fitted for temperatures above 10 K to a function similar to that used for the $\rho(H)|_T$ analysis (equation (5.6)), but which takes into account asymmetry in the transition [256]:

1 *Strictly speaking this also holds for the VSM characterization method. Although the full critical state is established also in bronze processed wires, less detail can be extracted from the results.*

$$\rho(T) = \left[\left(1 + \frac{L_0 W_0}{T_{c1} - T_{c0}} + \frac{L_1 W_1}{T_{c0} - T_{c1}} \right) - 2 \right] \times SC,$$

$$\text{with: } L_0 = \ln\left[2\cosh\left(\frac{T - T_{c0}}{W_0} \right) \right], \tag{5.7}$$

$$L_1 = \ln\left[2\cosh\left(\frac{T - T_{c1}}{W_1} \right) \right],$$

$$SC = \frac{C_1 + C_2 T + C_3 T^2}{1 + C_4 T},$$

in which T_{c1} is representative of the high temperature onset of the A15 transition using W_1 to define the curvature and T_{c0} and W_0 have similar meaning for the low temperature offset in the A15 transition. The *SC* polynomial part of the function uses C_{1-4} as fitting constants to define a fully superconducting state for the A15 transition for temperatures above 10 K, as represented by the bold 0% line in Figure 5.23. The bold line through the A15 data points is calculated using equation (5.7). The lines at 10, 50 and 90% now represent intersections that can be made on the A15 transition to define critical temperatures at a given percentage of the A15 in the normal state, resulting in e.g. $T_{c-10\%}$ through $T_{c-90\%}$.

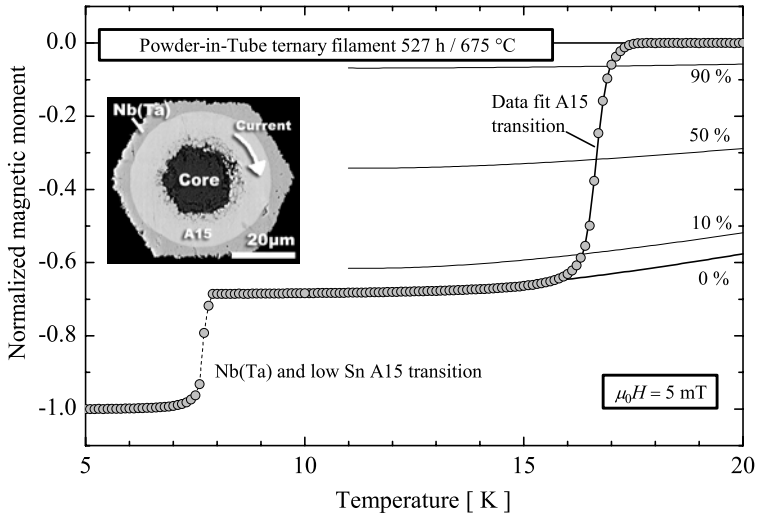

Figure 5.23 *Normalized magnetic moment versus temperature data, measured with a SQUID magnetometer on a SMI ternary Powder-in-Tube filament, heat treated for 527 hours at 675 °C with the applied field parallel to the filament axis. The inset shows a Scanning Electron Microscope cross-section of the measured filament.*

5.7 Summary

Multiple novel cryogenic analysis systems have been developed that enable accurate identification of the superconducting to normal transition of technical Nb_3Sn superconductors. Considerable progress is reported on existing measurement techniques and new methods have been developed.

More specifically, standard barrel techniques have been inverted to enable covering with a polyimide insulator cup to create a Helium gas volume (Section 5.2.4). This has been shown to be a convenient way to achieve variable temperature critical current measurements. The linearity in the resulting double logarithmic $E(J)$ transitions indicates thermally stable operation even at high current, low field and high temperature combinations.

The switch from brass to Ti-6Al-4V in the U-spring critical current versus strain system (Section 5.3.1) solves many experimental problems which were identified in the brass U-spring systems. Also the U-spring system has been inverted and was equipped with a polyimide insulating cup to achieve elevated temperatures (Section 5.3.2). This has resulted in the possibility to measure unprecedented high critical currents at elevated temperatures (beyond 600 A) on a variable temperature strain rig (Section 5.3.4).

The main disadvantage of the U-spring strain dependency measurement method, the limited available sample length, has been bypassed by a new circular bending beam (Section 5.4.4). Although the majority of the strain data in this thesis was characterized using U-spring systems, the length gain in the new Pacman device yields high resolution $E(J)$ transitions.

A new developed resistivity probe for insertion in resistive magnets that create very high magnetic background fields has proven to yield accurate resistivity data, even at the combination of very low normal state resistivity and the relatively noisy environment of a high current Bitter magnet. The possibility to investigate multiple samples in one run enables a large throughput and efficient use of limited high magnetic field availability.

Section 5.6 described how T_c and $H_{c2}(T)$ are defined in data generated by commercial equipment. These methods will specifically be applied for electro-magnetic investigations of the diffusion progress and compositions in Powder-in-Tube wires, and for characterizations of the field-temperature phase boundary.

Chapter 6

The Field-Temperature Phase Boundary

A description of the four dimensional critical surface in Nb_3Sn wires requires accurate knowledge of the field-temperature phase transitions. Most knowledge regarding $H_{c2}(T)$ in Nb_3Sn stems from homogeneous, well defined laboratory specimen as discussed in Chapter 2. The $H_{c2}(T)$ of Nb_3Sn in wires are, on the contrary, mainly determined by extrapolation of the transport $J_c(H)$ curve or magnetization measured $J_c(H)$ at moderate magnetic field (< 15 T). In this Chapter the field-temperature phase boundary in wires is investigated across the full range of relevance, i.e. $0\ T < \mu_0 H < 32\ T$ and $1.4\ K < T < T_c$. First, the effects of inhomogeneities on $H_{c2}(T)$ will be highlighted using low-field magnetic characterizations. These will then be compared to $H_{c2}(T)$ found with resistive measurements over the full range. It will be shown that $H_{c2}(T)$ distributions, which originate from Sn gradients in wires, can be reduced through extended heat treatments. Then the differences in $H_{c2}(T)$ in various conductors will be analyzed. It will be shown that areas with close to stoichiometric A15 can be found in all present wires, and that the differences in the measured field-temperature boundary originate from different Sn gradients in the wires. Finally, it is shown that the Maki-De Gennes relation, as introduced in Chapter 3, has general validity for the description of $H_{c2}(T)$ in all investigated Nb_3Sn wires and available literature results.

6.1 Introduction

The upper critical field of Nb_3Sn strongly depends on A15 composition. Although measurements covering the complete field-temperature (*H-T*) phase boundary are available for one set of pure Nb-Sn thin films [28, 29] and a few single- and polycrystals [36, 38], measurements of $H_{c2}(T)$ on practical, inhomogeneous conductors are sparse. The *H-T* behavior of wires may differ substantially from homogeneous films and crystals due to inherent inhomogeneities arising from their manufacture (Section 1.4). Wires exhibit Sn gradients resulting from the solid state diffusion process used for the formation of the A15 layers (Chapter 4). Wires also exhibit strain gradients caused by lattice imperfections and differences in thermal contraction of the various materials in the composite. The existence of the inhomogeneities as well as their potential influence on the superconducting properties has been recognized for a long time [Smathers in 18, Ekin in 19, 62, 63, 142, 257–259]. Also the introduction of a scaling field to describe the $J_c(H)$ curve which lies substantially below the maximum $\mu_0 H_{c2}$ is illustrative. This scaling field is often referred to as B_{c2}^* but in fact it is an inhomogeneity-averaged irreversibility field ($\mu_0 H_{c2}^*$) defined by a pinning force or Kramer function extrapolation as discussed in Section 3.3. However, to the author's knowledge, no systematic analysis of the influence of inhomogeneities on $H_{c2}(T)$ and $H_{c2}^*(T)$ across the entire *H-T* range is available in the literature. Moreover, the critical parameters are often defined at an arbitrary criterion of for example 50% or 90% of the superconducting to normal transition and the behavior at the operating temperature and higher fields is mostly extrapolated from the slope at $T_c(0)$. The analysis in this Chapter concentrates on the entire transition widths over the relevant *H-T* range in an attempt to extract the range of property distributions that are present in wires.

For wires, $H_{c2}(T)$ results are available at moderate magnetic fields [Flükiger *et al*. in 17, 30, 105–107, 147] while a few publications report a high magnetic field measurement of H_{c2} at liquid helium temperature [Suenaga and Welch in 18, 106–109]. Extrapolation of measured curves up to 22 T indicates a zero temperature upper critical field $\mu_0 H_{c2}(0)$ in thin films ranging from 26 to 29 T, depending on the normal state resistivity. Single- and polycrystals, measured over the entire magnetic field range, indicate either 24.5 T for the tetragonal phase or 29 T for the cubic phase (Section 2.5). The $\mu_0 H_{c2}^*(0)$ extracted from measurements on wires range from 20 T up to about 32 T. This large spread causes confusion about which value can be regarded as realistic in multifilament conductors and was the prime motivation for a systematic study of the influence of inhomogeneities in wires.

Bronze processed wires are strongly inhomogeneous with respect to Sn content and that the gradients are 1 to 5 at.% Sn/µm (Section 4.7, [62, 63]). Analysis of inhomogeneities in bronze processed wires is, however, complicated by their very small A15 layer thickness of 1 to 2 µm typically, imperfect circular symmetry and higher T_c A15 layers surrounding lower T_c regions. This renders analysis of the property distributions by magnetic characterizations not possible, since the outer, higher T_c regions magnetically shield the lower T_c sections. The thin layers make accurate measurements of the Sn gradients by electron probe microanalysis impossible, imposing the more complex, more local and less accurate study by transmission electron microscopy.

Filaments in modern PIT wires [110] are, in contrast to bronze conductors, nearly perfectly cylindrical, contain thick A15 layers of 5 to 10 µm typically, and have the higher T_c A15 located on the inside, making them magnetically transparent. Compositional analysis indicates

that they are much more homogeneous with respect to Sn content than bronze wires, exhibiting gradients on the order of 0.3 at.% Sn/μm (Section 4.7, [64, 65]). Magnetic (VSM) characterizations of PIT wires up to 14 T by Fischer [144, 232] identified a large difference between $H_K(T)$ found through a Kramer extrapolation and $H_{c2}(T)$, which was correlated to Sn gradients. The effect was visualized by a reduction of the difference between H_K and H_{c2} with increasing reaction times, which is associated with a much stronger rise of $H_K(T)$ than $H_{c2}(T)$. This initial conclusion is supported by *H-T* characterizations on homogeneous bulk materials [39] as well as modeling [197].

A second important difference between wires, and thin films and crystals is the presence of Cu and ternary additions as e.g. Ta and Ti. Cu is believed to lower the A15 formation temperature and only to exist at the grain boundaries (Section 2.6.1, [116, 121]), but its influence on the critical field surface is uncertain [39]. The general consensus on ternary additions of Ta and Ti is that they introduce scattering sites, thereby raising the resistivity and thus $H_{c2}(0)$ and also prevent the formation of tetragonal phases which reduce $H_{c2}(0)$, as was discussed more extensively in Section 2.6.2.

A third key characteristic of wires is the presence of non-uniform differential strain. Macroscopically, the strain dependence of $H_{c2}^*(T)$ is well understood in terms of axial strain [111, 112, 160, 198], or three dimensional strain [149–154], but its influence on the entire *H-T* phase transition is still uncertain [158]. The Cu or bronze matrix enforces a significant compressive axial strain on the A15 layers due to the larger contraction of the matrix with respect to the A15. This causes a thermal pre-compression in the A15 layer which is spatially inhomogeneous [Flükiger *et al*. in 17]. The combined effect of Sn gradients, the presence of Cu in the A15 layer, the influence of ternary additions and the presence of strain puts into question whether the *H-T* surfaces as derived from uniform and well defined laboratory samples can directly be applied to wires.

A second reason to perform a systematic characterization of the *H-T* phase transition in wires is that it yields a better understanding of the achievable performance boundaries of the critical current density. Practical scaling relations for the critical current density depend on the exact behavior of $H_{c2}^*(T)$, but are empirically based and generally rely on Kramer extrapolations of lower field data as discussed in Section 3.3. Moreover, the zero temperature Kramer extrapolated critical field [$\mu_0 H_K(0)$] often results in values far beyond 30 T [158]. This seems unrealistically high in comparison to actual measured results, which are limited to about 29.5 T for higher resistivity, slightly Sn-poor pure Nb-Sn film, although recent results suggest 31.4 T for a pure binary, strain free bulk sample (Section 2.5.3, [39]).

Expressions for the *H-T* phase transition, derived directly from microscopic theory are readily available in the literature (Section 3.4.2) and have been applied with success to well defined laboratory specimens [28, 106, 260, 261]. Most of the *H-T* results on wires are empirically described [81, 111, 112]. This leads to continuing discussions that partly result from the use of extrapolated $H_{c2}^*(0)$, without accounting for the inhomogeneous nature of the conductors. Although such empirical relations in principle yield sufficient accuracy for scaling of the critical current density, large discrepancies are present between the fitted values for $H_{c2}^*(0)$ and $T_c^*(0)$ and actual measurements of $H_{c2}(T)$ [158]. Though well justified empirically, this discrepancy clearly needs understanding.

6.2 Selected samples and measurement details

6.2.1 Selected samples

In Table 6.1 an overview is presented of the selected samples with their heat treatment conditions, mounting technique and the non-copper current density when measuring the resistive transition. The main parameters and cross-sections of the wires were presented in Chapter 4.

The ITER type Furukawa (FUR) and Vacuumschmelze (VAC) wires were selected because their transport critical current density was characterized extremely well in various laboratories during the ITER benchmark tests [111, 162, 163, 263–265]. They are representative for ternary conventional bronze processed manufacturing methods, have a relative low J_c, small filament size and probably large Sn gradients across the A15 areas. The Powder-In-Tube conductors from Shape Metal Innovation (SMI) were chosen since they are magnetically transparent [64, 65] due to their 'inside out' design, have a relatively large A15 cross section enabling EDX composition analysis and are therefore favorable research wires which were already characterized [144, 232] to some extend. They exhibit close to present record current densities and have, compared to bronze processed wires, less steep Sn gradients. A binary (B27) and two ternary versions (B34 and B134) of this wire type were selected. The pure Cu matrix ternary conductor (B34) was additionally selected for study of inhomogeneity effects using increased reaction times, which result in increased A15 layer thickness and less steep Sn gradients [144]. A bulk sample, manufactured by M.C. Jewell at the University of Wisconsin's Applied Superconductivity Center (UW-ASC), was used to investigate the behavior of pure binary, Cu-free Nb_3Sn.

The first set of ternary PIT wire (B34) samples was heat treated for various times at 675 °C. A reaction time of 64 hours is recommended by the manufacturer to yield optimal J_c. A specific mounting procedure was applied in an attempt to force the samples into a reproducible,

Table 6.1 *Overview of the specimen investigated.*

Sample	Heat treatment [*h* at °C]	Mounting procedure**	Excitation $J_{non\text{-}Cu}$ [A/mm^2]
Ternary PIT (SMI) (B34–4h)*	4 at 675	1	0.2
Ternary PIT (SMI) (B34–16h)*	16 at 675	1	0.2
Ternary PIT (SMI) (B34–64h)*	64 at 675	1 and 2	0.2
Ternary PIT (SMI) (B34–768h)*	768 at 675	1	0.2
Reinforced ternary PIT (SMI) (B134)	80 at 675	2	0.6
Binary PIT (SMI) (B27)	128 at 675	2	0.2
Ternary bronze (VAC)	220 at 570 + 175 at 650	2	0.5
Ternary bronze (FUR)*	240 at 650	2	0.5
Bulk (UW-ASC)*	320 at 1020	3	0.004

**1 → GE varnish on Cu
2 → Stycast® on Ti-6Al-4V
3 → GE varnish on Ti-6Al-4V

*Samples showing a measurement inconsistency of about 4%

although unknown, strain state after cool down to test temperatures as described in Section 5.5. Four wires were mounted with General Electric varnish onto a copper substrate. One sample, reacted for 64 hours was mounted with Stycast® 2850FT on a Ti-6Al-4V substrate of lower thermal contraction than Cu (–0.18% versus –0.35%). Intercomparisons of short sample resistive transitions and standard J_c measurements (Section 7.8.2) require the same mounting technique in an attempt to create identical strain states after cool down.

The second sample type in Table 6.1 is also a ternary PIT wire (B134) which is similar in build to B34 but has a Cu-Nb reinforcement tube surrounding the Cu matrix, as described in Section 4.2.3. It can be expected that the reinforcement results in a larger thermal pre-compression in the A15 layer from reaction temperature down to room temperature, caused by the higher strength of the Cu-Nb as compared to a pure Cu matrix.

The next sample in Table 6.1 is a binary PIT wire (B27). The only difference from the ternary PIT (B34) wire, according to the manufacturer, is the use of pure Nb tubes. This wire was heat treated beyond the manufacturer's recommended time of 47 hours at 675 °C since earlier magnetic characterizations on this wire indicated that a longer reaction time of 128 hours yields slightly improved properties [144].

The Vacuumschmelze bronze processed wire was heat treated following the manufacturer's recommended schedule. This wire uses Nb-7.5 w.% Ta rods that are embedded in a Sn rich bronze matrix, which is surrounded by a Ta diffusion barrier and embedded in a Cu matrix as described in Section 4.3.2.

The Furukawa bronze processed wire was also heat treated following the manufacturer's recommended schedule. This wire is constructed with Nb rods embedded in a Ti-containing Sn-rich bronze. The bronze is surrounded by a Ta diffusion barrier outside of which is pure Cu. Further details can be found in Section 4.3.1.

The nominally 24.4 at.% Sn needle shape bulk sample was prepared by M.C. Jewell for resistive characterization and mounted with GE varnish on Cu. It was not fully equilibrated and exhibits therefore three-dimensional inhomogeneities in contrast to the wire samples, which show mainly radial Sn gradients. Cross-sections of this not-equilibrated sample show local A15 areas that are stoichiometric, as well as others low in Sn [39]. This inhomogeneous A15 distribution results in the measuring current sampling a greater range of A15 Sn compositions than in the wires which are longitudinally rather homogeneous, although radially inhomogeneous. The sample is a cutout from a larger bulk section, manufactured by Hot Isostatic Pressing (HIP). Field Emission Scanning Electron Microscopy (FESEM) analysis, more details on the fabrication, as well as more extensive characterization of a larger bulk sample set, were published elsewhere [39].

6.2.2 Measurement details

Magnetic characterizations

The ternary wires, reacted for 4, 16, 64 and 768 hours at 675 °C, were magnetically analyzed in a Quantum Design 5.5 T SQUID magnetometer and an Oxford Instruments 14 T VSM. Both techniques were described in detail in Section 5.6. For the SQUID measurements, samples were cut to about 4 mm length, mounted with grease in a plastic straw with the wire axis parallel to the applied field. In VSM characterizations, sample sections of about 4 mm length were bound to a plastic holder with Teflon® tape with the wire axis oriented parallel to the

applied magnetic field. The magnetic moment was registered as a function of the ramping field at $d\mu_0 H / dt = 10$ mT/s at a constant temperature of 12 K. Upper critical fields H_{c2}(12 K) and Kramer extrapolated upper critical fields H_K(12 K) were extracted from the first visible deviation from the reversible normal-state magnetic response and by linear extrapolation respectively, as described in detail in Section 5.6.1.

Resistive characterizations

The majority of the *H-T* investigations in this Chapter were performed by measuring the resistive transition at a constant temperature and a constant magnetic field ramp. The resistive characterization techniques, as well as the data reduction techniques, were discussed in Section 5.5. The resistive transitions were least squares fitted to (5.6) and cut-offs were taken at a given percentage of the normal state resistivity to yield $H_{c2}(T)$ at the selected percentage. The $H_{c2}(T)$ points were then least squares fitted to the Maki-De Gennes relation (3.20).

A representative set of resistive transitions is shown for the ternary PIT wire (B34) in Figure 6.1. Intersections can be made at various percentages of the normal state resistivity, as indicated by the 10%, 50% and 90% lines to arrive at different criteria for H_{c2}.

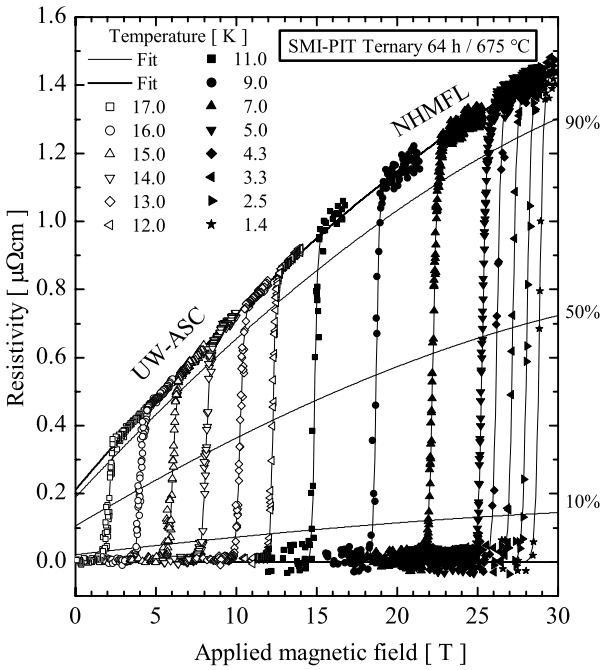

Figure 6.1 *Resistive transitions as function of magnetic field at constant temperature for the ternary PIT wire (B34) as measured at the UW-ASC (open symbols) and the NHMFL (closed symbols). The upper envelope line represents an overall fit of the magnetoresistance while the thin lines are fits to individual transitions using (5.6).*

6.3 Magnetic tests of inhomogeneity in variably reacted samples

Fischer's results [144, 232] will now shortly be summarized since they represent the starting point for the present full field-temperature investigations and unambiguously demonstrate the presence of A15 inhomogeneities, and their reduction through extended reaction times. Fischer's SQUID results at 5 mT are summarized in the left graph in Figure 6.2. The normalized magnetic moments as function of temperature are shown for the ternary PIT wires (B34) with 4, 16, 64 and 768 hour reactions at 675 °C.

At 5 K full flux exclusion can be observed. Around 8.5 K the initial transition occurs for the 4 h, 16 h and 64 h reactions. The first transition for the 768 h heat treatment occurs substantially lower, starting at 7 K and ending at 8.1 K. The main A15 transitions occur between 14 and 18 K. The steady progress of the reaction is clearly visible. The increased signal amplitude for longer time indicates an increase in A15 quantity, in agreement with the SEM observations, presented in Section 4.7.1. The Sn enrichment (or A15 quality improvement) is visualized by the shift of the transitions to higher temperatures, combined with a reduction of the transition widths. It is notable that extension of the reaction from 64 to 768 hours slightly increases the upper T_c, while barely enhancing the signal magnitude at $T = 10$ K. However, a depression of the "Nb" transition to about 7.5 K indicates some penetration of the A15 layer through the Nb which makes low T_c Nb-Sn phases visible.

The lines at 0, 10, 50 and 90% in the left graph in Figure 6.2 represent intersections that can be made on the 768 hour A15 transition using (5.7). The bold line is an extrapolation of a least squares fit on the data points between 10 and 14 K defining a 0% normal state for the A15 transitions. Intersections were derived in a similar way for the 4, 6 and 64 hour reactions. The 10% and 90% normal state intersections on the A15 transitions above 10 K were used to define $T_{c-10\%}$(5 mT) and $T_{c-90\%}$(5 mT) for plotting in the right graph in Figure 6.2.

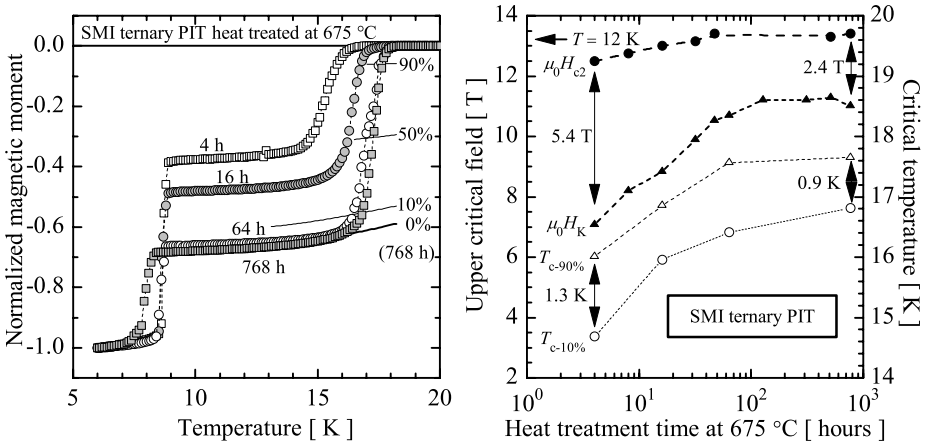

Figure 6.2 *Left: Normalized magnetic moment as a function of temperature measured by Fischer [144] in a SQUID magnetometer. Right: Kramer extrapolated upper critical field, upper critical field as function of heat treatment time measured by Fischer [144] in a VSM and critical temperature from the SQUID results.*

VSM characterizations were performed by Fischer on the same ternary PIT sample set and H_{c2}(12 K) and H_K(12 K) were extracted from the results at $T = 12$ K as described in Section 5.6.1. These are plotted in the right graph of Figure 6.2, together with the SQUID derived $T_{c-10\%}$(5 mT) and $T_{c-90\%}$(5 mT) versus reaction time. The upper critical field at 12 K rises from 12.5 T at 4 h to 13.4 T at 768 h while $\mu_0 H_K(T)$ increases from 7.1 T at 4 h to 11.0 T at 768 h. The difference between $\mu_0 H_{c2}$(12 K) and $\mu_0 H_K$(12 K) therefore reduces from 5.4 T at 4 h to 2.4 T at 768 h. The stronger rise in H_K with respect to H_{c2} can be attributed to Sn enrichment of the A15 layers with elongated reaction. The measured $T_{c-10\%}$(5 mT) raises from 14.7 K at 4 h to 16.8 K at 768 h and $T_{c-90\%}$(5 mT) increases from 16.0 K at 4 h to 17.7 K at 768 h. The T_c distribution width therefore reduces from 1.3 K at 4 h to 0.9 K at 768 h. The trend in critical magnetic field and critical temperature is therefore the same, although the effects are more enhanced at lower temperatures. Consequently it is concluded that longer heat treatment causes a thicker A15 layer which in addition becomes richer in Sn, resulting both in a rise of T_c, H_K and H_{c2} and a reduction of the width of the T_c and H_{c2} transitions.

6.4 Resistive visualization of inhomogeneity reduction

To expand the inhomogeneity investigations on the ternary PIT (B34) wire to the entire H–T range, a switch is made to the resistive characterization of the H_{c2} transition, as shown in Figure 6.3, where the points represent the 1, 10, 50, 90 and 99% normal state-resistance fits to (5.6). The lines are MDG fits to (3.20), using $T_c(0)$ and D^* as free parameters. The majority (about 50%) of the detected property distributions is present between the 10 and 90% normal state points. The UW-NHMFL data inconsistency mentioned in Section 5.5 is visible around $T = 11$ to 12 K, causing deviations from the overall $H_{c2}(T)$ fits at $T = 12$ to 17 K.

The $\mu_0 H_{c2}(0)$ transition width reduces from 1.2 T to 0.5 T as the reaction increases from 4 to 768 hours at 675 °C. The better A15 sections, represented by $\mu_0 H_{c2}$(90%), increase by 1.4 T from 28.1 T to 29.5 T. The A15 sections of lesser quality, represented by $\mu_0 H_{c2}$(10%), in contrast increase by 2.0 T from 27.0 T to 29.0 T and their stronger rise in comparison with H_{c2}(90%) is the origin of the transition width reduction with increasing reaction time. The majority of the reduction occurs between 16 h and 64 h. The width reduction effect on $T_c(0)$ is less pronounced but still visible, changing from 0.4 K to 0.2 K minimum (10–90%). The best A15 sections detected (99%) rise by about 3% in $H_{c2}(0)$ from 4 to 768 hours, whereas the lower transition (1%) rises about 10%. The extremes in $T_c(0)$ change by about 3% for the best detected sections and about 4% for the lower transition. Optimum critical current densities, expressed as the critical current divided by the total Nb(Ta) + A15 + core package area, are achieved at 64 hours. Maximum J_c appears to correlate to the rise to maximum H_{c2} seen on going from 16 to 64 hours, before any Sn escapes from the Nb(Ta) tube.

The MDG fits at 12 K, derived from the resistive transitions, are compared to the magnetic results in Figure 6.4. The points are derived from the resistive measurements in Figure 6.3 and the shaded areas are the magnetically (VSM and SQUID) derived property distributions from Figure 6.2. The decreasing difference from about 5.4 T to 2.4 T between the magnetically derived H_K(12 K) and H_{c2}(12 K) with increasing reaction time is a direct result of the Sn gradient reduction in the A15 layer, in agreement with recent simulations [197].

The reduction of the transition width in the resistive characterizations is less obvious (from about 1.1 T to 0.6 T for the 10 and 90% normal state resistance points) but still clear. The

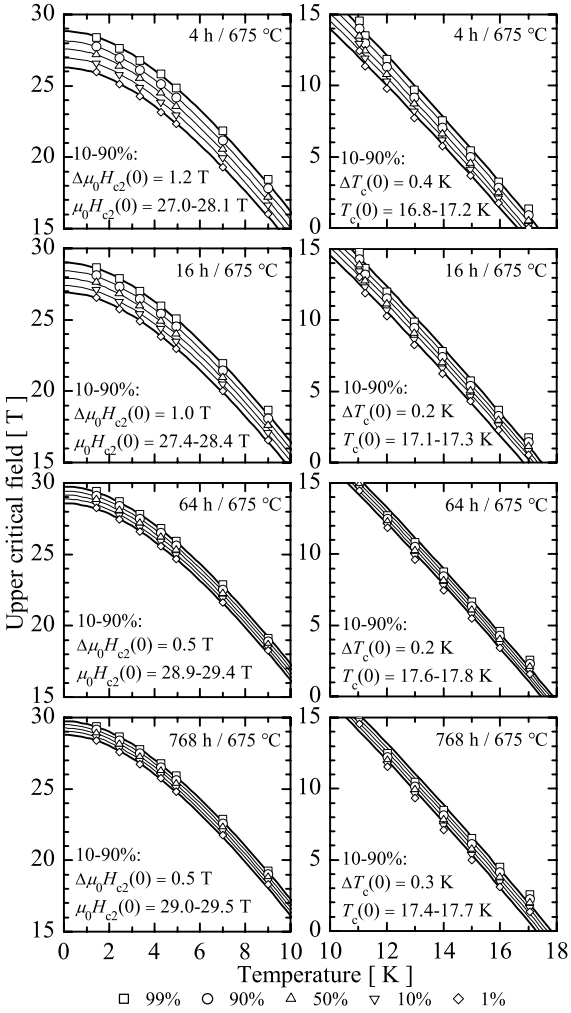

Figure 6.3 *Upper critical field transition points as function of temperature for increasing reaction time at 675 °C for a SMI ternary (B34) wire. The lines are calculated using (3.20) with the parameters from Table 6.2.*

highest H_{c2}(12 K) detected in the resistive characterizations (at 99% normal state resistance) is identical to, and increases in the same way, as the VSM determined H_{c2}(12 K).

The SQUID derived $T_c(0)$ transition width reduces from 1.3 K to 0.9 K, whereas the resistive transition width (between 10 and 99% normal state resistance) reduces from 0.4 K to 0.3 K. The SQUID derived $T_c(0)$ values, however, are substantially lower than in the resistive data. The magnetic and resistive characterization techniques are therefore, apart from the highest detected H_{c2} values, only qualitatively comparable. This lack of agreement is a direct consequence of the compositional variation of the A15 phase and shows that small current density resistive transitions sample only a small fraction of the A15 property distribution.

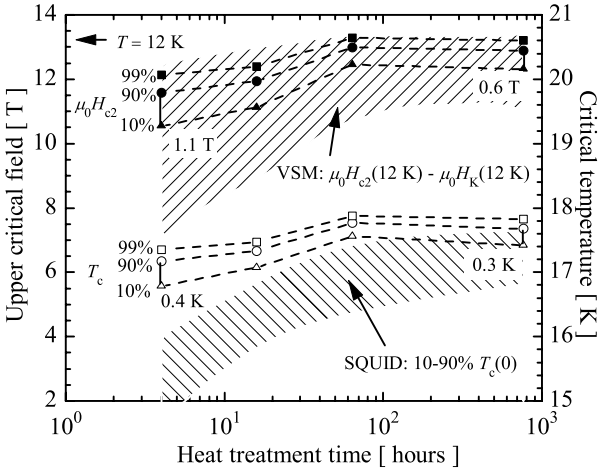

Figure 6.4 *Comparison of upper critical field and critical temperature transition widths as function of reaction time from resistive and magnetic characterizations. The lines result from the resistive characterizations and the shaded areas summarize the magnetic characterizations from Figure 6.2.*

6.5 Inhomogeneity differences in various conductors

An overview of the collected $H_{c2}(T)$ results for all resistively characterized samples, reacted 'normally' (see Table 6.1), is given in Figure 6.5 and summarized in Table 6.2. The graphs in Figure 6.5 are again separated in temperature for enhanced visibility and developed as for the ternary PIT data in Figure 6.3.

The order from top to bottom in Figure 6.5 is approximately of increasing inhomogeneity. The transition widths (10–90%) with respect to $\mu_0 H_{c2}(0)$ range from 0.5 T for the ternary PIT wire (B34, Figure 6.3) reacted at 64 hours, to 1.8 T for the bulk sample. The fitted $T_c(0)$ variation ranges from 0.1 K for the binary and reinforced ternary PIT wires and the bulk sample to 0.3 K for the Vacuumschmelze bronze processed wire. It is interesting to observe the differences that occur between the two bronze processed wires. The Ti-alloyed Furukawa wire exhibits a smaller distribution (0.9 T and 0.2 K) and slightly better overall properties than the Ta-alloyed Vacuumschmelze wire (1.2 T and 0.3 K).

Table 6.2 *Summary of zero-temperature upper critical field and zero-field critical temperature.*

Criterion	Parameter	Ternary							Binary	
		B34 4h	B34 16h	B34 64h	B34 768h	B134	FUR	VAC	B27	Bulk
10%	$\mu_0 H_{c2}$ [T]	27.0	27.4	28.9	29.0	28.2	28.0	27.3	26.6	26.5
	T_c [K]	16.8	17.1	17.6	17.4	17.8	17.2	17.4	17.8	16.5
90%	$\mu_0 H_{c2}$ [T]	28.1	28.4	29.4	29.5	29.1	28.9	28.5	27.4	28.3
	T_c [K]	17.2	17.3	17.8	17.7	17.9	17.4	17.7	17.9	16.6
99%	$\mu_0 H_{c2}$ [T]	28.8	29.0	29.7	29.7	29.6	29.3	29.2	27.8	29.3
	T_c [K]	17.3	17.5	17.9	17.8	18.0	17.5	17.8	17.9	16.7

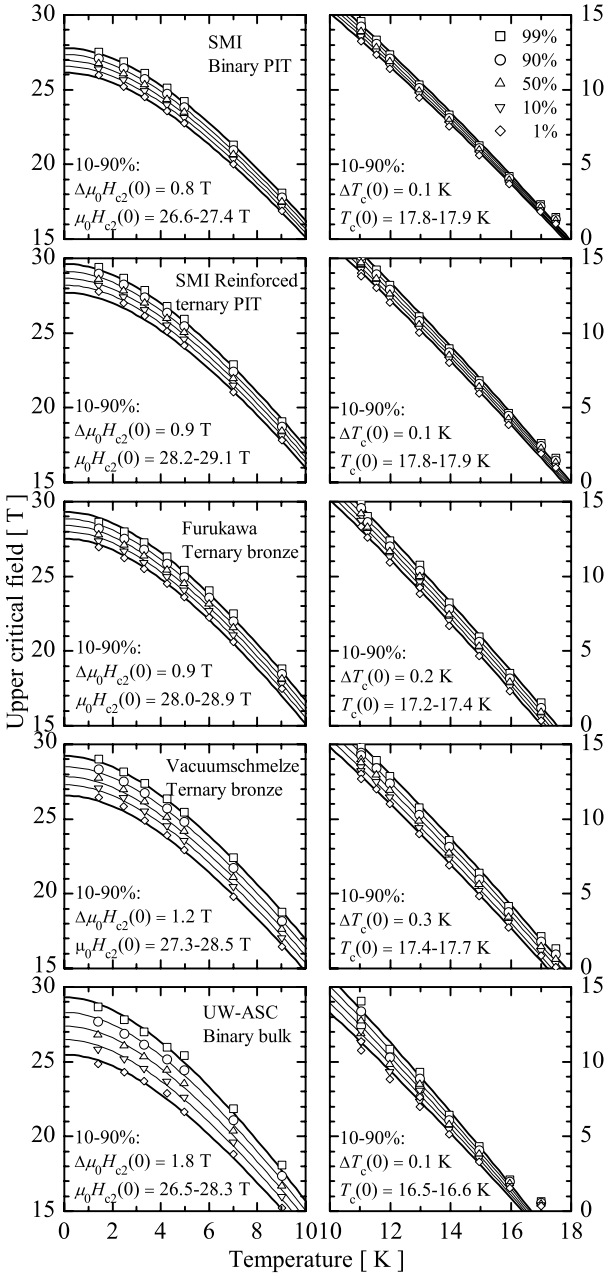

Figure 6.5 *Upper critical field transition points as function of temperature determined by resistive measurements for various wires with manufacturer's optimized reactions. The lines are calculated using (3.20) with the parameters from Table 6.2.*

The bulk needle sample shows a very large distribution in $\mu_0 H_{c2}(0)$ of 1.8 T, or even 3.9 T if the outer extremes (1 and 99%) are taken into account. This large spread is indicative of its three dimensional distribution of local areas of high and low Sn content [39], for which no continuous high A15 quality current path exists. The wire samples, in contrast, exhibit an essentially two dimensional radially distributed Sn gradient and thus have longitudinal parallel paths of different, but approximately constant Sn content. The ternary PIT wire (B34) is known to exhibit relatively low Sn gradients from the EDX results in Section 4.7.1.

6.6 Best properties detected in various conductors

The highest observed $H_{c2}(T)$ (at 99% normal state resistance) for all samples are collected in Figure 6.6 and Table 6.2. Considering the differences in transition width in Figure 6.5, the highest $H_{c2}(T)$ A15 sections in the ternary wires are strikingly similar. High $H_{c2}(T)$ A15 regions are present in all ternary wires and are very comparable: All MDG fits to the 99% normal state resistance transition points are within a window $\mu_0 H_{c2}(0) = 29.5 \pm 0.3$ T and $T_c(0) = 17.8 \pm 0.3$ K. The uncertainty in $H_{c2}(0)$ determination from the resistive transitions is ± 0.3 T as a result from the noise in the high magnetic field characterizations (see Figure 5.20). The highest detected properties are therefore within the experimental error bars identical, even if the systematic 4% inconsistency between the NHMFL and UW-ASC results for some of the samples is neglected. A systematic difference can be observed between the bronze and PIT processed conductors, the highest detected phase boundaries in the bronze processed wires being slightly lower than in the PIT processed wires. This small difference in $H_{c2}(T)$ is in strong contrast to their large critical current density differences which are approximately four times higher in the PIT wires (see Table 4.1).

The inset in Figure 6.6 compares the binary PIT wire to the binary bulk needle. The binary PIT

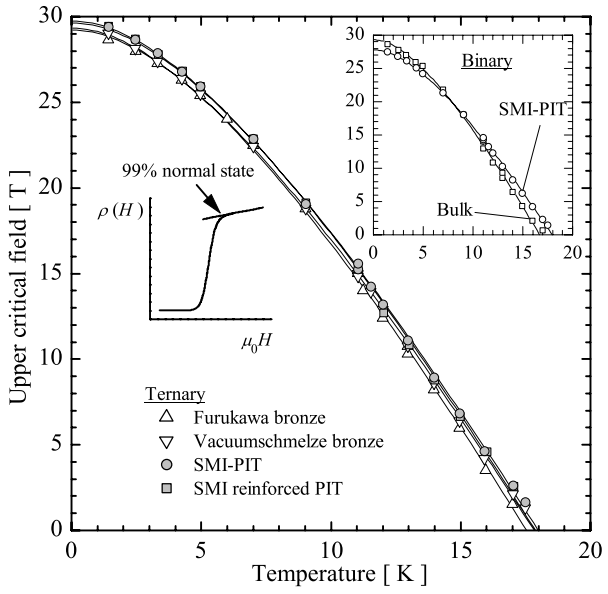

Figure 6.6 *Comparison of the highest detected upper critical fields as function of temperature in the ternary wires. The inset shows the highest detected phase boundaries for the binary PIT wire and the pure binary bulk needle sample. The lines are calculated using (3.20) with the parameters from Table 6.2.*

shows a reduced maximum $\mu_0 H_{c2}(0)_{-99\%}$ of 27.8 T but a comparable $T_c(0)_{-99\%}$ of 18.0 K. The bulk needle has a reduced $T_c(0)_{-99\%}$ of 16.7 K but, in comparison to the binary PIT wire, a very high $\mu_0 H_{c2}(0)_{-99\%}$ of 29.3 T which is in the range of the ternary wires.

6.7 Discussion

6.7.1 Overall behavior of the field-temperature phase boundary

The upper (90–99%) transitions of all ternary wires are remarkably similar (Figure 6.6), in contrast to the large range of transitions widths (Figure 6.3 and Figure 6.5) and grain morphology differences (Sections 4.2 and 4.3). The binary PIT processed wire has a suppressed $H_{c2}(0)$ while retaining a comparably high $T_c(0)$ in comparison to the ternary wires. The bulk needle exhibits an $H_{c2}(0)$ which is comparable to the ternary wires but shows a suppressed $T_c(0)$. Orlando *et al*. (Section 2.5.2, [29]) have shown similar behavior in thin films with varying resistivity: Increasing the resistivity caused $H_{c2}(0)$ to rise, at the cost of a reduction in $T_c(0)$. Their optimal dirty film ($\rho_n = 35$ μΩcm) had $\mu_0 H_{c2}(0) = 29.5$ T and $T_c(0) = 16.0$ K at a 50% resistive criterion, compared to 26.3 T and 17.4 K for a $\rho_n = 9$ μΩcm film. The bulk needle investigated here exhibited a resistivity just above $T_c(0)$ of 22 μΩcm and $\mu_0 H_{c2}(0)$ and $T_c(0)$ at a 50% normal state resistance criterion are 27.4 T and 16.5 K respectively. However, the bulk needle was far from fully homogenized, meaning that for a better comparison a higher resistive criterion is more suitable. A 90% normal state resistance results in $\mu_0 H_{c2}(0) = 28.3$ T and $T_c(0) = 16.6$ K. Both the 50% and 90% values are consistent with the thin film data from Orlando *et al*., i.e. at $\rho_n = 22$ μΩcm the bulk needle phase boundary is positioned between the 9 and 35 μΩcm thin film data. In addition, a (partial) transformation to the tetragonal phase could also reduce $H_{c2}(0)$.

The upper (90–99%) resistively determined H_{c2} for the ternary PIT processed wire are identical to the magnetically (VSM) derived H_{c2} results for the limited overlap that is available at $T = 12$ K. This comparison shows that the highest detectable H_{c2} can be probed using completely different characterization methods.

6.7.2 Applicability of the MDG description

The overall accuracy of the MDG description (3.20) is demonstrated in the normalized plot in Figure 6.7. All resistive transition results are well described by the MDG relation, independent of whether 1, 10, 50, 90, or 99% is applied as the criterion for defining H_{c2}. Included are resistive transition results on the samples from Table 6.1 (in bold) as well as resistive transition results on additional sample material [262], magnetic results using the onset of superconducting behavior [39], literature results that have been measured resistively and with RF techniques [28, 29, 36, 38], and Kramer extrapolated critical magnetic field data resulting from transport J_c characterizations [158, 163]. The route that was followed in order to arrive at Figure 6.7 is that all $H_{c2}(T)$ results for a specific sample were least squares fitted with the MDG relation and the resulting values for $H_{c2}(0)$ (calculated from $T_c(0)$ and D^*) and $T_c(0)$ were used as normalization parameters. The overall shape of the normalized phase boundary is practically identical.

The MDG description clearly is very accurate in describing the H–T phase transition for Nb_3Sn independent of the applied criterion, strain state or sample layout. It has the advantage of using only two fit parameters, of which $T_c(0)$ can be measured.

Physically more correct descriptions have been developed [169–173, 182] and applied [28, 106, 260, 261], but result in an increased number of fit parameters, the details of which are impossible to experimentally define in the case of real inhomogeneous wire samples.

Apparently, the shape of the field-temperature phase transition is constant and does not vary (within the practical measurement error) with the details of the underlying physics, which is hidden in D^* [or similar, the slope at $T_c(0)$], $T_c(0)$ and $H_{c2}(T)$ as discussed in Section 3.4.2. The fact that it holds for samples with 8.4 K ≤ $T_c(0)$ ≤ 18.0 K shows (see Sections 2.3 and 2.4) that it is validated for nearly the full A15 composition range and thus for strong, as well as weak coupling A15.

The use of the relatively simple MDG fit is therefore proposed as the best alternative to replace less convincing empirical relations describing wire results. The accuracy of the description is

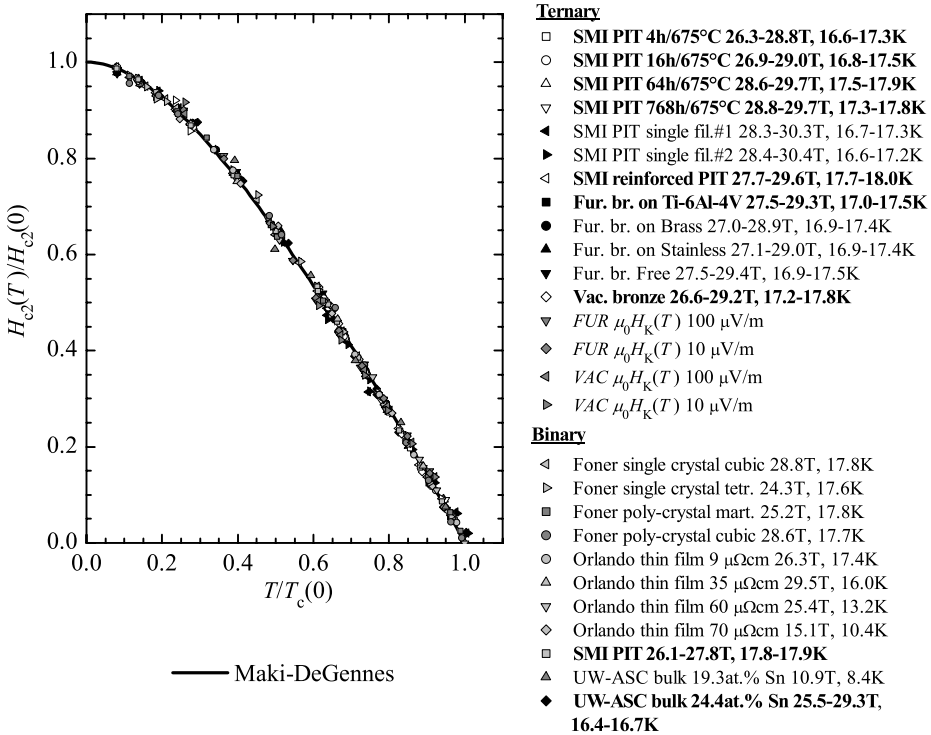

Figure 6.7 *Normalized $H_{c2}(T)$ for available measurements, including results taken from literature, demonstrating that the shape of the normalized H-T phase boundary is identical for all included Nb-Sn phases. The samples in bold are presented in this thesis. The normalization is valid for 1, 10, 50, 90 and 99% normal state criteria. The results from the literature used 50% (Orlando) and 50-90% (Foner) criteria. The normalization also holds for Kramer extrapolated critical fields using a 10 or 100 μV/m criterion. The numbers behind the sample names indicate the detected ranges for $\mu_0 H_{c2}(0)$ and $T_c(0)$.*

by far sufficient to reliably estimate the high magnetic field behavior starting with low magnetic field measurements up to about 15 T, which can be easily obtained with standard superconducting laboratory magnets. This conclusion is important for practical scaling relations, where many discussions of what is the optimal function for scaling the field-temperature phase boundary have taken place. The experimental results in Figure 6.7 prove that the rather simple generalized MDG relation is valid for all investigated Nb_3Sn materials.

6.8 Conclusions

An experimental study has been completed of the field-temperature phase boundary in several present generation optimized wires. The highest detected upper critical field at zero temperature and the critical temperature at zero magnetic field are, within the practical error bar of ± 0.3 T, constant for all investigated ternary wires and within 29.5 ± 0.3 T and 17.8 ± 0.3 K respectively. It is shown that these upper limit transitions are remarkably uniform across many wires and across transport and magnetic characterizations. The property distribution of wires can be visualized by measuring the resistive transition in transport or by separating the irreversibility field from H_{c2} in magnetization measurements.

Detailed measurements over a wide range of reaction conditions show that the often ignored A15 inhomogeneity can be clearly visualized, is significant and exists under all conditions. Ignoring the presence of inhomogeneities is the reason why magnetic and transport measurements mostly do not agree. It was shown in Section 6.4 that only the upper H_{c2} transition agrees well between transport and magnetic characterizations.

The Maki-De Gennes function has proven to yield an excellent description for the field-temperature behavior of Nb_3Sn for the entire range of investigated conductors as well as for the thin film and poly- and single crystal data from the literature. In normalized form all $H_{c2}(T)$ dependencies follow one single curve, independent of composition, strain state, sample layout or transition criterion. Additionally the function also fits the Kramer extrapolated critical magnetic fields. This shows that the Maki-De Gennes relation can also be used to describe the inhomogeneity averaged effective critical magnetic field, as used in practice for scaling of the critical current density in multifilament wires.

Chapter 7

Critical Current

In the previous Chapter it was established that the temperature dependence of the upper critical field can be described accurately by the Maki − De Gennes relation. This information will now be used in a systematic analysis of measured critical currents as a function of magnetic field, temperature and strain. It will be shown that existing scaling relations, based on the Kramer pinning descriptions (e.g. the Summers form), fail to describe the measured temperature dependence of the critical current in wires. An improved description is therefore proposed that accurately accounts for the observed temperature dependence. By using this improved temperature dependence, the observed strain dependence directly follows, without the need to introduce different dependencies of the bulk pinning force on $H_{c2}^{*}(\varepsilon)$ and $H_{c2}^{*}(T)$, as is usually done. It is shown that the strain dependence of the principal scaling constant, which is determined by flux pinning, can be regarded negligible. The deviatoric strain description, corrected to include asymmetry, is implemented and the improved scaling relation is compared to measured critical current data in the magnetic field range from 1 to 13 T, for temperatures from 4.2 to 16 K and for applied axial strains from –0.6 to + 0.5%. It is shown that the new scaling relation accurately describes the measurements over this entire range using a single set of parameters. The improved description is used to determine the hypothetical performance boundary of the present generation of high current density Nb_3Sn wires. It is demonstrated that present conductors operate at about 60 to 80% of their hypothetical limit.

7.1 Introduction

In Chapter 6 it was demonstrated that the Maki-De Gennes relation for $H_{c2}(T)$ (3.20) has general validity for all available Nb_3Sn data, independent of A15 composition, strain state or applied critical state criterion. This implies that the relation can also be used for the bulk average upper critical field that determines the scaling of the critical current density. The overall scaling relations for the critical current density can therefore be analyzed in the light of this temperature dependence of the bulk average upper critical field. A known temperature dependence of the upper critical field also leads to a known temperature dependence of the GL parameter, as was demonstrated in Section 3.5.2.

The central assumption in the analysis of the magnetic field dependence of the bulk pinning force was discussed in Section 3.3: Flux shearing is the main de-pinning mechanism and thus $F_P \propto (1 - h^2)$ for each A15 composition. This implies that non-linearities in Kramer plots when approaching the maximum present H_{c2} are attributed to inhomogeneity averaging and not to a different pinning behavior as was validated in [197]. Non-linearities above $h \cong 0.8$ are thus disregarded in the analysis.

The strain dependency is analyzed in terms of the corrected and renormalized empirical deviatoric strain description in axial form as given by (3.49). The relation between the strain dependence of the upper critical field and the critical temperature is assumed to follow (3.36) with $\varpi = 3$. It is assumed that the strain dependence of the GL parameter can be written in a similar way to the upper critical field and the critical temperature according to (3.65).

The next Section starts with a summary of the experimental details that are important for the analyses. The scaling relation will be developed through a systematic analysis of measured $J_c(H,T,\varepsilon)$ results. First the field dependence will be analyzed in detail. This results in the values for p and q in (3.64), $H_{c2}^*(T)$ and $F_{Pmax}(T)$. Then the temperature dependence will be analyzed in detail and it will be shown that the Kramer / Summers form fails to describe the temperature dependence through the use of $\nu = 2.5$ and $\gamma = 2$ in (3.64). The use of these constants results in a temperature dependent variation of the GL parameter that is significantly larger than expected from microscopic theory. Next the improved temperature dependence, through the use of different values for ν and γ, will be introduced and validated. This is followed by an analysis of the strain dependence using the improved deviatoric strain model. By using correct values for ν and γ, it is not required to separate the temperature and strain dependence of the bulk pinning force. Also the strain dependence of the GL parameter is determined from the measurements. The accuracy of the new $J_c(H,T,\varepsilon)$ relation is then demonstrated on the full dataset. Finally, critical current measurements in high magnetic field will be discussed in combination with the resistive transition data from Chapter 6 to arrive at an estimate of the ultimate performance of present multifilamentary wires.

7.2 Critical current measurements

Furukawa bronze processed wire (Figure 4.5) was selected for comparison of the scaling relations from Section 3.7.5 with measurements, since its behavior is representative of a large number of wires that were extensively analyzed during the ITER benchmark tests [111, 162, 163, 263, 264]. It was investigated in various laboratories [229, 265, 266] and exhibits highly reproducible properties [157]. Initial characterizations were performed on wires manufactured by Furukawa, Europa Metalli, Mitsubishi, Vacuumschmelze, Alstom and Teledyne Wah Chang. These included critical current measurements on a Ti-6Al-4V barrel

type sample holder over a magnetic field range from 7 to 13 T and for temperatures ranging from 4.2 K to 8 K. Also strain characterizations were performed on a brass U-spring sample holder for intrinsic axial strains of –0.8 to +0.2% at 10 and 13 T, and 4.2 and 6.5 K. The results could be scaled using one set of parameters per manufacturer. The Furukawa and Vacuumschmelze (Figure 4.6) wires were additionally characterized over a more extensive field range of 1 to 13 T and temperature range of 4.2 to 16 K and axial strains of –0.7 to +0.5% using Ti-6Al-4V barrels and a Ti-6Al-4V U-spring. Also these data were scalable with one single set of parameters per manufacturer. This extensive data set is too large to include in this thesis and only the Furukawa results will be analyzed in detail, keeping in mind that the behavior of the other wires is similar apart from different overall scaling constants.

In addition, critical current measurements on a ternary PIT processed wire (Figure 4.3) at high magnetic field will be compared to the resistive characterizations as described in Chapter 6 to analyze the critical current density in relation to the A15 Sn content. The PIT wire was selected since it is representative of modern high current density wires and was used extensively for investigations on the correlations between A15 composition and the field-temperature phase transition.

Critical current measurements on the Furukawa wire were performed using Ti-6Al-4V barrels and a Ti-6Al-4V U-spring as described in detail in Sections 5.2 and 5.3. Four samples were investigated. The barrel results were collected on two samples. One sample was used for 1 and 3 T measurements and a second sample for 2 and 5 to 13 T measurements. One sample was used on the U-spring and one on the Pacman as described in Section 5.4.4. The U-spring and the barrel samples were heat treated together. The Pacman sample was heat treated separately, using the same heat treatment schedule.

On the barrels, the wires were glued with Stycast® epoxy at about 50 °C. On the bending spring, the wires were fixed with Sn-4 wt.% Ag solder at about 200 °C. It is assumed that the substrate material (Ti-6Al-4V) determines the overall thermal contraction after gluing or soldering. The difference in mounting temperature on the barrel as compared to the U-spring can result in a difference in the thermal pre-compression after cool-down to 4.2 K. The thermal pre-strain in the A15 on the U-spring follows from the strain dependency curve. The pre-strain on the barrel follows from the difference in pre-strain compared to the U-spring. This difference is determined by comparing the critical current on the barrel to the strain dependence curve for the critical current at identical magnetic field and temperature.

Both the barrel and the U-spring measurements were corrected for self-field (see Section 5.2.2). For the barrel and the U-spring results self-field corrections of 0.3986 T/kA and 0.0174 T/kA respectively were used (different values arise from the different sample layouts). On the barrels, $E(J)$ transitions were recorded from $E < 10^{-6}$ V/m to about $E = 2\times10^{-4}$ V/m across approximately 50 cm sample length. Reliable critical currents and n-values were extracted at arbitrary E_c over the whole $E(J)$ transition. On the U-spring, however, such high electric field resolutions were not possible due to the limited sample length between the voltage taps of only a few mm, combined with current redistribution effects as described in Section 5.3.3. $E(J)$ transitions were therefore recorded from $E < 10^{-5}$ V/m to about $E = 10^{-3}$ V/m over approximately 5 mm sample length. Reliable current and n-value results can only be extracted at a relatively high criterion of $E_c = 5\times10^{-4}$ V/m as was described in Section 5.3.3. Comparison of both datasets is thus only possible at $E_c = 5\times10^{-4}$ V/m, whereby the barrel $E(J)$ transitions often had to be extrapolated from $E = 2\times10^{-4}$ V/m. The latter is assumed to be acceptable due

to the perfectly linear $E(J)$ dependence on a double logarithmic scale when properly corrected for parallel currents that run through the normal conducting materials surrounding the A15 (see Section 5.2.5). The temperature dependence can thus be analyzed at the "usual" criterion of $E_c = 10^{-5}$ V/m but the strain scaling has to be verified at $E_c = 5\times10^{-4}$ V/m.

At the relatively high criterion of $E_c = 5\times10^{-4}$ V/m the parallel current is no longer negligible and is thus corrected for as described in detail in Section 5.2.5. The parallel current is calculated from the overall resistivity at 20 K which, through the magneto-resistance, depends on the magnetic field. For the barrel characterizations on the Furukawa wire this magneto-resistance was measured. For the U-spring characterizations this was estimated based on measured values from the Vacuumschmelze wire. The parallel current is fitted to:

$$I_P = \frac{a}{\mu_0 H} + b\,, \tag{7.1}$$

where a and b are constants. The values for a and b which are used for the Furukawa analysis are given in Table 7.1.

Table 7.1 *Constants in (7.1) used to calculate the parallel currents in the characterizations of the Furukawa wire.*

$E_c = 5\times10^{-4}$ V/m	a [T]	b [A]
Barrel	1.19	2.72
U-spring	2.89	0.71

7.3 Normalized bulk pinning force

As a first step in determining the overall scaling relation, the magnetic field dependence was investigated. For this, each combination of temperature and strain was attributed to a unique but unknown effective upper critical field $H_{c2}^*(T,\varepsilon)$ and maximum bulk pinning force $F_{Pmax}(T,\varepsilon)$. The bulk pinning forces were calculated from the measured critical current densities through $F_P(H,T,\varepsilon) = J_c(H,T,\varepsilon)\times\mu_0 H$. Kramer plots are linear for this wire as will be shown below, indicating $q = 2$ and $p = 0.5$ as was shown in Section 3.3. To analyze consistency with these values in (3.13) for all temperatures and strains, a least squares fit was made to $F_P(H,T,\varepsilon) / F_{Pmax}(T,\varepsilon)$ in:

$$\frac{F_P(H,T,\varepsilon)}{F_{Pmax}(T,\varepsilon)} = \frac{h^{0.5}(1-h)^2}{0.2^{0.5}(1-0.2)^2} \cong \frac{h^{0.5}(1-h)^2}{0.286}\,, \tag{7.2}$$

where $h = H / H_{c2}^*(T,\varepsilon)$. The resulting normalized bulk pinning force dependencies on reduced field are shown in Figure 7.1.

The left graph shows the dependence for the $J_c(H,T)$ measurements at all temperatures (and constant strain). The right graph shows the reduced dependencies for the $J_c(H,T,\varepsilon)$ for all temperature and strain values. The fit values for $H_{c2}^*(T)$ and $F_{Pmax}(T)$ for the $J_c(H,T)$ measurements are summarized in Figure 7.2, including a calculated dependence for $H_{c2}^*(T)$ using the Maki-De Gennes relation (3.20) with $\mu_0 H_{c2}^*(0) = 30.1$ T and $T_c^*(0) = 16.7$ K. It should be noted that these are at –0.15% axial pre-compression, as will be shown in Section 7.6.2.

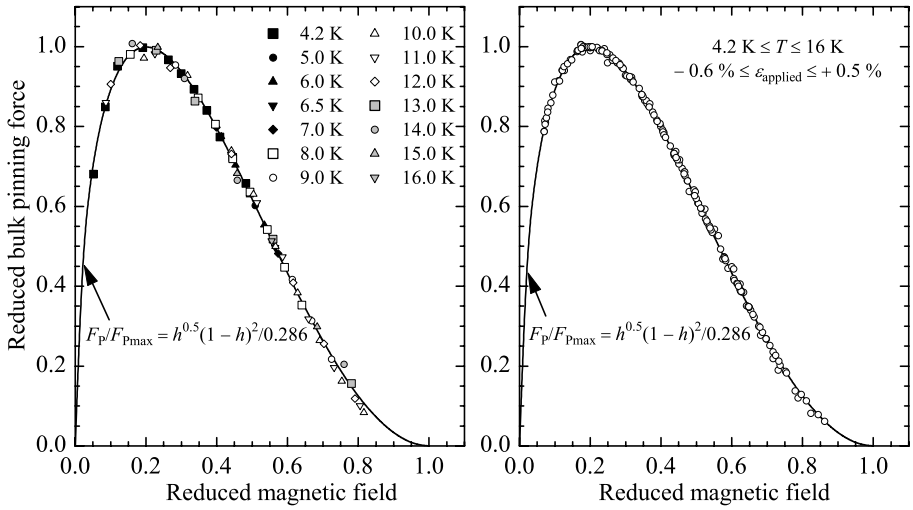

Figure 7.1 *Reduced bulk pinning force as function of reduced magnetic field for the barrel measurements at $E_c = 10^{-5}$ V/m (left graph) and the U-spring measurements at $E_c = 5{\times}10^{-4}$ V/m (right graph).*

The high value for $H_{c2}^*(0)$ in comparison to the measured maximum detectable value $\mu_0 H_{c2}(0) = 29.3$ T in Chapter 6 can be explained by inhomogeneities causing a downward tail in Kramer plots (see Section 3.3) thereby resulting in an overestimate of the extrapolated $H_{c2}^*(0)$. It should be emphasized that this high value is required to accurately describe the measurements in the range $h < 0.8$.

The bulk pinning force curves in Figure 7.1 demonstrate that $p = 0.5$ and $q = 2$ indeed yield the

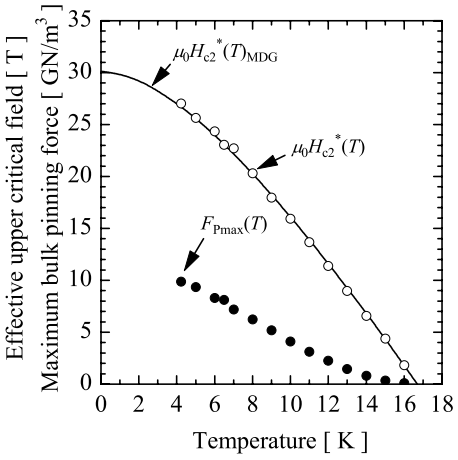

Figure 7.2 *Temperature dependence of the effective upper critical field and maximum bulk pinning force as measured on the ITER barrel at $E_c = 10^{-5}$ V/m .*

correct magnetic field dependence for the entire investigated temperature and strain regime. Above $h \cong 0.8$ deviations can occur, but these are attributed to inhomogeneities which are always present in the sample, as discussed in more detail in Section 3.3. It should be emphasized that the observed correspondence with $p = 0.5$ and $q = 2$ is not specific for this wire, but holds for all investigated sample materials and also for "normally" reacted PIT wires as demonstrated by Cooley *et al.* [137].

It is thus concluded that the field dependence is accurately described by $p = 0.5$ and $q = 2$ for all magnetic fields in the range $0.05 < h < 0.8$ for all temperatures and strains. It is also observed that the Maki-De Gennes relation indeed yields an accurate description for the temperature dependence of the effective upper critical field resulting from transport critical current measurements.

7.4 Temperature dependence

The temperature dependence of the bulk pinning force can now be analyzed. The fact that $q = 2$ indicates that flux shearing is the main de-pinning mechanism and that the well known Kramer plots of $J_c^{0.5}(\mu_0 H)^{0.25}$ as function of magnetic field at constant temperature should result in linear dependencies, as described in Section 3.3. That this is indeed the case is demonstrated in Figure 7.3. The slope in this Kramer plot is a function of $\kappa_1(T)$ and $H_{c2}(T)$, and depends on the selected values for ν and γ in (3.63). This can be seen by introducing $p = 0.5$ and $q = 2$ in (3.63) and rewriting to a Kramer function, as was done to arrive at (3.11).

The temperature dependencies for the upper critical field and the GL parameter are known. This means that only the temperature dependence of the maximum bulk pinning force has to be investigated to determine the overall temperature dependence of the bulk pinning force. The temperature dependence of the maximum bulk pinning force is determined by the values for ν and γ in (3.63).

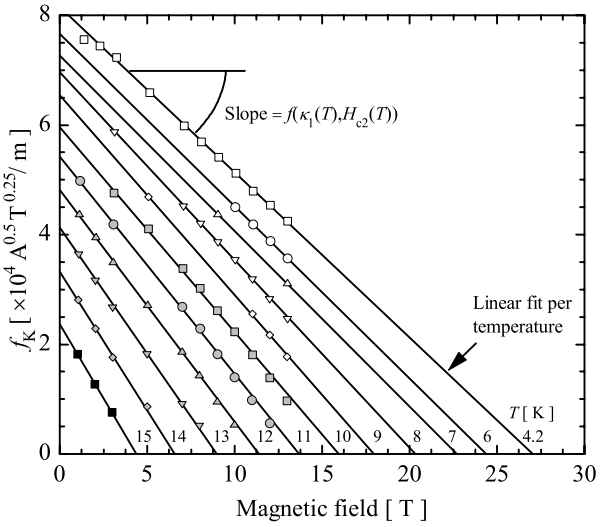

Figure 7.3 *Kramer plot of the ITER barrel results demonstrating a linear magnetic field dependence of the Kramer function at constant temperature and $E_c = 10^{-5}$ V/m.*

7.4.1 Incorrect temperature dependence of the Kramer / Summers form

In the Kramer / Summers form $\nu = 2.5$ and $\gamma = 2$ in (3.63) and (3.64), leading to:

$$F_{\mathrm{P}}(H,T) = C_1 \frac{\mathrm{MDG}(t)^{2.5}}{k(t)^2} h^{0.5}(1-h)^2 , \tag{7.3}$$

where $C_1 = C\,[\mu_0 H_{c2}^*(0)]^{2.5} / \kappa_1(0)^2$. The maximum pinning force is thus given by:

$$\begin{aligned} F_{\mathrm{Pmax}}(T) &= 0.286C \frac{\left[\mu_0 H_{c2}^*(T)\right]^{2.5}}{\kappa_1(T)^2} \\ &= 0.286C \frac{\left[\mu_0 H_{c2}^*(0)\right]^{2.5}}{\kappa_1(0)^2} \mathrm{MDG}(t)^{0.5}\left(1-t^2\right)^2 . \end{aligned} \tag{7.4}$$

There is unfortunately no direct way to extract either C or $\kappa_1(0)$ separately from the $J_c(H,T)$ results. Comparison to the measurements delivers C_1, $H_{c2}^*(0)$, $T_c^*(0)$, $H_{c2}^*(T)$ and $F_{\mathrm{Pmax}}(T)$ without free parameters, but $\kappa_1(0)$ depends on the choice of C. Note that C is not a fundamental constant here because F_{P} is evaluated from the non-copper cross-section.

An overall least squares fit of (7.3) on the measured $J_c(H,T)$ data, using $\mu_0 H_{c2}^*(0) = 30.1$ T and $T_c^*(0) = 16.7$ K from Section 7.3, results in $C_1 = 42.8\times10^9$ AT/m^2. The resulting maximum bulk pinning force according to (7.4) is shown in comparison to the actual data in Figure 7.4. Significant deviations occur above 9 K, which will also be present in predicted critical current densities.

The deviations in $F_{\mathrm{Pmax}}(T)$ can be illustrated through the resulting change in κ_1 with temperature. The variation in κ_1 with temperature, according to the Kramer / Summers form, can be calculated through (7.4) by using values for $F_{\mathrm{Pmax}}(T)$ and $H_{c2}^*(T)$ from Figure 7.2, and by inserting a value for $\kappa_1(0)$. Choosing $C = 12.8\times10^9$ AT$^{-1.5}$m^{-2} as proposed by Kramer (Section 3.3, [104]) results through (7.3) in $\kappa_1(0) = 38.6$; a reasonable value compared to the

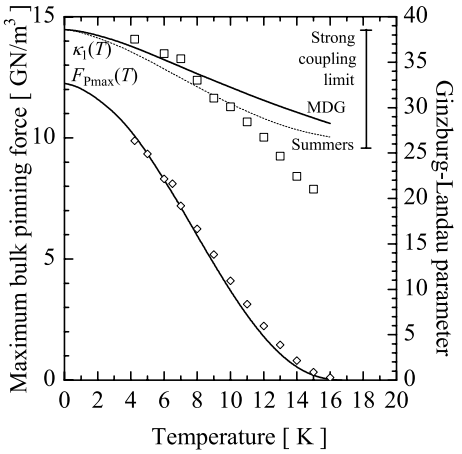

Figure 7.4 *Temperature dependence of the GL parameter and maximum bulk pinning force at $E_c = 10^{-5}$ V/m. The points are derived from the $J_c(H,T)$ characterizations and the lines are the calculated dependencies using (3.35) (MDG) and (7.4). For completeness, also the Summers empirical form for the GL parameter (3.30) is included.*

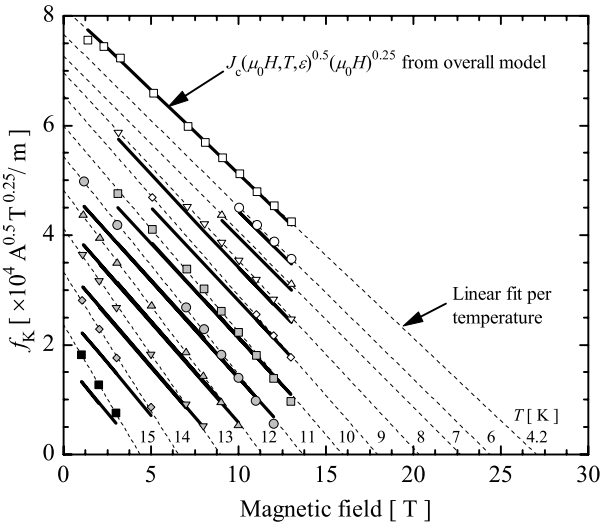

Figure 7.5 *Kramer plot of the measured $J_c(H,T)$ data, including linear fits according to (3.11) and the overall $J_c(H,T)$ fit according to (7.3) at $E_c = 10^{-5}$ V/m. The graph emphasizes the failure of the Kramer/Summers model to account for the correct slope at higher temperatures, which leads to significant deviations in the calculated $J_c(H,T)$ values.*

literature (Table 1.1). The resulting values for $\kappa_1(T)$, calculated from $F_{\mathrm{Pmax}}(T)$ and $H^*_{c2}(T)$ using (7.4) are plotted in Figure 7.4, together with the microscopic (3.35) and empirical (3.30) dependencies.

The change of $\kappa_1(T)$ of nearly 100% is unrealistic, since a maximum change of 20% is expected in the weak, and 50% in the strong coupling limit as discussed in Section 3.5.2. This is independent of the choice of C and thus $\kappa_1(0)$, since the calculations are normalized to $\kappa_1(0)$. The combination of $\nu = 2.5$ and $\gamma = 2$ therefore results in an unrealistically large change in $\kappa_1(T)$, calculated from $F_{\mathrm{Pmax}}(T)$ and $H^*_{c2}(T)$.

The Kramer function is given by (3.11) and the slope is therefore C / $\kappa_1(T)$. The large change in κ_1 with temperature thus translates to a larger change in the slope of a Kramer plot at higher temperatures. This is visualized by the Kramer plot given in Figure 7.5. The overall $J_c(H,T)$ least squares fit is optimized at 4.2 K in this graph, to emphasize the deviations that occur at higher temperatures. The error in the overall temperature dependence in the Kramer / Summers model, through the use of $\nu = 2.5$ and $\gamma = 2$, causes significant deviations in the slope of a Kramer plot at higher temperatures and thus in large errors in the calculated $J_c(H,T)$ values.

Deviations in the Kramer fit were observed also in earlier analysis [263, 264] and were attributed to incorrect (empirical) temperature dependencies of the effective upper critical field and the GL parameter. The temperature dependence of the maximum bulk pinning force was therefore taken to be unknown and ν and γ were used as free fit parameters. Now that $H^*_{c2}(T)$ and $\kappa_1(T)$ are replaced by microscopic based alternatives, it has to be concluded that the observable errors in $F_{\mathrm{Pmax}}(T)$ stem from incorrect values for ν and γ. This is supported by the unrealistic large change in the calculated κ_1 with temperature, surpassing the strong coupling limit.

7.4.2 Improved temperature dependence

In the above analysis it became clear that the temperature dependence of the bulk pinning force using $\nu = 2.5$ and $\gamma = 2$ is incorrect. It is therefore required to determine the optimal values for both constants that yield the highest accuracy for the calculation of the temperature dependence of the maximum bulk pinning force. The $F_{\mathrm{Pmax}}(T)$ data are, in the general form, described by:

$$\begin{aligned} F_{\mathrm{Pmax}}(T) &= 0.286C\frac{\left[\mu_0 H_{\mathrm{c2}}^{*}(T)\right]^{\nu}}{\kappa_1(T)^{\gamma}} \\ &= 0.286C\frac{\left[\mu_0 H_{\mathrm{c2}}^{*}(0)\right]^{\nu}}{\kappa_1(0)^{\gamma}}\mathrm{MDG}(t)^{\nu-\gamma}\left(1-t^2\right)^{\gamma}. \end{aligned} \tag{7.5}$$

Relation (7.5) is fitted against the $F_{\mathrm{Pmax}}(T)$ data from Section 7.3. Values of ν are chosen around 2.5 and the value for γ is least squares fitted. Various combinations of ν and γ are able to describe the measured $F_{\mathrm{Pmax}}(T)$, each with a specific remaining overall least squares error, as plotted in Figure 7.6. The possible combinations of ν and γ are related by $\gamma = 0.880\nu - 0.756$. The overall error shows a distinct minimum for the combination $\nu = 2$ and $\gamma = 1$ and these values therefore yield optimum accuracy for the temperature dependence of the maximum bulk pining force. Relation (7.5), using $\nu = 2$ and $\gamma = 1$ is plotted together with the $F_{\mathrm{Pmax}}(T)$ data from Section 7.3 in Figure 7.7. The accuracy in the calculated $F_{\mathrm{Pmax}}(T)$ is significantly improved compared to the use of $\nu = 2.5$ and $\gamma = 2$ in Figure 7.4.

The temperature dependence of the GL parameter, resulting from $F_{\mathrm{Pmax}}(T)$ and $H_{\mathrm{c2}}^{*}(T)$ using (7.5) with $\nu = 2$ and $\gamma = 1$ can also be calculated. The relation between C and $\kappa_1(0)$ now differs from the Kramer form (Section 3.3 (3.9), [104]). The value for $\kappa_1(0)$ is chosen consistent with the previous analysis, i.e. $\kappa_1(0) = 38.6$, leading to $C = 1.81\times10^{9}\ \mathrm{AT}^{-1.5}\mathrm{m}^{-2}$. This calculation yields a $\kappa_1(T)$ as plotted in Figure 7.7. The GL parameter now changes by about 35% which is in agreement with expectations (i.e. between 20 and 50%, see Section 3.5.2) and, moreover, follows the microscopic based description.

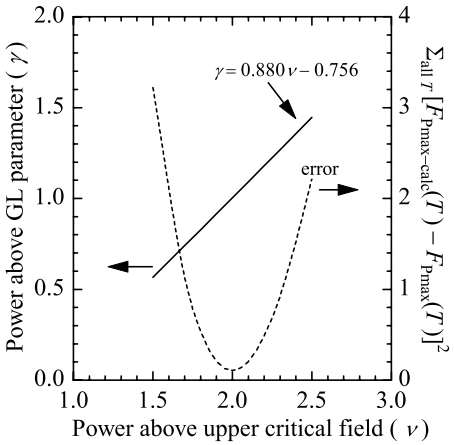

Figure 7.6 *Combinations of ν and γ and the overall least squares fit error in the maximum bulk pinning force.*

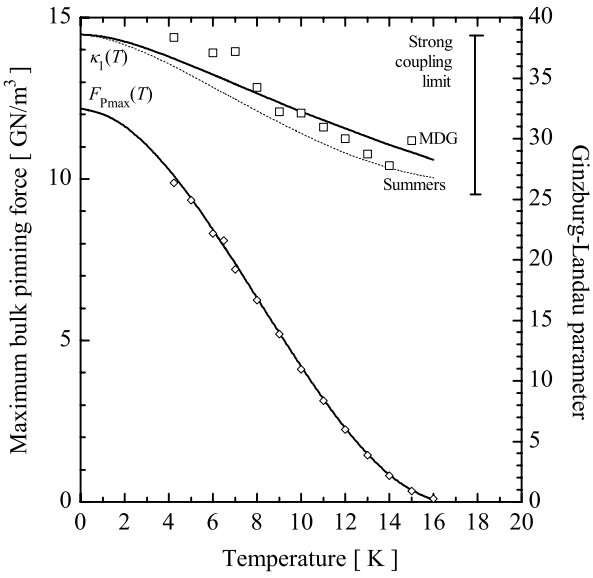

Figure 7.7 *Improved temperature dependence of the GL parameter and maximum bulk pinning force at $E_c = 10^{-5}$ V/m. The points are derived from the $J_c(H,T)$ characterizations and the lines are the calculated dependencies using (3.35) (MDG) and (7.5) with $\nu = 2$ and $\gamma = 1$. For completeness, also the Summers empirical form for the GL parameter (3.30) is included.*

The overall accuracy of the temperature dependence can again also be demonstrated using a Kramer plot. Using $\nu = 2$ and $\gamma = 1$ in (3.64) results in an overall description:

$$\begin{aligned} F_{\mathrm{p}}(H,T) &= \frac{C\left[\mu_0 H_{\mathrm{c2}}^{*}(0)\right]^2}{\kappa_1(0)} \frac{\mathrm{MDG}(t)^2}{k(t)} h^{0.5}(1-h)^2 \\ &= C_1 \mathrm{MDG}(t)\left(1-t^2\right) h^{0.5}(1-h)^2 , \end{aligned} \tag{7.6}$$

and the linear Kramer function becomes:

$$J_{\mathrm{c}}(H,T)^{0.5}\left(\mu_0 H\right)^{0.25} = \frac{C^{0.5}}{\kappa_1(T)^{0.5}\left[\mu_0 H_{\mathrm{c2}}^{*}(T)\right]^{0.25}} \mu_0\left(H_{\mathrm{c2}}^{*}(T) - H\right) . \tag{7.7}$$

Similar analysis as in the previous Section yields from the overall $J_c(H,T)$ least squares fit $C_1 = 42.6\times10^9$ AT/m^2. The small difference in C_1 compared to the Kramer / Summers form (42.8×10^9 AT/m^2) stems from the fact that in Figure 7.5 the fit was optimized for the 4.2 K results, whereas now the fit is optimized over the entire temperature range. The improved functionality yields slopes that are consistent with the measured results over the entire temperature range as is seen in Figure 7.8. The only significant deviations occur close to $H_{c2}^{*}(T)$, the regime where non-linearities in Kramer plots originate from A15 inhomogeneities (see Section 3.3).

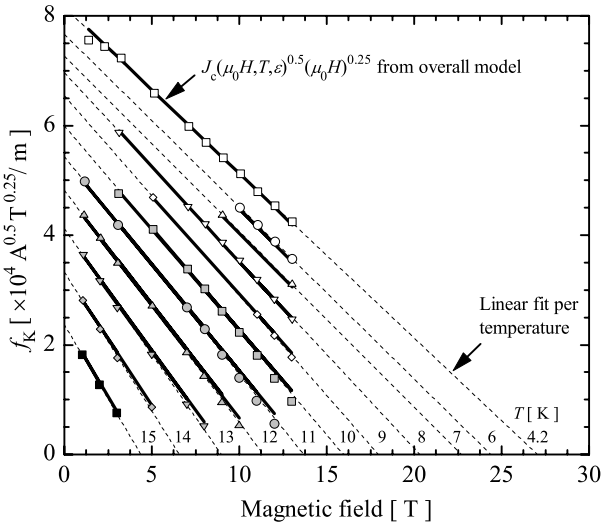

Figure 7.8 *Kramer plot of the measured $J_c(H,T)$ data at $E_c = 10^{-5}$ V/m, including linear fits according to (7.7) and the overall $J_c(H,T)$ fit according to (7.6). The improved overall temperature dependence using $\nu = 2$ and $\gamma = 1$ results in an accurate description across the entire temperature range.*

7.5 Strain dependence

Now that the magnetic field and temperature dependence are established the strain dependence is introduced by stating that the effective upper critical, the critical temperature and the GL parameter depend on strain. This leads through (3.64) to:

$$F_p\left(H,T,\varepsilon\right) = C\frac{\left[\mu_0 H^*_{c2}\left(T,\varepsilon\right)\right]^2}{\kappa_1\left(T,\varepsilon\right)} h^{0.5}\left(1-h\right)^2, \tag{7.8}$$

where $H^*_{c2}(T,\varepsilon) \equiv H^*_{c2m}(T)s(\varepsilon)$, $T^*_c(\varepsilon) \equiv T^*_{cm}s(\varepsilon)^{1/\varpi}$ and $\kappa_1(T,\varepsilon) \equiv \kappa_{1m}(T)s(\varepsilon)^{\alpha}$. It is assumed that $\varpi = 3$ since this was shown earlier to be consistent with measurements, and α has to be determined from experiment. In normalized form (7.8) becomes [through (3.64)]:

$$F_p\left(H,T,\varepsilon\right) = C_1 s\left(\varepsilon\right)^{2-\alpha} MDG\left(t\right)\left(1-t^2\right)h^{0.5}\left(1-h\right)^2, \tag{7.9}$$

where $C_1 = C\,[\mu_0 H^*_{c2m}(0)]^2 \,/\, \kappa_{1m}(0)$.

Note that this approach differs significantly from assuming a different dependence of the bulk pinning force on $H^*_{c2}(T)$ and $H^*_{c2}(\varepsilon)$, as is usually done in the literature (see Section 3.7). It will be shown below that the choice $\nu = 2$ and $\gamma = 1$, which yields the correct temperature dependence, results in a more consistent implementation of the strain dependence of the bulk pinning force.

First the function for $s(\varepsilon)$ will be determined. It will initially be assumed that $\alpha = 1$, since this is consistent with Ekin's [209] statement that $F_{Pmax}(4.2\text{ K}) \propto H^*_{c2}(\varepsilon)$, as well as earlier analysis. This choice for α has to be confirmed with experimental results. The improved and renormalized deviatoric strain model is chosen as description for $s(\varepsilon)$, i.e. relation (3.49). An accurate $J_c(H,T,\varepsilon)$ measurement with a high strain resolution is required to determine the

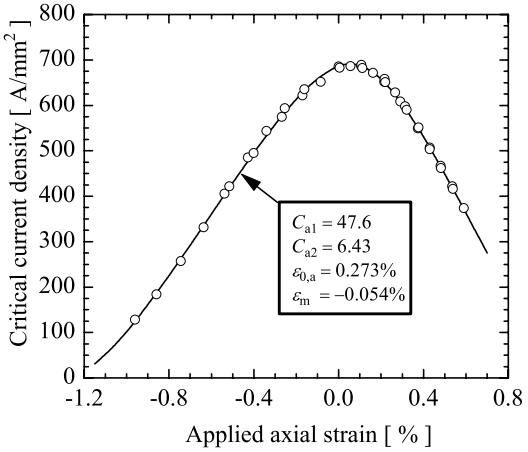

Figure 7.9 *Axial strain dependence of the critical current density at $E_c = 10^{-4}$ V/m, 12 T and 4.2 K measured on the Pacman and calculated from (7.9) and (3.49) using parameters as depicted in the graph.*

parameters in (3.49), i.e. C_{a1}, C_{a2}, $\varepsilon_{0,a}$ and ε_m. The mechanical parameters are therefore determined from the Pacman measurement on the Furukawa wire (Figure 5.17) at 12 T and 4.2 K, which are measured with the required strain resolution, as shown in Figure 7.9. The points are the $J_c(\varepsilon)$ results at 12 T and 4.2 K at a criterion of $E_c = 10^{-4}$ V/m. The line is calculated from (7.9) combined with (3.49) using the mechanical parameters depicted in the graph, $\alpha = 1$, $C_1 = 47.8$ kAT/mm^2, $\mu_0 H^*_{c2m}(0) = 30.7$ T and $T^*_{cm}(0) = 16.8$ K. It should be emphasized that C_1, $H^*_{c2m}(0)$ and $T^*_{cm}(0)$ are solely used as fit parameters to scale J_c. Since no field or temperature dependent measurements were performed on this specific sample they are arbitrary, but not unique, parameters resulting from a least squares fit of the 12 T, 4.2 K data points. As mentioned in Section 5.4.4 this sample was not heat treated together with the U-spring and barrel samples, rendering differences of a few percent in C_1, $H^*_{c2m}(0)$ and $T^*_{cm}(0)$ possible.

Figure 7.9 shows that the improved deviatoric strain model does accurately account for the measured behavior. In contrast to the original model, it is able to fit the entire strain curve and not just the compressive part, as is seen from comparison with Figure 5.17, which was calculated using the symmetric model given by (3.44). Note that the term C_{a2} effectively tilts the calculated curve around $H^*_{c2m}(T)$ at $\varepsilon_{axial} = 0$. This causes the fit values for C_{a1} and $\varepsilon_{0,a}$ to change compared to the earlier model. Overall, however, (3.49) accurately describes the strain dependence and $\alpha = 1$ in (7.9) appears to yield the correct strain dependence of the bulk pinning force.

Now that $s(\varepsilon)$ is confirmed to be accurate, $F_{Pmax}(\varepsilon) \propto s(\varepsilon)^{2-\alpha}$ has to be investigated to find the value for α from experiment. The power $2 - \alpha$ is determined by plotting the $F_{Pmax}(\varepsilon)$ values from Section 7.3 versus axial strain and comparing to $s(\varepsilon)^{2-\alpha}$. This is demonstrated in Figure 7.10 for the 4.2 K results, yielding $\alpha = 1.0 \pm 0.1$, in agreement with Ekin's result (Section 3.7.1). Similar analyses for higher temperatures suggest that α might decrease with temperature. At higher temperatures, however, the $F_{Pmax}(\varepsilon)$ analyses become significantly less accurate since they are based on much smaller current densities and limited data. Also inhomogeneity effects, which manifest themselves in the investigated magnetic field range at

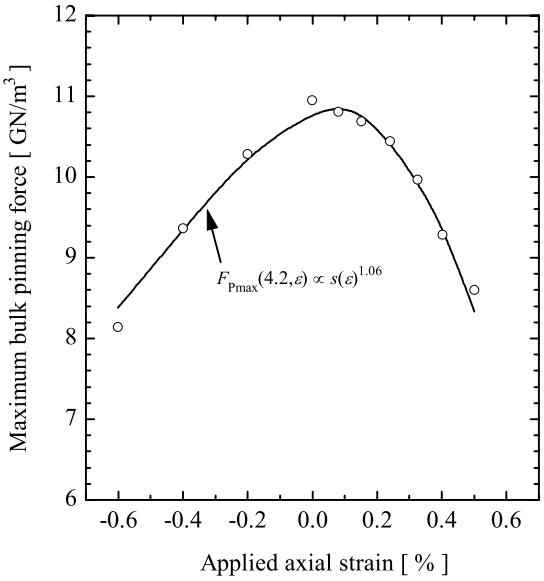

Figure 7.10 *Maximum bulk pinning force as function of applied axial strain at $E_c = 5\times10^{-4}$ V/m and 4.2 K, measured on the U-spring.*

higher temperatures, complicate a more precise determination of $2 - \alpha$. The results are therefore not sufficiently accurate to come to unambiguous conclusions on a possible temperature dependence of α. Moreover, strain dependency results are, for now, only available for inhomogeneous samples, rendering further speculations not very useful. With the available experimental results it can be assumed that $\alpha \cong 1$ for all temperatures.

It is concluded that strain dependence can be introduced in the bulk pinning force using a single dependence $F_{Pmax} \propto H_{c2}^*(T,\varepsilon)^2$, provided that $\alpha \cong 1$ for all temperatures. This is in contrast to the usual conclusion that $H_{c2}^*(T)$ and $H_{c2}^*(\varepsilon)$ have different dependencies (Section 3.7.1). This single function is enabled through the use of an overall temperature dependence that accurately agrees with measured results and by including the strain dependence of the GL parameter.

7.6 Overall scaling of measured results

7.6.1 Scaling relation for the critical current density

In the previous Sections an overall scaling function for $F_P(H,T,\varepsilon)$ was postulated and confirmed by systematic analysis of the separate dependencies on magnetic field, temperature and strain. The proposed function is given by (7.9), with $\alpha \cong 1$.

Solving the implicit Maki-De Gennes relation can be avoided by using its approximation $\mathrm{MDG}(t) \cong (1 - t^{1.52})$ which is sufficiently accurate for practical applications. As described before in Section 3.4.2, this approximation does not yield the correct slope at T_c, but has optimal accuracy over the entire temperature range. Using this approximation changes the overall function to the simple form:

$$J_c(H,T,\varepsilon) \cong \frac{C_1}{\mu_0 H} s(\varepsilon)\left(1-t^{1.52}\right)\left(1-t^2\right)h^{0.5}(1-h)^2,$$

with

$$C_1 = C\left[\mu_0 H^*_{c2m}(0)\right]^2 \Big/ \kappa_{1m}(0)$$

$$t \equiv T/T^*_c(\varepsilon), \quad h \equiv H/H^*_{c2}(T,\varepsilon),$$

$$H^*_{c2}(T,\varepsilon) \cong H^*_{c2m}(0)\, s(\varepsilon)\left(1-t^{1.52}\right), \tag{7.10}$$

$$T^*_c(\varepsilon) = T^*_{cm} s(\varepsilon)^{\frac{1}{3}},$$

$$s(\varepsilon_{axial}) = \frac{C_{a1}\left[\sqrt{(\varepsilon_{shift})^2+(\varepsilon_{0,a})^2} - \sqrt{(\varepsilon_{axial}-\varepsilon_{shift})^2+(\varepsilon_{0,a})^2}\right] - C_{a2}\varepsilon_{axial}}{1-C_{a1}\varepsilon_{0,a}} + 1,$$

$$\varepsilon_{shift} = \frac{C_{a2}\varepsilon_{0,a}}{\sqrt{(C_{a1})^2-(C_{a2})^2}}.$$

where $\varepsilon_{axial} = \varepsilon_{applied} + \varepsilon_m$. The superconducting parameters C_1, $H^*_{c2m}(0)$ and $T^*_{cm}(0)$ and the deformation related parameters C_{a1}, C_{a2}, $\varepsilon_{0,a}$ and ε_m have to be determined experimentally.

7.6.2 Overall $J_c(H,T,\varepsilon)$ scaling

The new scaling relation will now be applied to the entire Furukawa wire dataset $J_c(H,T,\varepsilon)$ to summarize its overall capability. An overall least squares fit to the measured results for the two barrel samples and one U-spring sample, which were all heat treated simultaneously, results in the superconducting parameters given in Table 7.2.

Table 7.2 *Overall parameters for the calculation of $J_c(H,T,\varepsilon)$ at $E_c = 5\times10^{-4}$ V/m.*

Deformation related parameters					Superconducting parameters		
C_{a1}	C_{a2}	$\varepsilon_{0,a}$ [%]	$\varepsilon_{m\text{-Barrel}}$ [%]	$\varepsilon_{m\text{-U-spring}}$ [%]	$\mu_0 H^*_{c2m}(0)$ [T]	$T^*_{cm}(0)$ [K]	C_1 [kAT/mm^2]
47.6	6.4	0.273	–0.153	–0.045	30.7	16.8	46.3

The mechanical parameters in Table 7.2 were derived from a fourth sample measured on the Pacman, as was described in Section 7.5. The fit to the $J_c(H,T)$ results is plotted in Figure 7.11. The calculated dependence follows the measured results accurately, justifying the overall relation for $J_c(H,T)$. The accuracy in the strain dependence is demonstrated at $\mu_0 H = 10$ T and at $T = 8$ K. These results are plotted in Figure 7.12. Deviations occur mainly at very low critical current densities (below 10 A/mm^2 which corresponds to $I_c = 2$ A) and at high tensile strains. The accuracy at low current density depends on the uncertainty in the parallel current subtractions.

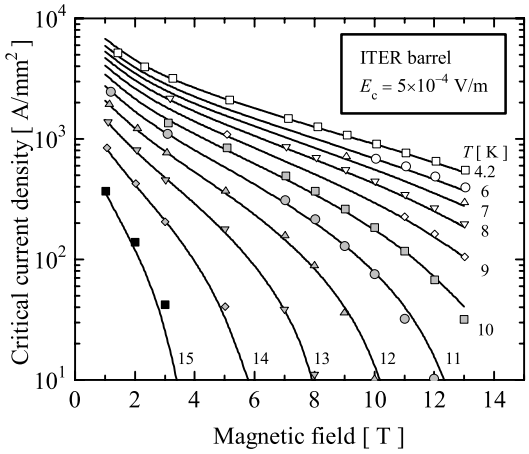

Figure 7.11 *Critical current density as function of magnetic field at temperatures from 4.2 to 15 K. The points are measured on the ITER barrel and the lines are calculated with (7.10).*

It is possible to achieve a slightly better fit on the U-spring results by allowing C_1 for the U-spring data to differ from the barrel results as was done previously [163]. Also the mechanical parameters derived on the Pacman might not be optimal for the U-spring due to small differences in overall mechanical behavior.

Such details can change the achievable accuracy and slightly modify the obtained optimal fit parameters given in Table 7.2 by a few percent. These are, however, more related to subjective choices in the fit analysis, the reproducibility across multiple characterization methods and samples as well as measurement accuracies in general.

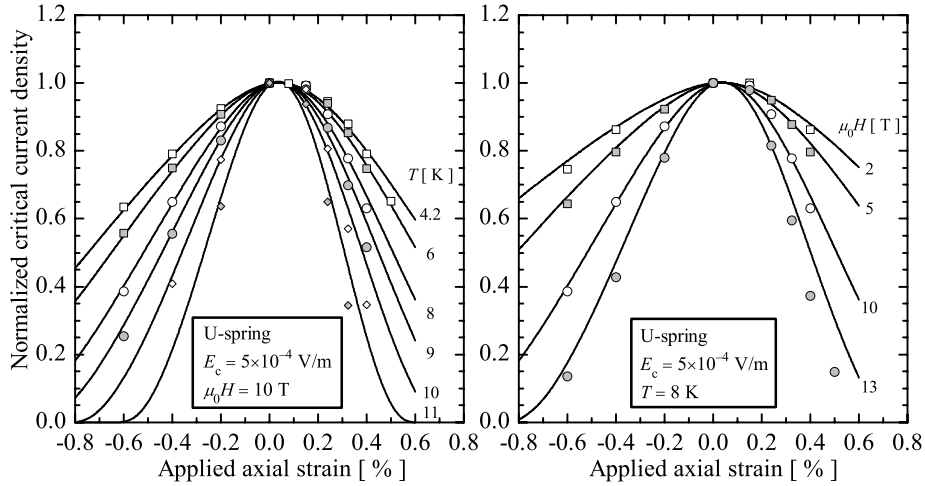

Figure 7.12 *Critical current density as function of strain for various temperatures at 10 T (left) and for various magnetic fields at 8 K (right). The points are measured on the U-spring and the lines are calculated with (7.10).*

The overall accuracy of a similar function that used the earlier deviatoric strain model (3.44) was investigated extensively in previous work and it was concluded that a standard deviation below 2% could be obtained [157]. The validity range is up to $h \cong 0.8$, i.e. the magnetic field at which inhomogeneity effects start to appear.

7.7 Discussion

7.7.1 Scaling accuracy

Through systematic comparison with measured results deficiencies in existing scaling relations can be highlighted. Improvements can, however, only be made empirically through a change of the bulk pinning force dependency on both $H_{c2}^{*}(T)$ and $\kappa_1(T)$ simultaneously. The resulting relation describes the measurements accurately (also for a multitude of other wires). The values $\nu = 2$ and $\gamma = 1$ are similar to those found earlier [111, 162, 163] through minimization of the error in the overall $J_c(H,T,\varepsilon)$ least squares fit. In the earlier analysis it was assumed that the deviating values for ν and γ originated from a wrong temperature dependence of the effective upper critical field and the GL parameter. It is now concluded that the Kramer form, which results from the Labusch [195] function for C_{66} (see Section 3.3), is in fact not accurate. These theories have been questioned in the literature, specifically by Brandt [187] and Dew-Hughes [138], emphasizing the difficulties in understanding and modeling the flux-line to pinning site interactions. A reasonable temperature dependence description can be achieved for the combinations $\gamma = 0.880\nu - 0.756$, but the overall error shows a distinct minimum at $\nu = 2$ and $\gamma = 1$. For a proper connection to theory these values should result from a fundamental form of these interactions. At present, to the author's knowledge, such a model is not available.

In the literature the value of ν, i.e. the power above $H_{c2}^{*}(T)$ in the pinning relation, is often determined through the use of a double logarithmic plot while neglecting the temperature dependence of the GL parameter. The resulting slope is then claimed to be the correct value for ν. Since, however, the change in κ_1 with temperature is about 35% this will result in a wrong dependence and values that deviate from 2 will be found. Such methods for the determination of ν are thus in error since both $H_{c2}^{*}(T)$ and $\kappa_1(T)$ should be considered simultaneously.

The validity of the new scaling relation was tested on a database derived from four samples, one of which was heat treated separately. The samples were characterized in three experimental setups. Deriving a singular parameter set for the Furukawa wire is complicated by small differences between the samples and characterization methods. A better fit to the U-spring strain results alone can for example be found by the use of slightly different parameters. This stems from small, for now unclear, differences between the separate samples and also from the stronger measured J_c reduction on the U-spring at high tensile strains in comparison to the Pacman results as can be seen from Figure 5.17. The latter might be an artifact of the U-spring device. These errors render an unambiguous determination of the scaling parameters for the Furukawa wire not possible. To do this, the uncertainties that arise from a multiple sample set and the use of different characterization instruments should be removed. Ideally all measurements should be performed on a single instrument and on a single wire and at one single, low criterion. The latter is preferred to remove inaccuracies arising from the parasitic current subtraction and for consistency with the "standard" criterion $E_c = 10^{-5}$ V/m. Such measurements could for example be done on the Pacman strain device, which allows for high

transport currents in combination with elevated temperatures and sufficient sample length for the required electric field resolution.

The observation that strain sensitivity of the critical current density increases with magnetic field and temperature could indicate that strain sensitivity depends on A15 composition. At higher magnetic field or temperature only the high-Sn content A15 sections carry superconducting current, whereas at lower magnetic field and temperature also the low Sn content regions are superconducting. This could suggest that strain sensitivity increases with Sn content. It was concluded by Ekin in [19], on the basis of $J_c(\varepsilon)$ measurements at 4.2 K on various binary and ternary wires, that strain sensitivity increases for wires with significant ternary additions. Unpublished data on binary and ternary PIT wires indicates, however, exactly the opposite, i.e. ternary wires show a reduced strain sensitivity of J_c. The strain sensitivity is, however, defined through $ds(\varepsilon) / d\varepsilon = dH^*_{c2}(\varepsilon) / d\varepsilon$ [and not $dJ_c(\varepsilon) / d\varepsilon$] and thus by the strain sensitivity of the effective upper critical field (or similarly the critical temperature). and might be influenced by the magnitude of $H^*_{c2m}(0)$. A fair comparison of ternary and binary wires should therefore occur through $s(\varepsilon)$ by determining the strain sensitivity of $H^*_{c2}(0)$ and not of J_c alone. This could remove the apparent contradiction between Ekin's results and the unpublished PIT results. How composition effects influence strain sensitivity is unknown and should be determined on well defined homogeneous samples for a better understanding of observed behavior in inhomogeneous systems such as wires.

7.7.2 Minimum required dataset

With a scaling relation available the question arises as to what is the minimum dataset needed to retrieve the critical current density. For the temperature dependence two $H^*_{c2}(T)$ points are required to determine the entire $H^*_{c2}(T)$ dependence through the MDG relation. These should be determined by transport J_c measurements since these yield the correct effective upper critical field required for scaling. From Figure 7.8 it can be seen that preferably at both ends of the temperature range the slope of the Kramer plot has to be determined to extrapolate to $H^*_{c2}(T)$. This is most simply done by a $J_c(H)$ measurement at 4.2 K at a few magnetic field values to check for linearity and thus validate the choice of $q = 2$. In addition this should be done at a higher temperature, e.g. 12 K might be a good compromise between temperature range and available magnetic field in a laboratory magnet. Non-linearities above $h = 0.8$ should be neglected since they most probably result from inhomogeneities. The results can then be extrapolated linearly in a Kramer plot to yield H^*_{c2}(4.2 K) and H^*_{c2}(12 K). The Maki-De Gennes relation or its approximation then yields $H^*_{c2}(0,\varepsilon = \varepsilon_m)$ and $T^*_c(0,\varepsilon = \varepsilon_m)$. $J_c(H,T,\varepsilon = \varepsilon_m)$ is known through (7.10) using a least squares fit to the J_c dataset. The strain dependence can then be determined by a 4.2 K strain measurement with sufficient strain resolution to accurately determine the mechanical parameters (e.g. as in Figure 7.9). The magnetic field for the strain characterization should preferably be chosen such, that over the entire strain range of interest, the critical current remains above about 10 A to avoid inaccuracies at low current measurements. The entire critical surface up to the magnetic field where inhomogeneity effects start to appear (i.e. $h \cong 0.8$) is then known. The characterizations should preferably be done using one sample and one instrument to avoid experimental errors.

The required dataset can thus be summarized as follows:

1. An $I_c(H)$ measurement at 4.2 K from about 5 T up to the maximum available magnetic field (see Figure 7.8), preferably 12 to 15 T.

2. An $I_c(H)$ measurement at about 12 K from 1 T or as low as possible, up to the maximum available magnetic field. The selectable temperature depends on the available magnetic field range (see Figure 7.8).
3. An $I_c(\varepsilon)$ measurement at 4.2 K and at a magnetic field where the critical current remains significant (e.g. > 10 A) over the entire strain range of interest (see Figure 7.9).

The first two datasets will yield two $H_{c2}^*(T)$ points that determine the full field-temperature scaling boundary and extrapolate, using the MDG relation (or its approximation), to yield $H_{c2}^*(0)$ and $T_c^*(0)$. Additionally the pre-constant C_1 results from these datasets. The strain measurement then finally delivers the mechanical parameters and the critical surface is determined.

7.8 Estimate of the J_c reduction through Sn deficiency

From the composition analysis in Chapter 4 it is clear that A15 in wires is never uniform and much of the layer is far from stoichiometric. The question arises how much J_c is lost through the observed Sn deficiency in the A15 sections. To answer this, an estimate will be given on the basis of simulations and measured results on a ternary PIT wire (B34, reacted for 64 h at 675 °C).

7.8.1 Simulations

Cooley *et al.* [197] have shown recently through simulation that the Kramer extrapolated upper critical field can be estimated from measured Sn gradients in PIT wires. For this, a model was developed that assumes parallel current paths of different A15 composition, as was summarized in Section 3.3. A PIT filament can then be modeled by assuming thin concentric shells of constant, but radially varying, composition. The Kramer extrapolated upper critical field is then found by a weighted summation of the local upper critical field in the shells. A similar analysis will be performed here (and also for T_c) based on the measured Sn gradients as function of radial position in the ternary PIT wire from Figure 4.12.

The EDX measured Sn gradients for three filaments are reproduced in the upper left graph in Figure 7.13. Since the EDX results are measured in an uncalibrated SEM, the measured Sn content is shifted by +1.5 at.% Sn, to force the core-A15 interface to the stoichiometric composition and yield a maximum $T_c(0)$ of about 18 K, close to the maximum value detected by the resistive measurements in Chapter 6. The A15 layer is present from $r_{min} = 12$ µm to $r_{max} = 22$ µm, where r represents the radial position with respect to the filament centers. The average atomic Sn content as function of radius is approximated by:

$$\beta(r) = \frac{1.2\times10^{-4} r}{-22.1 + r} - 3.23\times10^{-3} r + 0.295\,, \qquad (7.11)$$

which is represented by the bold curve in the upper left graph in Figure 7.13. The critical temperature as function of atomic Sn content is assumed to follow the results of Devantay *et al.* [30] which, as described in Section 2.4, can be summarized by (2.10). For the upper critical field as function of atomic Sn content two dependencies are assumed. The first includes the tetragonal phase transition and is described by the function that summarizes the literature results

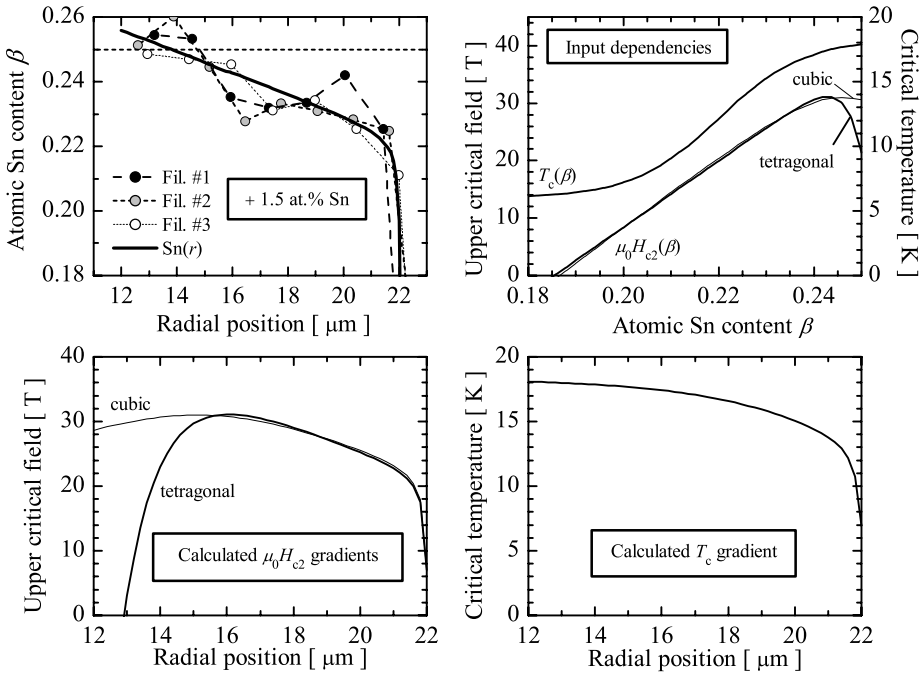

Figure 7.13 *Simulations of H_{c2} and T_c as function of radial position in a ternary PIT filament (B34-64 h, Figure 4.10). The calculated dependencies are based on EDX measured Sn gradients and literature dependencies of $H_{c2}(\beta)$ and $T_c(\beta)$.*

(2.11) as discussed in Section 2.4. The second dependence assumes that the A15 remains in the cubic phase (e.g. through the presence of Ta) and is given by:

$$\mu_0 H_{c2}(\beta) = 31\frac{1-16.5\sqrt{(\beta-0.246)^2+1.44\times10^{-4}}}{0.802}. \qquad (7.12)$$

The $T_c(\beta)$ and cubic and cubic + tetragonal $H_{c2}(\beta)$ input functions are plotted in the upper right graph in Figure 7.13. The upper critical field and critical temperature can be calculated as function of position using $H_{c2}[\beta(r)]$ and $T_c[\beta(r)]$ as given by (2.10), (2.11), (7.11) and (7.12). The resulting $H_{c2}(r)$ and $T_c(r)$ are plotted in lower graphs in Figure 7.13.

The effective upper critical field and critical temperature can now be calculated using the area weighted averages:

$$\mu_0 H_{c2}^* = \frac{2}{r_{max}^2 - r_{min}^2}\int_{r_{min}}^{r_{max}} r\mu_0 H_{c2}(r)dr \quad \text{and} \quad T_c^* = \frac{2}{r_{max}^2 - r_{min}^2}\int_{r_{min}}^{r_{max}} rT_c(r)dr. \qquad (7.13)$$

This results in $\mu_0 H_{c2}^*(0) = 22.4$ T for the cubic + tetragonal $H_{c2}(\beta)$ dependence, $\mu_0 H_{c2}^*(0) = 27.5$ T for the cubic $H_{c2}(\beta)$ dependence and $T_c^*(0) = 16.1$ K. Both effective values

therefore show a significant reduction compared to the stoichiometric values of about 30 T and 18 K. In an ideal, homogeneous, A15 layer the $\beta(r)$ is flat and close to stoichiometric and both $\mu_0 H_{c2}(r)$ and $T_c(r)$ are constant at about 30 T and 18 K. To investigate how much J_c reduction occurs as a consequence of the Sn gradient in actual wires, a J_c measurement at high magnetic field can be combined with a resistive measurement. The first will yield the effective upper critical field for J_c and the second delivers the maximum observed, or ideal value, as described in Chapter 6.

7.8.2 Measurements

A Kramer plot of a high magnetic field $J_c(H)$ measurement at 4.2 K on a ternary PIT wire (B34-64 h) is combined with a resistive $\rho(H)$ transition measurement at 4.2 K on the same wire in the left graph in Figure 7.14. The J_c sample was mounted with Stycast® epoxy on a helical Ti-6Al-4V barrel with reduced diameter and the resistive sample was mounted in an identical way on a Ti-6Al-4V substrate as described in Section 5.5 to reproduce the same strain state. The Kramer plot of the J_c data is highly linear, almost up to $H^*_{c2}(4.2\ \mathrm{K})$. The extrapolated value for $\mu_0 H^*_{c2}(4.2\ \mathrm{K}) = 24.9$ T, is in agreement with Kramer extrapolations on magnetic (VSM) results at 4.2 K found by Fischer [144]. His sample was measured in the range $\mu_0 H = 6$–14 T,

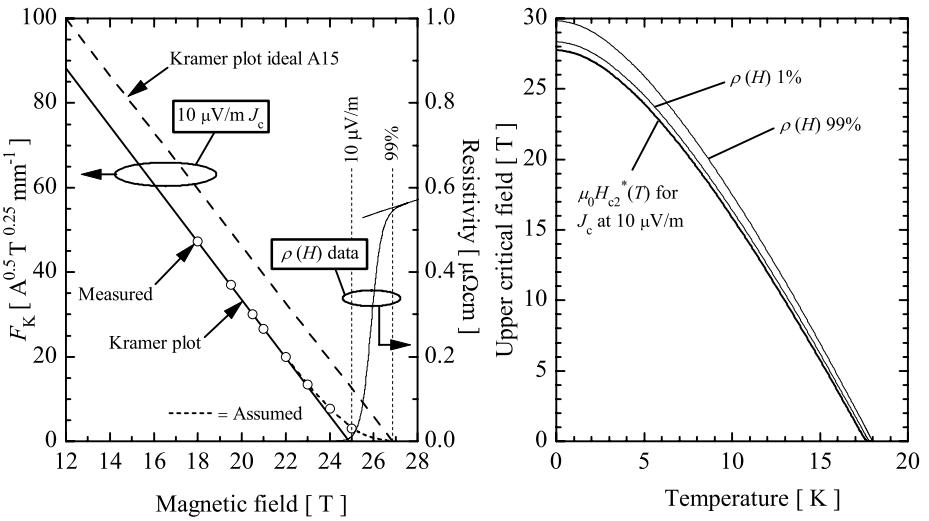

Figure 7.14 *Left: Kramer plot derived from high magnetic field transport J_c measurements at 4.2 K and $E_c = 10^{-5}$ V/m on a small diameter Ti-6Al-4V barrel for a ternary PIT wire (B34), reacted for 64 hours at 675 °C. Also a small current resistive transition at 4.2 K on a Ti-6Al-4V mounted sample (reacted together with the barrel sample) is included. The J_c data extrapolation (short dots) assumes a gradual reduction to $H_{c2\text{-}99\%}(4.2\ \mathrm{K})$ of the resistive transition. The ideal Kramer line (long dots) assumes a hypothetical ideal A15 layer with perfectly homogeneous properties equal to the measured $H_{c2}(T)_{\text{-}99\%}$ phase transition. Right: The approximate effective field-temperature boundary that is required for critical current density scaling in comparison to the resistively measured $H_{c2}(T)$ results.*

showed perfect Kramer linearity and also extrapolated to $\mu_0 H_{c2}^*(4.2\ \mathrm{K}) = 25$ T. This indicates a straight Kramer plot from 6 T to about 23 T, the magnetic field value for which the critical current measurement starts to deviate from linear Kramer behavior. The observed linearity and small tail for this PIT wire are in agreement with recent modeling using actual measured Sn gradients as input data [197].

Two particular points of the resistive transition are important: One occurs at 10 μV/m, the voltage criterion used in the transport J_c characterization, and one at 99% of the normal state resistance, identifying the highest observed value for $H_{c2}(4.2\ \mathrm{K})$. The 10 μV/m point on the resistive transition represents a critical current density of 0.2 A/mm^2 at 4.2 K and about 25 T (the excitation current) and yields $0.2^{0.5}25^{0.25} = 1\ \mathrm{A}^{0.5}\mathrm{T}^{0.25}$ on the axis of the Kramer function. The transport J_c results at 4.2 K and 25 T yield 3 $\mathrm{A}^{0.5}\mathrm{T}^{0.25}$, which is a good agreement.

The linear Kramer extrapolation of the measured J_c yields $\mu_0 H_{c2}^*(4.2\ \mathrm{K}) = 24.9$ T as the effective upper critical field for $J_c(4.2\ \mathrm{K})$. The highest $\mu_0 H_{c2}(4.2\ \mathrm{K})$ detected in the resistive transitions, yields 26.9 T for 99% normal state resistivity. The hypothetical $J_c(4.2\ \mathrm{K})$ gain can now be estimated. This would be achieved if the entire A15 layer would be of the highest $H_{c2}(4.2\ \mathrm{K})$ quality and grain size and grain boundary densities could be retained, in a way similar as recently done by Cooley *et al.* [197]. This is done by calculating the increase in $J_c(12\ \mathrm{T}, 4.2\ \mathrm{K})$ using the scaling relation given by (7.10). The ratio $C / \kappa_{1m}(0)$ is a constant and $\mu_0 H_{c2}^*(4.2\ \mathrm{K}) = 24.9$ T. Increasing the effective upper critical field from 24.9 to 26.9 T at 4.2 K would result in a rise in non-Cu $J_c(12\ \mathrm{T}, 4.2\ \mathrm{K})$ from 2250 A/mm^2 to about 2900 A/mm^2. This indicates that the non-Cu area in this PIT wire carries about 78% of what would hypothetically be achievable.

A Kramer extrapolated $\mu_0 H_{c2}^*(4.2\ \mathrm{K}) = 24.9$ T arises from a MDG fit using $\mu_0 H_{c2}^*(0) = 27.7$ T and $T_c^*(0) = 17.6$ K. This $H_{c2}^*(0)$ value is close to the estimated value for the cubic $H_{c2}(\beta)$ dependence in the simulation above (27.5 T). The agreement depends somewhat on the assumed error in the SEM-EDX results and the assumed cubic $H_{c2}(\beta)$. The effective upper critical field of 22.4 T taken from the literature dependence which includes the tetragonal transition, is certainly too low. This is a strong indication that the A15 remains in the cubic phase close to the stoichiometric composition, presumably through the Ta addition. The MDG fit value $T_c^*(0) = 17.6$ K is, however, significantly higher than $T_c^*(0) = 16.1$ K found from the simulation in Section 7.8.1. It is unclear why this difference occurs. Measurements of $J_c(H,T)$ are required to identify which effective critical temperature is suitable for scaling of J_c in this sample but unfortunately these are not available.

The effective values for J_c scaling found by either the simulation or by the high field characterizations are in any case both lower than the result from the lower resistive transition at 1% normal state resistance which yields $\mu_0 H_{c2}(0) = 28.3$ T and $T_c(0) = 17.8$ K as MDG fit values. This indicates that the values required for critical current density scaling are slightly below the range of transitions that are detected in the resistive characterizations. This is indicated in the right graph in Figure 7.14, where the highest- and lowest $H_{c2}(T)$ transitions detected resistively are plotted together with the effective transition that appears appropriate for J_c scaling.

7.9 Maximized critical current density in present wire layouts

An even higher limit for the present generation PIT wires can be estimated after having established the $J_c(12\mathrm{T}, 4.2\ \mathrm{K})$ gain that can be achieved if all A15 is of the highest observed

quality. The J_c(12T, 4.2 K) value of about 2900 A/mm^2 corresponds to the maximum field-temperature boundary based on the resistive measurements, i.e. $\mu_0 H_{c2}(0) = 29.7$ T and $T_c(0) = 17.9$ K as was given in Table 6.2. This determines the critical surface of an A15 ternary PIT wire mounted on Ti-6Al-4V through (7.10) with $C_1 \cong 200$ kAT/mm^2, $\mu_0 H_{c2}^*(0) = 29.7$ T and $T_c^*(0) = 17.9$ K for $s(\varepsilon) = 1$, i.e. any strain that is present is included in the values for the parameters.

In the present PIT wire only part of the Nb(Ta) is actually reacted (see Figure 4.1), and only about 40% of the non-Cu cross-section contains fine grain A15. If the remaining Nb(Ta) could be reacted and be of ideal A15 quality then 65% of the non-Cu cross-section would be A15. The J_c(12T, 4.2 K) could then increase to about 4700 A/mm^2 and $C_1 \cong 325$ kAT/mm^2 (C_1 is an area controlled parameter). Ultimately, if also the large grain area could be prevented and be fine-grain, ideal A15 then 75% of the non-Cu is A15 and J_c(12T, 4.2 K) can increase to about 5400 A/mm^2 and $C_1 \cong 375$ kAT/mm^2. The 25% core residue cannot be prevented since it has to provide the Sn. A final gain could be achieved by grain size reductions or pinning quality optimizations. The achievable gain through grain size reduction can be calculated using (2.14) or (2.15). If the average grain size could be halved from about 150 nm to about 75 nm, an additional J_c increase of about 50% could be expected.

The discussion above shows that the present wires perform well below their upper limits. Optimization of A15 Sn content, A15 area and grain refinement could result in more than 5 kA/mm^2 at 12 T and 4.2 K. Off course this improvement is not yet foreseeable, but it defines an upper limit to the achievable critical current density in the present generation wires. The upper limit is thus stated at the level of 5 kA/mm^2, for which the critical surface is described by $\mu_0 H_{c2}^*(0) = 29.7$ T, $T_c^*(0) = 17.9$ K and $C_1 \cong 350$ kAT/mm^2.

7.10 Conclusions

A systematic comparison of measured critical current as function of magnetic field, temperature and strain with scaling relations has shown that flux-line shear can be assumed to be the main de-pinning mechanism and that tails in Kramer plots can reasonably be attributed to A15 inhomogeneities. This results in a validation of the magnetic field dependence of the Kramer form, i.e. $F_P \propto h^{0.5}(1-h)^2$ within the range $0.05 < h < 0.8$, in which h represents the reduced magnetic field.

Through the analysis of the magnetic field and temperature dependence of the bulk pinning force it was shown that the Kramer / Summers form, i.e. $F_P \propto [H_{c2}(T)]^{2.5} / \kappa_1(T)^2$, fails to describe the observed temperature dependence with sufficient accuracy. The suggestion that this followed from an empirical temperature dependence of the upper critical field and the GL constant was contradicted through the use of microscopic based relations for both. The change in $\kappa_1(T)$ in the Kramer / Summers form is significantly larger than 50% as is expected from microscopic theory in the strong coupling limit. The improved temperature dependence of the form $F_P \propto [H_{c2}(T)]^2 / \kappa_1(T)$ does accurately describe the measurements. The resulting change in $\kappa_1(T)$ follows the microscopic form and is within the strong coupling limit. The new dependency is in disagreement with existing relations for the flux-line shear modulus C_{66}. It is suggested that the temperature dependence of C_{66} given by Labusch needs to be reevaluated.

The new temperature dependence of the bulk pinning force allows for an unambiguous introduction of the strain dependence of the bulk pinning force, without the need to include separate functions to describe the strain dependent upper critical field and temperature

dependent upper critical field, as is usually done in the literature. The measurements indicate that the Ginzburg-Landau parameter has similar strain dependence as the upper critical field.

The improved deviatoric strain model, which includes asymmetry, was tested and confirmed to yield a highly accurate description of measured behavior. Strain dependence is only analyzed in terms of axial strain and using inhomogeneous systems. Future strain experiments on well defined, compositionally homogeneous bulk samples are needed to remove the uncertainties related to strain dependence as function of A15 composition. This can also yield a thorough confirmation of the full invariant analysis. Such an analysis should concentrate on the shift in the field-temperature phase boundary with strain, to determine why the effective upper critical field changes significantly faster with strain than the critical temperature.

Simulations based on measured A15 compositions combined with high magnetic field transport $J_c(H)$ and resistive characterizations indicate that the present generation of PIT wires carry about 80% of the J_c(4.2 K,12 T) that can be achieved if all A15 were of the stoichiometric, fine-grain composition. Further efficiency increase through optimization of the A15 in the non-Cu area and grain refinement yields an estimated performance limit of about 5 kA/mm^2 at 4.2 K and 12 T.

Chapter 8

Conclusions

In the previous Chapters topics important for understanding of the current carrying capability in Nb_3Sn wires, were discussed. These included a review of the available literature on well defined binary A15 Nb_3Sn samples and of descriptions for the critical surface, investigations of the A15 formation and compositional gradients in wires, investigations of the upper critical field of wires and the scaling behavior of the critical current with magnetic field, temperature and axial strain. In this Chapter the findings of the previous Chapters and overall conclusions are summarized. The Chapter ends with recommendations for further research.

8.1 Upper limit for the critical current density

The main question that formed the basis for this research, i.e. what are the maximum current carrying capabilities in the present generation Nb_3Sn multifilament wires, can quantitatively be answered. The performance limiting factors are identified to be A15 compositional variation, grain size limitation of flux pinning, and optimization of the non-Cu area fraction used for A15 formation. A hypothetical wire can be constructed in which reduction of the Sn gradients, non-Cu area efficiency optimization, and grain size reduction all are incorporated.

The discussions in Chapter 7 show that the exact value of the performance limit depends on which improvements are regarded to be realistic from a wire manufacturing point of view. It is reasonable to expect that an optimal A15 composition throughout the entire cross-section is not realistic, due to the fact that heat treatments will always be a compromise between A15 enrichment and grain size limitation, which place contradictory demands on the reaction. The presence of strain introduces an additional uncertainty. Axial strain can be modeled rather well, but the three dimensional nature of strain complicates analysis of the strain dependence of the critical current density. A main question that remains unsolved on a fundamental level is why the upper critical field shows relatively a stronger suppression with strain than the critical temperature, which might for example be attributed to strain induced tetragonal distortions of the A15 lattice. Furthermore, there are indications that the strain sensitivity increases with increasing Sn content in the A15. This means that gains in critical current density, achieved through Sn enrichment of the A15, can possibly be achieved only at the cost of increased strain sensitivity. Until strain sensitivity and its relation to A15 composition is well described, this remains an open issue.

It should further be emphasized that it is easy to construct an idealized wire through calculations, but that this does not imply that such a wire can actually be made. Optimization of the A15 regions in PIT processed wires, for example, would in practice mean that more Sn should be made available in the core, Sn depletion of the core-A15 interface should be overcome, and poisoning of the Cu matrix by diffused Sn should be prevented through inclusion of a Sn diffusion barrier around each filament. These modifications will significantly change the optimal extrusion and wire drawing procedures for billets, which are both already very complicated and highly specialized processes.

The performance boundary for existing manufacturing techniques is therefore not exactly determined and depends on which optimizations can be practically achieved. In Section 7.9 the performance limit, using a PIT processed model wire and assuming a realistic combination of optimizations, was estimated at 5 kA/mm^2 non-Cu J_c at 12 T and 4.2 K. The entire $J_c(H,T,\varepsilon)$ critical surface is then described by scaling relations and defined by $\mu_0 H_{c2}^*(0) = 29.7$ T, $T_c^*(0) = 17.9$ K and $C_1 \cong 350$ kAT/mm^2 in relation (7.10). A realistic development target is estimated as 4 kA/mm^2 non-Cu J_c at 12 T and 4.2 K.

8.2 Scaling relations for the critical current density

It was shown in Chapter 3 and Chapter 7 that existing scaling relations for the critical current density with magnetic field, temperature and strain can significantly be improved upon. The basis of these improvements is the central assumption that for each composition, the bulk pinning force scales with $(1-h)^2$. This is assumed to be valid for all practical conductors where the flux-line spacing is much smaller that the average grain size (i.e. an average grain

size of about 100 nm or larger). For $F_P \propto (1-h)^2$, linear Kramer plots are observed. Such linearity is indeed observed for most practical wires throughout the literature.

The bulk average critical field, at which the critical current density extrapolates to zero, is then a weighted average of the local upper critical field which depends on Sn content and thus on position. Composition gradients translate into non-linearities in Kramer plots when approaching the maximum upper critical field. In one extreme, a parallel connection of better and worse A15 sections can be assumed, which results in a decreasing slope in Kramer plots when approaching the maximum upper critical field that is present in the wire. In the other extreme, a serial connection of better and worse A15 sections can be assumed, resulting in an increasing slope when approaching the maximum upper critical field in the wire. It is found that the PIT processed wires behave according to the parallel model, whereas bronze processed wires roughly behave according to a serial model. This is explainable from the filament cross-sections, which show a much more regular cross-section for the PIT processed wires than for the bronze processed wires. In the latter, a parallel path of better A15 quality is therefore less likely for high current densities.

The assumption that the bulk critical field is a weighted average of the local upper critical fields is supported by models on the PIT processed wire and the observation in Chapter 6 that the highest $H_{c2}(T)$ in all ternary wires is very similar. The observation that the best properties are similar implies that differences in the bulk critical field originate from differences in Sn gradient between wires.

The fact that Kramer plots are generally highly linear down to very low magnetic fields (until the flux-line spacing becomes comparable to the average grain size), results in a magnetic field scaling of the bulk pinning force according to $F_P \propto h^{0.5}(1-h)^2$. When inhomogeneities are neglected, however, a numerical fit to the observed field dependence will result in an apparent different pinning behavior with deviating powers ($p \neq 0.5$ and $q \neq 2$). Arbitrary fit parameters, though experimentally useful, break down the generality of the behavior postulated here and hide the important effects introduced by the generally ignored but always present compositional inhomogeneities that are a central conclusion of this thesis.

Through comparison to the measured temperature dependence of the critical current density it is concluded that the Kramer/Summer form for the temperature dependence, i.e. $F_P \propto [H_{c2}^*(T)^{2.5} / \kappa_1(T)^2]f(h)$ (which stems from the Labusch form for C_{66}), is inadequate. This is visualized through large deviations for the calculated pinning force at higher temperatures and through the fact that the resulting Ginzburg-Landau parameter changes significantly more with temperature than can be expected, even in the strong coupling limit.

It was assumed in earlier work that such deviations in the Kramer/Summers form could result from an incorrect empirical temperature dependence of the bulk average critical field and the Ginzburg-Landau parameter, as used in the Summers form. In Chapter 6 a microscopic based form for the temperature dependence of the upper critical field, the Maki-De Gennes relation, is validated for all available Nb_3Sn results. This relation is therefore a suitable alternative for the temperature dependence of the inhomogeneity-averaged bulk critical field. In addition, the validation of the Maki-De Gennes relation also yielded a microscopic based alternative for the temperature dependence of the Ginzburg-Landau parameter, as was described in Chapter 3. Including these in the Kramer/Summers description does not lead to the correct temperature dependence of the bulk pinning force, as was shown in Chapter 7.

It was then empirically found that the temperature dependence of the bulk pinning force can have the form $F_P \propto [H_{c2}^*(T)^2 / \kappa_1(T)]f(h)$, where $f(h)$ represents the aforementioned magnetic field dependence. This empirical observation should preferably result from an underlying flux-line lattice interaction model but this was not investigated further.

After $F_P \propto [H_{c2}^*(T)^2 / \kappa_1(T)]f(h)$ was established to yield the correct temperature and magnetic field dependence, the strain dependence was introduced simply by stating that both the bulk average critical field and the Ginzburg-Landau parameter are strain dependent in a similar formulation. The strain dependence of the bulk pinning force was determined from experimental results. This approach differs significantly from the usual approach, where a different dependence of the bulk pinning force on $H_{c2}^*(T)$ and $H_{c2}^*(\varepsilon)$ is assumed.

The strain dependence of the critical properties was introduced as a normalized term $s(\varepsilon)$, defined as the strain dependence of the critical field. Various approaches were discussed for $s(\varepsilon)$ in Chapter 3. It is mentioned that the most complete form is a three dimensional full invariant analysis, that introduces strain dependence through the change in the electron-phonon interaction spectrum. Such a model results in an axial strain dependence that is parabolic-like for small axial strain, becomes approximately linear for high axial strain and predicts asymmetry, as is usually observed in experiments. For the description of axial strain experiments, however, the calculations required might be too rigorous. The choice was therefore made to extend an existing, symmetric deviatoric strain model, which is based on the second strain invariant. The modification introduces an additional empirical term that represents the third (deviatoric) invariant and introduces the required asymmetry. This improved model was renormalized and verified to accurately describe measured critical current versus axial strain results.

8.3 Recommendations for future research

Although improvements on understanding of observable performance limitations were made, some remaining issues will have to be addressed in future work. First, the strain dependence as a function of the A15 composition requires more detailed investigation. In the present work, all strain experiments were performed on optimized, but still inhomogeneous wires. It is not well understood how Sn content, or ternary additions, change the strain sensitivity of the critical properties. This requires detailed investigation to clarify observable differences in strain sensitivity between wires. Non-hydrostatic strain experiments should therefore be performed on well defined laboratory samples that are homogeneous in composition (but representative of the polycrystalline A15 that is present in wires). Strain experiments on fully homogenized bulk samples of various compositions could deliver the necessary information.

Second, the full invariant analysis recently given in the literature focuses on the strain dependency of the critical temperature. For improved understanding of the change in the critical current density with strain, similar detailed calculations will have to be performed for the strain sensitivity of the upper critical field. Such analysis should explain why the relative change in the bulk average critical field with strain is stronger than for the critical temperature. This will yield well supported information on the shift of the field-temperature phase boundary with strain, which is required for understanding of the strain sensitivity of the critical current density.

Third, a connection should be established between the observed temperature dependence of the bulk pinning force, i.e. $F_P \propto [H_{c2}^*(T)^2 / \kappa_1(T)]f(h)$, and the theory of flux pinning.

References

References

1 B.T. Matthias, T.H. Geballe, S. Geller and E. Corenzwit, *Phys. Rev.* **95**, 1435 (1954).
2 G.F. Hardy and J.K. Hulm, *Phys. Rev.* **89**, 884 (1953).
3 J.J. Hanak, K. Strater, and R.W. Cullen, *RCA Review* **25**, 342 (1964).
4 A.R. Kaufmann and J.J. Pickett, *Bull. Am. Phys. Soc.* **15**, 838 (1970).
5 P.G. de Gennes, *Superconductivity of Metals and Alloys*, W.A. Benjamin, New York (1966); Addison-Wesley, Reading MA (1989).
6 M. Tinkham, *Introduction to Superconductivity*, 2nd ed. McGraw-Hill, New York (1996).
7 R.D. Parks (ed.), *Superconductivity*, Dekker, New York (1969).
8 V.Z. Kresin, H. Morawitz and S.A. Wolf, *Mechanisms of Conventional and High T_c Superconductivity*, Oxford University Press, New York (1993).
9 D. Saint-James, G. Sarma and E. Thomas, *Type II Superconductivity*, Pergamon, New York (1969).
10 A.C. Rose-Innes and E.H. Rhoderick, *Introduction to Superconductivity*, 2nd ed. Pergamon, Oxford (1978).
11 T.P. Orlando and K.A. Delin, *Foundations of Applied Superconductivity*, Addison-Wesley, Reading MA (1991).
12 K.H. Bennemann and J.B. Ketterson (eds.), *The Physics of Superconductors*, Springer-Verlag, Berlin (2003).
13 J.E. Evetts (ed.), *Concise encyclopedia of magnetic & superconducting materials*, Pergamon Press, Oxford (1992).
14 C.P. Poole Jr., H.A. Farach and R.J. Creswick, *Superconductivity*, Academic Press, San Diego (1995).
15 S. Foner and B.B. Schwartz (eds.), *Superconductor Material Science*, Plenum Press, New York (1981).
16 T. Luhman and D. Dew-Hughes (eds.), *Treatise on Materials Science and Technology* **14**, Metallurgy of Superconducting Materials, Academic Press, New York (1979).
17 W. Buckel and W. Weber (eds.), *Superconductivity in d- and f-Band Metals 1982*, Kernforschungszentrum Karlsruhe (1982).
18 M. Suenaga and A.F. Clark (eds.), *Filamentary A15 Superconductors*, Plenum Press, New York (1980).
19 T. Matsushita, K. Yamafuji and F. Irie (eds.), *Proc. of International Symposium on Flux Pinning and Electromagnetic Properties in Superconductors*, Fukuoka, Japan, 11-14 November 1985, Matsukuma Press, Fukuoka, (1985).
20 D. Dew-Hughes, *Rep. Prog. Phys.* **34**, 821 (1971).
21 A. Echarri and M. Spadoni, *Cryogenics* **11**, 274 (1971).
22 D. Dew-Hughes, *Cryogenics* **15**, 435 (1975).
23 D.B. Smathers in *Metals Handbook* **2**, ASM International, Metals Park OH, 1060 (1990).
24 R. Flükiger, *Atomic Ordering, Phase Stability and Superconductivity in Bulk and Filamentary A15 Type Compounds*, Kernforschungszentrum Karlsruhe (1987).
25 R.H. Hammond, *IEEE Trans. Magn.* **11**, 201 (1975).
26 R.H. Hammond, *J. Vac. Sci. Technol.* **15**, 382 (1978).
27 D.F. Moore, R.B. Zubeck, J.M. Rowell and M.R. Beasley, *Phys. Rev.* **20B**, 2721 (1979).
28 T.P. Orlando, E.J. McNiff, Jr., S. Foner, and M.R. Beasley, *Phys. Rev.* **19B**, 4545 (1979).

29 T.P. Orlando, J.A. Alexander, S.J. Bending, J. Kwo, S.J. Poon, R.H. Hammond, M.R. Beasley, E.J. McNiff, Jr., and S. Foner, *IEEE Trans. Magn.* **17**, 368 (1981).
30 H. Devantay, J.L. Jorda, M. Decroux, J. Muller and R. Flükiger, *J. Mat. Sci.* **16**, 2145 (1981).
31 W. Goldacker, R. Ahrens, M. Nindel, B. Obst and C. Meingast, *IEEE Trans. Appl. Supercond.* **3**, 1322 (1993).
32 D.W. Woodward and G.D. Cody, *RCA Review* **25**, 392 (1964).
33 K.R. Keller and J.J. Hanak, *Phys. Rev.* **154**, 628 (1967).
34 R. Mailfert, B.W. Batterman and J.J. Hanak, *Phys. Lett.* **24A**, 315 (1967).
35 L.J. Vieland and A.W. Wicklund, *Phys. Rev.* **166**, 424 (1968).
36 S. Foner and E.J. McNiff Jr., *Phys. Lett.* **58A**, 318 (1976).
37 A.J. Arko, D.H. Lowndes, F.A. Muller, L.W. Roeland, J. Wolfrat, A.T. van Kessel, H.W. Myron, F.M. Mueller and G.W. Webb, *Phys. Rev. Lett.* **40**, 1590 (1978).
38 S. Foner and E.J. McNiff Jr., *Solid State Commun.* **39**, 959 (1981).
39 M.C. Jewell, A. Godeke, P.J. Lee and D.C. Larbalestier, *Adv. Cryog. Eng. (Mat.)* **50B**, 474 (2004).
40 H. Kamerlingh Onnes, *Leiden Commun.* **124C** (1911).
41 J. Nagamatsu, N. Nakagawa, T. Muranaka, Y. Zenitani and J. Akimitsu, *Nature* **410**, 63 (2001).
42 W.A. Little, *Phys. Rev.* **134**, A1416 (1964).
43 J.G. Bednorz and K.A. Müller, Z. Phys. **64B**, 189 (1986).
44 W. Meissner and R. Ochsenfeld, *Naturwissenshaften* **21**, 787 (1933).
45 A.A. Abrikosov, *Zh. Eksperim. i Teor. Fiz.* **32**, 1442 (1957) [*Sov. Phys. JETP* **5**, 1174 (1957)].
46 A.A. Abrikosov, *Rev. Mod. Phys.* **76**, 975 (2004).
47 F. London and H. London, *Proc. R. Soc. London* **149A**, 71 (1935).
48 V.L. Ginzburg, and L.D. Landau, *Zh. Eksp. Teor. Fiz.* **20**, 1064 (1950) [translation in L.D. Landau, *Collected Papers*, Pergamon, Oxford (1965)].
49 V.L. Ginzburg, *Rev. Mod. Phys.* **76**, 981 (2004).
50 L.D. Landau, Zh. Eksp. Teor. Fiz. **11**, 592 (1941) [*J. Phys. (USSR)* **5**, 71 (1941)].
51 L.P. Gor'kov, *Zh. Eksperim. i Teor. Fiz.* **36**, 1918 (1959) [*Sov. Phys. JETP* **9**, 1364 (1959)].
52 J. Bardeen, L.N. Cooper and J.R. Schrieffer, *Phys. Rev.* **108**, 1175 (1957).
53 H. Fröhlich, *Phys. Rev.* **79**, 845 (1950).
54 E. Maxwell, Phys. Rev. **78**, 477 (1950).
55 L.N. Cooper, *Phys. Rev.* **104**, 1189 (1956).
56 G.M. Eliashberg, *Zh. Eksperim. i Teor. Fiz.* **38**, 966 (1960) [*Sov. Phys. JETP* **11**. 696 (1960)].
57 W. McMillan, *Phys. Rev.* **167**, 331 (1968).
58 V.Z. Kresin, *Phys. Lett.* **122A**, 434 (1987).
59 V. Guritanu, W. Goldacker, F. Bouquet, Y. Wang, R. Lortz, G. Goll and A. Junod, *Phys. Rev.* **70B**, 184526 (2004).
60 Y. Hashimoto, K. Yoshizaki and M. Tanaka, *Proc. 5th International Cryogenic Eng. Conf.*, Kyoto, Japan, 332 (1974).
61 J.D. Elen, C.A.M. van Beijnen and C.A.M. van der Klein, *IEEE Trans. Mag.* **MAG–13**, 470 (1977).

62 I.W. Wu, D.R. Dietderich, J.T. Holthuis, M. Hong, W.V. Hassenzahl and J.W. Morris Jr., *J. Appl. Phys.* **54**, 7139 (1983).
63 K.R. Marken, S.J. Kwon, P.J. Lee and D.C. Larbalestier, *Adv. Cryog. Eng. (Materials)* **32**, 967 (1986).
64 C.D. Hawes, P.J. Lee and D.C. Larbalestier, *IEEE Trans. Appl. Supercond.* **10**, 988 (2000).
65 C.D. Hawes, *Investigations of the Inhomogeneity of a Powder-in-Tube Nb_3Sn Conductor*, M.S. Thesis, Univ. of Wisconsin, Madison WI, USA (2002).
66 K. Tachikawa, H. Izawa, Y. Ikeda, T. Koyata, T. Takeuchi and K. Watanabe, *Adv. Cry. Eng. (Materials)* **50B**, 387 (2004).
67 K. Egawa, Y. Kubo, T. Nagai, T. Sone, K. Hiramoto, O. Taguchi, H. Kitakoga, M. Wake, T. Shintomi and S. Nakayama, *Adv. Cry. Eng. (Materials)* **50B**, 403 (2004).
68 A. Vorobieva, A. Shikov, V. Pantsyrnyi, E. Dergunova, K. Mariiv, D. Farafonov, L. Vojdaev and V. Lomaev, *Presented at the Applied Superconductivity Conference*, Oct. 3–8, Jacksonville FL, USA (2004).
69 A. Street, *Spectroscopy Europe* **15/1**, 10 (2003).
70 W.D. Markiewicz, L.A. Bonney, I.A. Dixon, Y.M. Eyssa, C.A. Swenson and H.J. Schneider-Muntau, *Phys.* **216B**, 200 (1996).
71 T. Miyazaki, Y. Murakami, T. Hase, M. Shimada, K. Itoh, T. Kiyoshi, T. Takeuchi, K. Inoue and H. Wada, *IEEE Trans. Appl. Supercond.* **9**, 2505 (1999).
72 I.R. Dixon, W.D. Markiewicz, K.W. Pickard and C.A. Swenson, *IEEE Trans. Appl. Supercond.* **9**, 2513 (1999).
73 T. Kiyoshi, A. Sato, T. Takeuchi, K. Itoh, S. Matsumoto, O. Ozaki, K. Fukushima, H. Wada, M. Yoshikawa, T. Kamikado, S. Ito, T. Miki, T. Hase, M. Hamada, S. Hayashi, Y. Kawate and R. Hirose, *IEEE Trans. Appl. Supercond.* **12**, 711 (2002).
74 A. den Ouden, S. Wessel, E. Krooshoop and H. ten Kate, *IEEE Trans. Appl. Supercond.* **7**, 733 (1997).
75 R.M. Scanlan, R.J. Benjegerdes, P.A. Bish, S. Caspi, K. Chow, D. Dell'Orco, D.R. Dietderich, M.A. Green, R. Hannaford, W. Harnden, H.C. Higley, A.F. Lietzke, A.D. McInturff, L. Morrison, M.E. Morisson, C.E. Taylor and J.M. Van Oort, *Inst. Phys. Conf. Ser.* **158**, 1503 (1997).
76 J.A. Parrell, M.B. Field, Y. Zhang and S. Hong, *Adv. Cryo. Eng. (Materials)* **50B**, 369 2004.
77 LBNL *Superconducting Magnet Program Newsletter*, Issue 2, October 2003.
78 D. Bessette, E. Zapretilina and N. Shatil, *IEEE Trans. Appl. Supercond.* **10**, 1074 (2000).
79 P. Bruzzone, H.H. ten Kate, M. Nishi, A. Shikov, J. Minervini and M. Takayasu, *Adv. Cryo. Eng. (Materials)* **42B**, 1351 (1997).
80 N. Mitchell, *Fusion Eng. and Design* **46**, 129 (1999).
81 L.T. Summers, M.W. Guinan, J.R. Miller and P.A. Hahn, *IEEE Trans. Magn.* **27**, 2041 (1991).
82 G.R. Stewart, L.R. Newkirk and F.A. Valencia, *Phys. Rev.* **21B**, 5055 (1980).
83 J.P. Charlesworth, I. MacPhail and P.E. Madsen, *J. Mater. Sci.* **5**, 580 (1970).
84 R.E. Enstrom, *J. Appl. Phys.* **37**, 4880 (1966).
85 J.P. Charlesworth, *Phys. Lett.* **21**, 501 (1966).
86 D.J. van Ooijen, J.H.N. van Vucht and W.F. Druyvesteyn, *Phys. Lett.* **3**, 128 (1962).
87 L.J. Vieland, *RCA Review* **25**, 366 (1964).

88 C. Toffolon, C. Servant and B. Sundman, *J. Phase Equil.* **19**, 479 (1998).
89 C. Toffolon, C. Servant, J.C. Gachon and B. Sundman, *J. Phase Equil.* **23**, 134 (2002).
90 R.A. Schiffman and D.M. Bailey, *High Temp. Sci.* **15**, 165 (1982).
91 R. Mailfert, B.W. Batterman and J.J. Hanak, *Physica Status Solidi* **32B**, k67 (1969).
92 C.W. Chu and L.J. Vieland, *J. Low Temp. Phys.* **17**, 25 (1974).
93 L.J. Vieland, *J. Phys. Chem. Solids* **31**, 1449 (1970).
94 A. Junod, J. Muller, H. Rietschel and E. Schneider, *J. Phys. Chem. Solids* **39**, 317 (1978).
95 L.J. Vieland and A.W. Wicklund, *Phys. Lett.* **34A**, 43 (1971).
96 R. Flükiger, *Adv. Cryo. Eng. (Materials)* **28**, 399 (1982).
97 M.E. Straumanis and S. Zyszczynsk, *J. Appl. Cryst.* **3**, 1 (1970).
98 R. Flükiger, R. Isernhagen, W. Goldacker and W. Specking, *Adv. Cryo. Eng. (Materials)* **30**, 851 (1984).
99 R. Flükiger, H. Küpfer, J.L. Jorda and J. Muller, IEEE Trans. on Magn. **MAG-23**, 980 (1987).
100 M.R. Beasley, *Adv. Cryo. Eng.* **28**, 345 (1982).
101 D.O. Welch, G.J. Dienes, O.W. Lazareth Jr. and R.D. Hatcher, *J. Phys. Chem. Solids* **45**, 1225 (1984).
102 C. Nölscher and G. Seamann-Ischenko, *Phys. Rev.* **32B**, 1519 (1985).
103 E. Drost, W. Specking and R. Flükiger, *IEEE Trans. Magn.* **MAG-21**, 281 (1985).
104 E.J. Kramer, *J. Appl. Phys.* **44**, 1360 (1973).
105 D.M. Kroeger, D.S. Easton, A. DasGupta, C.C. Koch and J.O. Scarbrough, *J. Appl. Phys.* **51**, 2184 (1980).
106 K. Hechler, G. Horn, G. Otto and E. Saur, *J. Low Temp. Phys.* **1**, 29 (1969).
107 M. Suenaga, D.O. Welch, R.L. Sabatini, O.F. Kammerer and S. Okuda, *J. Appl. Phys.* **59**, 840 (1986).
108 R. Akihama, K. Yasukochi and T. Ogasawara, *IEEE Trans. Magn.* **13**, 803 (1977).
109 K. Tachikawa, T. Asano and T. Takeuchi, *Appl. Phys. Lett.* **39**, 766 (1981).
110 J.L.H. Lindenhovius, E.M. Hornsveld, A. den Ouden, W.A.J. Wessel and H.H.J. ten Kate, *IEEE Trans. Appl. Supercond.* **10**, 975 (2000).
111 B. ten Haken, A. Godeke and H.H.J. ten Kate, *J. Appl. Phys.* **85**, 3247 (1999).
112 N. Cheggour and D.P. Hampshire, *Cryogenics* **42**, 299 (2002).
113 R.H. Hopkins, G.W. Roland and M.R. Daniel, *Metallurgical Trans.: Phys. Metallurgy and Mat. Sci.* **8A**, 91 (1977).
114 U. Zwicker and L. Rinderer, *Zeitschrift für Metallkunde* **66**, 738 (1975).
115 W.L. Neijmeijer and B.H. Kolster, *Zeitschrift für Metallkunde* **78**, 730 (1987).
116 G. Lefranc and A. Müller, *J. Less Common Metals* **45**, 339 (1976).
117 N.V. Ageeva and L.A. Petrovoj, in *Diagrammy Sostoyaniya Metallicheskikh Sistem* **28**, N.V. Ageeva (Ed.), Viniti, Moscow, 26 (1982).
118 W.L. Neijmeijer, *Microstructural and Kinetic Studies of the Manufacturing of Superconducting Nb_3Sn*, PhD thesis Univ. of Twente, Enschede, The Netherlands (1988).
119 J. Livingston, *Phys. Status Solidi* **44A**, 295 (1977).
120 D.B. Smathers and D.C. Larbalestier, *Adv. Cryo. Eng. (Materials)* **28**, 415 (1982).
121 M. Suenaga and W. Jansen, *Appl. Phys. Lett.* **43**, 791 (1983).
122 M. Suenaga, private communication on unpublished data (2004).
123 J.D. Livingston, *IEEE Trans. Mag.* **MAG–14**, 611 (1978).

124 R. Akihama, K. Yasukõchi and T Ogasawara, *IEEE Trans. Mag.* **MAG–13**, 803 (1977).
125 E. Springer, M. Wilhelm, H.J. Weisse and G. Rupp, *Adv. Cryog. Eng. (Materials)* **30**, 747 (1984).
126 M. Suenaga, *IEEE Trans. Mag.* **MAG–21**, 1122 (1985).
127 K. Tachikawa, T. Takeuchi, T. Asano, Y. Iijima and H. Sekine, *Adv. Cryo. Eng. (Materials)* **28**, 389 (1982).
128 D. Dew-Hughes, *IEEE Trans. Mag.* **13**, 651 (1977).
129 K. Togano, T. Asano and K. Tachikawa, *J. Less Common Met.* **68**, 15 (1979).
130 M. Suenaga, T.S. Luhman and W.B. Sampson, *J. Appl. Phys.* **45**, 4049 (1974).
131 T. Takeuchi, T. Asano, Y. Iijima and K. Tachikawa, *Cryogenics* **21**, 585 (1981).
132 H. Sekine, Y. Iijima, K. Itoh, K. Tachikawa. Y. Tanaka and Y. Furuto, *IEEE Trans. Mag.* **MAG–19**, 1429 (1983).
133 I.W. Wu, D.R. Dietderich, J.T. Holthuis, W.V. Hassenzahl and J.W. Morris, *IEEE Trans. Mag.* **MAG–19**, 1437 (1983).
134 H. Kurahashi, K. Itoh, S. Matsumoto, T. Kiyoshi, H. Wada, Y. Murakami, H. Yasunaka, S. Hayashi and Y. Otani, *Presented at the Applied Superconductivity Conference, Oct. 3–8*, Jacksonville FL, USA (2004).
135 V. Abächerli, D. Uglietti, P. Lezza, B. Seeber, R. Flükiger, M. Cantoni and P.-A. Buffat, *Presented at the Applied Superconductivity Conference, Oct. 3–8*, Jacksonville FL, USA (2004).
136 J. Tafto, M. Suenaga and D.O. Welch, *J. Appl. Phys.* **55**, 4330 (1984).
137 L.D. Cooley, P.J. Lee and D.C. Larbalestier, *Adv. Cryog. Eng. (Materials)* **48B**, 925 (2002).
138 D. Dew-Hughes, *Phil. Mag.* **30**, 293 (1974).
139 R.M. Scanlan, W.A. Fietz and E.F. Koch, *J. Appl. Phys.* **46**, 2244 (1975).
140 B.J. Shaw, *J. Appl. Phys.* **47**, 2143 (1976).
141 K.R. Marken, *Characterization Studies of Bronze-Process Filamentary Nb_3Sn Composites*, Ph.D. Thesis, University of Wisconsin-Madison (1986).
142 W. Schauer and W. Schelb, *IEEE Trans. Magn.* **MAG–17**, 374 (1981).
143 A.W. West and R.D. Rawlings, *J. Mat. Sci.* **12**, 1862 (1977).
144 C.M. Fischer, *Investigation of the Relationships Between Superconducting Properties and Nb_3Sn Reaction Conditions in Powder-in-Tube Nb_3Sn Conductors*, M.S. thesis, Univ. of Wisconsin, Madison WI, USA (2002).
145 P.J. Lee and D.C. Larbalestier, *Wire Journal International* **36**, 61 (2003).
146 E.M. Savitskii, M.I. Bychkova, V.V. Baron, B.E. Dzevitskii and N.I. Savateev, Physica Status Solidi A 37, K165, (1976).
147 R. Flükiger, W. Schauer, W. Specking, B. Schmidt and E. Springer, *IEEE Trans. Magn.* **17**, 2285 (1981).
148 C.L. Snead and M. Suenaga, *Appl. Phys. Lett.* **37**, 659 (1980).
149 B. ten Haken, *Strain effects on the critical properties of high-field superconductors*, PhD thesis, Univ. of Twente, Enschede, The Netherlands (1994).
150 L.R. Testardi, *Phys. Rev.* **3B**, 95 (1971).
151 D.O. Welch, *Adv. Cryo. Eng. (Materials)* **26**, 48 (1980).
152 W.D. Markiewicz, *Cryogenics* **44**, 767 (2004).
153 W.D. Markiewicz, *Cryogenics* **44**, 895 (2004).

154 W.D. Markiewicz, *Presented at the Applied Superconductivity Conference*, Oct. 3–8, Jacksonville FL, USA (2004).
155 K.C. Lim and J.D. Thompson, *Phys. Rev.* **27B**, 2781 (1983).
156 J.P. McEvoy, *Physica* **55**, 540 (1971).
157 A. Godeke, B. ten Haken and H.H.J. ten Kate, *IEEE Trans. Appl. Supercond.* **12**, 1029 (2002).
158 A. Godeke, M.C. Jewell, A.A. Golubov, B. ten Haken and D.C. Larbalestier, *Supercond. Sci. and Techn.* **16**, 1019 (2003).
159 S.A. Keys and D.P. Hampshire, *Supercond. Sci. Technol.* **16**, 1097 (2003).
160 N. Cheggour and D.P. Hampshire, *J. Appl. Phys.* **86**, 552 (1999).
161 A. Godeke, B. ten Haken and H.H.J. ten Kate, *Physica C* **372–376**, 1295 (2002).
162 A. Godeke, B. ten Haken and H.H.J. ten Kate, *IEEE Trans. Appl. Supercond.* **9**, 161 (1999).
163 A. Godeke, H.J.G. Krooshoop, B. ten Haken and H.H.J. ten Kate, *IEEE Trans. Appl. Supercond.* **11**, 1526 (2001).
164 R. Labusch, *Cryst. Lattice Defects* **1**, 1 (1969).
165 A.M. Campbell and J.E. Evetts, *Adv. Phys.* **21**, 199 (1972).
166 A.I. Larkin and Yu.N. Ovchinnikov, *J. Low. Temp. Phys.* **34**, 409 (1979).
167 K. Maki, *Physics* **1**, 127 (1964).
168 P.G. de Gennes, *Phys. Kondens. Materie* **3**, 79 (1964).
169 E. Helfand and N.R. Werthamer, *Phys. Rev. Lett.* **13**, 686 (1964).
170 E. Helfand and N.R. Werthamer, *Phys. Rev.* **147**, 288 (1966).
171 N.R. Werthamer, E. Helfand and P.C. Hohenberg, *Phys. Rev.* **147**, 295 (1966).
172 P.C. Hohenberg and N.R. Werthamer, *Phys. Rev.* **153**, 493 (1967).
173 N.R. Werthamer and W.L. McMillan, *Phys. Rev.* **158**, 415 (1967).
174 G. Eilenberger and V. Ambegaokar, *Phys. Rev.* **158**, 332 (1967).
175 K.D. Usadel, *Phys. Rev. Lett.* **25**, 507 (1970).
176 K.D. Usadel, *Phys. Rev.* **4B**, 99 (1971).
177 G. Bergmann and D. Rainer, *Z. Physik* **263**, 59 (1973).
178 D. Rainer, G. Bergmann and U. Eckhardt, *Phys. Rev.* **8B**, 5324 (1973).
179 D. Rainer and G. Bergmann, *J. Low Temp. Phys.* **14**, 501 (1974).
180 N. Schopohl and K. Scharnberg, *Physica* **107B**, 293 (1981).
181 N. Schopohl and K. Scharnberg, *Physica* **135B**, 482 (1985).
182 M. Schossmann and E. Schachinger, *Phys. Rev.* **33B**, 6123 (1986).
183 C.T. Rieck, K. Scharnberg and N. Schopohl, *J. Low Temp. Phys.* **84**, 381 (1991).
184 M. Arai and T. Kita, *Cond-Mat/0404628* (2004).
185 T. Kita and M. Arai, *Cond-Mat/0403314* (2005).
186 M. Dhallé in *Handbook of Superconducting Materials*, editors D. Cardwell and D. Ginley, Institute of Physics Publishing, Bristol UK, (2002).
187 E.H. Brandt, *Rep. Prog. Phys.* **58**, 1465 (1995).
188 M.N. Wilson, *Superconducting magnets*, Oxford University Press, Oxford (1983).
189 Y.B. Kim, C.F. Hempstead and A.R. Strnad, *Phys. Rev. Lett.* **9**, 306 (1962).
190 P.W. Anderson, *Phys. Rev. Lett.* **9**, 309 (1962).
191 K.A. Müller, M. Takashige and J.G. Bednorz, *Phys. Rev. Lett.* **58**, 1143 (1987).
192 M. Suenaga, A.K. Gosh, Y. Xu and D.O. Welch, *Phys. Rev. Lett.* **66**, 1777 (1991).

193 W.A. Fietz and W.W. Webb, *Phys. Rev.* **178**, 657 (1969).
194 D. Dew-Hughes, *Phil. Mag.* **55B**, 459 (1987).
195 R. Labusch, *Phys. Stat. Sol.* **32**, 439 (1969).
196 D.P. Hampshire, H. Jones and E.W.J. Mitchell, *IEEE Trans. Magn.* **MAG-21**, 289 (1985).
197 L.D. Cooley, C.M. Fischer, P.J. Lee and D.C. Larbalestier, *J. Appl. Phys.* **96**, 2122 (2004).
198 J.W. Ekin, *Cryogenics* **20**, 611 (1980).
199 E.H. Brandt, *J. Low Temp. Phys.* **26**, 709 (1977).
200 E. Drost, R. Flükiger and W. Specking, *Cryogenics* **24**, 622 (1984).
201 M. Abramowitz and I.A. Stegun (Ed.), *Handbook of mathematical functions with formulas, graphs, and mathematical tables*, Dover Publications, New York, (1965).
202 A. Godeke, M.C. Jewell, C.M. Fischer, A.A. Squitieri, P.J. Lee and D.C. Larbalestier, *J. Appl. Phys.* **97**, 093909 (2005).
203 T.P. Orlando and M.R. Beasley, *Phys. Rev. Lett.* **46**, 1598 (1981).
204 A.M. Clogston, *Phys. Rev. Lett.* **9**, 266 (1962).
205 B.S. Chandrasekhar, *Appl. Phys. Lett.* **1**, 7 (1962).
206 C.B. Müller and E. Saur, *Adv. Cryo. Eng.* **8**, 574 (1963).
207 W. Buehler and H.J. Levinstein, *J. Appl. Phys.* **36**, 3856 (1965).
208 J.W. Ekin, *IEEE Trans. Magn.* **MAG-13**, 127 (1977).
209 J.W. Ekin, *Cryogenics* **20**, 611 (1980).
210 J.W. Ekin, *IEEE Trans. Magn.* **MAG-17**, 658 (1981).
211 J.W. Ekin, *Adv. Cryo. Eng. (Materials)* **30**, 823 (1984).
212 M. Pulver, *Z. Physik* **257**, 261 (1972).
213 B. ten Haken, A. Godeke and H.H.J. ten Kate, *Inst. Phys. Conf. Ser.* **148**, 85 (1995).
214 B. ten Haken, A. Godeke and H.H.J. ten Kate, *Adv. Cryo. Eng. (Materials)* **42B**, 1463 (1997).
215 W. Goldacker and R. Flükiger, *Adv. Cryog. Eng. (Materials)* **34**, 561 (1983).
216 B. ten Haken, A. Godeke and H.H.J. ten Kate, *IEEE Trans. Magn.* **30**, 1867 (1994).
217 B. ten Haken, T.N. Zaitseva and H.H.J. ten Kate, *Cryogenics* **34** ICEC Supplement, 513 (1994).
218 N. Mitchell, *Proceedings 2004 Applied Superconductivity Conference*, Jacksonville FL, USA (2005).
219 L.R. Testardi in *Physical Acoustics* **10**, (W.P. Mason and R.N. Thurston, eds.), Academic Press, New York, 193 (1973).
220 L.R. Testardi, *Phys. Rev.* **5B**, 4342 (1972).
221 P.B. Allen and R.C. Dynes, *Phys. Rev.* **12B**, 905 (1975).
222 D.M.J. Taylor and D.P. Hampshire, to be published (2005).
223 S.A. Keys, N. Koizumi and D.P. Hampshire, *Supercond. Sci. Technol.* **15**, 991 (2002).
224 T. Luhman, M. Suenaga and C.J. Klamut, *Adv. Cryo. Eng.* **24**, 325 (1978).
225 B. ten Haken, A. Godeke and H.H.J. ten Kate, *IEEE Trans. Appl. Supercond.* **3**, 1273 (1993).
226 B. ten Haken, A. Godeke and H.H.J. ten Kate, *IEEE Trans. Appl. Supercond.* **5**, 1909 (1995).
227 B. ten Haken, A. Godeke and H.H.J. ten Kate, *IEEE Trans. Magn.* **32**, 2739 (1996).
228 W.D. Markiewicz, private communication (2005).

229 P.J. Lee, A.A. Squitieri and D.C. Larbalestier, *IEEE Trans. Appl. Supercond.* **10**, 979 (2000).
230 A. Martinez and J.L. Duchateau, *Cryogenics* **37**, 865 (1997).
231 P.J. Lee and D.C. Larbalestier, *IEEE Trans. Appl. Supercond.* **11**, 3671 (2001).
232 C.M. Fischer, P.J. Lee and D.C. Larbalestier, *Adv. Cryog. Eng. (Materials)* **48**, 1008 (2002).
233 P.J. Lee, private communication 2005.
234 M.T. Naus, *Optimization of Internal-Sn Nb_3Sn Composites*, PhD Thesis, University of Wisconsin - Madison (2002).
235 J.H. Lindenhovius, SMI, private communication 2004.
236 J.W. Ekin, *J. Appl. Phys.* **45**, 3406 (1978).
237 A. Godeke, A. Nijhuis, B. ten Haken, P. Bruzzone and H.H.J. ten Kate, *Inst. Phys. Conf. Ser.* **158**, 917 (1997).
238 M. Garber, A.K. Gosh and W.B. Sampson, *IEEE Trans. Magn.* **25**, 1940 (1989).
239 A. den Ouden, private communication (2003).
240 D.M.J. Taylor and D.P. Hampshire, *Supercond. Sci. Technol.* **18**, 356 (2005).
241 A. Godeke, *Design and Test of the 20 K Strain Apparatus*, B.S. Thesis, University of Twente, Enschede, The Netherlands (1992).
242 W. Specking and R. Flükiger, *J. de Physique* **45**, C1-79 (1984).
243 K. Arai, H. Tateishi, M. Umeda and K. Agatsuma, *Electr. Eng. In Japan* **114**, 1 (1994).
244 H. Sekine, K. Inoue, T. Kuroda and K. Tachikawa, *Cryogenics* **29**, 96 (1989).
245 G. Rupp, *Cryogenics* **18**, 663 (1978).
246 N. Cheggour and D.P. Hampshire, *Rev. Sci. Instr.* **71**, 4521 (2000).
247 D. Uglietti, B. Seeber, V. Abächerli, A. Pollini, D. Eckert and R. Flükiger, *Supercond. Sci. Techn.* **16**, 1000 (2003).
248 C.R. Walters, I.M. Davidson and G.E. Tuck, *Cryogenics* **26**, 406 (1986).
249 D. Uglietti, B. Seeber, V. Abächerli, P. Lezza and R. Flükiger, "*Critical current versus strain of long HTS and LTS technical superconductors up to 1000 A and 17 T*", presented at the Workshop on Accelerator Magnet Superconductors, 22-24 March, Archamps, France (2004).
250 H. Kitaguchi, K. Itoh, H. Kumakura, T. Takeuchi, K. Togano and H. Wada, *IEEE Trans. Appl. Supercond.* **11**, 3058 (2001).
251 B. ten Haken, A. Godeke and H.H.J. ten Kate, in *Proc. 15th Int. Conf. on Magnet Techn.*, edited by L. Liangzhen, S. Guoliao and Y. Luguang (Science Press, Beijing, China), 985 (1998).
252 M.C. Jewell, P.J. Lee and D.C. Larbalestier, *Supercond. Sci. Techn.* **16**, 1005 (2003).
253 H. Ford and J.M. Alexander, *Advanced Mechanics of Materials*, 2nd edition (Ellis Horwood, Chichester) Chap. 16, (1977).
254 A. Godeke, M. Dhalle, A. Morelli, L. Stobbelaar, H. van Weeren, H.J.N. van Eck, W. Abbas, A. Nijhuis, A. den Ouden and B. ten Haken, *Rev. Sci. Instr.* **75**, 5112 (2004).
255 B.L. Brandt, D.W. Liu and L.G. Rubin, "*Low temperature thermometry in high magnetic fields. VII. Cernox™ sensors to 32T*", Rev. Sci. Instr., Vol. **70**, 104 (1999).
256 M. Dhallé, private communication (2004).
257 D.R. Dietderich, J. Glazer, C. Lea, W.V. Hassenzahl and J.W. Morris, Jr., *IEEE Trans. Magn.* **21**, 297 (1985).

258 D.R. Dietderich, W.V. Hassenzahl and J.W. Morris, Jr., *Adv. Cryog. Eng. (Materials)* **32**, 881 (1986).
259 D.B. Smathers, K.R. Marken, D.C. Larbalestier and J. Evans, *IEEE Trans. Magn.* **19**, 1421 (1983).
260 L.J. Neuringer and Y. Shapira, *Phys. Rev. Lett.* **17**, 81 (1966).
261 R.R. Hake, *Phys. Rev.* **158**, 356 (1967).
262 A. Godeke, unpublished results (2004).
263 A. Godeke, H.G. Knoopers, A. Nijhuis, H.J.G. Krooshoop, B. ten Haken and H.H.J. ten Kate, *Characterization of ITER strands in the frame of the third benchmark tests*, Report UT-NET 98-5, University of Twente (1998).
264 A. Godeke, H.J.G. Krooshoop, H.G. Knoopers, B. ten Haken and H.H.J. ten Kate, *Wide temperature and field scaling relations in Nb_3Sn ITER strands*, Report UT-NET / EFDA 2000-5, University of Twente (2000).
265 D.P. Hampshire, D.M. Taylor, P. Foley and S.A. Keys, *Characterisation of Nb_3Sn and Nb_3Al strands for Model Coils*, Report DurSC0601, Durham University (2001).
266 D. Uglietti, private communication (2003).

Symbols and Acronyms

Symbols and acronyms

Symbol	Description	Unit
a	Constant	
a	Lattice constant	[m]
a_0	Flux-line lattice spacing	[m]
a_Δ	Triangular flux-line lattice spacing	[m]
A	Constant	
A	Area	[m^2]
A_1, A_2, A_3	Amplitudes of harmonic strain terms	[Nm^{-2}]
b	Reduced critical magnetic field	
B	Magnetic induction	[T]
B_1, B_2, B_3	Amplitudes of anharmonic strain terms	[Nm^{-2}]
B_{c2}^*	Scaling upper critical field	[T]
c	Lattice constant	[m]
C, C_1, C_2, C_3, C_4	Constant	
C_{66}	Shear modulus of the flux-line lattice	[Nm^{-2}]
C_a, C_a'	Axial strain sensitivity	[–], [T]
C_{a1}, C_{a1}'	Second invariant axial strain sensitivity	[–], [T]
C_{a2}, C_{a2}'	Third invariant axial strain sensitivity	[–], [T]
C_{dev}, C_{inv2}	Second invariant three dimensional strain sensitivity	[T]
C_{inv3}	Third invariant three dimensional strain sensitivity	[T]
d	Distance	[m]
d_{av}	Average grain size	[m]
$d_{fil.\ A}$	Filament area diameter	[m]
D	Diffusion constant	[m^2s^{-1}]
D^*	Effective diffusion constant	[m^2s^{-1}]
e	Elementary charge quantum	[C]
e	Base number of natural logarithm	
E	Young's modulus	[Nm^{-2}]
E, E_y	Electric field	[Vm^{-1}]
E_c	Electric field criterion	[Vm^{-1}]
E_F	Fermi surface electron energy level	[J]
f	Function	
f_K	Kramer pinning force function	
$F(\omega)$	Phonon density of states	[J^{-1}]
F_P	Bulk pinning force	[Nm^{-3}]
$F_{P,\ max}$	Maximum bulk pinning force	[Nm^{-3}]
$GB_{l/A}$	Grain boundary length per area	[m^{-1}]
h	Planck constant	[Js]
h	Reduced magnetic field	
h^2	Bending beam shape factor	[m^2]
$\hbar$	Dirac's constant	[Js]
h_{c2}	Reduced upper critical field	
H	Macroscopic field	[Am^{-1}]

$H_{I/2}$	Magnetic field at half a resistive transition height	[Am^{-1}]
$H_{applied}$	Applied magnetic field	[Am^{-1}]
H_c	Thermodynamic critical field	[Am^{-1}]
H_{c1}	Lower critical field	[Am^{-1}]
H_{c2}	Upper critical field	[Am^{-1}]
H_{c2}^{+}	Critical magnetic field due to orbital pair breaking alone	[Am^{-1}]
H_{c2}^{*}	Inhomogeneity averaged, effective, scaling critical field	[Am^{-1}]
H_{c2m}	Maximum upper critical field in strain dependency results	[Am^{-1}]
H_{c2m}^{*}	Inhomogeneity averaged maximum critical magnetic field in strain dependency results	[Am^{-1}]
$H_{c2-xx\%}$	Critical magnetic field at xx% of a transition	[Am^{-1}]
H_{irr}	Irreversibility field	[Am^{-1}]
H_K	Kramer extrapolated critical field	[Am^{-1}]
H_{Km}	Maximum Kramer extrapolated critical field in strain dependency results	[Am^{-1}]
H_{LC}	Magnetic loop closure magnetic field	[Am^{-1}]
H_p	Critical magnetic field due to Pauli paramagnetic limiting alone	[Am^{-1}]
H_P^{SO}	Pauli field in the limit of strong spin-orbit scattering	[Am^{-1}]
H_{peak}	Peak magnetic field at a conductor	[Am^{-1}]
H_W	Magnetic field width of a resistive transition	[Am^{-1}]
I	Current	[A]
I_1	Hydrostatic strain invariant	
I_c	Critical current	[A]
I_P	Current through resistive parallel sections	[A]
J, J_y	Current density	[Am^{-2}]
J_2, J_3, J_{21}, J_{22}, J_{31}, J_{32}, J_{33}	Non-hydrostatic strain invariants	
J_c	Critical current density	[Am^{-2}]
J_d	Depairing current density	[Am^{-2}]
k	Reduced Ginzburg-Landau parameter	
k_B	Boltzmann constant	[JK^{-1}]
L	Length	[m]
m	Magnetic moment	[Am^2]
M	Torque	[Nm]
MDG	Maki-De Gennes function	
n	Constant	
n	N-value	
$N(E_F)$	Electron density of states at the Fermi energy level	[$J^{-1}m^{-3}$]
p	Constant	
P	Pressure	[Nm^{-2}]
q	Constant	
Q_{GB}	Effective grain boundary pinning force	[Nm^{-2}]
r	Radius	[m]
r_a, r_b	Atomic occupation factors	
R, R_0	Radius	[m]

s	Reduced strain dependence	
S, S_a, S_b	Order parameter	
SC	A15 transition fit function	
t	Time	[s]
t	Reduced temperature	
T	Temperature	[K]
T_c	Critical temperature	[K]
$T_{c-xx\%}$	Critical temperature at xx% of a transition	[K]
T_c^*	Inhomogeneity averaged critical temperature	[K]
T_{c1}, T_{c0}	Onset and offset temperature of an A15 transition	[K]
T_{cm}	Maximum critical temperature in strain dependency results	[K]
T_{cm}^*	Inhomogeneity averaged maximum critical temperature in strain dependency results	[K]
T_m	Martensitic (tetragonal) transformation temperature	[K]
u	Constant	
U	Strain energy potential	[J]
U_P	Pinning energy potential	[J]
v	Velocity	[ms^{-1}]
v_F	Electron velocity at the Fermi energy level	[ms^{-1}]
V	Voltage	[V]
V	Volume	[m^3]
V_0	BCS Cooper pair attractive interaction potential	[Jm^3]
V_{Mol}	Molair volume	[m^3]
W, W_0	Energy	[J]
x	Coordinate	[m]
y	Coordinate	[m]
z	Coordinate	[m]
Z	Atomic number	
α	Constant	
α	Phase	
α	Angle	[°]
$\alpha^2(\omega)$	Electron-phonon interaction	[J]
β	Angle	[°]
β	Phase	
β	Relative atomic fraction	
δ	Axial precompression relative to a minimum in the second deviatoric strain invariant	
Δ, Δ_0	Electron energy gap in the superconducting state	[J]
ε	Strain	
$\varepsilon_{0,a}$	Axial remaining strain term	
$\varepsilon_{0,d}$	Three dimensional remaining strain term	
ε_{axial}, ε_a	Axial strain	
$\varepsilon_{applied}$	Applied strain	
ε_{dev}	Deviatoric strain (second invariant)	
ε_{irr}	Axial irreversible strain limit	
ε_m	Precompression in axial strain sensitivity results	

ε_{shift}	Axial difference between a three dimensional deviatoric stain minimum and the position of the maximum in axial strain sensitivity results	
ε_x, ε_y, ε_z,	Components of the strain tensor in an orthogonal coordinate system	
ε_{xx}	Strain along a path in x-direction	
$\varepsilon_{\theta\theta}$	Circumferential strain	
ϕ_0	Elementary flux quantum	[Wb]
γ	Constant	
γ	Angle	[°]
γ	Electronic specific heat	$[JK^{-2}mol^{-1}]$
γ_E	Euler's constant	
η	Grain boundary pinning efficiency	
κ	Ginzburg-Landau parameter close to $T_c(0)$	
κ_1	Ginzburg-Landau parameter from the ratio H_{c2} / H_c	
κ_{1m}	Maximum Ginzburg-Landau parameter in strain dependence results	
λ	Penetration depth	[m]
λ_{eff}	Effective electron-phonon interaction constant	
λ_{ep}	Electron-phonon interaction constant	
λ_{SO}	Spin-orbit scattering constant	
μ^*	Coulomb pseudopotential	
μ_0	Magnetic permeability of vacuum	$[Hm^{-1}]$
μ_B	Bohr magneton	$[Am^2]$
ν	Constant	
ν_x, ν_y	Poisson ratio (effective)	
Θ_D	Debye temperature	[K]
ρ	Normal state resistivity	[Ωm]
ρ_n	Normal state resistivity just above T_c	[Ωm]
ρ_{77K}	Normal state resistivity at 77K	[Ωm]
ρ_{300K}	Normal state resistivity at 300K	[Ωm]
$\sqrt{\rho}$	Pinning plane density	$[m^{-1}]$
υ	Frequency	$[s^{-1}]$
ϖ	Constant	
ω	Phonon frequency	$[s^{-1}]$
ω_c	Cut-off phonon frequency	$[s^{-1}]$
ξ	Coherence length	[m]
ψ	Digamma function	
ℓ	Electron mean free path	[m]

Summary

Summary

Superconducting magnets for High Energy Physics, Fusion, Magnetic Resonance Imaging (NMR) and Nuclear Magnetic Resonance, benefit from the extremely high current densities that can be achieved in superconductors compared to normal conducting materials. These magnets are usually constructed starting with a composite wire of typically 1 mm in diameter, in which the superconducting material is embedded in a copper matrix in the form of micrometer scale filaments. The present superconducting workhorse is Niobium-Titanium. This material remains superconducting up to an upper critical magnetic field of about 14 T and up to a critical temperature of about 9 K and its superconducting properties are virtually insensitive to strain. The fabrication processes of Niobium-Titanium superconducting wires have been, within present understanding, optimized that far that the maximum current carrying capacities in practical wires have been achieved. Future application upgrades, using magnets that are designed to operate beyond the limits that are available using Niobium-Titanium wires, will have to be constructed using an alternative superconducting material with superior specifications such as Niobium-Tin. Also existing applications, such as NMR, that utilise the higher performance of Niobium-Tin, can be upgraded using improved Niobium-Tin wires.

The superconductor Niobium-Tin is presently the only alternative material sufficiently adult for large scale applications and is therefore considered as the successor for Niobium-Titanium in the aforementioned applications. It is superconducting up to an upper critical magnetic field of about 30 T and up to a critical temperature of about 18 K and thus approximately doubles the achievable performance boundary in comparison to Niobium-titanium. A disadvantage of Niobium-Tin is that the superconducting phase of interest (the A15 phase) is brittle and its superconducting properties are very sensitive to strain. Wires are manufactured while the Niobium and Tin are still separated and ductile and A15 formation occurs through a solid state diffusion reaction at about 700 °C only after the conductor is in its final shape. The A15 phase is stable from about 18 at.% Sn to about 25 at.% Sn. Grain growth during the A15 formation reaction has to be prevented since small grain sizes are required for high current densities. This limits the heat treatment temperature and time. The diffusion reaction is thus never complete to thermodynamic equilibrium, which results in the presence of Tin gradients and thus various A15 compositions in reacted wires. In this thesis these inhomogeneities are analyzed and used to explain differences between wires and measurement techniques.

The maximum achievable current density is the main parameter of interest for applications. Comparisons between Niobium-Tin wires are mostly made by stating the non-copper critical current density at 12 T or 20 T and 4.2 K or 2.2 K. Efforts to optimize the critical current density have resulted in a linear increase with time. The achieved non-copper critical current density at 12 T and 4.2 K has approximately doubled from 1.7 kA/mm^2 in 1993, to 3 kA/mm^2 in 2003. The key question that this thesis tries to answer is to what extend this non-copper critical current density can be further improved using available wire fabrication technologies. To answer this, detailed knowledge is required on the influence that the A15 inhomogeneities in wires have on the current carrying capacities.

The maximum critical current density depends on the effective field-temperature phase boundary, or more specifically, the effective temperature dependent upper critical field. This boundary changes with A15 composition and the presence of strain and determines, together with the A15 grain size, the achievable critical current density. How the field-temperature boundary changes with A15 composition is known from the literature on well defined, quasi-

homogeneous laboratory samples. How the field-temperature phase boundary changes with strain and how the phase boundary is averaged over the various A15 compositions in a wire is not well understood. It is shown throughout this thesis that the inhomogeneity averaging of the upper critical field per composition can be described through a specific summation (depending on wire layout) of better and worse A15 sections. An estimate of achievable wire performance can then be made by assuming that all the A15 in a wire is of the best observed quality.

To determine the change in critical current density with a shift in the field-temperature phase boundary, also the scaling relations for the critical current density with magnetic field, temperature and strain are re-evaluated. The temperature dependence of the upper critical field in well defined and quasi-homogeneous samples can be reasonably understood on the basis of the microscopic theory of superconductivity. These descriptions have also been verified in the literature by measurements of the temperature dependent upper critical field over the full range of relevance (i.e. approaching 30 T). This yields upper critical fields ranging from 24.5 T up to 29 T, depending on A15 composition. The scaling relations for the critical current density in wires, on the contrary, contain only empirical descriptions for an extrapolated, effective upper critical field. The relations are mainly validated for the lower half of the magnetic field range (typically up to 15 T), since high magnetic field measurements of the upper critical field in wires are sparse. This leads to a large uncertainty in the magnitude of the upper critical field in wires, for which (extrapolated) values ranging from about 20 T up to more than 32 T have been stated.

In this thesis it is shown that the empirical based temperature dependence of the upper critical field can be replaced by a better founded, existing microscopic alternative. This alternative description is validated for all available measured upper critical fields and also confirmed using measurements of the upper critical field in a multitude of wires over the full relevant magnetic field range up to 30 T. It is shown that differences between extrapolated, effective upper critical fields in wires originate from differences in Tin gradients and inhomogeneity averaging, but that the best A15 sections in all wires are very similar. The alternative description for the upper critical field in Niobium-Tin superconductors is used to develop a new scaling relation for the critical current density in wires with a significantly improved accuracy for the temperature dependence.

Also the strain dependence of the critical properties of Niobium-Tin is re-evaluated. The available strain sensitivity descriptions are summarized and a new description is proposed which is based on an existing empirical relation. The existing relation is modified to account for asymmetry in strain dependency results which is predicted from microscopic based relations and also observed experimentally. This new relation is verified using strain dependence results of the critical current density in wires and implemented in the proposed new relation for the critical current density as function of magnetic field, temperature and strain. The improved scaling relation is verified using critical current measurements in magnetic fields ranging from 1 to 13 T, temperatures from 4.2 to 16 K and longitudinal strains from −1 to +0.6%.

Finally the maximum performance boundary for the present generation Niobium-Tin wires is estimated based on the observed compositional variations and upper critical field versus temperature results. This boundary is determined to be at a magnetic field of 30 T and a temperature of 18 K, combined with a non-copper critical current density of 5 kA/mm^2 at 12 T and 4.2 K.

Samenvatting (Summary in Dutch)

Samenvatting

Supergeleidende magneten voor hoge energie fysika, kernfusie en kernmagnetische resonantie toepassingen (MRI en NMR), maken gebruik van de extreem hoge stroomdichtheden die bereikt kunnen worden in supergeleiders in vergelijking met normaalgeleidende materialen. Deze magneten zijn over het algemeen geconstrueerd uitgaande van een koperdraad met een diameter van ongeveer 1 mm, met daarin het supergeleidende materiaal in de vorm van filamenten met een karakteristieke diameter van 2 tot 50 micrometer. Het huidige standaard materiaal voor toepassingen is Niobium-Titaan. Dit materiaal behoudt zijn supergeleidende eigenschappen tot het bovenste kritieke magnetisch veld van ongeveer 14 T en tot een kritieke temperatuur van ongeveer 9 K en de supergeleidende eigenschappen zijn vrijwel onafhankelijk van rek. De fabrikagetechnieken voor Niobium-Titaan supergeleidende draden zijn, volgens de huidige kennis, zo ver geoptimaliseerd dat de maximale stroomvoerende eigenschappen bereikt zijn. Toekomstige verbeteringen in toepassingen, die gebruik maken van magneten die werken voorbij het toepassingsgebied van Niobium-Titaan, zullen gebouwd moeten worden met behulp van een alternatief supergeleidend materiaal met superieure specifikaties zoals Niobium-Tin. Ook bestaande toepassingen, zoals NMR, die gebruik maken van de hogere prestaties van Niobium-Tin, kunnen opgewaardeerd worden door Niobium-Tin draden met verbeterde eigenschappen te gebruiken.

De supergeleider Niobium-Tin is momenteel het enige alternatieve materiaal dat voeldoende intwikkeld is voor grootschalige toepassingen en wordt daarom gezien als de opvolger voor Niobium-Titaan in bovengenoemde toepassingen. Het is supergeleidend tot een bovenste kritiek magnetisch veld van ongeveer 30 T en tot een kritieke temperatuur van ongeveer 18 K en verdubbeld dus ongeveer het toepassingsgebied in vergelijking met Niobium-Titaan. Een nadeel van Niobium-Tin is dat de relevante supergeleidende fase (de A15 fase) bros is en dat de supergeleidende eigenschappen sterk afhankelijk zijn van rek. Draden worden gemaakt met het Niobium en het Tin gescheiden binnen de draad en zijn daarom dus rekbaar. De vorming van het A15 gebeurt door een vaste stof diffusiereactie by ongeveer 700 °C, pas nadat de geleider in zijn uiteindelijke vorm in de magneet is gewikkeld. De A15 fase is stabiel van ongeveer 18 at.% Sn tot ongeveer 25 at.% Sn. Korrelgroei tijdens de A15 reactie moet worden voorkomen omdat een kleine korrelgrootte vereist is voor hoge stroomdichtheden. Dit beperkt de reactietemperatuur en de reactietijd. De diffusiereactie is daarom nooit volledig en er wordt geen thermodynamisch evenwicht bereikt, wat resulteerd in de aanwezigheid van Tin gradiënten en dus verschillende A15 composities in de gereageerde draden. In dit proefschrift worden deze inhomogeniteiten geanalyseerd en gebruikt om verschillen tussen draden en meetprocedures te verklaren.

De maximaal haalbare stroomdichtheid is de belangrijkste eigenschap voor de toepassingen. Niobium-Tin draden worden meestal vergeleken door vermelding van de kritieke stroomdichtheid in de niet-koper doorsnede bij 12 T of 20 T bij 4.2 K of 2.2 K. Onderzoek met als doel de kritieke stroomdichtheid te optimaliseren heeft geresulteerd in een lineaire toename met de tijd. De behaalde niet-koper kritieke stroomdichtheid bij 12 T en 4.2 K is ongeveer verdubbeld van 1.7 kA/mm^2 in 1993, tot 3 kA/mm^2 in 2003. De belangrijkste vraag die dit proefschrift tracht te beantwoorden is in hoeverre deze niet-koper kritieke stroomdichtheid verder kan worden verhoogd, uitgaande van de bestaande draadfabrikagetechnieken. Om dit te beantwoorden is gedetailleerde kennis nodig over de invloed van de A15 inhomogeniteiten in draden op de stroomvoerende eigenschappen.

De maximale kritieke stroomdichtheid hangt af van de effectieve veld-temperatuur fasegrens, of meer specifiek, het effectieve temperatuur afhankelijke bovenste kritieke veld. Deze grens verandert met de A15 samenstelling en de aanwezigheid van rek en bepaalt, samen met de A15 korrelgrootte, de haalbare kritieke stroomdichtheid. Hoe de veld-temperatuur grens verandert met de A15 samenstelling is bekend uit de literatuur voor goed gedefiniëerde, quasi-homogene laboratorium testmaterialen. Hoe de veld-temperatuur fase grens verandert met rek en hoe de fasegrens wordt gemiddeld over de verschillende A15 samenstellingen in een draad is onduidelijk. In dit proefschrift wordt aangetoond dat het middelen over de inhomogeniteiten van de bovenste kritieke velden per compositie beschreven kan worden door een specifieke sommatie (die afhangt van de draad opbouw) van betere en slechtere A15 gebieden. Een afschatting van haalbare draadeigenschappen kan vervolgens worden gemaakt door aan te nemen dat al het A15 in de draad van de als best waargenomen kwaliteit is.

Om te bepalen hoeveel de kritieke stroomdichtheid verandert door een verschuiving in de veld-temperatuur fasegrens worden tevens de schalingsrelaties voor de kritieke stroomdichtheid als functie van magnetisch veld, temperatuur en rek opnieuw belicht. De temperatuur-afhankelijkheid van het bovenste kritieke veld in goed gedefiniëerde en quasi-homogene testmaterialen is redelijk goed te beschrijven met de microscopische theorie van supergeleiding. Deze beschrijvingen zijn tevens geverifieerd in de literatuur met metingen van het temperatuur afhankelijke bovenste kritieke veld over het gehele relevante gebied (naderend tot 30 T). Dit resulteert in bovenste kritieke velden in het bereik van 24.5 T tot 29 T, afhankelijk van de A15 samenstelling. De schalingsrelaties voor de kritieke stroomdichtheid in draden bestaan echter alleen uit empirische vergelijkingen voor een geëxtrapoleerd, effektief bovenste kritiek veld. De relaties zijn voornamelijk geverifieerd voor de onderste helft van het magneetveldbereik (voornamelijk tot 15 T), omdat metingen van het bovenste kritieke veld in hoger magneetveld voor draden maar sporadisch onderzocht is. Dit leidt tot een grote onzekerheid in de waarde van het bovenste kritieke veld in draden, waarvoor (geëxtrapoleerde) waarden in het bereik van 20 T tot meer dan 32 T worden vermeld.

Dit proefschrift laat zien dat de empirisch gebaseerde temperatuurafhankelijkheid van het bovenste kritieke veld vervangen kan worden door een beter onderbouwd, bestaand alternatief uit de microscopische theorie. Deze alternatieve beschrijving is geverifieerd voor alle beschikbare gemeten bovenste kritieke velden en is tevens bevestigd gebruikmakend van metingen van het bovenste kritieke veld in een veelvoud van draden over het volledige relevante magneetveldbereik tot 30 T. Er wordt aangetoond dat de verschillen tussen geëxtrapoleerde, effektieve bovenste kritieke velden in draden het gevolg zijn van verschillen in Tin gradienten en middeling over de inhomogeniteiten, maar dat de beste A15 secties in alle draden vrijwel identiek zijn. De alternatieve beschrijving voor het bovenste kritieke veld in Niobium-Tin supergeleiders wordt gebruikt om een nieuwe schalingsrelatie te ontwikkelen voor de kritieke stroomdichtheid in draden met een substantieel verbeterde nauwkeurigheid voor de temperatuurafhankelijkheid.

Tevens wordt de rekgevoeligheid van de kritieke eigenschappen van Niobium-Tin opnieuw belicht. De beschikbare beschrijvingen voor de rekafhankelijkheid worden samengevat en een nieuwe beschrijving wordt geïntroduceerd, gebaseerd op een bestaande empirische relatie. De bestaande relatie is aangepast om rekening te houden met asymmetrie in de resultaten van de rekafhankelijkheid zoals voorspeld wordt door microscopisch gebaseerde relaties en zoals tevens experimenteel wordt waargenomen. Deze nieuwe relatie is geverifieerd aan de hand van resultaten voor de rek afhankelijkheid van de kritieke stroomdichtheid in draden en

geimplementeerd in de voorgestelde nieuwe relatie voor de kritieke stroomdichtheid als functie van mageneetveld, temperatuur en rek. De verbeterde schalingsrelatie is geverifieerd met behulp van metingen van de kritieke stroomdichtheid in magneetvelden van 1 tot 13 T, over een temperatuurbereik van 4.2 tot 16 K en voor longitudinale rek van −1 tot +0.6%.

Uiteindelijk is het maximaal haalbare toepassingsgebied voor de huidige generatie Niobium-Tin draden geschat op basis van waargenomen compositievariaties en resultaten voor het bovenste kritieke veld als functie van de temperatuur. Deze grens is vastgesteld op een magneetveld van 30 T en een temperatuur van 18 K, gecombineerd met een niet-koper kritieke stroomdichtheid van 5 kA/mm^2 bij 12 T en 4.2 K.

Peer Reviewed Publications

Peer reviewed publications

1. A. Godeke, M.C. Jewell, C.M. Fisher, A.A. Squitieri, P.J. Lee and D.C. Larbalestier, *The Upper Critical Field of Filamentary Nb_3Sn Conductors*, J. Appl. Phys. **97**, 093909 (2005).
2. A. Godeke, M. Dhalle, A. Morelli, L. Stobbelaar, H. van Weeren, H.J.N. van Eck, W. Abbas, A. Nijhuis, A. den Ouden and B. ten Haken, *A New Device to Investigate the Axial Strain Dependence of the Critical Current Density in Superconductors*, Rev. Sci. Instr. **75**, 5112 (2004).
3. M.C. Jewell, A. Godeke, P.J. Lee and D.C. Larbalestier, *The Upper Critical Field of Stochiometric and Off-Stochiometric Bulk, Binary Nb_3Sn*, Adv. Cryo. Eng. **50B**, 474 (2004).
4. A. Godeke, M.C. Jewell, A.A. Golubov, B. ten Haken and D.C. Larbalestier, *Inconsistencies Between Extrapolated and Actual Critical Fields in Nb_3Sn Wires as Demonstrated by Direct Measurements of H_{c2}, H^* and T_c*, Supercond., Sci. Techn. **16**, 1019, (2003).
5. A. Godeke, B. ten Haken and H.H.J. ten Kate, *Toward an accurate scaling relation for the critical current in niobium-tin conductors*, IEEE Trans. Appl. Supercond. **12**, 1029, (2002).
6. A. Godeke, B. ten Haken and H.H.J. ten Kate, *The deviatoric strain description of the critical properties of Nb_3Sn conductors*, Physica C: Supercond. **372-376**, 1295, (2002).
7. A. Godeke, O.A. Shevchenko, J.J. Rabbers, B. ten Haken, C.J.G. Spoorenberg, P. Klein Schiphorst, G.C. Damstra and H.H.J. ten Kate, *Performance test results of a low-loss 1MVA BSCCO resonator coil system*, Physica C: Supercond. **372-376**, 1719, (2002).
8. A. Nijhuis, H.G. Knoopers, Y. Ilyin, A. Godeke, B. ten Haken, H.H.J. ten Kate, *Effect of self-field and current non-uniformity on the voltage-temperature characteristic of the ITER central solenoid insert coil by numerical calculations*, Cryogenics **42**, 469, (2002).
9. A. Godeke, O.A. Shevchenko, J.J. Rabbers, B. ten Haken, H.H.J. ten Kate, C.J.G. Spoorenberg, P. Klein Schiphorst and G.C. Damstra, *Construction and Test of a 1MVA-Class High-T_c Resonator Coil*, IEEE Trans. Appl. Supercond. **11**, 1570, (2001).
10. A. Godeke, H.J.G. Krooshoop, B. ten Haken and H.H.J. ten Kate, *Experimental Verification of the Temperature and Strain Dependence of the Critical Properties in Nb_3Sn Wires*, IEEE Trans. Appl. Supercond. **11**, 1526, (2001).
11. O.A. Shevchenko, J.J. Rabbers, A. Godeke, B. ten Haken and H.H.J. ten Kate, *V-I curves of 100kVA class high-T_c resonator coil*, IEEE Trans. Appl. Supercond. **11**, 2204 (2001).
12. A. Godeke, O.A. Shevchenko, H.J.G. Krooshoop, B. ten Haken, H.H.J. ten Kate, G. Rutten, B. Broeren, C.J.G. Spoorenberg, A. Scholten, P. Klein Schiphorst, G.C. Damstra, *An Optimized BSCCO/Ag Resonator Coil for Utility Use*, IEEE on Appl. Supercond. **10**, 849, (2000).
13. O.A. Shevchenko, A. Godeke, H.J.G. Krooshoop, J.J. Rabbers, B. ten Haken, G.C. Damstra, G. Rutten, C.J.G. Spoorenberg, H.H.J. ten Kate, *A High-T_c Resonator Coil with an Air-Gap Iron Yoke*. Inst. Phys. Conf. Ser. **167**, 1147, (2000).
14. A. Godeke, B. ten Haken, H.H.J. ten Kate, *Scaling of the Critical Current in ITER Type Niobium-tin Superconductors in Relation to the Applied Field, Temperature and Uni-axial Applied Strain*, IEEE Trans. Appl. Supercond. **9**, 161 (1999).

15. H.W. Weijers, Q.Y. Hu, Y.S. Hascicek, A. Godeke, Y. Vouchkov, E. Celik, J. Schwarz, K. Marken, W. Dai, J. Parrell, *Development of 3T Class Bi2212 Insert Coils for High Field NMR*, IEEE Trans. Appl. Supercond. **9**, 563 (1999).
16. B. ten Haken, A. Godeke, H.H.J. ten Kate, *The Strain Dependence of the Critical Properties of Nb_3Sn Conductors*, J. Appl. Phys. **85**, 3247 (1999).
17. B. ten Haken, A. Godeke, H.H.J. ten Kate, *The Strain Dependence of ITER Related Nb_3Sn Superconductors in the Temperature Range from 4 to 10 Kelvin*, Proc. MT-15 Conf. Beijing, China, eds. L. Liangzhen, S. Guoliao, Y. Luguang, ISBN 7-03-006720-7/TN.204, 985 (1998).
18. O.A. Shevchenko, J.J. Rabbers, A. Godeke, B. ten Haken and H.H.J. ten Kate, *AC Loss in a High Temperature Superconducting Coil*, Physica C: Supercond. **310**, 106 (1998).
19. A. Godeke, A. Nijhuis, B. ten Haken, P. Bruzzone and H.H.J. ten Kate, *Angular Dependence of Critical Current versus Magnetic Field in Nb_3Sn Wires at 9-15 T*, Proc. EUCAS'97 Veldhoven, The Netherlands, Appl. Supercond. ISBN 0750304871 **158**, 917 (1997).
20. B. ten Haken, A. Godeke and H.H.J. ten Kate, *Investigation of Microscopic Strain by X-ray Diffraction in Nb_3Sn Tape Conductors Subjected to Compressive and Tensile Strains*, Adv. Cryog. Eng. (Materials) **42B**, 1463, (1997).
21. B. ten Haken, A. Godeke, H.J. Schuver and H.H.J. ten Kate, *Strain Reduced Critical Current in Bi-2223/Ag Superconductors under Axial Tension and Compression*, Adv. Cryog. Eng. (Materials) **42B**, 651, (1997).
22. B.A. Smith, J.R. Hale, A. Zhukovsky, P.C. Michael, J. Minervini, M.M. Olmstead, G.L. Dekow, J. Rosati, R.J. Camille, C.Y. Gung, D. Gwinn, F. Silva, S. Fairfax, S. Shen, H.G. Knoopers, W.A.J. Wessel, H.J.G. Krooshoop, O.A. Shevchenko, A. Godeke and H.H.J. ten Kate, *PTF; a New Facility for Pulse Field Testing of Large Scale Superconducting Cables and Joints*, IEEE Trans. Appl. Supercond. **7**, 1049. (1997).
23. H.G. Knoopers, W.A.J. Wessel, H.J.G. Krooshoop, O.A. Shevchenko, A. Godeke, H.H.J. ten Kate, B.A. Smith, R.J. Camille and J. Minervini, *Fast Ramp 50kA Superconducting Transformer for Testing Full-size ITER Cable Joints*, Proc. 16th Intern. Cryogenic Eng. Conf. (ICEC), Kitakyushu, Japan. ISBN 0-08-042688-3, 803, (1997).
24. B. ten Haken, A. Godeke, H.J. Schuver and H.H.J. ten Kate, *A Descriptive Model for the Critical Current as a Function of Axial Strain in Bi-2212/Ag Wires*, IEEE Trans. Magn. **32**, 2720, (1996).
25. B. ten Haken, A. Godeke, H.H.J. ten Kate and W. Specking, *The Critical Current of Nb_3Sn Wires for ITER as a Function of Axial Tension and Compression*, IEEE Trans. Magn. **32**, 2720, (1996).
26. B. ten Haken, A. Godeke and H.H.J. ten Kate, *The Influence of Compressive and Tensile Axial Strain on the Critical Properties of Nb_3Sn conductors*, IEEE Trans. Appl. Supercond. **5**, 1909, (1995).
27. B. ten Haken, A. Godeke and H.H.J. ten Kate, *A Reversible Rise in the Critical Current of a Nb_3Sn-bronze Tape due to a Transverse Pressure*, Proc. EUCAS'95, Appl. Supercond., Inst. of Phys. Conf. Series **148**, 85, (1995).

28. B. ten Haken, A. Godeke and H.H.J. ten Kate, *The Influence of Various Strain Components on the Critical Parameters of Layer Shaped Nb_3Sn*, Adv. Cryog. Eng. (Materials) **40**, 875, (1994).

29. H.H.J. ten Kate, B. ten Haken, A. Godeke and J. Tenbrink, *The Influence of Tension and Compression on the Critical Current Density in BSCCO-2212/Ag Wires and Tapes.* Critical Currents in Superconductors, ed. H.W. Weber, World Scientific, London, 549, (1994).

30. B. ten Haken, A. Godeke and H.H.J. ten Kate, *Calculation of the Critical Current Reduction in a Brittle Round Multifilamentary Wire due to External Forces*, IEEE Trans. Magn. **30**, 1867, (1994).

31. H.W. Weijers, A. Godeke, B. ten Haken, W.A.J. Wessel and H.H.J. ten Kate, *Improved Superconducting Direct Current Meter for 25-50 kA*, Adv. Cryog. Eng. **39**, 1147, (1994).

32. B. ten Haken, A. Godeke and H.H.J. ten Kate, *New Devices for Measuring the Critical Current in a Tape as a Function of the Axial and Transverse Strain, the Magnetic Field and Temperature*, IEEE Trans. Appl. Supercond. **3**, 1273 (1993).

Arno Godeke

Performance Boundaries in Nb_3Sn Superconductors

ISBN 90-365-2224-2

Uitnodiging

Hierbij nodig ik u uit voor het bijwonen van de openbare verdediging van mijn proefschrift

op vrijdag
15 Juli 2005
om 15:00 uur.

De verdediging zal plaatsvinden in zaal 2 van het gebouw Spiegel op de campus van de Universiteit Twente. Voorafgaand aan de verdediging zal ik om 14:45 uur het proefschrift kort toelichten.

Aansluitend aan de plechtigheid zal er een receptie worden verzorgd.

Paranimf:
Nina Godeke

Arno Godeke
Landmansweg 94
7556 LX Hengelo
074 - 2596643